Theoretical and Experimental Studies of Semiconductor Based Photonic Devices for All-Optical Signal Processing at 40 Gbit/s and Beyond

Minh Nguyet Ngo

HAL Id: tel-00554333

https://theses.hal.science/tel-00554333

Submitted on 10 Jan 2011

UNIVERSITÉ DE RENNES 1

ueb

Thèse / Université de Rennes 1
sous le sceau de l'Université Européenne de Bretagne

pour le grade de
Docteur de l'Université de Rennes 1
Mention : Physique
École Doctorale : Sciences de la Matière
présentée par

Minh Nguyêt Ngô

préparée à l'unité de recherche Foton CNRS UMR 6082
Équipe Foton-Enssat/FOT et PERSYST
U.F.R. S.D.L.M.

Theoretical and Experimental Studies of Semiconductor Based Photonic Devices for All-Optical Signal Processing at 40 Gbit/s and Beyond

**Thèse soutenue à Lannion
le 20/07/2010**

devant le jury composé de :

Hervé FOLLIOT
Professeur - INSA de Rennes / *Président*

Jean-Louis OUDAR
Directeur de Recherche CNRS - LPN / *Rapporteur*

Daniel DOLFI
Ingénieur de Recherche, Expert - Thales R&T / *Rapporteur*

Ernesto CIARAMELLA
Maître de Conférences - Scuola Superiore Sant'Anna / *Examinateur*

Romain BRENOT
Ingénieur de Recherche et de Formation- Alcatel-Lucent Thales III-V Lab / *Examinateur*

Jean-Claude SIMON
Professeur - Université de Rennes 1 / *Directeur de thèse*

To Grandma,
to Dad,
to Mom
to my dear sis.

A ma grand-mère,
à mes parents
à ma p'tite-soeur.

Remerciements

Cette thèse comme beaucoup d'autres ne peut pas être menée à bien sans la collaboration et le soutien de nombreuses personnes.

Avant tout, je voudrais exprimer toute ma gratitude à Jean-Claude Simon, directeur du laboratoire FOTON, pour m'avoir accueilli dans son laboratoire et surtout pour sa direction de cette thèse. Jean-Claude a su être efficace malgré les lourdes tâches qui l'incombaient.

Je tiens évidemment à remercier les membres du jury, Jean-Louis Oudar, Daniel Dolfi, pour avoir accepter d'être rapporteurs, Hervé Folliot, Romain Brenot et Ernesto Ciaramella pour avoir d'accepter de participer à l'évaluation de mes travaux lors de la soutenance.

On n'oublie pas ses premiers pas. Je souhaite remercier particulièrement Gwenaëlle Vaudel et Vincent Roncin pour m'avoir fait découvrir le monde de la recherche en m'accompagnant pendant toutes premières manips et tous premiers articles.

Les travaux de cette thèse ne sont certainement pas menés jusqu'aux résultats aujourd'hui sans le travail quotidien de l'équipe du platforme Persyst. Je voudrais remercier Laurent Bramerie et Mathilde Gay pour tous leurs conseils et tout le temps qu'ils m'ont accordée, Sébastien Lobo pour avoir été toujours disponible dans le laboratoire, Marcia De Costa Silva et Kévin Lenglé pour m'avoir accompagnée avec leur bonne humeur.

Merci à Arthur O'Hare, avec qui j'ai travaillé pendant tout un été à la fin de la thèse. Un moment 'stressant' a devenu finalement un bon souvenir. Son air apaisant, son humour, ses histoires m'ont donné la force pour rester optimiste et motivée. Un ami à qui j'ai partagé des moments inoubliables.

Je n'oublie pas des gens qui ont donné beaucoup de temps pour me transférer leurs compétences et leurs précieuses expériences. Merci à Monique Thual pour m'avoir appris à faire des fibres microlentillées (que j'en fait pleines plus tard), merci à Philippe Rochard pour m'avoir appris à faire des modules de laser (que je puisse en fait toute seule maintenant comme une grande). Et merci à Stéphane Balac qui m'a fait tellement progressé sur mes compétences en modélisation.

Je tiens aussi à remercier toutes les personnes du laboratoire FOTON avec lesquelles j'ai pu travaillé ou simplement passé un bon café ensemble : Pascal Bernard, Thierry Chartier, Patrice Féron, Jean-Marc Goujon, Olivier Vaudel, Stéphane Blin, Jean-François Hayau, Alexandra Lagrost, Sylvain Fève, Ronan Le Page. J'ai une pensée particulière aux personnels administratifs et techniques : Danielle Graviou, Réjane Le Roy, Nelly Vaucelle, Catherine Delen, Michelle Grout, Serge Le Flécher, Henry L'her, Michel Guillou, Stéphane Chehayed, Christian Sauquet, sans qui je n'aurai pas eu un esprit aussi libre pour plonger dans mon travail dans le laboratoire.

Je voudrais également remercier Liam Barry, Douglas Reid, Jesper Mork, Mike Van Der Poel, Per Lunnemann Hansen, Sara Ek pour m'avoir accueilli pendant plusieurs semaines dans leurs laboratoires à Dublin et à Copenhague. Avec peu de temps mais si bon environnement, j'ai pu profité des échanges d'idées très fructueux.

J'adresse une grande gratitude à Irène et Michel Joindot, qui ont accepté de relire le manuscrit, sans qui le rapport de thèse n'aura certainement pas la qualité d'aujourd'hui.

Merci à mes amis : Ngoc, Romain, Shan, et mes amis vietnamiens à Lannion pour leur amitié et leur humour.

Merci à ma famille pour leur inconditionnel amour et leur confiance (comme toujours). Merci à Trung qui était toujours là, à mes côtés et qui a devenu ma famille.

Contents

List of Acronyms

1R	Reamplifying
2R	Reshaping Reamplifying
3R	Retiming Reshaping Reamplifying
AR	Anti-Reflection
ASE	Amplified Spontaneous Emission
ASK	Amplitude Shift Keying
BER	Bit Error Rate
BG-FP filter	Bragg Grating Fabry-Perot filter
BH	Buried Heterostructure
BP	Band-Pass
CB	Conduction Band
CH	Carrier Heating
CR	Clock Recovery
CW	Continuous Wave
DBR	Distributed Bragg Reflector
DCF	Dispersion Compensating Fibre
DFB	Distributed FeedBack
DGD	Differential Group Delay
DH	Double Heterojunctions
DI	Delay Interferometer
DPSK	Differential Phase Shift Keying
DSF	Dispersion Shifted Fibre
EA	ElectroAbsorption
EAM	ElectroAbsorption Modulator
EDFA	Erbium Doped Fibre Amplifier
ER	Extinction Ratio
ETDM	Electrical Time Division Multiplexing
FEC	Forward Error Correction Code
FSK	Frequency Shift Keying
FSR	Free Spectral Range
FWM	Four Wave Mixing
FTTH	Fiber To The Home
GVD	Group Velocity Dispersion
HNL	Highly Non-Linear
IC	Integrated Circuit
ISI	InterSymbole Interference

LAN	Local Area Network
MAN	Metro Area Network
MFD	Mode Field Diameter
NF	Noise Figure
NOLM	Non-linear Optical Loop Mirror
NRZ	Non Return to Zero
NZ-DSF	Non Zero Dispersion Shifted Fibre
OC	Optical Circulator
OCR	Optical Clock Recovery
OSA	Optical Spectrum Analyser
OSNR	Optical Signal to Noise Ratio
OSO	Optical Sampling Oscilloscope
OTDM	Optical Time Division Multiplexing
PC	Polarisation Controller
PLL	Phase Locked Loop
PMD	Polarisation Mode Dispersion
PON	Passive Optical Network
PRBS	Pseudo Random Bit Sequence
PSD	Power Spectral Density
PSK	Phase Shift Keying
QD	Quantum-Dot
QW	Quantum-Well
QWR	Quantum-Wire
RF	Radio Frequency
RMS	Root-Mean Square
R-SOA	Reflective Semiconductor Optical Amplifier
RZ	Return to Zero
SA	Saturable Absorber
SBS	Stimulated Brillouin Scattering
SHB	Spectral Hole Burning
SMF	Single Mode Fibre
SOA	Semiconductor Optical Amplifier
SOA-MZI	SOA-based Mach-Zehnder Interferometer
SP	Self-Pulsating
SPM	Self Phase Modulation
SRS	Stimulated Raman Scattering
SSB	Single Side Band
TDM	Time Division Multiplexing
TE	Transverse Electric
TM	Transverse Magnetic
TPA	Two Photon Absorption
VB	Valence Band
VCO	Voltage Controlled Oscillator
VOA	Variable Optical Attenuator
WAN	Wide Area Network
WDM	Wavelength Division Multiplexing
WL	Wetting Layer
XGM	Cross Gain Modulation
XPM	Cross Phase Modulation

List of Figures

List of Tables

Introduction

Today, information is transmitted throughout the world mainly through digital communication systems with a bit rate, expressed in number of transmitted bits per second, depending on the applications. Data flow from your USB key to your computer at typical speed of 480 Mbit/s. Internet providers announce 100 Mbit/s subscriber connections thanks to recent FTTH (Fibre-To-The-Home) deployments [5]. The optical fibres of the SEA-ME-WE 3 cables [6], which connect 33 countries and 4 continents from Western Europe (including France) to the Far East (including Vietnam) and Australia, offer a total capacity of 480 Gbit/s (48 wavelengths carrying 10 Gbit/s). Regardless of the position in the networks, the bandwidth demand grows continuously, mainly due to the growth of data traffic. The transmission capacity of the optical fibre links can be expanded by increasing both the number of WDM (Wavelength Division Multiplexing) channels and the bit rate per WDM channel. The base rate of the backbone networks is likely moving from 10 Gbit/s to 40 Gbit/s [7]. The capacity limit of the present networks is set largely by the use of electronic elements. For the generation 160 Gbit/s TDM systems, while electronic signal processing is not available yet, many fundamental functions based on optical devices are attracting a lot of investigations [8].

In long and ultralong haul links such as submarine intercontinental connections, the transmitted optical signal has to be amplified periodically. For the bit rates exceeding 40 Gbit/s, deployment of only opto-electronic repeaters will increase dramatically the system complexity, cost and power consumption. Long term solutions for signal regeneration in future high capacity optical networks concern all-optical regeneration which could allow optical data transmission over virtually unlimited distances. All-optical regenerators used for future WDM networks must satisfy at least the conditions of low power consumption, compactness, low-cost and WDM compatibility. Since many years, all-optical regenerators and their sub-functions have been extensively studied at FOTON laboratory, where this thesis has been realised. Some important works should be mentioned. A polarisation insensitive 3R regenerator based on semiconductor based NOLM architecture which allows a cascade of at least 1000 repeaters without any detected error has been demonstrated at 10 Gbit/s [9]. At this bit rate, a high performance WDM compatible 2R regenerator based on a Saturable Absorber (SA) and a Semiconductor Optical Amplifier (SOA) allowing the transmission over 11000 km with only 18 cascaded regenerators for a BER of 10^{-4} [10]. 2R and 3R regenerators for 40 Gbit/s operation have been also successfully developed. The 2R regenerator, which is a combination of an SA and a fibre followed by an optical filter, allows a distance improvement ratio of at least 3.3 among its 8 channels [11]. The regenerator is WDM compatible and potentially low-cost. 3R regeneration using synchronous modulation allows significant margin enhancements on receiver decision time and threshold to be obtained [12]. The transmission distance has been also improved from 13000 km to 90000 km in comparison with 2R regeneration case (without the synchronous modulation). Such 3R regeneration quality could not be obtained without the Optical Clock Recovery (OCR) consisting of a cascade of a bulk based Self-Pulsating (bulk-SP) laser and a Quantum-Dot

Self-Pulsating (QD-SP) laser. The good timing jitter filtering of the OCR is attributed to the QD-SP laser, which was demonstrated multi-data-rate compatible [13] and therefore totally adequate for applications in high bit rate OTDM systems.

The key elements of the all-optical regenerators are non-linear optical gate and OCR device. The objectives of this thesis were to develop and explore different non-linear gates and OCRs based on semiconductor technology for optical signal regeneration at 40 Gbit/s and beyond. As sub-functions for 2R regeneration, non-linear gates based on Semiconductor Optical Amplifier (SOA) were considered. The high non-linearity of the SOA is its greatest advantage for optical signal processing. Besides its cost efficiency, compactness, potential integrability, wide spectral bandwidth and low power consumption are other features which explain why the SOA continues to receive a lot of attention. As far as OCR devices are concerned, different configurations using SP lasers were assessed in system environment. A simple solution was also proposed to enhance the recovered clock quality.

The content of the thesis is divided into two parts with 4 and 2 chapters respectively.

The first part including 4 chapters is dedicated to the results of the investigations on SOA based non-linear optical gates for 2R regeneration.

Chapter 1 outlines basic notions about optical fibre communication systems which are used in the manuscript. The reviewed definitions are point-to-point transmission link, usual modulation formats (RZ and NRZ), transmitter and receiver. Signal degradations during propagation inside optical fibres are described to highlight the need for signal regeneration and typical criteria used to specify signal quality are defined. To limit signal impairments and increase the transmission distance, in-line repeaters are inserted periodically into the fibre link. The repeaters could provide different regeneration capacities. The principles of 1R (Reamplifying), 2R (Reamplifying and Reshaping) and 3R (Reamplifying, Reshaping and Retiming) regenerations are described. Finally, a brief review on SOA based 2R regenerators is presented.

Chapter 2 is devoted to a basic description of Semiconductor Optical Amplifiers and especially their non-linear properties and high speed dynamics which are used for signal regeneration. Under saturation by short pulses (of a few picoseconds), it is found that ultrafast dynamics due to intraband relaxation effects could be exploited for high speed signal processing. Results of experimental study of different SOA structures are summarised. These SOAs have been designed and manufactured by the Alcatel-Lucent Thales III-V Lab in the framework of the French national project FUTUR for all-optical regeneration applications. The experimental investigations are focused on two main aspects: gain non-linearity and gain dynamics. The results suggest that highly confined bulk based SOAs and long quantum-dot SOAs are good candidates for operations at bit rates exceeding 40 Gbit/s. Numerical investigations demonstrate that by associating the long quantum-dot liked sample with assist techniques such as shifted filtering, operation at 160 Gbit/s without patterning

effects could be possible.

Chapter 3 is dedicated to numerical study of the SOA dynamics. According to the experimental results presented in Chapter 2, numerical investigations are necessary to examine the influences of ultrafast processes on the gain dynamics and consequently on the reshaping capability of the SOA based 2R regenerator schemes. A simple phenomelogical SOA model including intraband effects will be useful to realise these preliminary studies. Such an SOA model, based on that proposed by [14] and then developed by [15], allows deeper understanding of SOA gain and phase dynamics to be obtained.

Chapter 4 investigates signal reshaping capability of cascades of an SOA and a saturable absorber. Amplitude noise compression experiments demonstrate the signal regeneration capability of the SOA-SA regenerators. The complementary roles of the SOA and SA in the reshaping task are clarified by analysing noise transformation effects when the two devices operate separately. Finally, a numerical study using the SOA model developed in Chapter 3 explains how the regenerator performance changes when the device intrinsic parameters change.

The second part including 2 chapters is devoted to the study on SP laser based OCR devices for 3R regeneration.

Chapter 5 reviews the different roles of the clock recovery (CR) function in transmission systems. Usual clock extraction techniques and their advantages as well as their limitations are discussed. Especially, the principle and the state-of-the-art of the CR technique using SP semiconductor lasers are detailed.

Chapter 6 presents all experimental assessments realised on different OCR configurations. The optical clock signal extracted by the OCR based on a bulk-SP laser exhibits insufficient quality to be used for regeneration applications. The introduction of a passive pre-filtering in front of the laser is explored to enhance the recovered clock quality. Otherwise, a quantum-dot SP laser allows high quality clock to be obtained but such OCR function is strongly polarisation sensitive. Therefore, polarisation sensitivity of the different OCRs is assessed. At last, a primary study is devoted to OCR resistance to Polarisation Mode Dispersion.

Part I

Semiconductor Optical Amplifiers for 2R Regeneration

Chapter 1

Optical fibre communication systems and all-optical regeneration

In this chapter, basic notions on optical fibre communication systems are reviewed. The basics of all-optical regeneration as well as the devoted techniques are also developed. The purpose of the chapter is to describe the thesis context and to present the essential notions in the manuscript.

In the first section, a basic transmission link concept of optical fibre communication systems is depicted. The largely used modulation formats (NRZ and RZ) are then described. Fundamental elements of the transmission link including transmitter and receiver are discussed. Next, we focus on the main signal degradations induced during the transmission over fibre links. At last, typical criteria used to specify signal quality are defined.

In the second section, all-optical regeneration processes (1R, 2R and 3R) and associated techniques are firstly developed. Secondly, reshaping devices using SOA which are studied during this thesis are discussed. Their different operating configurations are described and a review of literature is also presented.

1.1 Optical fibre communication systems

The optical fibre communication systems can be found in any level of the network: core network, Wide Area Network (WAN), Metro Area Network (MAN), Local Area Network (LAN) and access network. Long haul fibre links (thousands of kilometres) such as submarine cables constitute the backbone or the core of a telecommunication network. A WAN is usually constituted of communication links covering a broad area such as a country. A MAN is optimized for a geographical area ranging from several blocks of buildings to entire cities. A LAN is a network covering a smaller area such as a campus or a building. On one hand, access network are likely in the same order as a LAN. On the other hand, the 'access
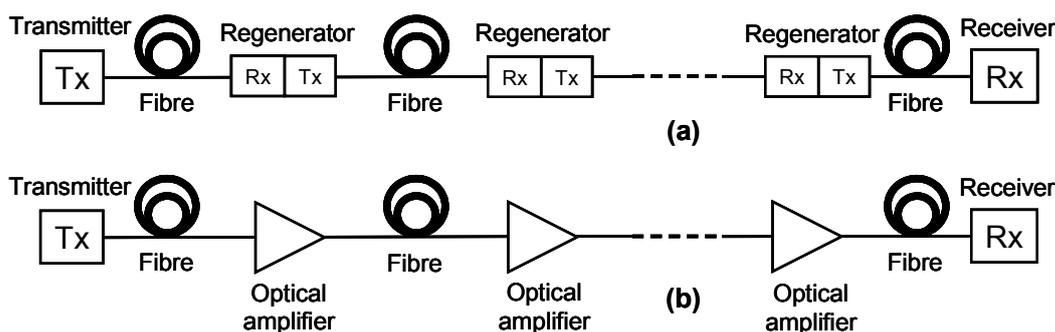
Figure 1.1: Point-to-point fibre links with periodic loss compensation through (a) regenerators and (b) optical amplifiers

network' term refers to the last transmission links which connect final users (subscribers) to their immediate service (telephone, television, Internet) provider. As an example of fibre links in access network, Fibre-To-The-Home (FTTH) service has been available in France from March 2007. All these networks can be designed by using point-to-point, point-to-multipoint, hub, ring or star topology. However, the most practical topology varies from one to another.

1.1.1   Transmission link description

The simplest network topology is probably the point-to-point link which is largely used in fibre submarine connections between continents. For such long distances, two common schemes are used to compensate for the fibre losses as shown in Figure (1.1) (reprinted from [2]). The basic elements of a point-to-point fibre link are the transmitter, the optical fibre, the regenerators or optical amplifiers and the receiver. The transmitter Tx emits an optical signal which is modulated by an electrical signal carrying the information to be sent. The optical fibre is the transmission medium. At the receiver, the optical signal is detected and converted into an electrical signal which is used for the decoding of the transmitted information. Before the invention of the Erbium Doped Fibre Amplifier (EDFA) in the years ninety, the regenerators (Figure (1.1 (a))) were exclusively optoelectronic repeaters. Arriving on the regenerator, the optical signal is converted into electrical signal by a receiver Rx. After being treated in electronic domain, the electrical signal is converted into optical signal to be transmitted further. Since the EDFAs have been available, fibre losses can be compensated for by optical amplifiers (EDFA) directly in the optical domain without any Optic/Electric (O/E) conversion (Figure (1.1 (b))). The system power consumption and the optoelectronic regenerator cost increase rapidly with the data bit rate. In backbone networks, the bit rate per channel is exceeding 40 Gbit/s and it is of great interest to reduce the in-line regenerator cost and consumption. At these ultrahigh speed operations, optical devices are likely more cost competitive and less power-consumption compared to electrical devices. Therefore, all-optical regeneration could have a promising future.
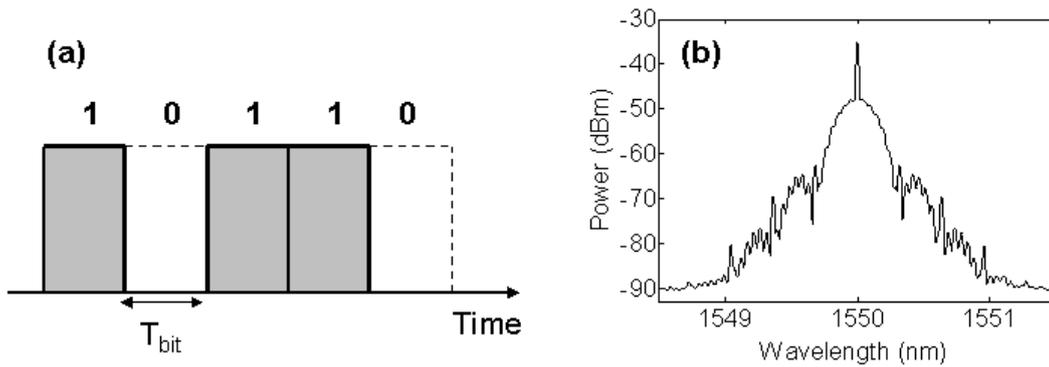
Figure 1.2: Example of an NRZ format signal in time (a) and in spectral domains (b)

1.1.2 Modulation formats

Signals which are transmitted in backbone links as described in Paragraph 1.1.1 rely on digital encoding. This indicates that information is represented by sequences of '1' and '0' symbols called bit sequences. The value of each bit (1 or 0) is related to the transmitted information. The data rate or bit rate is the number of bits transmitted in a time interval of one second and expressed in bit/s. It is also called the bit sequence frequency or the modulation frequency. Each bit corresponds to an elementary interval called bit duration (T_bit) which is equal to the inverse of the bit rate. Modulation formats define the association between bits '0' and '1' and a physical parameter of the optical carrier signal. In general, they could be amplitude modulation (ASK for Amplitude Shift Keying), frequency modulation (FSK for Frequency Shift Keying) or phase modulation (PSK for Phase Shift Keying). The most largely used format in current telecommunication systems is the amplitude modulation. For an optical signal carrying bit streams obtained from an ASK encoding, the '1' symbol is represented by presence of light and '0' symbol is represented by absence of light. The two most common formats of amplitude modulation are NRZ (Non-Return-to-Zero) and RZ (Return-to-Zero).

1.1.2.1 NRZ format

For an NRZ format signal, the signal amplitude is maintained constant during the whole bit duration and remains unchanged between two consecutive bits exhibiting identical symbols. Therefore, there is no return to the zero level between two consecutive '1' symbols. In other words, a succession of several '1' symbols corresponds to a constant intensity of the optical signal during the total duration of all these bits. An example of an NRZ signal in time and spectral domains is displayed in Figure (1.2).
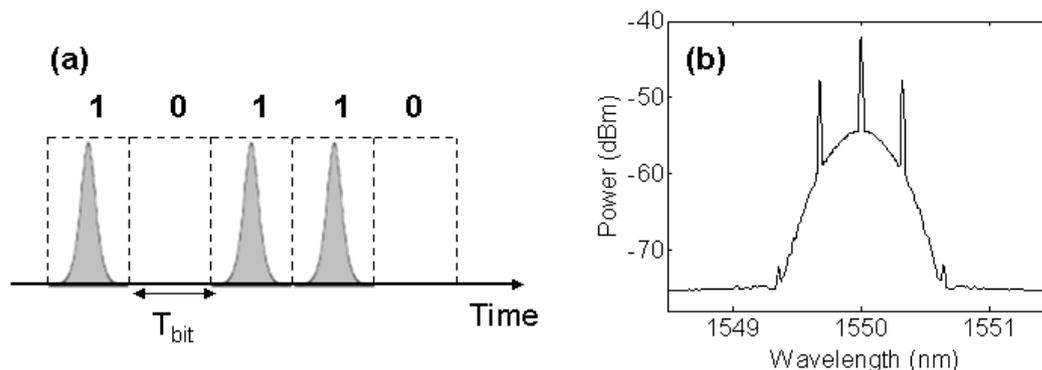
Figure 1.3: Example of an RZ format signal in time (a) and in spectral domain (b)

1.1.2.2   RZ format

For an RZ format signal, the signal amplitude is not always constant during the whole bit duration. A '0' symbol corresponds to absence of light, and a '1' symbol corresponds to presence of light exhibiting time dependent amplitude. In this case, it is said that '1' symbols are expressed by optical pulses. An example of an RZ signal in time and spectral domains is displayed in Figure (1.3).

The NRZ format appears advantageous compared to the RZ format in terms of spectral efficiency. In other words, for the same bit rate, the RZ signal exhibits a larger spectrum bandwidth (Figure (1.3(b))) than the NRZ signal (Figure (1.2(b))). Otherwise, RZ signals are more robust to Polarisation-Mode Dispersion (PMD) [16]. The RZ format became more and more attractive since the soliton transmission potential was demonstrated [17] and the multiplexing technique in time domain was considered. The potential of the RZ format for TDM (Time Division Multiplexing) could be explained by observing Figure (1.3 (a)). The pulse duration is shorter than the bit duration. It is then possible to insert several pulses of different bit streams within one bit interval. By this way, the total data rate can be increased. A TDM signal can be obtained in optical domain (OTDM for Optical Time Division Multiplexing) or in electrical domain (ETDM for Electrical Time Division Multiplexing). At last but not least, another technique called WDM (Wavelength Division Multiplexing) used for line data rate increase should be also mentioned. It consists in transmitting simultaneously different optical signals, which are centred on different wavelengths, in the same optical fibre. In the context of this thesis, all works consider RZ format signals because it is likely the adequate format for future ultrahigh bit rate OTDM systems.

1.1.3   Transmitter

The role of an optical transmitter is to convert an electrical signal carrying data into an optical signal carrying the same data. The generic scheme of a transmitter can be simply depicted as shown in Figure (1.4). The two main components are the laser source and the
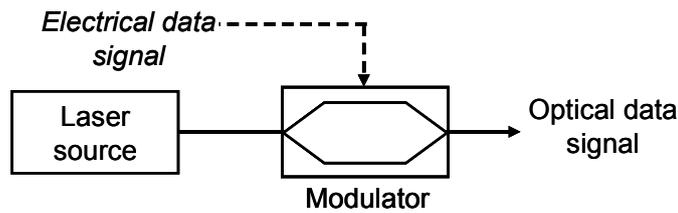
Figure 1.4: Generic scheme of an optical transmitter

modulator. Optical transmission systems often use semiconductor laser sources because they exhibit a lot of advantages for optical fibre communication: compact size, high electron/photon conversion efficiency, emission in the 1550 nm wavelength range, compatibility with the fibre optical mode dimensions and possibility of direct modulation through the injection current. The most widely used semiconductor structure is the Distributed FeedBack (DFB) laser. The laser source provides an optical carrier wave. The optical data signal is obtained by modulating the optical carrier thanks to the modulator. In some cases, the external modulator is not present because the output light of the semiconductor laser is modulated directly through the injection current. The direct modulation possibility allows the transmitter cost to be significantly reduced. However, the technique is rarely used at bit rates exceeding 10 Gbit/s because of the instantaneous frequency changes (chirp) induced by the laser current modulation. In addition to chromatic dispersion, this chirp limits the propagation distance of the ultrahigh bit rate signals. Therefore, an external modulator is used in most cases.

Two common modulator types could be found in current systems: ElectroAbsorption (EA) modulator and $LiNbO_3$ modulator in the Mach-Zehnder configuration. One of the EA modulator advantages is the potential modulation speed as high as 100 GHz. But the most attractive feature that motivates extensive investigations of the EA modulators is that they could be easily integrated on the same chip with a semiconductor laser to achieve compact, low cost, tunable transmitters. A high performance 40 Gbit/s transmitter with wavelength tunability covering the whole C-band was demonstrated [18]. However, the residual chirp on the optical signal generated by EA modulators still limit their application range. Otherwise, the $LiNbO_3$ modulators in the Mach-Zehnder configuration could provide chirpless optical signal. This property, among others, explains their presence in a large number of optical transmission systems. Another great advantage of this type modulator is high on-off ratios (also called extinction ratios) which exceed 20 dB. They could be also modulated at high speeds, up to 75 GHz. Recent advances allow 40 Gbit/s $LiNbO_3$ modulator to be fabricated with commercial compatible processes [19]. To obtain the amplitude modulation formats described in Paragraph 1.1.2, either EA modulators or $LiNbO_3$ modulators can be used.
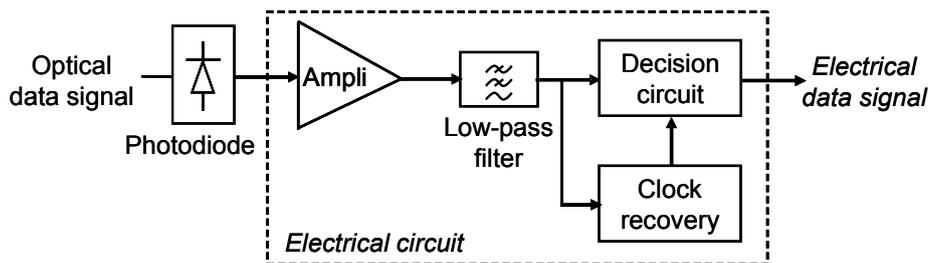
Figure 1.5: Generic scheme of a digital optical receiver

1.1.4   Receiver

Receiver and transmitter are located at the ends of transmission links. If the role of the transmitter is to convert an electrical signal into an optical signal, the conversion from the transmitted optical signal to an electrical signal is performed by the receiver. The generic scheme of a receiver which is used in cases of intensity modulation with direct detection is illustrated in Figure (1.5).

The optical data signal arriving on the receiver is launched firstly onto a photodiode. The photodiode converts the optical data stream into a time-dependent electrical signal which is further completely processed in the electrical domain. In general, an electrical pre-amplifier, which is not displayed in the present generic scheme, is placed behind the photodiode to amplify the electrical signal for further processing. The signal is next amplified by a high-gain amplifier (main amplifier) and filtered by a low-pass filter for noise reduction. In our experiment, the main amplifier is a limiting amplifier which allows the output average voltage to be maintained at a fixed level irrespective of the incident average optical power. After being filtered, the signal is processed by a decision circuit for data recovery. Simultaneously, a fraction of the signal is sent to a clock recovery circuit which provides a time reference for sampling. At a regular rhythm, the decision circuit compares the input voltage to a threshold (also called decision threshold) and takes a decision concerning the detected bit, '1' or '0'.

From a standpoint of data rate growth, it appears likely that a high speed optical transmitter is more difficult to be implemented than a high speed optical receiver. At 10 Gbit/s, all the receiver components, with the exception of the photodiode, are standard electrical components and generally integrated on the same chip. Thanks to remarkable advances in Integrated Circuit (IC) technology developed for high speed microelectronic devices, electronic circuitry for 40 Gbit/s operations is already commercially available. An entirely integrated ETDM receiver operating at 100 Gbit/s has been recently reported [20]. As far as photodetection is concerned, a 100 GHz photodetector is also already commercialized [21] and photodetector bandwidth keeps increasing [22].
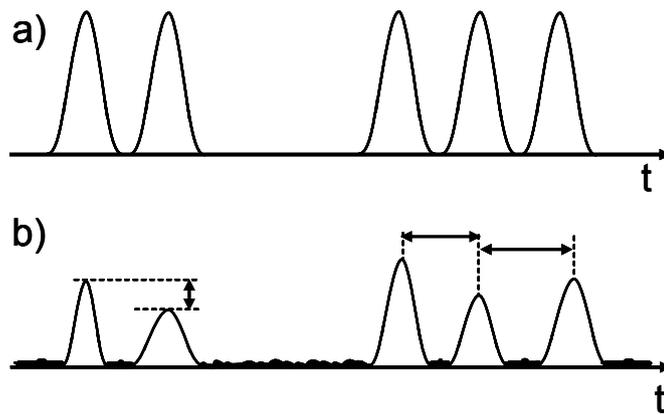
Figure 1.6: Illustration of an RZ format signal at a transmitter output (a) and the signal after a long fibre transmission (b)

1.1.5 Signal degradations

At the transmitter output, the emitted optical signal is coupled into the optical fibre. As any transmission medium, the optical fibre induces undesirable changes of the optical signal characteristics during the propagation, resulting into signal quality degradations. Figure (1.6) illustrates an RZ format signal at a transmitter output (a) and the signal having been degraded after a long fibre transmission (b). At the transmitter output (Figure (1.6 (a))), the optical signal exhibits high quality, i.e all the pulses are identical, all pulse positions are at the centre of the bit slot and all '0' bits correspondent to absence of light (infinite extinction ratio). After the propagation in a long fibre link, the transmitted optical signal exhibits typical degradations such as lower average power, pulse intensity fluctuations, pulse duration fluctuations, pulse position fluctuations and non infinite extinction ratio (Figure (1.6 (b))). The origins of these impairments (fibre losses, chromatic dispersion, polarisation mode dispersion, non-linear effects and amplified spontaneous emission noise) are detailed in this paragraph.

1.1.5.1 Fibre losses

Fibre losses reduce the optical signal power arriving on the receiver and therefore limit the transmission distance. As described previously in the case of a point-to-point link, signal losses are compensated for periodically by in-line optical amplifiers. The distance between the amplifiers is imposed by the transmission channel losses, i.e the fibre losses. Even if some fibre links are long enough to cover the whole globe, it is always of great interest to develop low-loss fibre to increase the transmission distance or reduce the amplifier number and consequently the system cost. Various phenomena occurring in the fibre contribute to the signal attenuation. The two most important causes are material absorption and Rayleigh scattering. The material absorption includes intrinsic and extrinsic losses. The first one corresponds to the absorption by the fibre material itself, i.e fused silica. The second one is
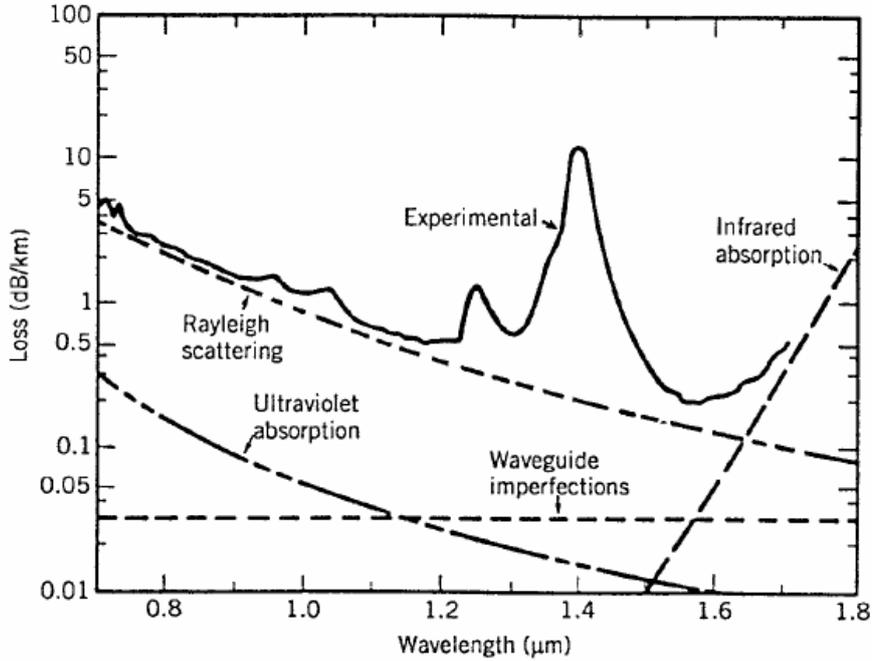
Figure 1.7: Attenuation of a single-mode fibre versus wavelength (reprinted from [1])

due to the presence of impurities. The fibre imperfections and bends constitute also other sources of losses.

The fibre losses depend on the wavelength of the transmitted light. Figure (1.7) reprinted from [1] displays the attenuation of a single mode fibre versus the wavelength. The fibre exhibits a loss of only 0.2 dB/km in the wavelength region near 1.55 μm. This is the explanation of the 1.55 μm wavelength region choice for telecommunications. The two attenuation peaks around 1.24 μm and 1.4 μm correspond to the resonances of the OH ion. The curve of Figure (1.7) is representative for typical current Single-Mode Fibres (SMF) today.

In general, the losses of a fibre are represented by a global loss parameter called attenuation coefficient. The power of the optical signal propagating in a fibre decreases exponentially with the distance. The signal attenuation is governed by Equation (1-1).

$$P_{out}(L) = P_{in}(0) \exp(-\alpha L) \tag{1-1}$$

where α is the attenuation coefficient of the optical fibre. It is commonly referred in dB/km and deduced by using Equation (1-2).

$$a\,(dB/km) = -\frac{10}{L} \log_{10} \left(\frac{P_{out}}{P_{in}} \right) \tag{1-2}$$

Even if the attenuation coefficient is as low as 0.2 dB/km, a 100 km link exhibits an attenuation of 20 dB. It is clear that the fibre losses are the first source of signal degradations. In the undersea systems connecting North America and Europe, optical amplifiers are inserted every 50 km to compensate for the signal attenuation [17].
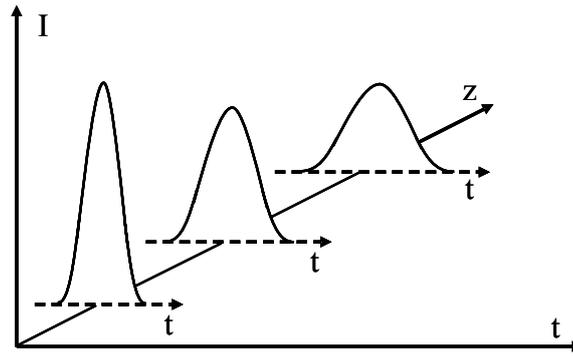
Figure 1.8: Description of pulse broadening due to chromatic dispersion

1.1.5.2 Chromatic dispersion

On one hand, the refractive index of any material, in particular the fused silica, is wavelength-dependent. The phenomenon is called chromatic dispersion or Group Velocity Dispersion (GVD). It implies that signals at different wavelengths (or frequencies) propagate at different velocities in an optical fibre. On the other hand, no optical signal is ideally monochromatic, it has always a finite spectral bandwidth. Thus, the different spectral components of the transmitted optical signal slide far from each other as the propagation distance increases. In an SMF, the spectral components of the pulse at short wavelengths travel faster than those at longer wavelengths. The chromatic dispersion impacts on system performance by broadening the propagating pulses as described in Figure (1.8). When the pulse broadening is large enough, the unwanted phenomenon - intersymbol interference (ISI), i.e pulse overlapping, takes place. For a typical single-mode fibre, the chromatic dispersion is mainly due to the material dispersion and the modal dispersion. The material dispersion represents the intrinsic wavelength-dependent of the material refractive index. The modal dispersion represents the wavelength-dependent of the propagation constant of the guided modes.

The chromatic dispersion of a conventional SMF fibre and the relative contributions of the material and modal dispersions are depicted in Figure (1.9). The dispersion parameter D is expressed in ps/nm/km. In the 1.55 μm window, D is about 17 ps/nm/km. The dispersion parameter cancels around 1.3 μm.

If the spectral width of the emitted signal is given, the pulse broadening can be estimated at any transmission distance. The chromatic dispersion imposes a limit on the maximum transmission distance without signal regenerating. A specific distance called dispersion length is defined by Equation (1-3).

$$L_D = \frac{T_0^2}{|\beta_2|}$$
(1-3)

with T_0 and β_2 are respectively the pulse duration and the second-order dispersion at the
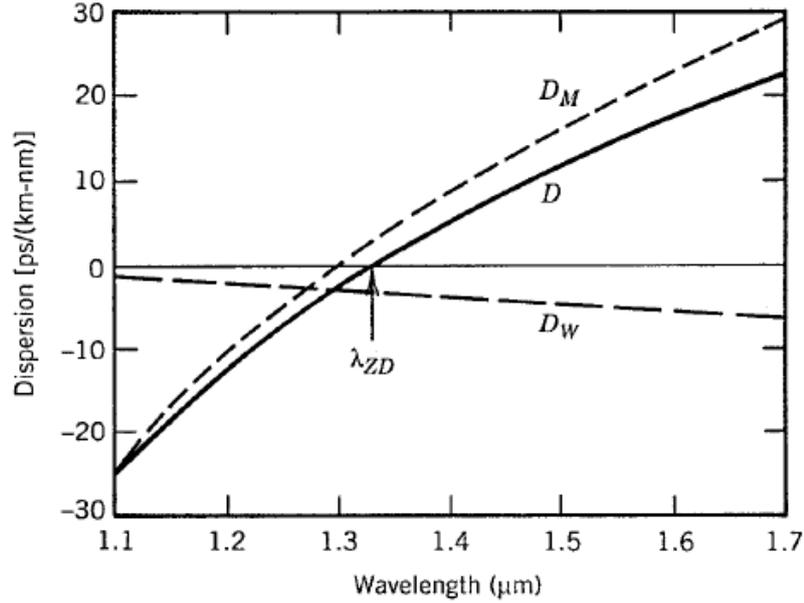
Figure 1.9: Total dispersion parameter D and relative contributions of material dispersion D_M and waveguide dispersion D_W for a conventional single mode fibre (reprinted from [2])

signal wavelength. If a Gaussian pulse is considered, L_D is the transmission distance at which the pulse has broadened by a factor of $\sqrt{2}$. Equation (1-3) indicates also that when the data rate increases, the dispersion length decreases rapidly because the pulse duration is shorter. Similar to the signal degradations caused by the fibre losses, it appears clearly that the signal degradations caused by the chromatic dispersion have to be compensated for in high bit rate systems. The conventional fibre exhibits unfortunately zero dispersion at 1.3 μm and not at 1.55 μm. However, fibres exhibiting zero or nearly zero dispersion at 1.55 μm called Dispersion Shifted Fibre (DSF) and Non Zero Dispersion Shifted Fibre (NZ-DSF) are available. They are designed such that the modal contribution to the total chromatic dispersion compensates for the material contribution and the zero dispersion is shifted to an expected wavelength in 1.55 μm region. Although the use of these fibres will enhance significantly the system performance, non-linear effects such as FWM occur easily and become drawbacks for WDM systems. Hence, most of current links deploy conventional single mode fibres. Another technique to mitigate the signal degradations caused by the chromatic dispersion is using Dispersion Compensating Fibres (DCF). A DCF is a single-mode fibre exhibiting negative dispersion. The dispersion induced by an L-length conventional fibre (D is positive around 1.55 μm) could be compensated for by using a DCF fibre with a length of L_{DCF} which satisfies Equation (1-4).

$$L_{SMF} \times D_{SMF} = L_{DCF} \times D_{DCF} \qquad (1\text{-}4)$$
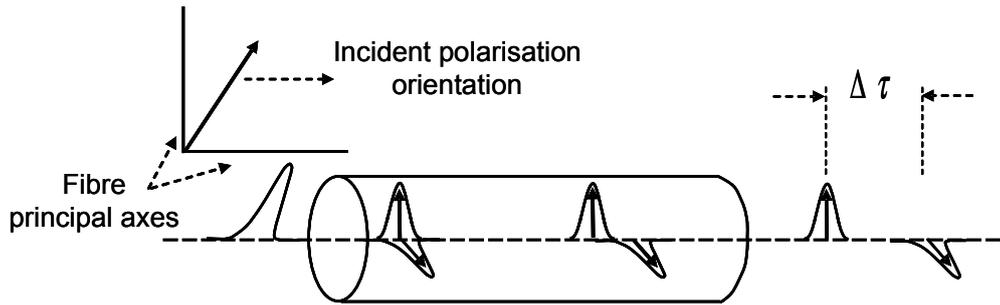
Figure 1.10: Illustration of PMD effect in a polarisation-maintaining fibre

1.1.5.3   Polarisation Mode Dispersion

Optical fibres are not ideally isotropic. They exhibit a non-zero birefringence. The sources of the fibre birefringence can be divided into two categories: intrinsic birefringence and extrinsic birefringence induced by environmental factors. The intrinsic birefringence is introduced during the manufacturing process and is due to noncircular core, non-symmetrical stress around the core region, etc... The environmental factors such as outside fibre stress, bends, constraints, etc... induce the extrinsic birefringence. The fibre birefringence makes that the two polarisation modes corresponding to the two principal axes of the fibre propagate with different group velocities. The phenomenon is called Polarisation Mode Dispersion (PMD). For a polarisation-maintaining fibre without external mechanic stress, the PMD effect could be naively described by a delay $\Delta\tau$ between the two polarisation modes as shown in Figure (1.10). $\Delta\tau$ is commonly called Differential Group Delay (DGD) and in that case, it is calculated by using Equation (1-5).

$$\Delta\tau = \frac{L\Delta n_{eff}}{c} \tag{1-5}$$

with L is the fibre length, c is the light velocity in vacuum and Δn_{eff} is the difference between effective index corresponding to the fibre principal axes. In a conventional single mode fibre, the PMD effect is much more complicated than that described in Figure (1.10) because the two principal axes change randomly along the fibre. The PMD effect results firstly in pulse broadening. Figure (1.11) displayed experimental eye diagrams of a 40 Gbit/s RZ format signal which has the two polarisation states exhibiting a DGD of 0 ps in one case and of 14 ps in the other case. It is observed that the eye diagrams in the second case are strongly distorted.

In practice, the signal degradations induced by the PMD is very difficult to be compensated for because the PMD effect is a random process. The signal polarisation changes randomly during the propagation because of the random variations of the perturbations along the fibre. In the current long haul transmission systems where the base bit rates do not exceed 10 Gbit/s yet, the optical pulse broadening induced by the PMD is still small

10 ps/div
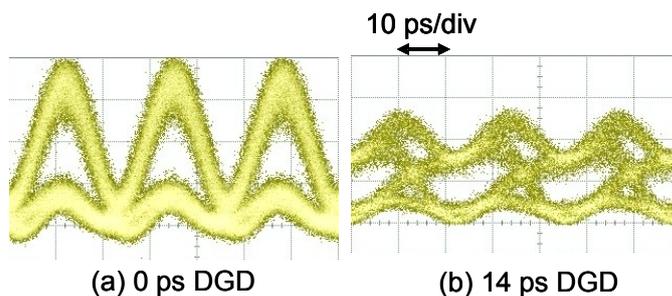
(a) 0 ps DGD   (b) 14 ps DGD

Figure 1.11: Experimental eye diagrams of a 40 Gbit/s RZ format signal exhibiting 0 ps DGD (a) and 14 ps DGD (b)

compared with the GVD effects. However, when the bit rate increases, the pulse duration becomes shorter and shorter, and then the PMD-induced impairments on the system performance become also stronger and stronger.

1.1.5.4   Non-linear effects

When the intensity is high enough, the optical field can change the medium characteristics and non-linear effects take place. The signal-medium mutual interaction modifies the signal itself and the others propagating in the same medium. In the current systems at 10 Gbit/s, the transmission links are managed such that they are in quasi-linear regime, i.e the signal intensity is small enough and the non-linear effects are not yet significant. Nevertheless, in high capacity WDM systems, optical nonlinearities will be a real problem. Interaction between different WDM channels and the transmission medium leads to interference, distortion and attenuation of transmitted optical signals. In the case of silica fibres, the non-linear effects that occur firstly are: Brillouin and Raman scatterings, non-linear phase modulation and Four-Wave-Mixing (FWM).

Brillouin scattering describes an interaction of light with acoustic waves in a transmission medium and it occurs when the optical signal power exceeds a certain threshold. In the case of the Stimulated Brillouin Scattering (SBS) in optical fibres, new optical signals are generated at frequencies shifted with respect to the incident signal and they propagate only in backward direction. The frequency shift is determined by the medium and the incident wavelength. For example, the frequency shift is in order of 10 GHz for a 1550 nm signal propagating in silica fibres. The signals generated at lower and higher frequencies are referred respectively as Stokes and Anti-Stokes waves. The main impact of the SBS is the signal power transfer in the backward direction which corresponds to an attenuation of the forward travelling wave.

Stimulated Raman Scattering (SRS) is similar to the SBS but much weaker. The main difference is the new optical waves generated by the SRS propagate in both backward and

forward directions. The other difference is the frequency shift is much greater in the case of the SRS (around 10 THz for silica fibres) than in the case of the SBS. The generated signals are also called Stokes and Anti-Stokes waves.

A high power signal does not cause only stimulated scatterings but also refractive index dependence on intensity which is known as optical Kerr effect. In a silica fibre, the refractive index varies nearly instantaneously with the optical intensity. As the signal intensity is time dependent, the optical signal phase is modulated through the refractive index and the phenomenon is called Self-Phase-Modulation (SPM). If in the same fibre, several signals propagate simultaneously, the refractive index modulation induced by one signal modulates the phases of all the other channels. The phenomenon is referred as Cross-Phase-Modulation (XPM). Both SPM and XPM induce spectral broadenings which cause interferences between the different channels of the WDM system. System impact of the SPM and XPM is significantly reinforced by the chromatic dispersion. The presence of the fibre chromatic dispersion transforms spectral broadenings into time domain broadenings.

Finally, Four-Wave-Mixing (FWM) should be mentioned. The FWM is another phenomenon due to the optical Kerr effect. The FWM occurs when two optical signals interact through the third-order electric susceptibility of the optical fibre and a phase matching condition is satisfied. The beating of the two signals at frequencies f_i, f_j creates new tones at frequencies f_k, f_m satisfying Equation (1-6).

$$f_k + f_m = f_i + f_j \qquad (1\text{-}6)$$

An illustration of the FMW effect in a silica fibre is given in Figure (1.12). The spectrum was obtained at the output of a 10 km Dispersion shifted Fibre. The two incident signals were at 1550.4 nm and 1551.4 nm. Numerous conjugated waves generated by the FWM can be observed.

In WDM systems exhibiting equally spaced channels, all the conjugated waves generated by the FWM within the system bandwidth fall at the channel frequencies and give cross-talks between the channels. The two common techniques deployed to lighten the FWM impairments are the use of unequal channel spacing and dispersion management.

1.1.5.5 Amplified spontaneous emission

As described previously in Paragraph 1.1.1, a transmission link is constituted of numerous fibre sections, optical amplifiers (EDFA) and/or optoelectronic repeaters. The optical amplifiers are used to compensate for the fibre losses. Amplification of an optical signal relies on stimulated emission mechanisms. Unfortunately, it is always accompanied spontaneous emission. The spontaneous emission light is also amplified during the propagation inside the amplifiers and is considered as a noise source for the transmitted signal. The amplifiers
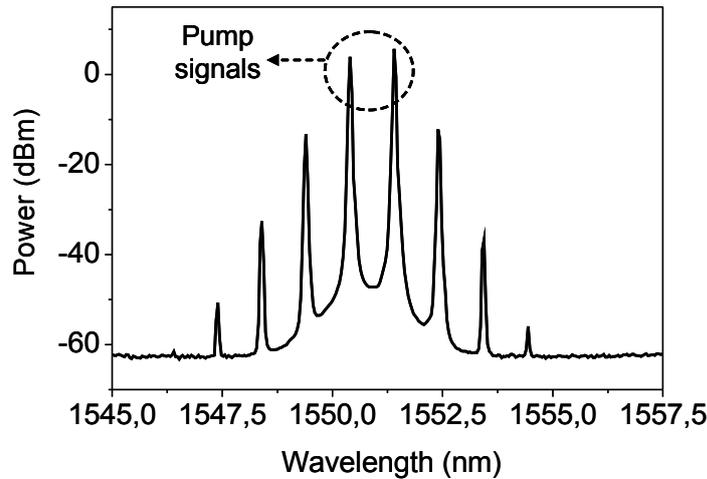
Figure 1.12: Illustration of FWM in a 10 km Dispersion Shifted Fibre

enhance the signal quality in terms of power but they could also degrade the signal quality by adding Amplified Spontaneous Emission (ASE) noise.

1.1.6   Transmission quality criteria

Various quality criteria are used to specify the quality of an optical transmission. The most common criteria are probably Optical Signal to Noise Ratio (OSNR), eye diagrams, quality factors and Bit Error Rate (BER). In laboratory, pseudo Random Bit Sequences (PRBS) are emitted to test a transmission link with new modulation formats, new fibres, or new signal processing devices, etc... These criteria are applied to the transmitted signal arriving on the receiver to estimate the performance of the interested transmission. The OSNR is measured in the optical domain. The signal eye diagrams could be considered both in optical and electrical (after detection) domains. The quality factors are generally evaluated in electrical domain (after the detection). And BER measurements are performed on the detected data sequence exclusively in electrical domain.

1.1.6.1   Optical Signal to Noise Ratio

At the receiver, the optical signal is detected and the electrical signal is expressed in voltage. During the detection, beatings between photons of the ASE noise generated by the amplifiers and the transmitted signal take place and add noise to the electrical signal. In amplified transmission systems such as undersea links, the ASE noise of the in-line amplifiers is dominant and the receiver noise can be neglected. The electrical signal noise is partially attenuated by the electrical low-pass filter of the receiver, but the residual noise causes always impairments to the electrical signal quality. Thus, to quantify the ASE noise ahead of the receiver, the Optical Signal to Noise Ratio (OSNR) is used. OSNR is defined as the
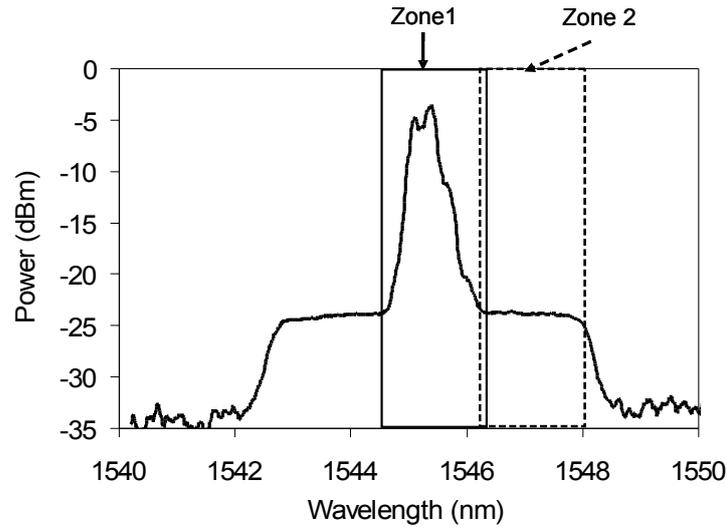
Figure 1.13: Principle of OSNR measurement using OSA

ratio of the signal power to the noise power measured over a given spectral bandwidth and calculated by using Equation (1-7).

$$OSNR = \frac{P_{signal}}{P_{noise}} \tag{1-7}$$

The OSNR over a spectral band of width B can be measured by using an Optical Spectrum Analyser (OSA). Principle of the measurement is described in Figure (1.13).

The power integrated within the signal bandwidth B (zone 1) includes both signal and noise power contributions and thus corresponds to $P_{signal} + P_{noise}$. The power integrated within zone 2 (spectral bandwidth of B) corresponds to the noise power P_{noise} only. If the measured powers are expressed in dBm and the OSNR is expressed in dB, their relations are given by Equation (1-8).

$$OSNR_{dB} = 10 \log_{10} \left(10^{\frac{\left(P_{signal}+P_{noise}\right)_{dBm} - \left(P_{noise}\right)_{dBm}}{10}} - 1 \right) \tag{1-8}$$

If $P_{signal} >> P_{noise}$, then ONSR could be approximated by Equation (1-9). However, this approximation is reliable only if $OSNR_{dB} > 13dB$.

$$OSNR_{dB} = (P_{signal} + P_{noise})_{dBm} - (P_{noise})_{dBm} \tag{1-9}$$

1.1.6.2   Eye diagrams

An eye diagram is the superposition of all the waveforms corresponding to all the possible bit sequences. In general, signal eye diagrams are achieved in the electrical domain after being detected by a photodiode, and are observed thanks to an electrical sampling oscilloscope. The electrical eye diagrams are representative for the optical signal only if the photodiode
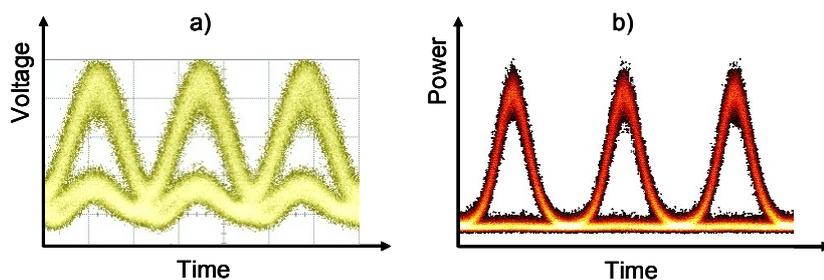
Figure 1.14: Electrical (a) and optical (b) eye diagrams of an RZ signal

speed is high enough, i.e its bandwidth is at least equal to half the bit rate (Nyquist criterion [23]). In practice, a photodiode bandwidth exceeding this value is necessary. Since a few time, high performance (time resolution of 1 ps) Optical Sampling Oscilloscopes (OSO) have been available. Figure (1.14) displays the electrical (a) and optical (b) eye diagrams of an RZ format optical signal. The quality of the electrical eye diagrams is limited by the photodiode bandwidth which is around 50 GHz. By using the OSO, the visualisation quality is clearly better.

The observation of signal eye diagrams can provide a qualitative estimation of signal degradations such as intensity fluctuations, timing jitter and intersymbol interference. The lower the signal quality is, the more closed the eye diagram is. A quantitative estimation of the signal quality which could be deduced from the electrical eye diagrams is the signal extinction ratio (ER). ER is defined by Equation (1-10).

$$ER = \frac{V_1}{V_0} \tag{1-10}$$

with V_0 and V_1 are average values of the detected voltages corresponding to the '0' and '1' bits at the decision instant.

1.1.6.3 Quality factors

The signal quality in terms of intensity fluctuation and timing jitter could be referred quantitatively by the corresponding quality factors.

The intensity fluctuations of the optical signal induce amplitude fluctuations of the electrical signal entering the decision circuit. The sampled value V fluctuates from bit to bit around a conditional average value V_0 or V_1, depending on whether the bit corresponds to '0' or '1' in the bit stream. Figure (1.15) depicts schematically the fluctuating signal received by the decision circuit. If the conditional variances of the detected voltage are σ_0^2 and σ_1^2, then the amplitude quality factor(Q_a) of the transmitted optical signal is defined by Equation (1-11).

$$Q_a = \frac{V_1 - V_0}{\sigma_1 + \sigma_0} \tag{1-11}$$

In order to take into account the timing jitter of the transmitted optical signal, the
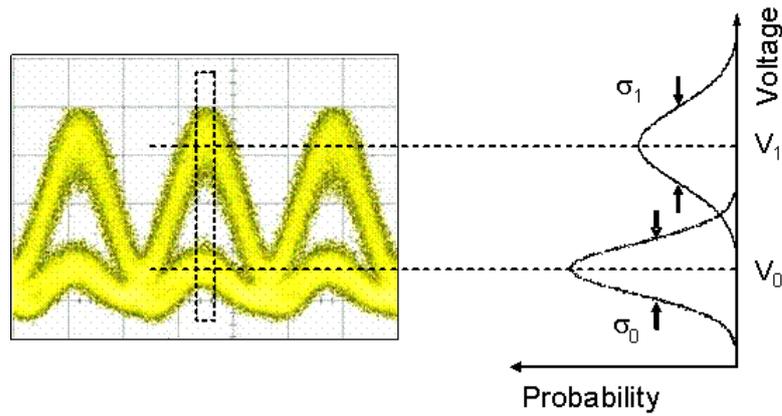
Figure 1.15: Illustration of amplitude fluctuation on electrical eye diagrams and detected voltage histogram

quality factor in time Q_t is defined similarly to Q_a as shown in Equation (1-12).

$$Q_t = \frac{T_T - T_L}{\sigma_T + \sigma_L} \tag{1-12}$$

with T_T and T_L are average time positions corresponding to the trailing edge and the leading edge of the pulses at the decision threshold voltage. The variances of these positions are σ_T^2 and σ_L^2. Figure (1.16) gives an illustration of electrical eye diagrams of an optical signal exhibiting timing jitter and the corresponding histogram. The quality factors are sometimes expressed in dB by using Equation (1-13).

$$(Q_{a,t})_{dB} = 20 \log_{10} (Q_{a,t}) \tag{1-13}$$

1.1.6.4   Bit Error Rate

Bit-Error-Rate (BER) is the ultimate criterion used to quantify the quality of an optical transmission and is related to the error probability P_E. The error probability is defined as the probability of incorrect identification of a bit by the decision circuit of the receiver. In laboratory, error detectors are used to measure the BER at the receiver. The BER measured by error detectors are calculated by dividing the number of errors to the total number of transmitted bits. For example, a BER of 5.10^{-3} corresponds to on average 5 errors per one thousand bits.

Bit detection is performed by the decision circuit of the receiver. At each decision instant (determined by the clock recovery), the decision circuit compares the detected voltage V to a threshold V_S. If $V > V_S$, the transmitted bit is considered as being '1' and if $V < V_S$, the transmitted bit is considered as being '0'. An error occurs when $V < V_S$ while the transmitted bit is '1', and $V > V_S$ while the transmitted bit is '0', and is due to noise. The error probability (P_E) is defined by Equation (1-14).

$$P_E = p(1) P(0|1) + p(0) P(1|0) \tag{1-14}$$
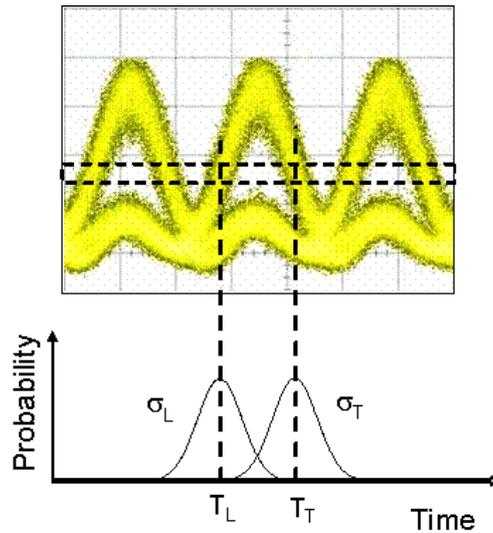
Figure 1.16: Illustration of timing jitter on electrical eye diagrams and corresponding histogram

where $p(1)$ and $p(0)$ are the probabilities of '1' and '0' in the transmitted data stream, respectively, $P(0\,|1)$ is the probability of deciding '0' when '1' has been sent, and $P(1\,|0)$ is the probability of deciding '1' when '0' has been sent. A common approximation describes noise in optical transmission as Gaussian, then $P(0\,|1)$ and $P(1\,|0)$ can be calculated by Gaussian statistics. Moreover, '0' and '1' symbols seem to occur in the real messages with the same probability, then $p(1) = p(0) = 1/2$. Finally, the error probability can be expressed by Equation (1-15).

$$P_E(V_S) = \frac{1}{4}\left[erfc\left(\frac{V_1 - V_S}{\sigma_1\sqrt{2}}\right) + erfc\left(\frac{V_S - V_0}{\sigma_0\sqrt{2}}\right)\right] \qquad (1\text{-}15)$$

erfc is the complementary error function which is defined by Equation (1-16).

$$erfc(x) = \frac{2}{\sqrt{\pi}}\int\limits_{x}^{+\infty}\exp\left(-y^2\right)dy \qquad (1\text{-}16)$$

P_E is minimal if

$$V_s = \left(\frac{V_1\sigma_1 + V_0\sigma_0}{\sigma_1 + \sigma_0}\right) \qquad (1\text{-}17)$$

and in that case, its value is given by Equation (1-18).

$$P_{E\,\min} = \frac{1}{2}\left[erfc\left(\frac{V_1 - V_0}{(\sigma_1 + \sigma_0)\sqrt{2}}\right)\right] \qquad (1\text{-}18)$$

It is interesting to note that in case of Gaussian distribution assumptions, the BER, which is representative for P_E, and the amplitude quality factor are related by Equation (1-19).

$$BER_{\min} = \frac{1}{2}\left[erfc\left(\frac{Q_a}{\sqrt{2}}\right)\right] \qquad (1\text{-}19)$$
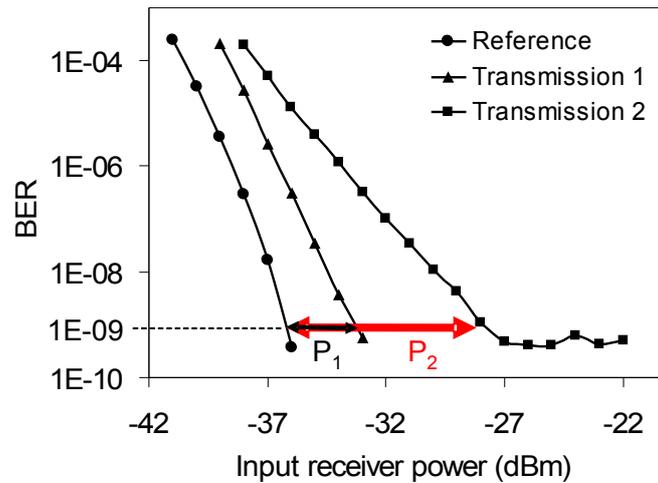
Figure 1.17: Examples of BER vs input receiver power curves

In actual telecommunication systems, a BER of 10^{-12}, which corresponds in average to one error per thousand billion of transmitted bits, is commonly required by network operators. However, the implementation of the recently reported Forward Error Correction Codes (FEC) [24] allows a 10 dB gain for the required Q_a (to achieve BER=10^{-13}) to be obtained. In laboratory, a transmission (without FEC) exhibiting BER=10^{-9} is considered as reliable.

The performance of a receiver is characterised by the measured BER as a function of the average optical power arriving on the receiver. The obtained curve is sometimes referred as the 'receiver sensitivity curve'. The required optical power to obtain BER=10^{-9} is defined as the receiver sensitivity. It is also possible to evaluate the sensitivity degradation resulting from signal propagation inside a fibre link. The studied fibre link could include optical fibres, optical amplifiers and regenerators. The procedure is described as follows. Firstly, BER is plotted versus the input receiver power in the back-to-back configuration, i.e the transmitter and receiver are connected directly, without the fibre link under study. The obtained curve is commonly called the reference curve. Then, the fibre link under study is inserted and BER is plotted again versus the input receiver power. The additional power required in front of the receiver to obtain BER=10^{-9} is called the penalty and it is usually used to quantify the signal degradations induced by the studied transmission. Figure (1.17) shows examples of receiver sensitivity curves of a back-to-back transmission (circles) and of two other cases (triangles and squares).

The inserted transmission links lead to different penalties on the receiver sensitivity. The induced penalties at BER=10^{-9} of the transmissions n°1 and n°2 are respectively about 3 dB and 8 dB. This difference indicates that the transmission n°2 degrades the optical signal quality stronger than the other one. In other words, the performance of transmission n°1 is better. Moreover, it could be observed that the signal degradations induced by the

transmission n°2 are so important that the BER of 10^{-10} would be unreachable because an error floor appears at a BER superior to 10^{-10}.

1.2 Signal regeneration and all-optical techniques

1.2.1 Signal regeneration

As described in Paragraph 1.1.5, the signal propagating in a fibre undergoes several impairments. These degradations can be classified into three categories: attenuation of average power signal, amplitude noise and timing jitter. A bad quality will be associated to a high bit error rate. Thus, signal impairments have to be reduced or compensated to avoid errors at the receiver. A solution to limit the signal impairments and increase the possible transmission distance is the introduction of in-line regenerators. They are inserted periodically into the fibre link to compensate for degradations induced during the signal propagation. Three levels (1R, 2R and 3R) of signal regeneration are illustrated in Figure (1.18). The 1R regeneration (Reamplifying) compensates for attenuation of the signal average power. The 2R regeneration (Reamplifying and Reshaping) compensates for the attenuation of the signal average power and reduces the amplitude noise. The 3R regeneration (Reamplifying, Reshaping and Retiming) compensates for the attenuation of the signal average power, reduces the amplitude noise and synchronises all transmitted symbols.
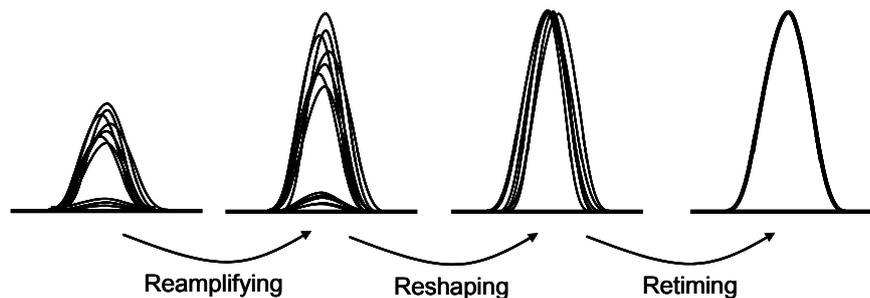
Figure 1.18: Illustration of three regeneration levels: reamplifying, reshaping and retiming of an RZ format signal

These regeneration processes are especially implemented in point-to-point links of the long haul transmission systems. The wide use of optoelectronic repeaters illustrates clearly the maturity of the solution and its advantages for 10 Gbit/s operation. The main principle of optoelectronic regeneration is to treat the degraded signal completely in electronic domain as described in Paragraph 1.1.1. The existing WDM transmission systems do not use any in-line optical regenerator: they use amplifiers, and optoelectronic regeneration is carried out at the ends of the link. However, such a design is probably not adequate for future optical networks at 40 Gbit/s and beyond because the reach of the transmission systems decreases rapidly when the bit rate increases. Insertion of all-optical regenerators inside fibre links will enhance the transmission distance. An all-optical solution will be attractive if the following conditions are satisfied: low-cost, low power-consumption, small size, high speed operation, polarisation independent and WDM compatible. In the rest of this paragraph, the basic principles of optical 1R, 2R and 3R regeneration are presented.
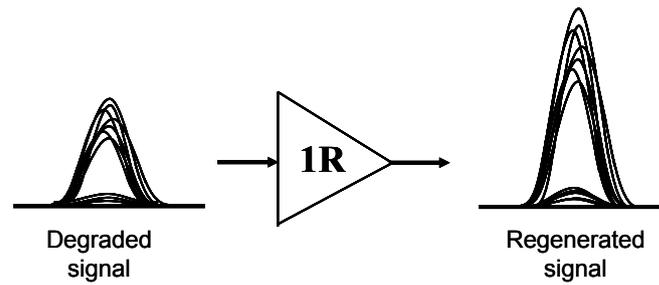
Figure 1.19: Principle of 1R regeneration

1.2.1.1   1R regeneration

1R regeneration, for 'Reamplifying', consists in amplifying the transmitted optical signal to compensate for fibre losses. Figure (1.19) depicts principle of the 1R regeneration. Optical 1R regeneration uses optical amplifiers. In this context, the amplifier must exhibit a high gain, a high linearity, a wide spectral bandwidth and a low noise figure. Despite its high gain and potential integrability [25], semiconductor optical amplifiers (SOAs) are not used as in-line amplifiers because of their high gain non-linearity and high gain-phase coupling. The most used optical amplifier used for 1R regeneration is the EDFA. In general, EDFAs provide typical optical gain of 18 dB, large spectral bandwidth (from 1530 nm to 1565 nm), polarisation independent and long response time (>1 ms). This last characteristic allows linear amplification (at actual and higher bit rates) to be achieved.

The other type of optical amplifiers, Raman amplifiers, is currently used for 1R regeneration. They exhibit high gain, low noise [26] and therefore appear very suitable for in-line amplification. Furthermore, their amplification bandwidth in the optical telecommunication window is as large as 104 nm.

The 1R regeneration allows signal attenuation to be compensated, and thus transmission distance to be increased. However, the amplitude fluctuations and timing jitter remain and cause detection errors. Furthermore, the ASE noise of optical amplifiers is unavoidable. In general, the ASE of in-line amplifiers is far from negligible. Consequently, the signal OSNR is degraded after each amplifier. In the transmission links where optical amplifiers are cascaded, the ASE noise accumulates and increases significantly the amplitude noise as well as the timing jitter. These signal degradations could be reduced thanks to 2R or 3R regeneration.

1.2.1.2   2R regeneration

2R regeneration, for 'Reshaping Reamplifying', compensates for fibre losses, reduces the amplitude noise and increases extinction ratio. An optical 2R regenerator is usually constituted of an optical amplifier and a non-linear optical gate. The non-linear gate performs the reshaping task (amplitude noise reducing and extinction ratio increasing) of the 2R

regenerator. If the characteristic function is defined as the relation between the output power and the input power, then the best non-linear gate exhibits a step-like characteristic with two non-linearities as shown in Figure (1.20). The two nearly flattened floors of the characteristic curve allow the amplitude fluctuations of '0' and '1' symbol levels (sometimes referred as 'space' and 'mark' levels) to be compressed. Moreover, if the distance between the two floors is large enough, a signal extinction ratio improvement is also performed.
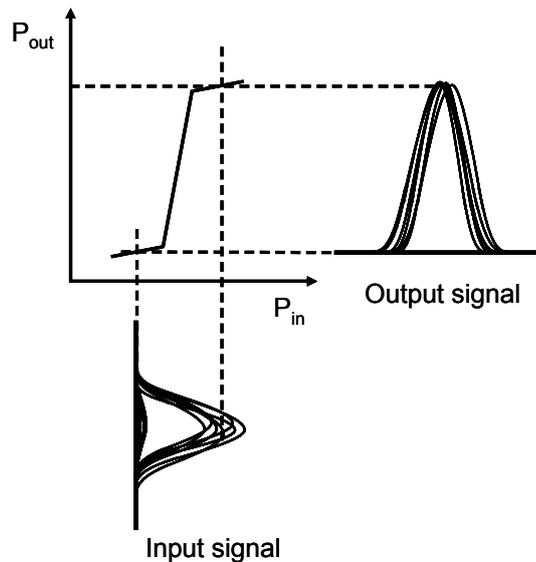
Figure 1.20: Reshaping principle with step-like characteristic function

The two typical configurations of 2R regenerators are self-modulation and cross-modulation regimes. The generic scheme of a 2R regenerator in self-modulation regime is displayed in Figure (1.21). The degraded signal, after being reamplified, is injected into the non-linear gate and transformed through its transfer function. At the gate output, the regenerated signal is achieved. In this case, the regenerated signal exhibits usually an improved extinction ratio.

The generic scheme of a 2R regenerator in cross-modulation regime is displayed in Figure (1.22). On one hand, the degraded signal is always injected into the non-linear gate, after having been amplified, to drive the non-linear transfer function. On the other hand, a
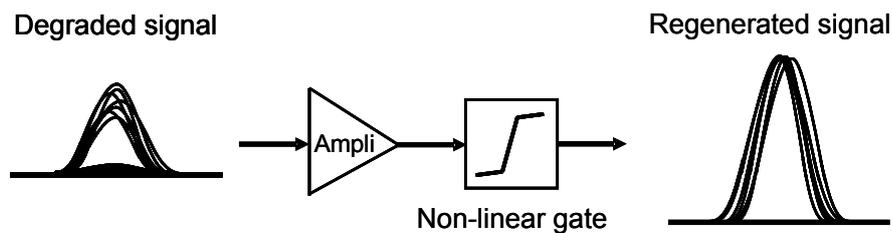
Figure 1.21: Generic scheme of 2R regenerator in self-modulation regime
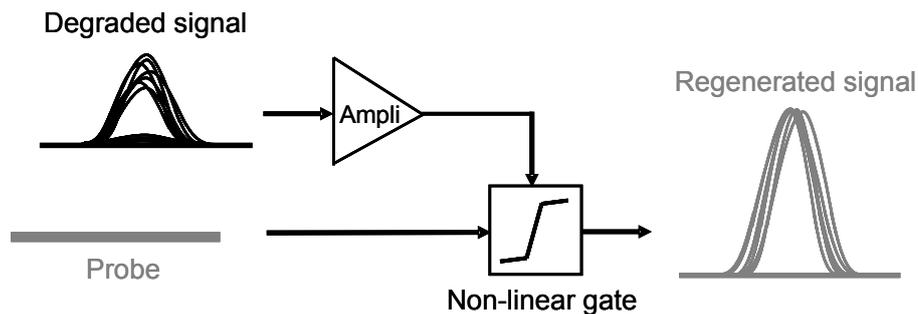
Figure 1.22: Generic scheme of 2R regenerator in cross-modulation regime

continuous light at another wavelength, called the probe signal, is simultaneously launched into the gate. This signal is non-linearly modulated inside the gate and the regenerated signal is achieved at the output. A wavelength conversion is hence performed during the reshaping process. By passing through the regenerator, the transmitted data is transferred from an initial carrier, at the degraded signal wavelength, to another carrier, at the probe signal wavelength. In some cases, the wavelength conversion could be useful for network routing. In another case as in point-to-point links, it could be a drawback, because a second regenerator is required to reconvert to the initial wavelength.

Among various criteria for 2R regenerators, the response time of the non-linear gate is a key requirement. The gate must be able to follow the instantaneous signal power variations, which requires a gate recovery time usually much shorter than the bit duration. Finally, the 2R regeneration is efficient to reamplify the attenuated signal and reduce the amplitude noise. Nevertheless, the signal timing jitter is not considered yet. To overcome the timing jitter problem, a complete regeneration is necessary, 3R regeneration.

1.2.1.3   3R regeneration

The generic scheme of 3R regeneration, for 'Retiming Reshaping Reamplifying', is shown in Figure (1.23). Besides the optical amplifier and non-linear gate used for reamplifying and reshaping tasks, a 3R regenerator requires in addition a clock recovery for signal resynchronisation. A fraction of the transmitted signal is extracted for the clock recovery device. The clock recovery generates an optical (or electrical) clock which is synchronised with the arriving signal. The extracted clock contributes to the non-linear gate control and allows the timing jitter suppression to be performed. Details on clock recovery device operation as well as different clock recovery techniques are discussed in Part 2 of the current manuscript.

Regenerators do not allow the bit error rate to be reduced because they do not correct errors. The regenerators compensate for the signal power losses and reduce the fluctuations in amplitude and in time. By that way, they limit the accumulation of signal degradations occurring during the propagation and increase the optical reach in comparison with
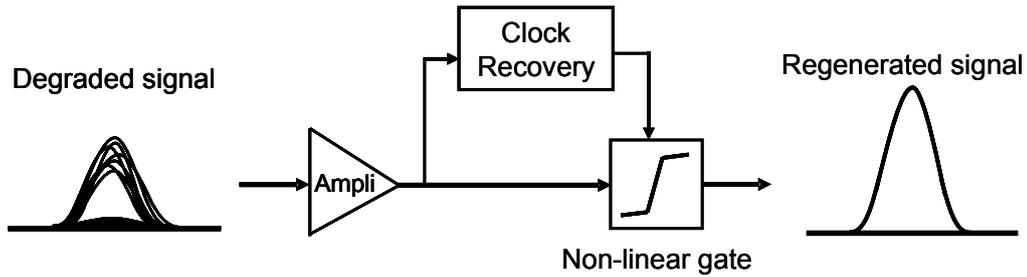
Figure 1.23: Generic scheme of 3R regeneration

a transmission without any regeneration. In general, regenerators are inserted periodically in a transmission link and thus, signal degradations are mitigated regularly.

1.2.2 Techniques for all-optical 2R regeneration

The current thesis focuses on two sub-functions for 2R and 3R regenerations: non-linear optical gate and clock recovery. Chapter 5 and Chapter 6 are entirely devoted to clock recovery. In this paragraph, a brief review of literature on techniques for all-optical 2R regeneration is presented. The purpose is to provide some outlines of the most popular techniques and thus clarify the position of the solution studied in this work. There are many non-linear media in which non-linear processes could be exploited for 2R regeneration. Almost 2R regenerators reported in the literature exploit reshaping gates which are based on optical fibre, semiconductor optical amplifier or microcavity saturable absorber.

1.2.2.1 Fibre based devices

Non-linear Optical Loop Mirror (NOLM) was proposed for the first time in [27] as a switching device. Later, 2R regenerators using NOLM structure were successfully demonstrated [28], [29]. The operating principle is based on non-linear phase induced by Self-Phase-Modulation (SPM) in a fibre in an interferometric Sagnac configuration. In 2R regenerators, the NOLM is usually used as non-linear gate in self-modulation. A simplified scheme of a NOLM is shown in Figure (1.24).

The arriving data signal is divided into two counter-propagating waves by the asymmetric coupler. The polarisation controller PC adjusts the polarization states. The two counter-propagating waves travel in the loop and recombine in the coupler where interferences occur. The input signal power is controlled to obtain SPM effects in the Highly Non-Linear (HNL) fibre. The propagation effect is not identical for the two waves because the phase velocity is intensity dependent and the coupler is asymmetric. Thus, the device responds to phase shifts between the two counter-propagating waves. Thanks to the ultra-fast nature (fs range) of the Kerr effect, the regenerators using NOLM demonstrated high performance at ultrahigh bit rates. NOLMs were assessed as in-line 2R regenerators and allowed an error-free transmission of 10 Gbit/s bit streams over 100000 km [28]. 2R regen-
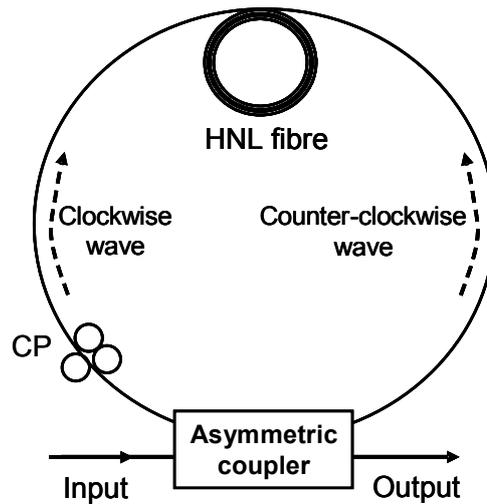
Figure 1.24: Generic scheme of fibre based NOLM

eration performance at 40 Gbit/s was also demonstrated in loop experiment [29]. The fibre based NOLM are passive and partly WDM compatible solutions for 2R regeneration. Otherwise, the main drawbacks of the fibre NOLM gates should be their polarisation sensitivity and the peak power × length product requirements. However, new highly non-linear fibres which have been intensively investigated could allow to decrease significantly the operating power.

The Mamyshev regenerator is another popular fibre device. The solution was first proposed by Mamyshev in [3]. The regenerator operation relies on the SPM effect in a fibre with a subsequent optical filtering at a wavelength which is shifted with respect to the input signal carrier wavelength. The method suppresses both the noise in '0' and amplitude fluctuations in '1' of RZ optical data streams. The schematic diagram of the regenerator (reprinted from [3]) is shown in Figure (1.25).
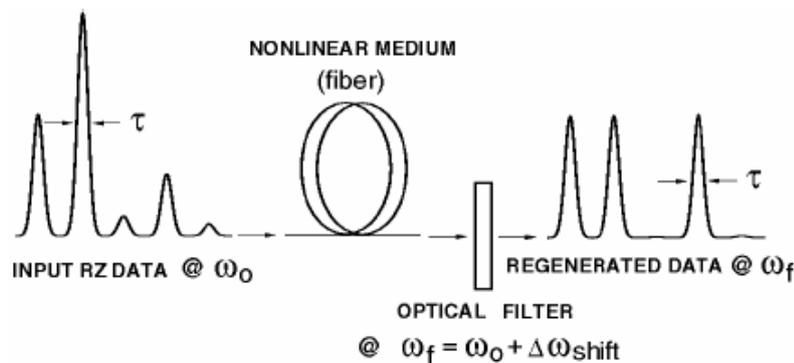
Figure 1.25: Schematic diagram of Mamyshev regenerator (reprinted from [3])

The generic idea of the method can be described as follow. The input signal (at pulsation ω_0) power is adjusted such that the SPM effect takes place inside the fibre. The pulse spectrum are therefore broadened. The optical filter which follows the fibre is shifted (to pulsation ω_f) with respect to the input signal carrier. If the spectral broadening of a pulse is small enough, the pulse is rejected by the filter. This happens when the pulse intensity is too small which corresponds to noise of '0' symbols. If the pulse intensity is high enough, a part of the SPM-broadened spectrum passes through the filter. It is important to note that the intensity of the output pulse could be independent of the input pulse intensity. The major advantage of Mamyshev regenerators is the ultrafast response of non-linearity similar to the NOLM. Otherwise, the wavelength conversion (ω_0 to ω_f) could be undesirable in some cases. However, wavelength-conversion-free schemes are available by using a bidirectional configuration [30]. The proposed 2R regenerator allowed an ER improvement as large as 24 dB at 10 Gbit/s. WDM compatibility of a Mamyshev 2R regenerator scheme was also demonstrated [31]. The regenerator allowed simultaneous 2R regeneration of two 40 Gbit/s WDM optical streams without XPM- and FWM-induced interference. High performance operations up to 130 Gbit/s of the same regenerator have been recently obtained and reported [32].

1.2.2.2 Semiconductor Optical Amplifier based devices

SOA-based optical gates are not as fast as fibre-based ones, but they are much more compact. At high bit rates, exceeding 10 Gbit/s, the use of simple cross gain modulation is limited by the gain recovery time of the SOA. Consequently, most of the reported work on SOA optical gates is based on interferometric configurations, using both phase and amplitude self- or cross-modulation effects.

SOA-based Mach-Zehnder interferometers (SOA-MZI) appear as one of the most efficient non-linear gates for both 3R and 2R regenerations. Such a regenerator consists of one fibre Mach-Zehnder interferometer in which one or two SOAs are inserted in one or both arms of the interferometer. An SOA-MZI in differential configuration allows the highest operation bit rates. The scheme of an SOA-MZI in differential configuration is depicted in Figure (1.26). Two SOAs are inserted in both interferometer arms. The waves propagating in the two arms are delayed by using an optical delay line. The regenerator operation can be described as follow. Initially, the interferometer is set for 'low' transmission of the probe signal. Then a pump pulse (extracted from the degraded signal to be regenerated) is coupled into one SOA which changes the gain and refractive index of the SOA. These changes unbalance the interferometer and switch it to 'high' transmission. The gate is hence opened. To obtain the gate switch-off, a second pulse (delayed pulse) is fed to the other SOA with a energy amount necessary to change its gain and refractive index back to the interferometer 'low' transmission conditions. 2R regeneration is obtained by using a
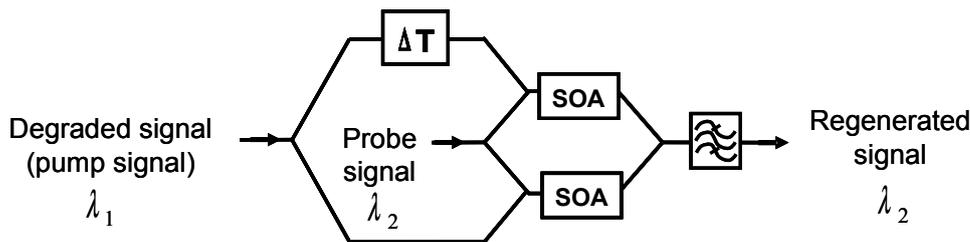
Figure 1.26: Principle scheme of an SOA Mach-Zehnder Interferometer in differential configuration

continuous light for the probe signal. The amplitude noise reduction is achieved thanks to the non-linear interferometer transmission response with respect to data power.

The greatest advantages of SOA-MZI gates should be their high non-linearity and integration capability. Different possibilities using SOA MZI gates allow efficient 2R regenerations for NRZ signal at 10 Gbit/s [33] and RZ signal at 40 Gbit/s [34].

SOAs could be also used in other interferometer types such as NOLM and Delay Interferometer (DI). In [35], the SOA is inserted into a NOLM to play the role of the non-linear element. Significant improvement in both pulse waveform and extinction ratio were achieved for a 10 Gbit/s NRZ format signal. In [36], the wavelength converter using SOA combined DI was demonstrated to exhibit power equalization and 2R regeneration capability.

2R regeneration solutions which exploit SOA non-linearity but do not require any interferometric configuration are possible. An SOA followed by a filter is a simple scheme for both 2R and 3R regenerations [37]. The non-linear gate operating principle relies on the combination of XPM effect in the SOA and the very sharp frequency response of the filter. The regenerator scheme allowed a 20000 km transmission of a 10 Gbit/s RZ format signal. Other 2R regenerator scheme based on cross gain compression in SOA was proposed [38]. The regenerative properties of cross gain compression between to logical inverted signals in an SOA were demonstrated at 40 Gbit/s for both RZ and NRZ format signals [39]. Moreover, the regenerator scheme is wavelength preserving, polarization insensitive and exhibits on-chip integrable potential.

1.2.2.3 Microcavity Saturable Absorber based devices

Regeneration capability of Microcavity Saturable Absorber (SA) has been largely demonstrated [40], [11]. The non-linear phenomenon exploited in an SA is the saturation of the absorption. When the SA is illuminated with an optical signal with low peak power, the SA absorption is high end the device is considered as opaque to the signal. Above a certain threshold, the SA transmittance increases rapidly with the signal power and saturates toward a transparency. Such a non-linear function makes the SA possible to reduced noise

on the '0' level, resulting in a higher contrast between '1' and '0' levels.

SAs do not suppress amplitude noise on the '1' level, which makes it incomplete for a regenerator. Various complementary devices have been proposed to be combined with an SA for a complete 2R regenerator solution. One passive scheme is using optical filtering of non-linear (soliton) pulses for '1' noise suppression [41]. In the absence of chirp, a pulse intensity increase or decrease corresponds to a spectral broadening or narrowing. An optical filter will cause higher loss when intensity increases, and lower loss when intensity decreases. Thus, the filter plays the role of a power control or power equalisation function. The 2R regenerator scheme was demonstrated its efficiency at 40 Gbit/s in loop experiment [41]. It allows the transmission distance to be increased from 1300 km (without regenerator) to 7600 km (with regenerator) for a Q-factor of 13 dB. The first advantage of such regenerator is that it is totally passive. Moreover, the solution is WDM compatible, it demonstrates efficient 2R regeneration over a 13 nm wavelength range in the 1550 nm window [11]. Another solution is using SOA for '1' level noise suppression. 2R regeneration at 10 Gbit/s and WDM compatibility of the SOA-SA regenerator has been proven [10]. The regenerator scheme is fully compatible with photonic integration and hence promises compact, low-cost WDM 2R regeneration. Recently, novel saturable absorber which treats the high power levels was proposed [42] and cascaded with the classical saturable absorber to constitute a complete 2R regenerator scheme [43]. The dual-stage SA gate demonstrates its regenerative properties at 40 Gbit/s. The two SAs are based on the same technology which promises compact, low-cost, passive solutions for high speed 2R regeneration.

1.3   Chapter summary

This first chapter presented the context of the thesis and introduced the basic notions of optical fibre communication systems.

Our studies rely mainly on the point-to-point link type which is described in the first section. The functional blocks used to emit and receive the transmitted optical signal as well as the common modulation formats (RZ and NRZ) are described. Signal degradations occurring during the propagation are also developed to show the necessity of signal regeneration, especially for long and ultralong haul transmissions. Fibre losses are the first factor that leads to signal degradations and limits the transmission distance. When the bit rate increases impairments caused by chromatic and polarisation mode dispersions become rapidly critical factors. Non-linear effects and ASE accumulation are other sources of signal degradations which could not be neglected. Finally, various criteria which are employed to estimate the performance of a transmission are presented. Signal quality could be evaluated qualitatively by observing electrical and/or optical eye diagrams. Quantitative criteria such as the optical signal to noise ratio, quality factor and bit error rate are used to specify the signal quality and estimate the system performance.

In the second section, regeneration processes (1R, 2R and 3R) and their principles are reviewed. It seems likely that all-optical regeneration solutions are more adequate for future ultrahigh speed transmission systems rather than complex and 'power hungry' optoelectronic solutions. A brief review of literature on 2R regeneration techniques is presented. Fibre-based devices are advantageous for ultrahigh bit rate systems thanks to the ultrafast response of the Kerr effect. Otherwise, semiconductor based devices could provide entirely integrable and low cost solutions for 2R regeneration.

Chapter 2

Experimental characterisation of different SOA structures

2.1 Semiconductor Optical Amplifiers for optical signal processing

When monomode fibre imposed as the main information transporter in backbone network, signal attenuation became the first factor that limited transmission distance. Optical amplifiers based on semiconductor or erbium-doped fibre were studied and developed with the first goal of amplifying optical signal and thus improving the link budget. The Erbium Doped Fibre Amplifier (EDFA) was invented in 1985 and led to a revolution in optical communication systems in association with Wavelength Division Multiplexing (WDM). Only in the 90s, optical amplifiers began being introduced in commercial transmission system, firstly in terrestrial links. Nowadays, EDFA found their place in long haul links inside the 1550 nm window as linear amplifier.

First Semiconductor Optical Amplifiers (SOAs) were studied nearly at the same time as the invention of semiconductor laser in the sixties. SOAs began attracting particular interest for functional applications since the late of the eighties when InP/InGaAsP SOAs designed to operate in the 1300 nm and 1550 nm windows appeared [25] and progress in anti-reflection coating technology enabled fabrication of true travelling-wave amplifiers [44]. The main applications of SOAs in current advanced optical communications could be divided into 2 categories: booster amplification and non-linear signal processing applications.

There is an increasing interest in using SOA for booster amplification, particularly in Metro and Access Networks. In this type of applications, a medium gain SOA is acceptable as it is used to compensate for the loss of tens of km of SMF fibre. Broad optical bandwidths (up to 80 nm [45]) of SOA exhibit also advantage as an amplifier in transparent network. Another type of SOA called Reflective SOA (R-SOA) finds its place in reflective WDM-PON architectures, where the R-SOA is used as an amplifying modulator within a 'colourless' optical network unit.

For many years, our laboratory has been working on optical functions for backbone networks, such as all-optical regeneration and wavelength conversion. SOA with its potential in non-linear applications does not escape from our interest. The reason why EDFA, not SOA, is chosen for long haul optical communications systems is also the reason why SOA, not EDFA, is the active element of choice for optical signal processing: combination of non-linearity and response time. Fibre amplifiers exhibit negligible non-linearities while SOAs' non-linearities can be severe. This fact makes that SOAs are much more suitable for optical signal processing than fibre based amplifiers. The difference of response times between EDFA and SOA (from several milliseconds down to tens of picoseconds respectively) is another reason. Amplification of an optical signal consumes carriers. When a modulated light is injected into an amplifier, its gain is not maintained constant but passes transiently by saturating state where the gain is depleted. If the amplifier does not provide the same gain for all the data bits, patterning effects take place and quality of the optical data signal is significantly degraded. To avoid distortion of the signal, the magnitude of gain saturation must be sufficiently small, or the amplifier must be fast enough such that transient gain changes do not affect the following bits. In the case of an EDFA, the gain recovery time is typically in the millisecond region. For data rates of several Gigabit-per-second regime (typical in point-to-point links of backbone networks), EDFA operates in the regime of mean power saturation. The recovery time is much longer than the bit period (around hundreds picoseconds) so that the amplifier effectively averages the power over very long bit sequences. On the other hand, the order of magnitude of the carrier lifetimes in a SOA is between some nanoseconds and some tens of picoseconds, which is much shorter than those of an EDFA and are comparable to bit time slot for data rates of several Gbit/s. Such dynamics of SOAs promise a potential for bit-by-bit signal processing.

The main goal of this chapter is to present experimental characterisation results of different SOA structures. These SOAs are designed and fabricated by the Alcatel-Lucent Thales III-V Lab in the frame work of the project FUTUR in order to perform functions of optical regeneration and wavelength conversion at 40 Gbit/s and up to 160 Gbit/s. As far as bulk based SOAs, two chips with a same waveguide length but with different confinement factors are studied. As far as quantum-dot based SOAs are concerned, two chips with different waveguide lengths are analysed. A quantum-dash SOA is also studied. Our experimental studies concentrate on two mains aspects: gain non-linearity and gain dynamics. All results are given in Sections 2.2 and 2.3. In the following of this section 2.1, we remind briefly some basic descriptions of an SOA and some essential backgrounds about gain saturation and SOA dynamics behaviour. These basic descriptions are principally based on those of [46], [47], [48].
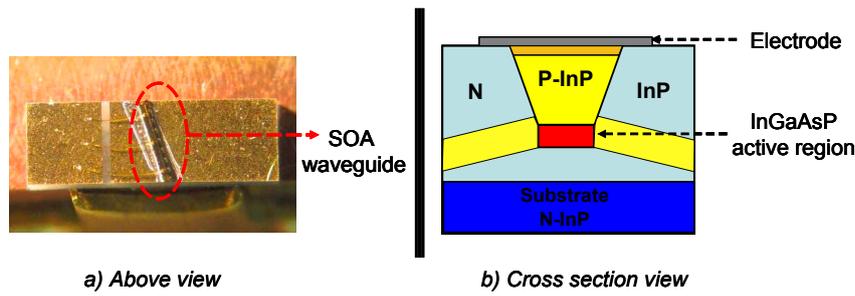
Figure 2.1: Picture of an SOA (a) and cross-section scheme of a buried heterostructure (b)

2.1.1 SOA basic description

A typical SOA is essentially a semiconductor laser without laser cavity, i.e. SOA facets are anti-reflection (AR) coated to suppress cavity effect. SOA amplification mechanism relies on stimulated emission of radiation.

Our studied SOA structures are quaternary III-V travelling-wave semiconductor optical amplifiers. They consist in double heterojunctions (DH) constituted of an intrinsic semiconductor material for active region inserted in 'sandwich' between two doped semiconductor materials: one n-type and one p-type for cladding regions. Concerning the bulk material device's active region, InGaAsP is used as its bandgap corresponds exactly to telecommunication wavelength regions. Moreover, InGaAsP is a direct bandgap material. In such a material the Valence Band (VB) maximum and the Conduction Band (CB) minimum energy levels have the same momentum vector. In such situation, the probability of radiative transitions from the CB to the VB is much greater than in the case of indirect bandgap material. This leads to a greater device efficiency, i.e. a higher conversion efficiency of injected electrons into photons. The 'sandwich' exploited in our SOAs is InP/InGaAsP/InP as the InGaAsP material is lattice matched with the largely used substrate InP. Most of SOA structures are ridge waveguide or buried heterostructure type. The SOAs studied in our work belong to the second type as shown in Figure (2.1) (reprinted from [48]). Active region has a thickness and a width of typically 0.5 and 1 μm respectively and a length varies from 1 mm up to 6 mm.

The basic amplifier operating principle can be described as follows. The combination of a 'sandwich' InP/InGaAsP/InP creates a lower bandgap in the active region compared to surrounding layers. By applying a forward bias over the structure, electrons from n-type material and holes from p-type material are forced to diffuse toward the active layer where they recombine. The active layer plays the role of a low bandgap potential well and electrical carriers are trapped and accumulate inside. If the applied currents are large enough, large concentrations of electrons and holes are obtained and population inversion can be achieved. Once the population inversion is set-up, injected photons with appropriate energies passing through the active region can stimulate radiative recombination of the car-

riers, resulting in amplification of the light. This effect called stimulated emission enables the structure to act as an optical amplifier. Simultaneously, other photons originate from spontaneous emission phenomenon are also produced. These photons are not coherent with the incident signal but are also amplified during propagation in waveguide. This is called Amplified Spontaneous Emission (ASE) and considered as noise of the optical amplifier.

Waveguide: In a BH structure, light guiding is obtained in a dielectric waveguide. The InGaAsP material which constitutes the active region has a higher refractive index than the surrounding InP region which acts as the waveguide cladding. The structure can be therefore considered as a dielectric waveguide with a rectangular cross-section. This waveguide configuration enables the light to remain confined when travelling along the device in the active region and thus optimises amplification efficiency. If the cross section dimensions of the waveguide are sufficiently small, it will only support a single fundamental transverse mode with two possible polarisation states, the transverse electric mode (TE) and the transverse magnetic mode (TM). If the mode is not too much confined, single transverse mode operation allows to reduce the modal gain dependency and to make easier the coupling from the device to the optical fibre.

Gain ripple: As mentioned above, the SOA uses the same gain medium (active region) as a semiconductor laser but without any cavity. Nevertheless, the existence of partially reflected light will cause cavity resonances. Certain photons at frequencies corresponding to cavity resonance will be strongly amplified thanks to interference phenomenon while photons at the other frequencies will be less amplified. This fact results in a gain inhomogeneity across the whole amplifier optical bandwidth. This phenomenon is so-called gain ripple. It can be easily observed on SOA ASE spectrum. An example of ASE spectrum with strong ripple is shown in Figure (2.2).

Travelling wave operation in a SOA requires suppression of all feedback of light or in other words of all reflections on facets. Main techniques employed to suppress reflections and hence reduce the gain ripple are: antireflection coatings, tilted waveguide and mode taper. Recent SOA generations use the combination of these three techniques as depicted in Figure (2.3) [49]. Consequently excellent reflectivity as low as 10^{-5} can be obtained.

New material for new SOA generations: for the last twenty five years, quantum materials have been a hot topic for researchers and were the source of advanced technology investigations. In the last recent years, most of attentions have been paid to quantum-dot devices with outstanding progresses. Research on QDs based optical devices has been focused firstly on lasers. Theory predicts distinguished features for semiconductor lasers with QDs based active region: ultralow threshold current, temperature-insensitive operation, narrow spectral linewidth, and large modulation bandwidth [50]. Among the numerous contributors on QD devices technology, our partner from Alcatel-Lucent Thales III-V Lab
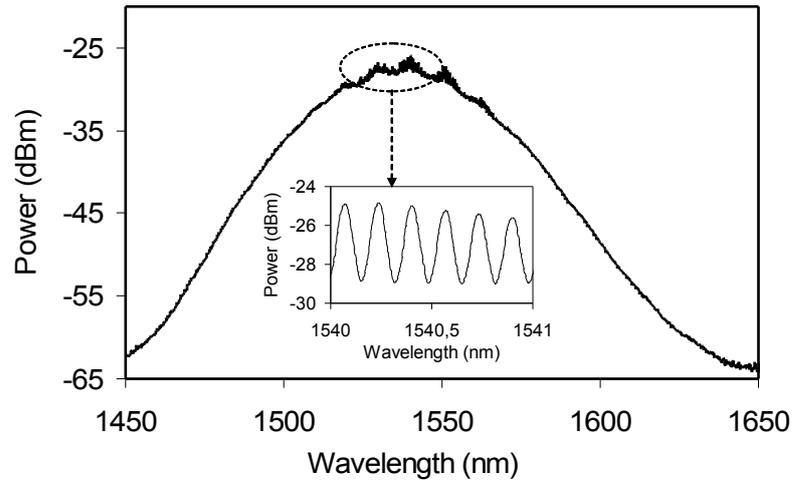
Figure 2.2: Amplified spontaneous emission spectrum of an SOA. In the inset, ripple is zoomed in.
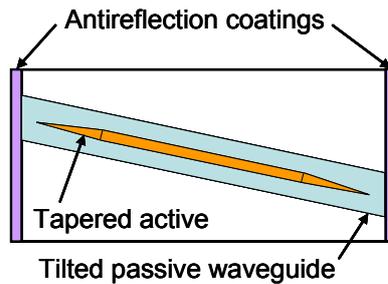
Figure 2.3: Different techniques using for SOA ripple suppression

should be mentioned, from whom we received sophisticated types of semiconductor lasers and optical amplifiers. Today, the technology of self-assembled semiconductor QDs reaches a certain maturity and QD lasers exhibit almost predicted characteristics [51].

Density of states and gain characteristics: To have a first understanding about the strong 'seduction' given by quantum materials, we can begin with their energy band structures of electronic carriers. Semiconductors that present one, two or three dimensions of the order of nanoscale are called quantum-well (QW), quantum-wire (QWR) and quantum-dot (QD) structures respectively. A schematic description of the density of states for regular bulk semiconductor and different quantum structures is displayed in Figure (2.4(a)) [4]. For a bulk material, the density of states versus energy is continuous with a nearly parabolic form. In a QW material, the density of states is divided into subbands with sharp steps. In a QWR material, the density of states attains sharp maxima at each position of different discrete energy states. At last, in a QD structure, where electron motion is quantified in all directions, the density of states is high only for the possible discrete energy states and
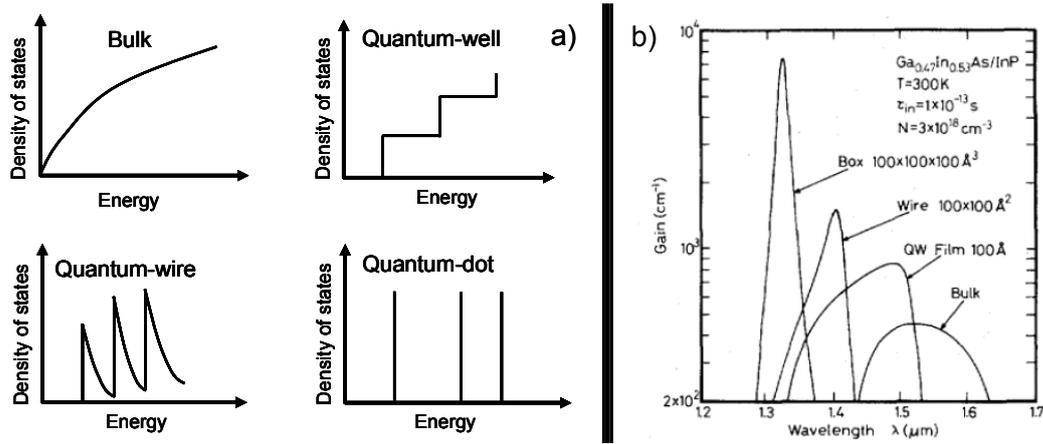
Figure 2.4: On the left, densities of states of electron with the increase of the quantum confinement (a). On the right, gain spectra calculated for $Ga_{0.47}In_{0.53}As/InP$ 100A°x100A°x100A° cubic quantum box (quantum-dot), 100A°x100A° quantum-wire, 100A° thick quantum film (quantum-well), and bulk crystal at T=300 K (b - reprinted from [4])

can be expressed by delta functions. In practice, the QW and QWR density of states are not so sharp. They are broadened by intraband carrier relaxation by scattering. For a QD material, the density of states is also broadened because of the distribution of dot sizes and interactions with surrounding material.

For simplicity, the following description will be focused only on characteristics of QD structures and will save any detail about QW and QWR structures features. Corresponding to these band structure descriptions, calculations derived from density-matrix theory give gain spectra as shown in Figure (2.4(b)) reprinted from reference [4]. All gain spectra are calculated at 300 K, at a constant carrier density, N, of 3.10^{18} cm^{-3} and with an intraband relaxation time τ_{in} of 1.10^{-13} s. Except for the bulk structure, the thickness of quantum-confined direction was set at 100A°. QDs structure gain spectra present higher peak of material gain and narrower gain bandwidth. This fact is assumed as results of an increase of the quantum confinement from bulk to quantum-dot structure. This figure also implies that the differential gain is drastically improved in the QD due to important peak gain and the improvement is more accentuated with a narrow gain bandwidth. The first consequence of a great differential gain is a low threshold current density. The second consequence consists in an expected linewidth enhancement factor of nearly zero. For lasers, that means smaller spectral linewidth of emission. High differential gain can also result in enhancement of dynamic characteristics.

SOAs with QD gain material promise broadband gain, low noise figure (NF), high saturation output power and ultrafast gain dynamics [52]. Due to the concentration of the injected carriers into small QDs, the Fermi level at the maximum of current density,

which is limited by the thermal effect, is significantly increased. Direct consequence of this phenomenon is the expansion of gain wavelength range [46], [47]. High saturation output power and low NF result from a combination of a highly filled carrier reservoir (assigned to wetting-layer) and a small overlap between the optical field and the QDs [53]. A general description of ultrafast gain dynamics of QD SOA will be presented later in Section 2.1.3. QD SOA with record widest bandwidth of 120 nm and high output saturation power higher than 19 dBm was demonstrated [52], a low NF close to 5 dB was achieved [52], [51]. Ultrafast dynamics of QD SOA also make effective all-optical signal processing without important patterning effects possible at ultrahigh bit rates of 40 Gbit/s and 160 Gbit/s [54], [55].

2.1.2 Gain saturation

If a large enough forward current is applied to a SOA, a population inversion in active region can be achieved. The SOA presents a gain for optical signals satisfying the Bernard and Duraffourg condition (Equation (2-1)), i.e. if the photon energies are larger than the energy bandgap between the conduction and the valence bands and smaller than the gap between their Fermi levels, which are representative of how the bands are filled with carriers.

$$E_g < E < \Delta E_F \tag{2-1}$$

E is the photon energy
E_g is the bandgap
ΔE_F is the distance between the Fermi levels of the conduction and valance bands

Amplification of light consumes carriers as it relies on electron-hole recombinations by stimulated emission. The amplification of an optical signal therefore decreases the density of carriers. If the optical signal power is large enough such that consequent stimulated emission consumes more carriers than that could be supplied by injected bias current, then the presence of optical signal leads to a drop of total carrier density or in other words a decrease of overall-optical gain. The phenomenon is called gain saturation. When the injected light is a modulated signal, i.e. a pulse stream, the gain saturation varies in time and the phenomenon is rather called gain compression or dynamic gain saturation. This dynamic gain saturation of an SOA will be discussed in details in Section 2.1.3. In this section, we consider the gain saturation by an injected continuous optical signal. In this case the SOA gain is in a steady state, and gain saturation analysis provides primary information about the non-linearity provided by SOAs.

There are a lot of SOA models with varying complexity [56], [57], [15], [58]. To describe the gain saturation in a steady state, we use the model presented by [56] which appears as one of the simplest models while providing a clear understanding about gain saturation.

The model considers an optical signal propagating along a travelling-wave SOA. It is assumed that the width w and the thickness d of the active region are small enough

compared to the scattering length to consider the carrier density as nearly uniform along the transverse dimensions. In practice, our SOA are in order of 1 μm of width and 0.5 μm of thickness, the assumption is then verified. By averaging over the active region, carrier density evolution is given by the differential Equation (2-2):

$$\frac{\partial M}{\partial t} = \frac{I}{qV} - \frac{M}{\tau_s} - \frac{g(M)}{\hbar\omega_0}|A|^2 \qquad (2\text{-}2)$$

M is the carrier density

I is the injected current

V is the volume of the active region

τ_s is the carrier relaxation time

$\hbar$ is the reduced Planck constant

ω_0 is the signal pulsation in vacuum

$A(z,t)$ is the slowly-varying envelope associated with the optical field

t is the time

z is the spatial variable along the amplifier length

$g(M)$ is the intrinsic gain of the SOA

On the right side of Equation (2-2), the first term represents the carrier density supplied by external injected current. The second one represents the loss of carrier density due to interband relaxation and the last one represents the drop of carrier density due to stimulated emission. In a static regime, the carrier density M is a constant; the left side of Equation (2-2) cancels. The carrier density value satisfies Equation (2-3):

$$\frac{I}{qV} - \frac{M}{\tau_s} - \frac{g(M)}{\hbar\omega_0}|A|^2 = 0 \qquad (2\text{-}3)$$

The intrinsic gain is a function of carrier density and defined by Equation (2-4):

$$g(M) = \Gamma a(M - M_0) \qquad (2\text{-}4)$$

Γ is the confinement factor

a is the material gain coefficient

M_0 is the carrier density required for transparency

If we define the saturation energy E_{sat} and the small-signal intrinsic gain g_0 by (2-5) and (2-6):

$$E_{sat} = \frac{\hbar\omega_0\sigma}{a} \qquad (2\text{-}5)$$

$$g_0 = \Gamma a M_0\left(\frac{I}{I_0} - 1\right) \qquad (2\text{-}6)$$

with the mode cross section:

$$\sigma = \frac{wd}{\Gamma} \qquad (2\text{-}7)$$

the current at the transparency

$$I_0 = \frac{qV M_0}{\tau_s} \tag{2-8}$$

and the power of the optical signal:

$$P = |A|^2 \tag{2-9}$$

then, Equation (2-3) can be written as Equation (2-10):

$$\frac{g_0 - g}{\tau_s} - \frac{gP}{E_{sat}} = 0 \tag{2-10}$$

Equation (2-10) can be resolved directly to obtain Equation (2-11) relating the intrinsic gain g as a function of the signal input power.

$$g(z) = \frac{g_0}{1 + \frac{P(z)}{P_{sat}}} \tag{2-11}$$

with the saturation power defined as:

$$P_{sat} = \frac{E_{sat}}{\tau_s} \tag{2-12}$$

Equation (2-12) demonstrates clearly the phenomenon of gain saturation mentioned above. A large enough input power will lead to a decrease of the intrinsic gain and consequently of the overall amplifier gain. P_{sat} is a parameter characterising the SOA gain saturation. It represents the input signal power value such that the intrinsic gain drops to a half of its maximal value, i.e $g_0/2$.

In practice, it is not possible to measure the intrinsic gain g. On the contrary, we can measure the signal power at the SOA input and output to deduce the amplifier gain, i.e the gain accumulated by the signal along the amplifier length. We remind also that the considered optical signal is continuous, then if we consider in the reference frame moving at the group velocity of light, the signal power P will be a function of only z and not be a function of time t any more. By neglecting internal loss of the amplifier, equation governing the evolution of the optical power is given by Equation (2-13):

$$\frac{dP}{dz} = gP \tag{2-13}$$

By integrating Equation (2-13) over the amplifier length, we obtain Equation (2-14):

$$P(L) = P(0) \exp\left(\int_0^L g(z)\,dz\right) \tag{2-14}$$

Amplifier gain G accumulated by the incident signal by passing through the SOA is defined by Equation (2-15):

$$G = \frac{P(L)}{P(0)} = \exp\left(\int_0^L g(z)\,dz\right) \tag{2-15}$$
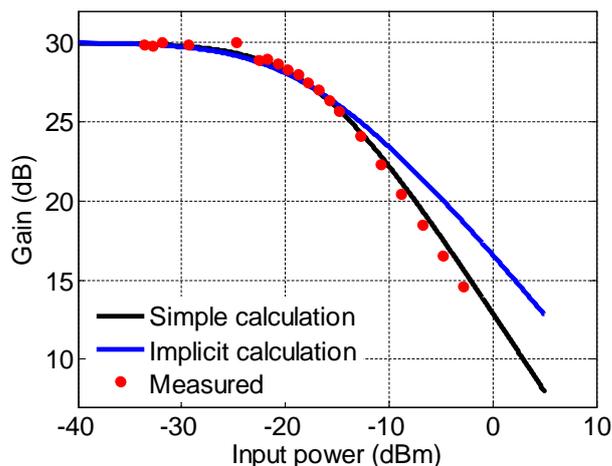
Figure 2.5: Gain as a function of input power of an SOA exhibiting 30-dB and -17 dBm for amplifier small-signal gain and 3-dB saturation power respectively

If we integrate (2-11), and make use of (2-13), (2-14) and (2-15), we obtain Equation (2-16):

$$G = G_0 \exp\left[(1 - G)\frac{P_{in}}{P_{sat}}\right] \qquad (2\text{-}16)$$

where the amplifier small-signal gain is defined by Equation (2-17):

$$G_0 = \exp(g_0 L) \qquad (2\text{-}17)$$

G as a function of input power is then the stationary solution of Equation (2-16). The saturation of amplifier gain G led by the saturation of intrinsic gain g is less explicit compared to Equation (2-11). This Equation (2-16) allows also to determine a novel parameter that can be measurable. It is the power value of the input signal such that the amplifier gain G drops to half of its maximal value, i.e $G_0/2$ and we will henceforth call it the 3-dB saturation input power P_{3dB}. Similar to the case of gain, the saturation power P_{sat} is not directly measurable while the P_{3dB} can be extracted easily by varying the input signal power and measuring the amplifier gain G. By using Equation (2-16), the relation between the saturation power P_{sat} and P_{3dB} is given by Equation (2-18):

$$P_{3dB} = \frac{2.\ln(2).P_{sat}}{G_0 - 2} \qquad (2\text{-}18)$$

By a simple analogy with Equation (2-11), Equation (2-19) is another way to express the amplifier gain G dependence on input power:

$$G = \frac{G_0}{1 + \frac{P}{P_{3dB}}} \qquad (2\text{-}19)$$

Figure (2.5) depicts three gain curves of an SOA amplifier as a function of input power obtained by experiment and calculations. Details of static gain measurements will be reported in Paragraph 2.2.3. The experimental results (red points) are first measured. We

deduce an amplifier small-signal gain G_0 of 30 dB and a 3-dB saturation power of -17 dBm that corresponds to a saturation power P_{sat} of 11.65 dBm. The theoretical curves are then calculated using the implicit Equation (2-16) and the simple Equation (2-19) (blue and black curves respectively). Shapes of all the curves are similar and show clearly a gain compression for high input powers. Results of simple calculation and implicit calculation seem in good agreement with those of experiment for signal input power below P_{3dB}. For higher powers, simple calculation results obtained by using Equation (2-19) are in better agreement with experimental data than those of implicit calculation. Then, for any SOA, by measuring its amplifier small-signal gain and 3-dB saturation power, we can extrapolate the static gain versus the input signal power.

Static gain curves versus the input signal power illustrate clearly the SOA non-linear response which is widely exploited in all signal processing configurations based on SOAs, i.e. the input signal dependence of the SOA gain when the input power level becomes high compared to the saturation power.

2.1.3 SOA dynamics

In most applications, especially in all-optical signal processing, optical data signal injected into an SOA is not a continuous beam. As discussed in the first chapter, for digital communications systems, information is coded by means of binary symbols '1' and '0'. Physically, the information is transposed into intensity or phase modulation of a pulse stream. On the component side, an SOA is mainly used as the key non-linear active element of an optical function, its dynamics reflect the dynamics of the optical function and hence the time response of the function is determined essentially by the SOA speed. It is therefore of great interest to study SOAs' dynamic behaviour under injection of a pulse sequence.

If the amplifier is operated in the linear regime, the output amplified pulse is a replica of the input pulse. However, it is not the case in our goal applications, where SOAs are employed as non-linear devices. Injected pulses have a typical width between a few ps and 100 ps (for the bit rate of 10 Gbit/s and higher). Power is controlled in such a way that the SOA operates in a saturated regime. This results in a time dependent optical gain of the SOA.

2.1.3.1 Gain dynamics

For simplicity, the gain dynamics of a classical bulk SOA that undergoes an optical pulse passage can be described as shown in Figure (2.6) (reproduced from [53]).

Figure (2.6(a)) depicts the energy band state before the pulse passage. When an ultra-short optical pulse (femtosecond pulse) is injected into an SOA, carriers in excited states are depleted because of the stimulated emission, which is responsible for amplification of the input pulse. As the carrier density is reduced, the amplifier gain is reduced. The pulse passage causes a local deviation from the Fermi-Dirac distribution at the carrier energies
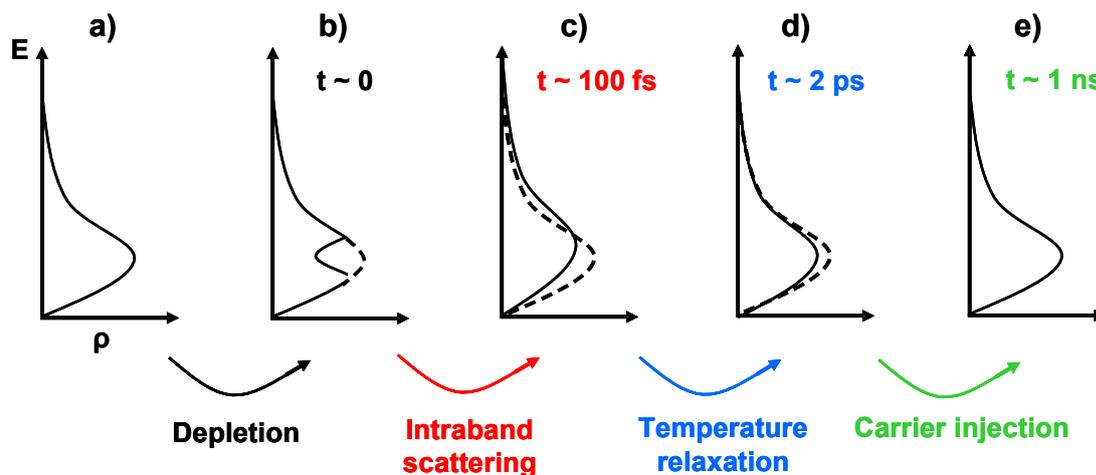
Figure 2.6: Qualitative illustration of the carrier distribution evolution (electron density ρ vs. electron energy E) of an SOA active region after a passage of a short optical pulse

corresponding to the optical transition. The effect is called Spectral Hole Burning (SHB). Moreover, the pump pulse heats up the carrier distributions due to free carrier absorption and stimulated emission. This transient heating of electron and hole temperature is called Carrier Heating (CH). SHB and CH imply that the carrier density is not in a thermal equilibrium Fermi-Dirac distribution anymore [53]. Instantaneously following the pulse, the carriers begin reorganize via intraband scattering in a time scale of 50-100 fs to fill the spectral hole, as shown in Figure (2.6) from (b) to (c). After this first 100 fs, the effect of carriers cooling down to the lattice temperature is dominant. This temperature relaxation takes place in a time scale of 0.5-2 ps (in Figure (2.6) from (c) to (d)). After a few ps, a quasi-equilibrium Fermi-Dirac distribution at the lattice temperature is established and the amplifier begins recovering its initial state, i.e. its initial optical gain through the total carrier density recovery. This density progresses on a time scale from 40 ps up to hundreds of ps depending on different SOAs, thanks to carrier replacement by external current injection. In summary, for SOA with bulk based active region, the mechanisms associated to gain recovery are current injection, CH and SHB. The first one is usually assigned as interband relaxations and the two last ones are usually assigned as intraband relaxations.

QD based SOAs are expected to provide promising features, including ultrafast gain dynamics. For self-assembled QDs, the dots are immersed in a Wetting Layer (WL). Hence, an active region based on self-assembled QDs is usually described as two discrete levels of the dots including a ground state and an excited state; and a upper continuum state of the wetting layer. This discrete nature of the QD system makes that in a QD SOA, the wetting layer serves as a carrier reservoir layer while in a regular bulk SOA, the reservoir states and the optically active states are strongly coupled within the upper energy band. The wetting layer is populated by the injected current. The carrier relaxation time from the wetting
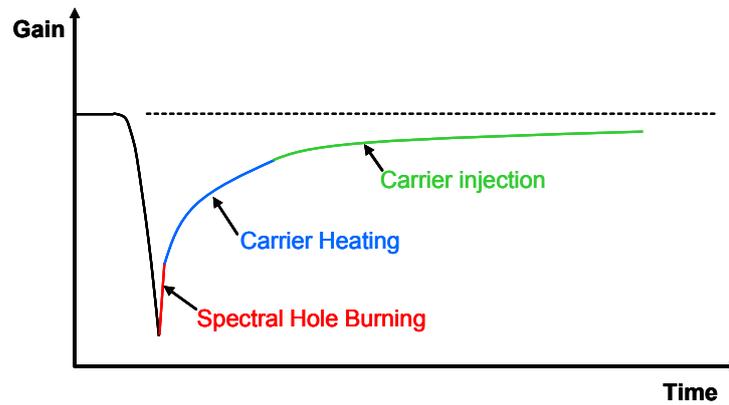
Figure 2.7: Qualitative bulk SOA's gain recovery after saturation by a fs pulse

layer to the QDs is in the range of 0.5-10 ps [59]. The carriers that are injected into the wetting layer can make a fast transfer to the QD excited state. Therefore, with increasing current, more carriers are present for transitions in the QDs and this leads to an increasing saturation power and a faster gain recovery. Possible signal processing at 160 Gbit/s with negligible pattern effect was predicted thanks to a time response smaller than 10 ps of QD SOAs [59].

In order to observe the fast gain recovery, sufficiently short pulses must be used. The temporal characteristics of the ultrafast processes (SHB and CH) can be characterized through pump-probe measurements using femtosecond optical pulses [60]. After such high temporal resolution measurements, qualitative gain evolution shape can be described as shown in Figure (2.7).

All mechanisms with different response times lead to different temporal characteristics of the SOA gain recovery. The SOA gain recovery can split in three steps: a sharp rising corresponding to an ultrafast recovery associated to SHB, a smoother recovery with a time constant of a few ps associated to CH and at last a long slow recovery on a time scale from 40 ps up to 1 ns associated to interband relaxation resulting from carrier injection. Time characteristics of an SOA involving intraband and interband relaxation processes can be estimated by comparison with a model.

2.1.3.2 Phase dynamics

The SOA carrier density depletion following a saturated pulse passage results not only in a gain compression but also in a refractive index change. This last effect leads to a time dependent phase shift of the signals that travel the SOA. The coupling between gain and phase is governed by the theory of semiconductor laser linewidth developed by Charles H. Henry [61]. The phase change is proportional to the gain change via a constant called the linewidth enhancement factor or Henry factor or α factor. As previously discussed,
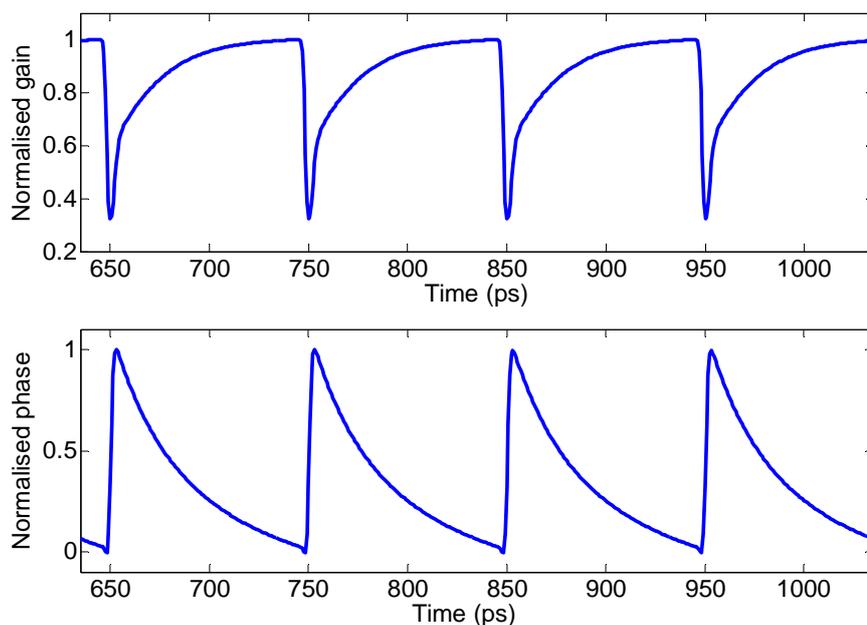
Figure 2.8: SOA dynamics: Gain recovery exhibits an ultrafast component and a slow component (upper trace) while phase recovery exhibits only a slow component (lower trace)

the gain is recovered through three different mechanisms: SHB, CH and carrier interband relaxation. Separate measurements of gain and phase recovery have shown different α-factor values associated to the three processes [62]. The α value has been estimated to be $\tilde{0}$ for the SHB process, $\tilde{1}$ for the CH process and $\tilde{5}$-8 for the normal carrier band to band relaxation [63]. The small α factors for fast processes suggest that the phase recovery is slower than the gain recovery. This last prediction has been demonstrated by some experiments [64], [62], [65]. Trace examples of gain and of phase recoveries are illustrated in Figure (2.8) obtained by simulation using the model that will be developed in Chapter 3. The SOA is supposed to be saturated by a 2 ps pulse stream.

The gain recovery trace displays two steps with two different temporal characteristics. The first step can be characterised by a time constant in order of few ps. This first gain recovery part is dominated by intraband relaxations (SHB and CH). The SHB effect is masked by the pulse length which is much longer than the SHB process and can not be observed because of the long pulse duration compared to the time scale of SHB effect (2 ps vs. 100 fs). However, as the pulse length is a little bit longer than the CH dynamics, this last contribution can be seen in the first part of the gain recovery curve. The second step exhibits a temporal characteristic in order of 100 ps that is the signature of carrier interband relaxation. On the other side, phase recovery rather seems to be characterised by only one time constant in the same order of 100 ps. This last observation illustrates the fact that the coupling between phase and gain changes caused by total carrier density reduction is much stronger than the coupling phase gain associated to the ultrafast intraband processes. This phase-gain dynamics difference should be taken into account carefully in signal processing

configurations that exploit simultaneously cross-gain and cross-phase modulations in SOAs.

2.2   Static characteristics

2.2.1   Description of the investigated SOAs

As previously mentioned in Section 2.1, all the SOAs studied in this thesis have been supplied by the Alcatel-Lucent Thales III-V Lab in the framework of the national project FUTUR. SOAs with different structures and materials are designed and fabricated in order to perform functions of optical regeneration and wavelength conversion at 40 Gbit/s up to 160 Gbit/s. The main factor that limits SOA based signal processing function performances for bit rates superior to 10 Gbit/s is the SOA dynamics that is not so fast. It is shown that the effective carrier lifetime which is related to the SOA time response, can be reduced by increasing the waveguide confinement factor [66]. Ultrafast gain dynamics are also expected from new quantum structures [50], [53]. In such vision, we investigated various SOA structures described in Table (2.1). The SOA structure information is given by our SOA supplier.

Chip number	Material	Confinement	Waveguide length (mm)	Maximal bias current (mA)
1	Bulk	20 %	1	300
2	Bulk	80 %	1	400
3	Quantum-dot	6 QDot layers	2	500
4	Quantum-dash	6 QDash layers	2	300
5	Quantum-dot	3 QDot layers	5	800

Table 2.1: Characterised SOAs

All SOAs are buried heterostructures except for the sample n°5 which is a ridge waveguide. For standard SOAs based on bulk material, two chips with the same waveguide length but different confinement factors are studied. The material of active region is In-GaAsP which is grown on an InP substrate. As far as quantum material based SOAs are concerned, two quantum-dot SOAs with different waveguide length are analysed, as well as a quantum-dash (elongated dot) SOA [51]. Supplied SOAs are chips on submount. The last three SOAs are constituted of InAs/InP QD material allowing operation in the telecom wavelength window [1.4 μm-1.6 μm] [51]. For all characterisations, unless mentioned, SOAs are controlled at typical room temperature, i.e. 25°C.

In almost characterisation experiments, laser signal that is injected into SOAs is guided by an optical fibre and signal emitted by SOAs has to be transported also by an optical fibre to the analysis instrument. Coupling between SOA chips and fibres is realised by two injection benches using micro-lensed fibres and lenses for coupling.

Micro-lensed fibre coupling bed

Micro-lensed fibre coupling bed is shown in Figure (2.9). It consists mainly of a chip support including temperature control and translation in y and z directions, a bias current
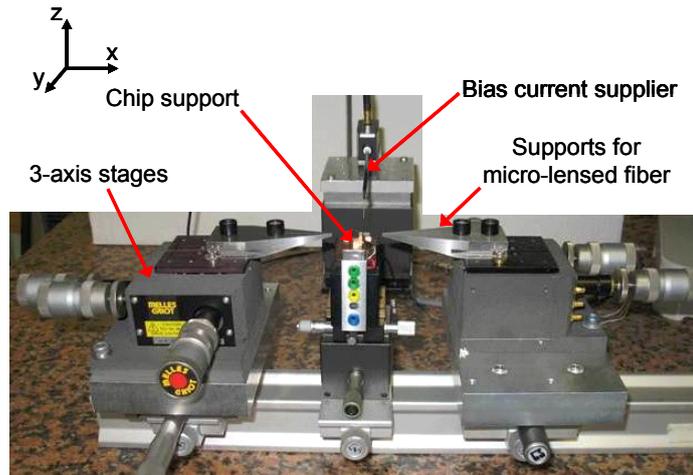
Figure 2.9: Micro-lensed fibres coupling bed

supplier and two micro-lensed fibre supports mounted on 3-axis stages allowing an accurate chip waveguide - fibres alignment.

The optical mode diameter of an SOA can be very different from one to other. In general, it is comprised in the range from 2 μm up to tens of micrometers depending on the tapers implemented at active region waveguides ends. We use micro-lensed fibres whose mode diameter can be adapted to the SOA mode to minimise the fibre-chip coupling loss. These micro-lensed fibres are fabricated in the CCLO platform of our laboratory and can provide a wide mode diameter range of [2 μm-140 μm] [67], [68]. Moreover, these micro-lensed fibres are anti-reflection coated to avoid any feedback reflection that can disturb the SOA operation and even damage the AR coatings of the SOA if intense optical signals present. For each SOA chip, the mode diameter is measured via near-field and far-field measurements and mode-adapted micro-lensed fibres for injection are manufactured consequently. Depending on mode diameter, one side loss of a micro-lensed fibre chip coupling can be lower than 2 dB. All of tested SOAs have a mode diameter in the range of [2 μm-8 μm]. It is not difficult to obtain a typical loss of [2 dB-3 dB].

This micro-lensed fibre coupling bed is convenient for all preliminary characterisations such as P(I) curve, amplified spontaneous emission spectrum, static and dynamic gain measurements, etc... However, this injection system is cumbersome and not transportable because of the 3-axis stages size and micro-lensed fibre fragility.

SOA module using lenses

Once, the tested SOA is shown compatible in terms of operating wavelength, ripple and gain, it is in a module consisting of a lenses coupling bed for more mobility. The SOA module bench is depicted in Figure (2.10). It consists of a chip support including the temperature control system and 6 lenses (3 lenses for each side) for light coupling between
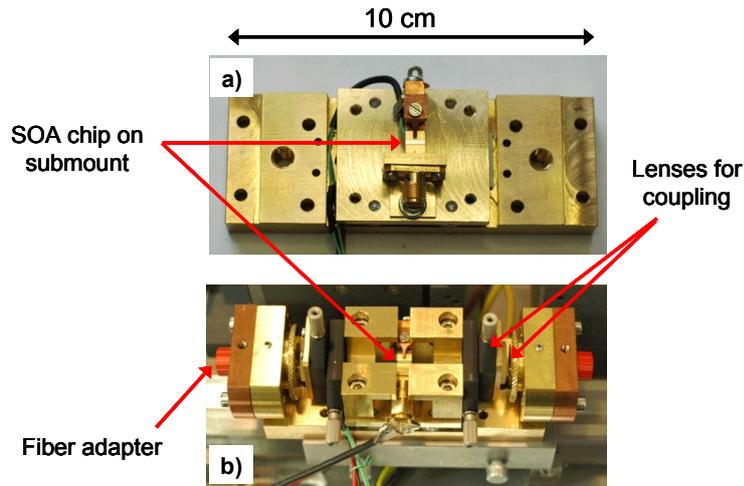
Figure 2.10: SOA module without lenses (a) and SOA module with lenses for chip-fibre light coupling (b)

chip and terminal fibres. Chip-fibre light coupling is based on the principle of a 2f or a 4f correlator. The module system is compact and very robust. The manipulation of SOA module becomes much more comfortable compared to micro-lensed fibre coupling bed. In general, coupling loss of the module is otherwise higher than that of micro-lensed fibre bed. One-side loss of [3 dB-4 dB] can be easily achieved; a minimal loss of 1.5 dB can be obtained in the best cases.

2.2.2 Amplified spontaneous emission investigation

P(I) curve

At first, the ASE power of tested SOA is measured as a function of bias current. The power emitted by each facet of the SOA is collected and measured by an integrating sphere. An example of P(I) curve of the SOA n°3 (2-mm length QDot SOA) is displayed in Figure (2.11).

The first observation is the co-propagating and counter-propagating ASE powers have to be equivalent and it is the case of the SOA n°3. A large difference between the two curves can indicate that one of the SOA waveguide outputs is damaged or the ARs on the two facets are not identical. The ASE curves provide also information about the transparency current and the maximal current that can be supported by the SOA. For SOA n°3, ASE curve presents a transparency current at around 100 mA. Above 500 mA of bias current, the ASE power does not increase anymore with the current exhibiting a beginning of ASE saturation phenomenon. For currents superior to 500 mA, the SOA is more and more strongly heated and it is observed that this heating disturbs operation of Peltier thermoelectric devices using for temperature control. This last information about the maximal bias current is very important as it will be seen in Paragraph 2.3.3. By increasing the current, SOA gain
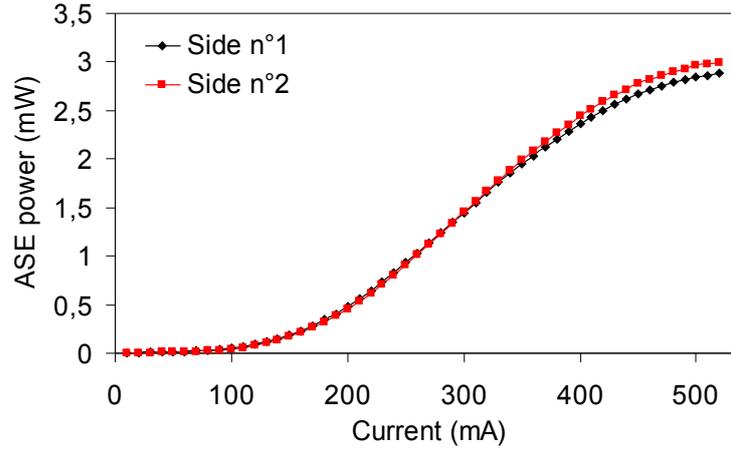
Figure 2.11: ASE power as a function of bias current of the SOA n°3

dynamics can be drastically sped up promising operation at ultrahigh bit rates. However, the current can not be increased without limit. P(I) curves is the simplest way to know the maximum current supported by the SOA. Transparency and maximum currents for the 5 investigated SOA samples are summarised in Table (2.2).

Chip number	Description	Transparency current (mA)	Maximal current (mA)
1	Bulk 20 %	50	300
2	Bulk 80 %	50	**500**
3	QDot 2 mm length	100	500
4	QDash 2 mm length	50	300
5	QDot 5 mm length	100	800

Table 2.2: Characteristics of the 5 investigated SOA samples raised from the measurements of ASE power as function of bias current

Almost maximal current values are consistent with those given by the SOA supplier (Table 2.1), except for the SOA n°2. We observe that up to 500 mA of bias current (compared to 400 mA given by our supplier), the SOA maintains a stable operation without heating.

ASE spectra

ASE spectra are simply obtained by using an Optical Spectrum Analyser (OSA). All presented ASE spectra are achieved with an OSA from Anritsu (MS9710B) with a wavelength range of [600 nm-1750 nm] and a resolution of 0.07 nm. ASE spectra show approximate images of carrier energy distribution or in other words a good estimation of the gain versus wavelength. ASE spectrum measurements provide basic information such SOA operating wavelength range and gain ripple levels.

Figure (2.12(a)) describes ASE spectra of the SOA n°4 (QDash SOA) for different
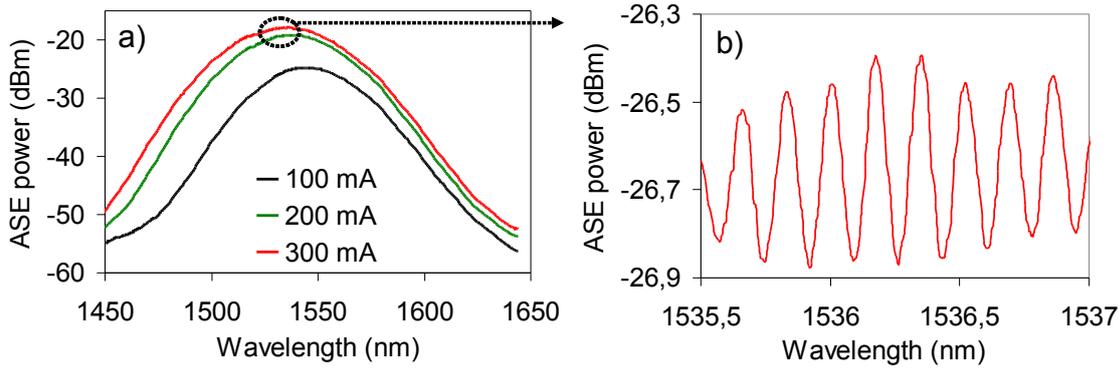
Figure 2.12: ASE spectra of the quantum-dash based SOA n°4 (a) for various bias current and (b) its ripple observed at 300 mA

bias currents. We observe that the bias current growth results in an increase of the ASE power, a blue shift of the ASE peak and a wider spectrum. These changes result from the increase of distance between Fermi levels related with the carrier density expanse caused by electrical pumping. The SOA exhibits a wide range of operating wavelength. At 300 mA of bias current, its ASE spectrum is centred at 1538 nm and the optical bandwith at half-maximum spreads from 1514 nm up to 1560 nm. This optical bandwidth covers almost the whole C-band which is the operating wavelength window of practically all the transmission systems.

The second information directly given by ASE spectrum measurements is ripple level. In general, ripple increases also with the bias current as the modal gain increases. Figure (2.12(b)) displays the SOA ripple presents at the spectrum peak for the bias current of 300 mA. Oscillations show highest amplitude of 0.5 dB and an FSR of 0.17 nm corresponding to a cavity length of 1.9 mm. The cavity length deduced from ripple measurement corresponds to the active region waveguide length given by the SOA manufacturer. Hence residual reflections are intrinsic of the SOA and do not due to external fibres used for injection. Results of ripple measurements of all SOAs at maximum bias current are presented in Table (2.3).

Chip number	Description	Ripple (dB)
1	Bulk 20 %	< 0.5
2	Bulk 80 %	4
3	QDot 2 mm length	2
4	QDash 2 mm length	0.5
5	QDot 5 mm length	6

Table 2.3: Ripple level of the 5 investigated SOA samples

A ripple of 0.5 dB implies a good AR treatment; it is closed to the actual limit of reflection suppression techniques. A ripple inferior to 1 dB ensures an optimal operation of
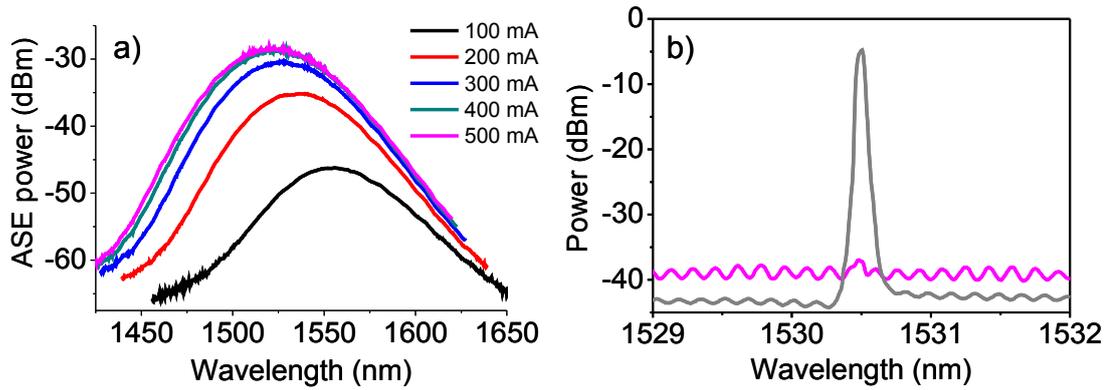
Figure 2.13: ASE spectra of the quantum-dot based SOA n°3 (a) for various bias current and (b) output signals for a TE(gray) and a TM(light purple) polarised continuous signal injected into the SOA

the SOA. SOAs n°1 and n°4 are then quite adequate following this criterion, while SOAs n°2 and n°3 exhibit higher ripple levels. Nevertheless, these ripples can be still tolerated in certain configurations. A ripple of 1 dB is difficult to attain especially for high gain SOA. Influences of cavity resonances can be lightened by using a continuous beam to saturate partially the SOA. Minimising the ripple impact is only one of benefits of using a saturating continuous beam. This technique is exploited mainly to reduce the SOA gain recovery time as we will see in Paragraph 2.3.1 with more details. Finally, large ripple of 6 dB of the SOA n°5 will be a major obstacle for its applications.

At last, in Figure (2.12(a)), separate peaks corresponding to emissions from the ground state, second state and wetting layers are not observed as expected for a SOA with a quantum-dot or quantum-dash based active region. This is also the case of the SOA n°3, its ASE spectra for different electric pumping levels are shown in Figure (2.13(a)). These spectra look like rather to bulk based SOAs than deeply confined quantum-dot SOAs [69]. This fact is reflections of a large variation in dots/dashes size and this leads to a dispersion of excited state energy. Consequently, there is a strong coupling between the active states in the dots/dashes and the surrounding continuums states of wetting layers (thin layers which are formed beneath the QDs). On the other side, it is important to note that these ASE spectra are measured at room temperature (25°C, around 300 K) and it is demonstrated that at lower temperature (to ~100 K), energy states of the dots/dashes can be decoupled from both those of the wetting layer and each other [70].

Despite quantum confinement characteristics do not appear in the ASE spectra, the fact that active regions are based on QDot/Qdash materials results in a strong sensitivity of the SOAs to injected signal polarisation, which can be observed easily by injecting a linearly polarised continuous wave into the SOAs. Figure (2.13(b)) shows the output signal spectra emitted by the QD based SOA n°3 for different modes (TE and TM) of the injected
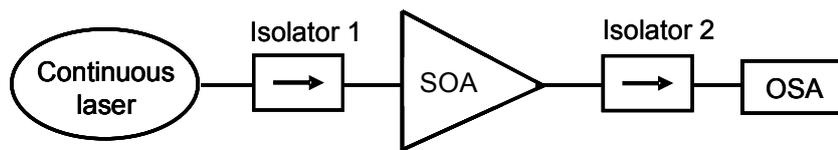
Figure 2.14: Experimental set-up of static gain measurement in self-saturation scheme

light. Linearly polarised continuous signal is delivered by a laser source. Polarisations TE or TM of the signal at the SOA input are obtained by placing a polarisation controller between the laser source and the SOA while the input power is fixed. When the input signal is TE polarised, the output spectrum (gray) presents a strong peak at the input light wavelength. And in other case, when the input signal is TM polarised, the output spectrum (light purple) is completely flat. That means that the SOA exhibits a high gain for TE polarised input signal and no gain for TM polarised input signal. It is well-known that Stranski-Krastanow QDs structures generally show TE polarised gain [71], [54]. The flat shape of QDs and the compressive in-plane strain make that near the bandgap heavy-hole transition is TE polarised [54]. Then a signal injected into a QD SOA will undergo different gains and even attenuations according to its polarisation state. The first consequence is an undesirable strong fluctuation of signal output power. This is one the highest barriers to be overcome for most QD SOA applications in telecommunications.

2.2.3   Static gain measurements

As mentioned in Paragraph 2.1.2, SOAs' non-linearity appears clearly on the gain saturation curve which can be obtained simply by injecting a continuous beam into the tested SOA. By adjusting the signal input power, a decrease of the amplifier gain is observed. We call this type of experiment the static gain measurement. Such a measurement allows the parameters characterising the SOA non-linearity to be evaluated: the small-signal gain and the saturation power. As already mentioned in Chapter 1, an SOA in self-saturation or in cross saturation regime can act as a non-linear gate in a regenerator or a wavelength converter. It is therefore necessary to study its non-linear behaviour in the two configurations. We measure then the SOA static gains in two configurations: self-saturation and cross saturation. The first experiment consists in injecting only one continuous signal into the SOA. The second one consists in injecting two continuous signals respectively called 'pump' and 'probe'.

Static gain measurement in self-saturation configuration

The experimental set-up of the static gain measurement in self-saturation regime is depicted in Figure (2.14). A continuous signal is injected into the investigated SOA. The laser is wavelength tunable. The signal power at the SOA input is varied, the signal power at the SOA output is measured and the gain is then deduced by subtracting the input
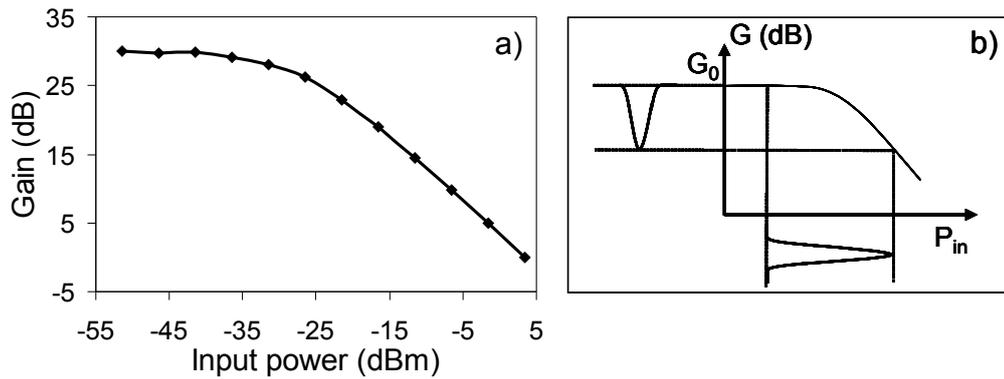
Figure 2.15: Static gain curve in self-saturation configuration of an SOA (a) and illustration of gain compression for a pulsed signal (b)

power from the output power thanks to an OSA. OSA utilisation allows ASE noise to be taken into account especially when the input signal is weak and the ASE noise can not be neglected. Isolators are used to protect different elements in the experimental scheme. The first one is for cutting down the emitting ASE that could damage the laser source. The second one is for cutting down all possible feedbacks that could disturb the SOA operation. An example of static gain curve in self-saturation configuration of the SOA n°1 is shown in Figure (2.15(a)).

The curve allows the amplifier small-signal gain of the SOA $G_0 = 30$ dB and the 3-dB saturation power $P_{3dB} = -27$ dBm to be measured. By increasing the input signal power, the static gain curve illustrates two different regimes of the SOA behaviour. When the input power is much smaller than -27 dBm, the SOA is in a linear amplification regime called 'small-signal regime' characterised by a gain of 30 dB. When the input power reaches and exceeds $P_{3dB} = -27$ dBm, the SOA is in the saturation regime and the amplifier gain drops with the signal power growth. In this regime, the -1 dB/dB slope indicates that the output signal power is constant despite the input power increase. Behaviour of a power equaliser is observed. Static gain curve can be also useful to demonstrate the SOA gain compression caused by a powerful pulse as shown in Figure (2.15(b)). From the most naïve point of view, the peak of the pulse will undergo a smaller gain compared to its pedestals. It is easy to see that the steeper the slope is, the deeper the compression is. In fact, the SOA gain compression is much more complicated than what is described here. To have a complete view of gain compression of an SOA, it is necessary to take into account temporal characteristics of the pulse stream and the SOA dynamics. This is the main topic of studies presented in Section 2.3. Similar measurements and analyses are also realised for others SOAs. Results are briefly summarised in Table (2.4).

The static gain curve of the long QDot SOA (SOA n°5) could not be measured. Its ripple shown in the ASE study is too strong and did not allow an accurate signal power

Chip number	Description	Current (mA)	G_0 (dB)	P_{3dB} (dBm)
1	Bulk 20 %	200	30	-27
2	Bulk 80 %	300	30	-25
3	QDot 2 mm length	300	20	-16
4	QDash 2 mm length	200	27.5	-23

Table 2.4: Gain saturation characteristics of the studied SOAs

measurement by OSA especially for small input power. The two bulk based SOAs (SOA n°1 & n°2) show similar small-signal gains and 3 dB saturation powers. The QDot SOA (SOA n°3) exhibits the smallest amplifier small-signal gain principally because of its very small confinement compared to others samples. Concerning its high 3-dB saturation power, it is difficult to know which is the main factor responsible for. The QDash SOA (SOA n°4) presents intermediate characteristics. However, they look like those of bulk based SOA rather than those of QDot SOA. We also observe that the static gain curve slopes of the two bulk based SOAs are the steepest and the QDot SOA shows the smoothest slope. These observations are in good agreement with respective measured saturation powers because at strong input signal powers the gain curve slope is inversely proportional to the saturation power.

In general, the measured static gain curve depends on the bias current. When the electric pumping increases the small-signal gain increases because there are more carriers. On the other side, the electric pumping increase leads also to an ASE increase and this last participates stronger to gain saturation and results in a smaller saturation power. At last, for a bulk based SOA, the static gain curve in self-saturation does not exhibit significant changes when the signal wavelength changes for a large wavelength range that is related to the SOA optical bandwidth. On the other side, for quantum-dot/dash based SOAs, it is theoretically predicted that the static gain saturation dependence to signal wavelength is much stronger as their gain spectrum is much more selective. We do not observe this fact for our quantum based SOAs. This fact is probably consequent of the strong coupling between the active energy states in the dots/dashes and the surrounding continuums energy states of wetting layers which is already raised by ASE spectrum measurements.

Static gain measurement in cross saturation configuration

Characterising an SOA operates in a cross saturation regime requires to inject into the SOA two signals, respectively called 'pump' and 'probe' signal. If the static gain curve in self-saturation regime allows information about SOA small-signal gain and SOA saturation power to be picked up, the static gain curves obtained in cross saturation configuration provide information about how these parameters change for a probe signal when the SOA is driven by a pump signal. The experimental set-up for static gain measurement in cross saturation scheme is displayed in Figure (2.16).
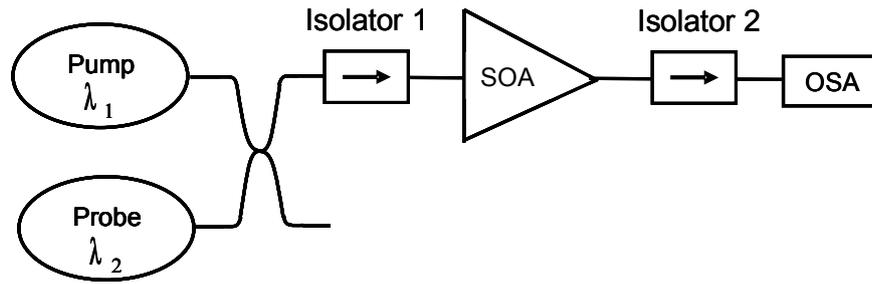
Figure 2.16: Experimental set-up of static gain measurement in cross saturation scheme
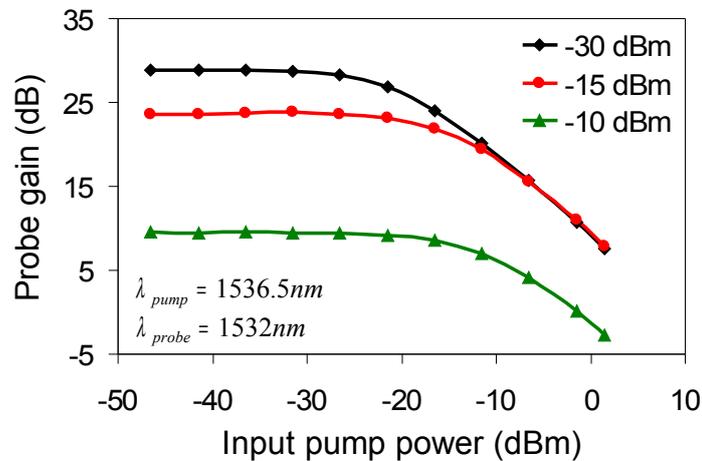
Figure 2.17: Static gain curves of SOA n°1 in cross saturation versus input pump power for various input probe power levels -30 dBm (black), -15 dBm (red) and -10 dBm (green)

The measurement is very similar to the case of the self-saturation regime except that a probe signal at a different wavelength from the pump signal is simultaneously injected into the SOA. By varying the input pump powers, it is observed that amplifier gain accumulated by the probe signal is affected. The static gain curves versus the input pump power are plotted for various input probe power levels. Results for the SOA n°1 are presented in Figure (2.17).

The SOA gain (represented through the probe gain) depicted by these curves exhibits a similar behaviour as in self-saturation configuration which is described by two operation regimes: small-signal regime for low input pump powers and saturation regime for high input pump powers. However, these curves exhibit a change of characteristics (small-signal gain and 3-dB saturation power) when the input probe level changes. These parameters are also different from those of the gain curve in self-saturation regime. Because of the presence of a probe signal that consumes partially carrier population, the SOA global small-signal gain is reduced and it is clear that the stronger the input probe power is, the smaller the amplifier gain is. The partial reduction of carrier population leads also to a weaker ASE

noise and a direct consequent is a higher saturation power. At last, it is interesting to note that for small input powers such that pump signal can be neglected compared to the probe signal, gain self-saturation caused by the probe signal can be observed. Amplifier gain drops from 29 dB to 10 dB when the input probe power increases from -30 dBm to -10 dBm.

All static characterisations must not be skipped. They provide primary and practical information about an SOA. P(I) measurement allows to determine the maximum bias current supported by the SOA. The study of the ASE spectra allows the adequate operating wavelength range and the gain ripple level to be determined. At last, static gain curves gives information about the SOA gain non-linearity in different operating situations: self-saturation and cross saturation. SOA parameters achieved through these characterisations are primordial to evaluate if the SOA could be used as a non-linear gate in signal processing applications. The SOA should exhibit a high small-signal gain, small ripple, low saturation power and a steep slope of static gain curve. Furthermore, these characteristics allow operation of any concrete application scheme based on the tested SOA to be optimised.

Once static characterisations are realised, the SOA dynamics must to be investigated because they define the limit operating bit rate of an SOA based regenerator or wavelength converter.

2.3 Dynamics characterisation

SOAs have been used in several optical transmission experiments with good performance. In applications such pre-amplification, the amplifier is operated mostly in the linear regime in which the amplified pulse is a replica of the input pulse. However, in a large number of other applications such optical logical gates, optical clock recovery and especially in wavelength converters and regenerators, the amplifier is used as a non-linear optical gate which implies operating in saturation regime. When the SOA is saturated by a pulsed signal, its optical gain becomes time dependent, which means also a time dependence of the refractive index. This may be viewed simply as follows. The gain saturation leads to a change in carrier density which results in a change in refractive index and then of the signal phase. These SOA gain and phase dynamics are important for SOA based non-linear optical gates.

SOA based wavelength conversion and regeneration schemes exploit gain modulation, cross phase modulation or four wave mixing. When the gain modulation is used, attention must be paid to the gain recovery time of the SOA. On the other side, in interferometer configurations which exploit simultaneously gain and phase modulations, both gain and phase dynamics should be considered. Gain and phase recovery times are key parameters which determine patterning effects and the bit rate limit at which the SOA could be operated. SOA gain and phase dynamics can be measured by exploiting pump-probe technique with two types of experiment. The first one is a degenerate pump-probe experiment using pulse streams at low repetition rate (below 100 MHz), with heterodyne detection and femtosecond time resolution [60], [72]. The second one is a usual wavelength conversion configuration using pulse streams at high repetition rate (up to 40 GHz), with picosecond time resolution [64]. The dynamics experiment with femtosecond pulses offers a high time resolution measurement and allows different characteristic time constants of the SOA to be identified. The second dynamics experiment with picosecond pulses at high repetition rate is useful to understand how external operating parameters (signal wavelength, pulsewidth, data rate...) influence the SOA dynamics as the SOA is operated under conditions that are very similar to those of actual backbone transmissions.

In order to find adequate SOAs that could be used in a wavelength converter or in an all-optical regenerator for ultrahigh bit rate transmission, we elaborate in our laboratory a gain dynamics measurement based on wavelength conversion scheme with picosecond time resolution as presented in Paragraph 2.3.1. Phase dynamics measurement has been not possible yet but it could be elaborated by using an interferometer. This Section 2.3 is dedicated to gain dynamics experiment presentation and experimental results obtained for various SOAs. Impacts of operating conditions such as signals pulsewidth and wavelength, bias current, waveguide length and output filtering are investigated.
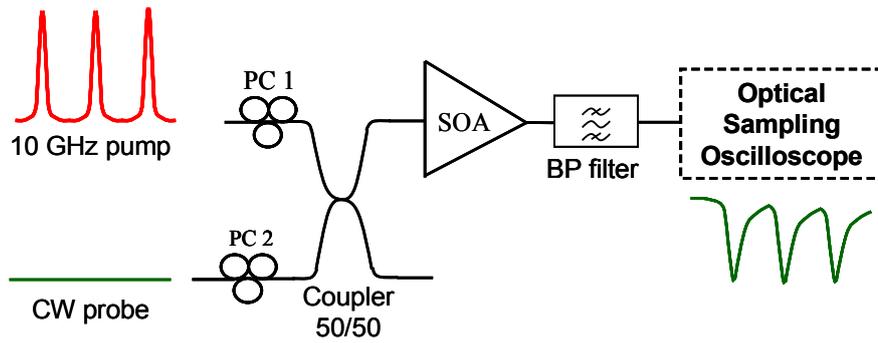
Figure 2.18: Experimental set-up of gain dynamics measurement

2.3.1 Gain dynamics experiment

Gain dynamics characterisation addresses SOA gain behaviour in response to excitation of pulsed signals. When a pulse stream with a high enough power is injected into an SOA, its gain is modulated. To measure the gain dynamic response of an SOA, we use a pump-probe experiment scheme as depicted in Figure (2.18).

The basic principle of the experiment relies on SOA cross gain modulation. Note that there are other set-ups which are used in the litterature, where the probe is also a short pulse (typically 150 fs [60]). this allows to reach a much better time resolution than which is expected from a high speed Optical Sampling Oscilloscope. However, the experiment set-up is much more sophisticated than the one we are using, which is quite sufficient for the interested applications in this work. High power pulsed signal saturates the amplifier gain. This results in gain depletion and consequently leads to a decrease of the CW probe signal at the SOA output. The gain dynamics is therefore reflected on the probe transmission waveforms as a function of time. After reaching a maximal gain compression caused by pulse presence, the SOA gain recovers due to redistribution of carriers and injected current. Physical mechanisms of gain recovery have been presented in Paragraph 2.1.3. We remind that the main phenomena occurring during gain recovery are associated to spectral hole burning (SHB), carrier heating (CH) and interband relaxation via carrier injection.

The pump signal is a pulse stream at a repetition rate that is small enough to allow the observation of the complete recovery of gain. In our experiments, a pulse rate at 10 GHz is used. Pump power and pump wavelength can be changed easily. The wavelength range of pump signal covers almost the C-band. Typical pulsewidth is about 2 ps and can be increased by inserting narrow band filters. Probe signal is provided by a CW laser and is set-up at a different wavelength from the pump signal. Power and wavelength of the probe signal are also tunable. In most of our measurements, the probe input power is high and comparable to the average pump signal power. Strong probe signal contributes to SOA gain saturation and otherwise accelerates the gain recovery. Two polarisation controllers are used when quantum-dot/dash SOA are under investigation to align signal polarisations
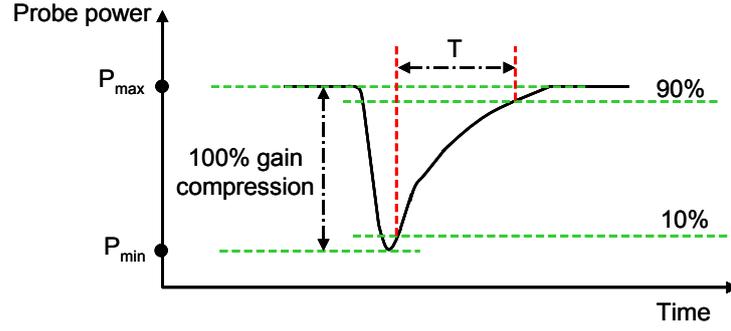
Figure 2.19: Typical probe waveform measured in pump-probe experiment

to the privileged axis of the QD waveguide. A 3-dB coupler is used to inject simultaneously pump signal and probe signal into the SOA. A band-pass filter is placed at the SOA output to reject the amplified pump signal and ASE noise. In general, the filter is a 5-nm flat-top filter (except special mention) and is centred on the probe wavelength. Output probe waveform is measured thanks to an Optical Sampling Oscilloscope (OSO) with a timing resolution of 1 ps (Picosolve, psO 100 Series). Typical probe evolution at the SOA output is depicted in Figure (2.19).

Such a trace allows to measure the gain recovery time T and the gain compression. We consider the gain recovery time as the time that gain needs to recover from 10% to 90% of its steady-state value. The gain compression express in dB is given by Equation (2-20):

$$\Delta G = 10 \times \log_{10} \left(\frac{P_{\max}}{P_{\min}} \right) \tag{2-20}$$

The parameters T and ΔG are related to pump and probe characteristics (wavelength, power, pulsewidth). T allows the maximum bit rate at which the SOA can operate without patterning effect to be estimated directly. When the bit duration exceeds T, SOA is fast enough to provide good performance without patterning effect due to its gain dynamics. For higher bit rates where the bit duration is smaller than T, patterning effects appear and degrade SOA based function performance. This measurement provides also information about T and ΔG dependence that is very useful when an optimum trade-off between SOA gain compression and response time has to be found in any cross-modulation scheme.

In general, intrinsic time constants characterising gain dynamics of an SOA are difficult to estimate. Results of our experiment can be further exploited by fitting with simple SOA phenomenological model to deduce different time constants associated to intraband and interband relaxation effects. Once these time constants are evaluated, the SOA can be modelled in various regenerator/wavelength converter configurations by associating with other components. This fit procedure allows a realistic SOA behaviour to be modelled.
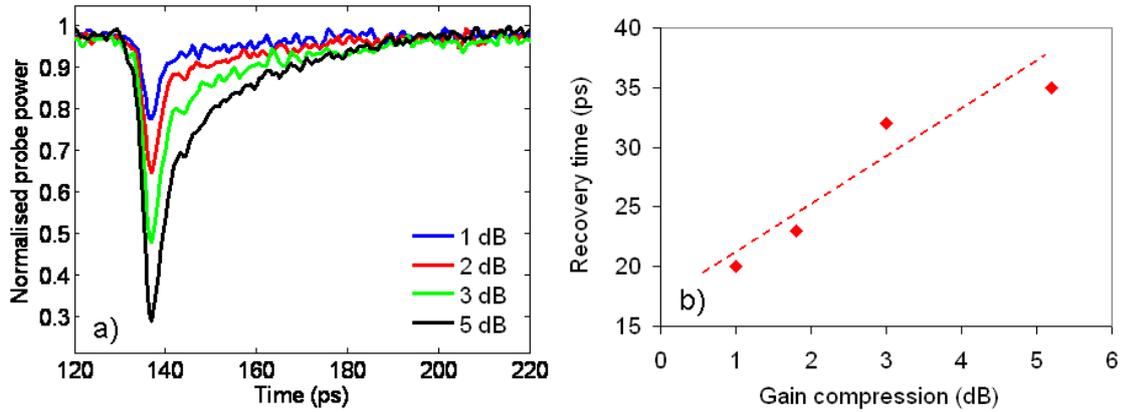
Figure 2.20: Gain recovery profiles of the SOA n°2 for various compressions (a) and deduced recovery time as a function of gain compression (b)

2.3.2 Gain compression-response time trade-off

SOA acts in a wavelength converter or a regenerator as a non-linear element. It is always preferable to operate the SOA in large gain compression regime to achieve an efficient operation. However, the greater the gain compression is, the more carriers are consumed by stimulated emission and consequently the device takes more time to return to its maximal value of gain. If the gain compression induced by pump signal is too strong, the SOA gain does not have enough time to recover completely when the next bit arrives; then patterning effects take place and output processed signal will not have a good performance as expected. For a first experiment, we studied the SOA gain dynamics for various gain compressions by changing input pump power, while keeping all other experimental parameters such as SOA bias current, probe power and signal wavelengths constant.

The SOA is pumped by a 300 mA current at which the ASE peak occurs at 1550 nm. The pump wavelength is set very close to the gain peak, 1548 nm. The probe wavelength is 1538 nm and its input power is -5 dBm. As expected, both gain compression and gain recovery time increase with pump pulse power. Similar SOA dynamic behaviour was observed despite different pump-probe configurations [73]. Figure (2.20) shows experimental results obtained for the SOA n°2, gain recovery traces for various gain compression values (a) and corresponding measured gain recovery times (b).

For any gain compression, both fast and slow processes of gain recovery are observed. After the compression induced by the pump pulse, the gain shows a fast recovery. This fast process shows that heated carriers cool down to the lattice temperature. Our resolution that is limited by the pump pulse duration of 2.2 ps is not high enough to resolve the recovery associated to faster effects such spectral hole burning. After the fast gain recovery, the gain recovery by slow interband relaxations is observed. Results demonstrate clearly that the gain recovery time is longer when the gain compression is greater. At maximal compression
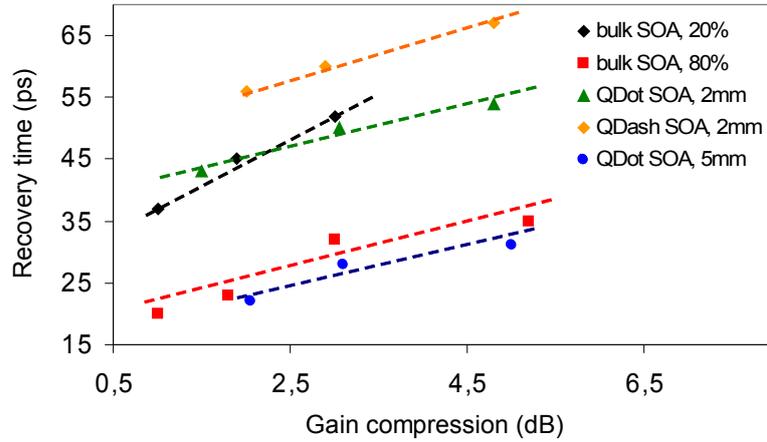
Figure 2.21: Gain recovery times of all SOAs as functions of gain compression

measured (5 dB), gain recovers from 10% to 90% of its maximal value within 35 ps. It is a short recovery time in comparison to long-lived lifetimes of interband recombinations that are in order of hundreds of picoseconds [58], [65]. These 'fast' recoveries are possible thanks to a strong probe signal that accelerates slow interband recombination processes and thanks to pump pulse duration as short as 2.2 ps. Otherwise, at this gain compression the SOA gain recovery is not fast enough to be compatible with bit rates exceeding or equal to 40 Gbit/s. At 40 Gbit/s, the bit duration is 25 ps and SOA response of an optical signal processing function must be shorter than 25 ps to avoid pattern effects and signal quality degradation. For this SOA, gain recovery times are smaller than 25 ps for gain compressions inferior to 2.5 dB.

It is clear that if this SOA is used in the same experimental conditions in a signal processing function, good performance could be achieved for data rates up to 40 Gbit/s only with limited gain compression. At 160 Gbit/s, where the bit slot is about 6 ps, patterning effects are predicted. Nevertheless, these results are well consistent with the state-of-the-art of simple SOA based wavelength converters [74] or of SOA based regenerators [54], which do not use assisted technique such as interferometer and shifted filtering.

Similar measurements are also investigated for the other studied SOAs. Operating conditions are adjusted for each SOA in such a way that all SOA operate in close operation conditions and hence results can be compared. In each case, pump wavelength is set in the SOA gain peak range and probe power level is set at about 0 dBm. Gain recovery shapes of all the investigated SOAs are similar to those depicted in Figure (2.20(a)). Measured gain recovery times are summarised in Figure (2.21).

The studied SOAs can be divided into two groups according to their recovery time ranges. The first ones comprises the SOA n°1 which is a bulk material based SOA with a small-optical confinement of 20%, the SOA n°3 which is a quantum-dot material based

SOA with a waveguide length of 2 mm and the SOA n°4 which is a quantum-dash material based SOA with the same length of 2 mm. These SOAs show long recovery times of at least 35 ps even for gain compression as low as 1 dB. They will be not efficient for operation at the bit rate of 40 Gbit/s and higher. Large patterning effects will degrade signal quality. The second group comprises the SOA n°2, which is a bulk based SOA with a high optical confinement of 80% and the SOA n°5, which is a quantum-dot material based SOA with a ultralong waveguide of 5 mm. These samples exhibit recovery times as low as 25 ps for gain compressions of about 2.5 dB. This result shows a potential of the two components for non-linear optical gates operating at 40 Gbit/s. By using techniques such as interferometer configurations or shifted filtering, operation at 160 Gbit/s can be expected.

As far as bulk based components are concerned, even if the two components are based on the same material and the waveguides have the same length, they display very different dynamics. The SOA n°2 appears much faster than the SOA n°1. This dynamics difference results mainly from the different optical confinement factors (20% for the n°1 and 80% for the n°2) and can be viewed as follow. In presence of intense photon density, carrier recovery process is characterised by an effective carrier lifetime τ_e that is defined by Equation (2-21) [66]:

$$\frac{1}{\tau_e} = \frac{1}{\tau} + \frac{1}{\tau'} \tag{2-21}$$

τ is the intrinsic carrier lifetime and τ' is due to stimulated emission. The first term τ is intrinsic to the SOA material. For the two bulk material based SOAs, this term is the same because both SOA active regions are constituted of InGaAsP material. The second term τ' is inversely proportional to the SOA confinement factor. It is evident that the effective carrier lifetime τ_e can be decreased by reducing τ'. On the other side, τ' reducing can be achieved by increasing the optical confinement. Finally, the effective carrier lifetime is smaller if the optical confinement is larger. Then, high confinement SOAs must be preferred for ultrahigh bit rate functions thanks to faster effective dynamic response.

Concerning quantum material based SOAs, the quantum-dash based SOA displays a slower gain recovery compared to the two quantum-dot based samples. This result is in agreement with other experimental works reported in the literature [75], [65]. In our experiment, the 2-mm QDash device (SOA n°4) and the 2-mm QDot device (SOA n°3) were pumped at the same current density and probe powers were nearly identical. Different gain recovery speeds reflects therefore the difference of intrinsic dynamics of the two devices. At 3 dB of gain compression, QDot SOA shows a recovery time of 50 ps and this time is raised to 60 ps for the QDash sample. It is shown that in gain regime, short lifetimes associated to ultrafast processes such as SHB and CH are similar for QDot and QDash based SOAs. The SHB and CH physical mechanisms are independent of the degree of quantum confinement. On the contrary, the degree of quantum confinement leads to a significant difference of long lifetimes of the two SOAs. The dynamics behaviour of QDash SOA is considered

similar to that of a wire like quantum confinement (1-D). Because capture processes are faster for higher quantum-confined material, QDot SOAs (0-D) exhibit therefore a shorter long-lived lifetime [65]. Then the global gain recovery time in a QDot SOA is shorter than in a QDash SOA. This result indicates that QDot SOA is the most promising for ultrafast signal processing functions.

At last, comparing the two quantum-dot based SOAs, it is observed that recovery times drop drastically from about 50 ps for the 2-mm QDot SOA to about 25 ps for the 5-mm QDot SOA. If the short QDot SOA exhibits too slow response to be used at 40 Gbit/s, the use of the long QDot SOA appears possible under small gain compression. Dimensions of the two SOA structures are different, especially the active region length. An explanation of this difference will be presented later in Paragraph 2.3.5. However, a qualitative explanation can be given as follows. Amplifier length can affect SOA gain dynamics [76], [77], [78], [79]. In long devices, ASE propagation in an SOA can not be neglected anymore. ASE induces stimulated emission recombination and hence speed up gain recovery dynamics. By increasing the SOA length, not only the amplifier gain is increased but also the ASE power and the last can shorten gain recovery [76].

The results show that even if gain recovery of all SOAs exhibits partially ultrafast processes, they are not all suitable for signal processing function at 40 Gbit/s and higher. Only the SOA n°2 and the SOA n°5 show recovery times as short as 25 ps at a gain compression of 2.5 dB and then are promising for operation at 40 Gbit/s and above. However, by associating these SOAs with techniques such as shifted filtering or use in an interferometer configuration, signal processing functions operating at 160 Gbit/s can be expected. Gain recovery durations can be shortened by decreasing the gain compression but this fact can limit efficiency of the SOA used as a non-linear element. Depending on specific signal processing function, a trade-off between gain compression and response time of the SOA must be found to obtain the best performance of a regenerator or a wavelength converter. It appears also that by increasing optical confinement and waveguide length, SOA gain recovery dynamics can be enhanced. Therefore highly confined and longer SOA are preferable for signal processing at ultrahigh bit rate. At last, in spite of very small confinement factor ($\tilde{1}$%), quantum-dot based SOAs demonstrate gain dynamics as fast as highly confined bulk based SOA. This ultrafast carrier dynamics of QD SOA is one of the advantages offered by quantum confined material.

2.3.3 Impact of bias current

Despite the presence of an ultrafast contribution in gain recovery processes under saturation by pump pulses as short as 2 ps, applications of SOAs in signal processing at 40 Gbit/s and higher are still limited especially in functions exploiting gain modulation. SOA response remains 'too long' compared to bit slot of 25 ps because of the slow recovery component that
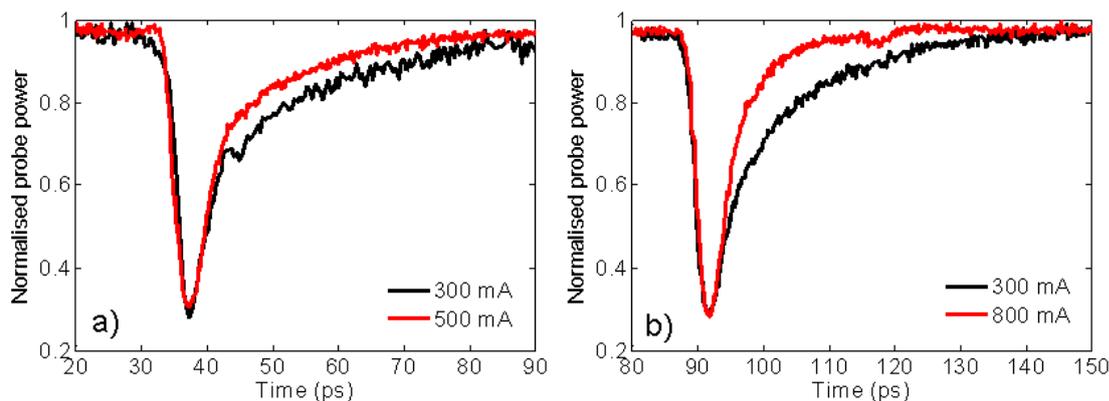
Figure 2.22: Gain recovery profiles of the highly confined bulk based SOA n°2 (a) and of the long quantum-dot based SOA n°5 (b), for various bias currents

is characterised generally by a long carrier lifetime in order of hundreds of picoseconds. The simplest technique to obtain shorter gain recovery times is to maximize the bias current. Figures (2.12(a)) and (2.13(a)) show that the ASE amount is higher for larger bias currents. Strong ASE means that there are more possible electron-hole recombinations. Hence, interband relaxations will be faster thanks to stimulated emission. Finally, the global gain recovery time is reduced. However, the carrier density can not be raised infinitely with bias current. At the limit of the pumping current density, the carrier density and the modal gain reach maximal values. Any additional increase of pumping current leads only to heating of the device. In previous experiments, the SOAs are set at typical operating bias currents exceeding the transparency currents and under the maximum currents supported by the SOAs.

In this experiment, we study SOA gain dynamics behaviours by pushing the bias current to its maximum value while avoiding heating. Gain recovery shapes of the highly confined bulk based SOA (SOA n°2) and of the long quantum-dot based SOA (SOA n°5) at typical and maximum bias current are depicted in Figure (2.22). Results demonstrate clearly faster gain recovery for higher bias current. For both cases, bias current does not seem to affect the fast gain recovery, or it is possible that changes involving fast processes are masked by pump pulse duration. However it has been shown that the lifetimes of intraband effects such as CH and SHB do not depend on the bias current density [65]. This confirms that fast recovery speed dominated by intraband relaxations is not influenced by current density increase. On the other side, acceleration of interband relaxation in recovery tail is clearly observed. As discussed previously, this could be a consequence of a greater carrier density supplied by a greater electrical current density.

We remind also that the active region widths of the two SOAs are similar while the QD SOA is five times longer, which means that the current density applied to the bulk SOA
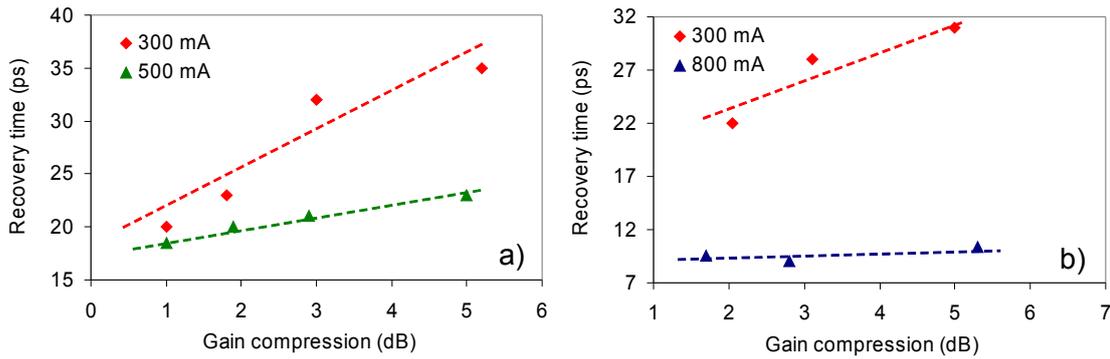
Figure 2.23: Gain recovery times as function of gain compression of the highly confined bulk based SOA-SOA n°2 (a) and of the long quantum-dot based SOA-SOA n°5 (b) for various bias currents

is greater than that of the QD SOA in all cases. However it is shown that recovery time enhancement is stronger with the QD SOA than with the bulk based SOA. It has been demonstrated that increasing the carrier density (by increasing the current density) is more efficient with a QD SOA than with a bulk material based SOA. The much longer waveguide of the QD sample also certainly contributes to the stronger enhancement of gain recovery speed due to higher ASE.

Gain compression - response time trade-off of both SOAs for different bias current is also investigated. The results are displayed in Figure (2.23). Thanks to the enhancement of SOA responses due to current density increase, the gain compression - response time trade-off at high bit rates is largely improved. At its maximal bias current of 500 mA, the bulk SOA exhibits gain recovery times less than 25 ps for all gain compressions less than 5 dB. Operation of this SOA at 40 Gbit/s without important patterning effects, which is limited at 2.5 dB of gain compression at 300 mA, can be achieved up to 5 dB of gain compression at 500 mA. Similar results are also reported in [79] where recovery time constant decreases from 30 ps to 20 ps when the injection current increases from 300 mA to 400 mA. Reduction of gain recovery times of the QD SOA is much more pronounced. The average recovery time decreases drastically from 30 ps to 10 ps when the bias current changes from 300 mA to 800 mA. At maximum bias current, the QD SOA can offer excellent response time for operation at 40 Gbit/s without any patterning effects. The QD SOA gain response is not far from the bit slot 6 ps of the data rate 160 Gbit/s. By using assisting techniques, solutions for signal processing at 160 Gbit/s should be possible.

By increasing the bias current density, gain recovery times are demonstrated to be shortened significantly. The bulk SOA promises operation at 40 Gbit/s for gain compressions as large as 5 dB. The QD SOA can not only offer excellent dynamics for regenerators and wavelength converters at 40 Gbit/s but also appears very promising for these applications at 160 Gbit/s.
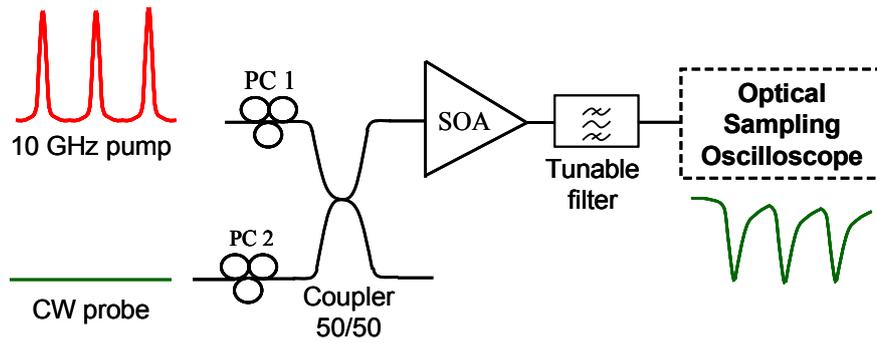
Figure 2.24: Experimental set-up for assessment of SOA dynamics enhancement by shifted filtering

2.3.4 Recovery acceleration by shifted filtering in wavelength conversion

It has been shown that a SOA can be used at 320 Gbit/s as a wavelength converter [80]. Despite the SOA response due to electron-hole interband relaxations is much longer than the bit duration of about 3 ps at this data rate, an error-free wavelength conversion is possible thanks to shifted filtering technique. As mentioned in [81], by adjusting parameters of the filter that follows the SOA, response of the system can be shorter than the SOA recovery duration and wavelength conversions with or without polarity preservation can be obtained. In this paragraph, we bring out the dynamics enhancement of the system SOA+filter offered by shifted filtering technique that allows signal processing functions for ultrahigh bit rates beyond 40 Gbit/s to be achieved. We remind the experiment scheme as shown in Figure (2.24), which has been already presented in Paragraph 2.3.1. In this experiment, the band-pass filter placed at the SOA output is a tunable filter with a tuning range covering the whole C-band.

2.3.4.1 Physical mechanisms

Pump signal and CW probe signal are simultaneously injected into the SOA. Inside the SOA, the probe suffers cross gain modulation (XGM) as well as cross phase modulation (XPM). The pump pulse stream consumes carriers and therefore modulates the carrier density. Carrier density modulation leads not only to a gain modulation but also to a refractive index modulation resulting in a phase modulation. Gain changes and phase changes induced by an optically excited SOA are coupled via the linewidth enhancement factor α [61]. If the factor α is not 0, a gain modulation is always accompanied by a phase modulation. At the SOA output, the probe signal is intensity-modulated as shown in Figure (2.2(a)). Besides this intensity modulation, a phase modulation appears also, resulting in a spectral broadening. The broadening induced by XPM is observed in Figure 2.25 (b) by comparing the probe spectra before filtering, with and without the pump signal turned on. The leading edge of the modulated probe is shifted towards lower frequencies (red-shift), whereas the trailing
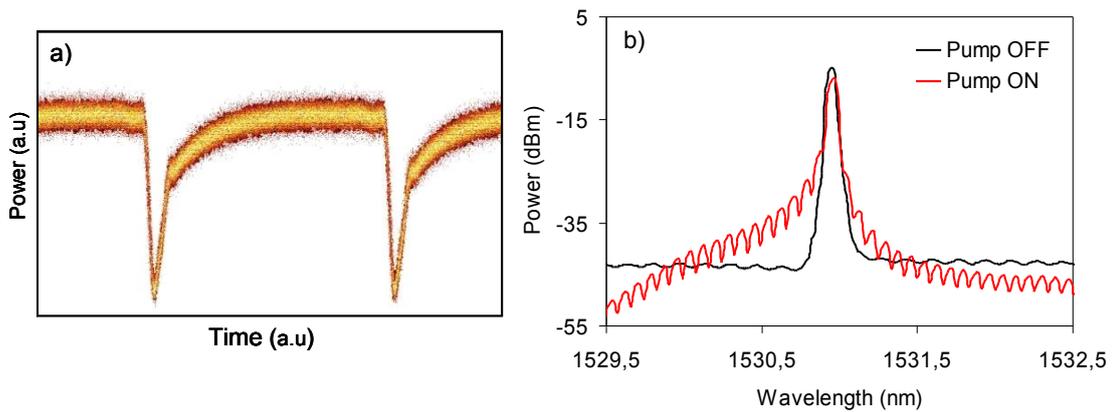
Figure 2.25: Intensity modulation induced by XGM (a) and spectral broadening induced by XPM (b) on the probe signal at the SOA output in pump-probe experiment
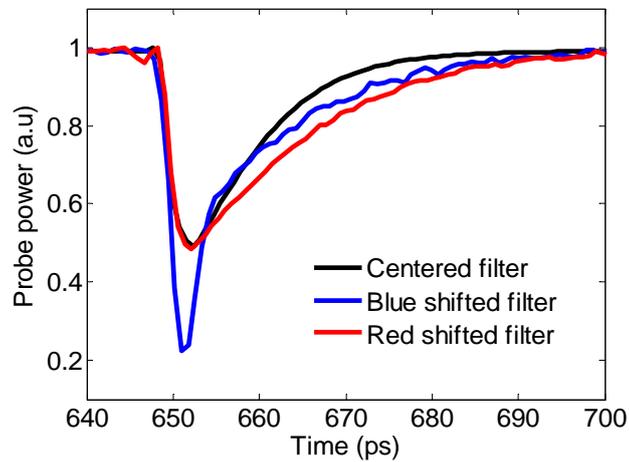
Figure 2.26: Simulated impact of filter position with respect to the initial probe signal wavelength on recovery profile

edge is shifted towards higher frequencies (blue-shift). The shifted filtering technique is based on this active chirp induced on the probe signal. By shifting the filter away from the probe wavelength, it is possible to transform the phase modulation into an intensity modulation. Probe modulation at the output of the system SOA+filter is then distributed by both XGM and XPM in the SOA. It is shown that by moving the central wavelength of the filter towards short wavelengths with respect to the initial probe wavelength, recovery of the SOA+filter system can be sped up [82], [83], [81], [84].

To illustrate the influence of filter position on device response, we use the well-known SOA model presented by [56] to simulate the experiment shown in Figure (2.24). The SOA model details are presented in Appendix 2. All operation parameters are fixed, only the filter central wavelength is adjusted and we observe the different system responses reflected on signal waveform at the output of the filter. Results are displayed in Figure (2.26).
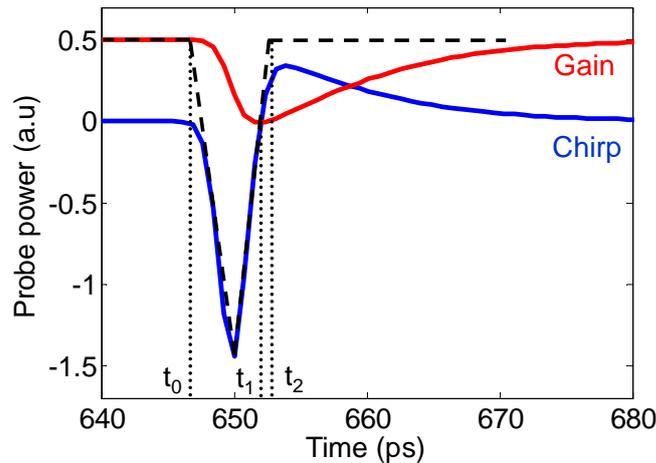
Figure 2.27: Probe transmittance (dashed line) at the blue-shifted filter output and evolutions of the SOA gain (red line) and of the induced chirp (blue line)

The blue curve exhibits a clear improvement of the gain compression-recovery time parameter, compared to the classical configuration in which the filter is centred on the initial probe wavelength (black curve). The gain compression is significantly increased while the recovery time remains unchanged. On the other side, when the filter is shifted towards long wavelength (red curve), no enhancement in gain compression is observed while the recovery becomes even slower. These observations could be slightly different depending on a lot of other parameters such the probe wavelength, the filter bandwidth, the filter slope, the shift magnitude, the SOA linewidth enhancement factor, etc... However, general conclusion is that using a blue-shifted could provide the best gain compression recovery time trate-off of the SOA+filter system and it is not the case if the filter is red-shifted. This is due to the fact that the chirp induced by gain modulation in an SOA is not symmetrical. The red-side chirp is much faster than the blue-side chirp [85]. Figure (2.27) depicts simultaneously the evolutions of the SOA gain and the induced chirp after a pump pulse having passed through the SOA. The curves are obtained in the same simulation.

The system recovery acceleration brought by a blue-shifted filtering can be explained as follows [81]. When the pump pulse appears at t_0, the SOA carrier population is depleted and the gain drops down rapidly, reaching its minimum at t_1. In the time slot $[t_0$-$t_1]$, the probe wavelength slides to longer wavelengths (red chirp) and therefore the probe light is less transmitted by the filter and this is added to the reduction of probe transmittance due to SOA gain saturation. As a result, the probe attenuation is increased. At t_1, the SOA gain reaches its minimum and starts recovery, the chirp is 0. From this time, the probe wavelength slides to shorter wavelengths (blue chirp) leading to an increase of the probe transmittance. If the filter slope is optimised in such a way that the transmittance enhancement due to blue chirp compensates for the gain saturation, the transmittance at t_2 can be equal to the one at t_0. After t_2, the blue chirp and the SOA gain recover slowly on the
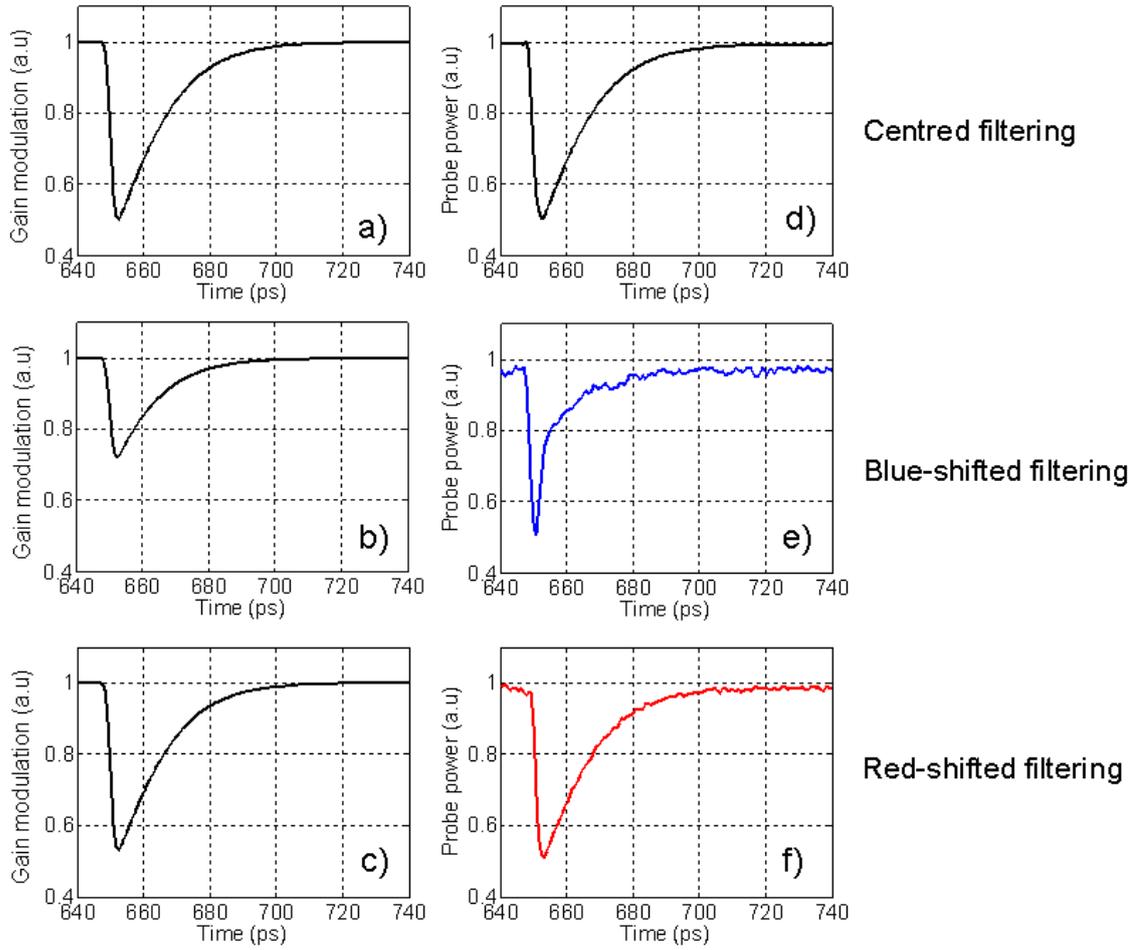
Figure 2.28: Numerical results of SOA+filter system dynamics for a fixed output modulation ratio of 3 dB for different position of filter. (a-c) SOA gain modulation in three cases and(d-f) corresponding output probe signal

same timescale and their effects on the probe transmittance cancel each other resulting in constant probe intensity at the filter output. The system composed by the SOA following by the blue-shifted band-pass filter effectively recovers much faster than the SOA gain.

In case of a wavelength converter or a regenerator, it is more practical to compare the device response in different configurations with the same modulation ratio of the output signal. To do this, input pump power is adjusted in order to obtain the same modulation ratio on the output probe signal for the three cases of centred filtering, blue-shifted filtering and red-shifted filtering. Numerical results are shown in Figure (2.28).

In this simulation, the output modulation ratio is fixed at a typical value of 3 dB, the SOA carrier lifetime parameter is 45 ps and the α factor is 5. Figures (2.28(a-c)) display the SOA gain modulation and Figures (2.28(d-f)) display the output probe signal, corresponding to the three filtering configurations. When the filter is blue-shifted the 10% 90% recovery

time is decreased from 30 ps (Figure (2.28(d))) down to 20 ps (Figure (2.28(e))). On the other side, when the filter is red-shifted (Figure (2.28(f))), the system recovery time is maintained very close to 30 ps. At last, it should be noted that the SOA gain compression needed to obtain 3 dB of modulation ratio at the system output is significantly smaller in the blue-shifted filtering configuration than the two others cases. That means also that the input pump power required at the SOA input is lower.

In summary, the theoretical study through simulations predicts that using blue-shifted filtering can enhance dynamics performance of non-linear optical gates constituted of an SOA followed by a band-pass filter. When the filter centre is moved towards shorter wavelengths with respect to the initial probe wavelength, the gate response is faster and the required power level of the input control signal (pump signal) can be reduced. Therefore, the blue-shifted filtering technique allows an SOA to be used as a non-linear optical gate for signal processing functions at ultrahigh bit rates beyond slow SOA carrier lifetime.

2.3.4.2   Experimental results

The impact of shifted filtering on recovery acceleration is also investigated experimentally for all SOA samples. The experimental scheme is always the same as shown in Figure (2.24). The shortest recovery time is obtained with the long QD SOA (SOA n°5). In the experiment, the output modulation ratio is fixed at a typical value of 3 dB and the SOA current is fixed at its maximum value of 800 mA. The filter following the QD SOA is a flat-top tunable filter with a bandwidth of 3.7 nm at half-maximum. In Figures (2.29(a)&(c)), the black curve is the probe spectrum at the SOA output and in front of the filter; the blue curve is the filter shape with a blue shift of 2.3 nm with respect to the probe wavelength and the red curve is the filter shape with a red-shift of 2.3 nm. Experimental probe spectra at the filter output in cases of blue-shifted filtering and red-shifted filtering are displayed in Figures (2.29(b)&(d)) respectively.

In our case, the filter is large enough not to induce any change in pulse shape when it is centered on the probe wavelength. The modulated probe spectrum at the output of the SOA (black curve) is not symmetrical indicating clearly that red chirp and blue chirp induced by SOA gain modulation are not equal. By comparing the probe spectra at the filter input (Figure (2.29(a))) and output (Figure (2.29(b))), it is shown that the blue-shifted filter plays the role of attenuating the red spectral components and inversely for the red-shifted filter.

Temporal waveforms of the probe signal at the filter output corresponding to the previous filter positions are displayed in Figure (2.30). The results demonstrate clearly the theoretical predictions of simulations. The SOA+filter system recovery is much faster when the filter is blue-shifted with respect to the initial probe central wavelength. Observations are coherent with those of Paragraph 2.3.3, at maximum of bias current, the SOA n°5
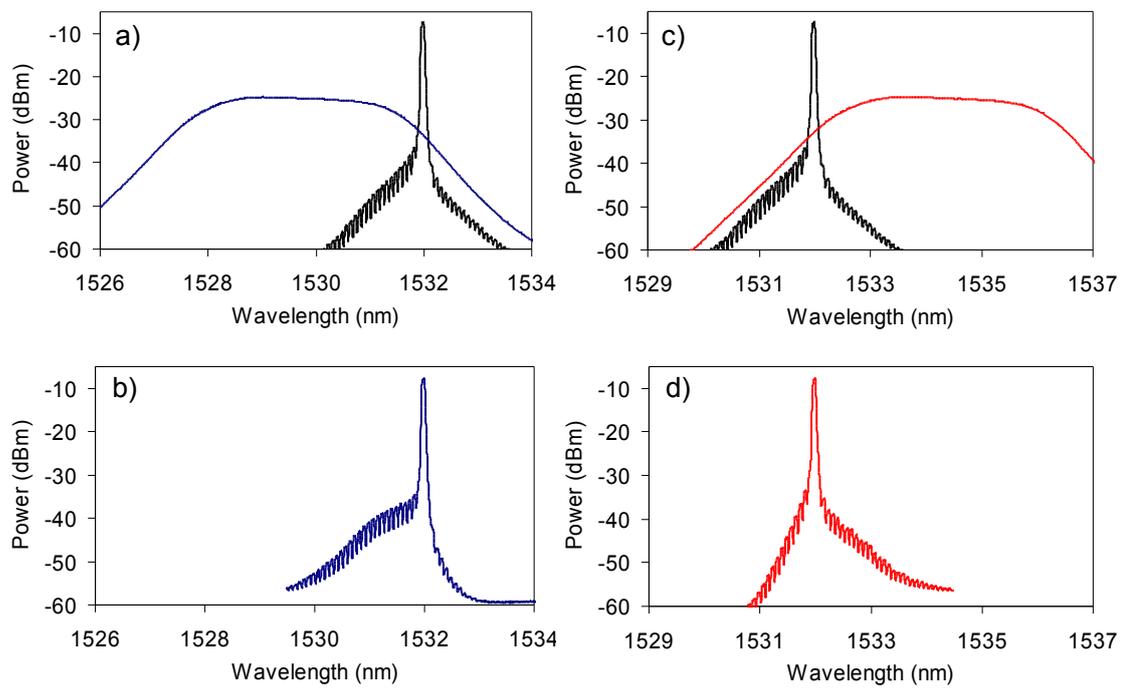
Figure 2.29: Experimental probe spectra at the SOA output and in front of the filter (black curves) and the filter shapes with a blue-shift (blue curve) in (a) and with a red-shift (red curve) in (c). Probe spectra at the filter output in case of blue-shifted filtering (b) and of red-shifted filtering (d)
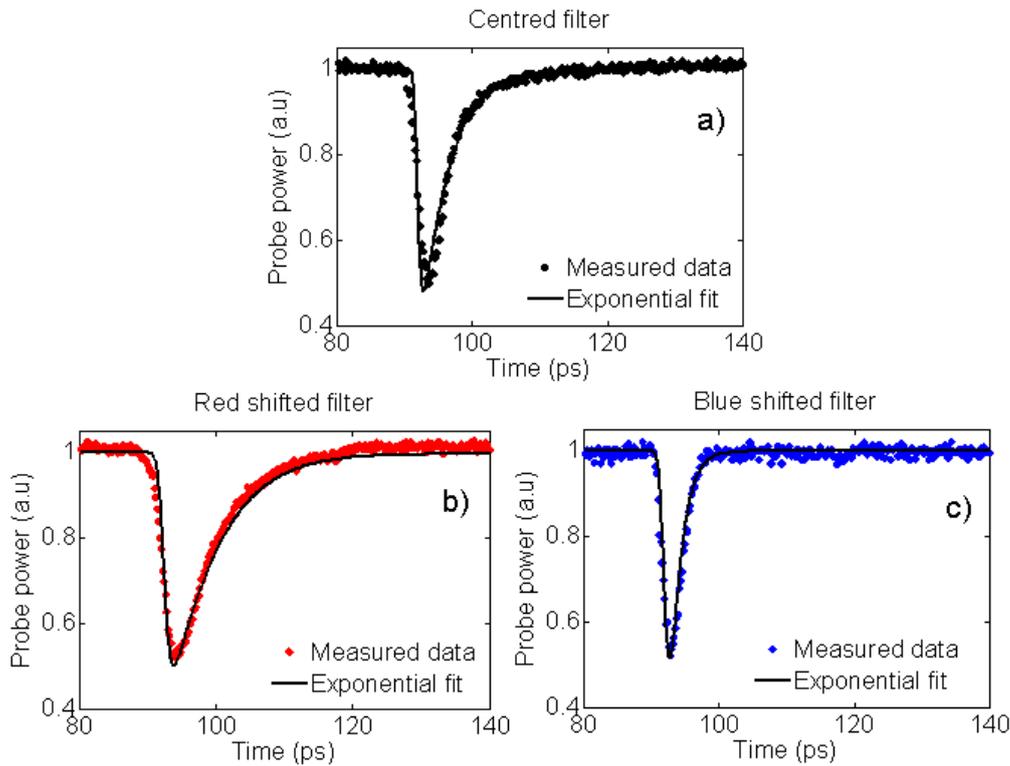
Figure 2.30: Experimental probe waveforms at the (QDot SOA + filter) output for different configurations: (a) centred filter, (b) red-shifted filter and (c) blue-shifted filter

exhibits an ultrafast recovery that could be characterised by one time constant while the other SOAs presents always two distinct time constants. The SOA+filter system response can therefore be represented by a simple exponential function. By fitting with measured data, the system lifetimes at $1/e$ corresponding to the cases of centered filter, red-shifted filter and blue-shifted filter are respectively 3.5 ps, 6 ps and 1.5 ps respectively. By moving the filter towards shorter wavelength, the system response is effectively faster. We can also compare the practical 10%-90% recovery times. It is about 9 ps when the filter is centered (Figure (2.30(a))) and is decreased down to 3 ps when the filter is blue-shifted (Figure (2.30(c))). On the other side, when the filter is red-shifted, the recovery time is about 15 ps (Figure (2.30(b))). For all the three filter positions, the non-linear optical gate constituted of SOA+filter is suitable for 40 Gbit/s applications. Especially, with a recovery time as short as 3 ps, the long QD SOA assisted by blue-shifted filtering promises pattern free operation at 160 Gbit/s where the bit slot is 6.25 ps.

In summary, it is demonstrated experimentally and theoretically by simulations that shifted filtering influences the dynamics performances of optical non-linear gate based on SOAs. The effective recovery time of an optical gate based on a QDot SOA followed by a band-pass filter is reduced drastically from 9 ps to 3 ps when the filter is moved 2.3 nm
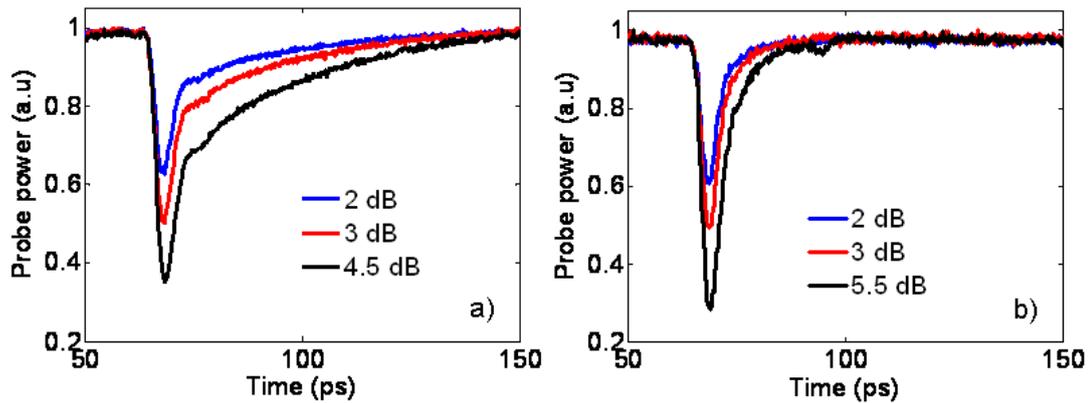
Figure 2.31: Measured gain recovery waveforms at maximum bias current of the 2-mm QDot SOA (a) and of the 5-mm QDot SOA (b) for various gain compressions

towards shorter wavelengths with respect to the input probe signal. This ultrafast recovery makes operation at 160 Gbit/s possible.

2.3.5   Impact of the SOA length

Following the experimental results presented in Paragraph 2.3.2, it is shown that the long QDot SOA (SOA n°5) exhibits a faster gain dynamics compared to the shorter QDot SOA (SOA n°3). Both SOAs are based on the same quantum-dot material, their carrier lifetimes intrinsic to material are identical. However, it is found that the active region dimensions also affect the effective recovery speed [76], [77], [79]. Hence, the SOA length difference is considered as the main factor that leads to the different recovery speeds of the two samples. Figure (2.31) displays typical gain recovery shapes for various gain compression of both QDot SOAs at their maximum bias currents (500 mA and 800 mA for short and long samples respectively). The corresponding current densities for the 2-mm QDot SOA and for the 5-mm QDot SOA are respectively 20 kA/cm^2 and 8 kA/cm^2.

We observe that despite the current density is three times greater in the short sample than in the long sample, the last one presents a much faster gain dynamics. At 3 dB gain compression, recovery time of the 5-mm SOA is 9 ps compared to 38.5 ps for the 2-mm SOA. Furthermore, output probe waveforms reflect distinct gain recovery shapes of the two SOAs. While the short SOA recovery exhibits clearly the presence of fast intraband processes followed by slow interband recombinations, the long SOA recovery displays a smooth recovery in order of a few picoseconds that could be modelled by a simple exponential function. The slow recovery due to interband relaxations nearly disappears.

These different behaviours can be explained by the ASE amount in the SOAs [76]. In short SOAs, ASE power is not high, especially compared to pump and probe signal powers, and can be neglected. In that case, SOA dynamics are dominated mainly by electrical pumping level, pump and probe power levels. In the other case, if the SOA is
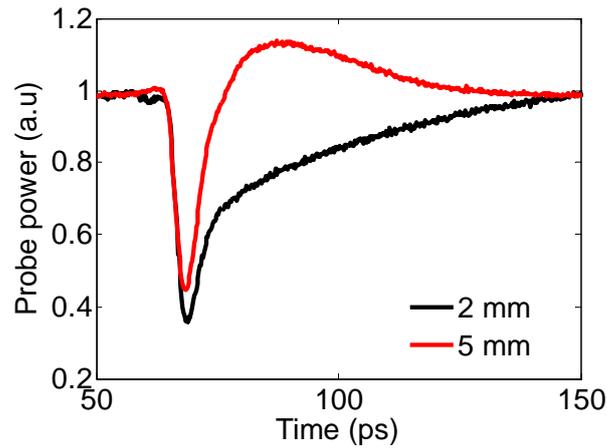
Figure 2.32: Measured gain recovery waveforms at low input probe power level for the 2-mm length QDot SOA and the 5-mm length QDot SOA

long enough, ASE power can be important enough to contribute to SOA gain saturation and gain recovery. In this case, ASE must be taken into account when gain recovery is studied, even with a strong probe. In long SOAs, theoretical calculations, which take into account the propagations of the pump signal, probe signal and ASE in both forward and backward directions [76], show that the carrier density and the ASE power are strongly inhomogeneous along the SOA waveguide. Combination of these facts leads to a speeding up of gain recovery dynamics. The presence of strong and non uniform ASE in long SOAs is represented by an overshoot appearing on recovery trace in some configurations [76]. In the experiment giving results depicted in Figure (2.31), no overshoot is observed even for the 5-mm QDot SOA because it is significantly reduced by the strong probe power of 0 dBm at the SOA input. By decreasing the probe power level, overshoot on gain recovery trace can be observed. Figure (2.32) describes the gain recoveries obtained for the two QDot SOAs with an input probe power of -10 dBm.

A large overshoot is observed on the gain recovery of the 5-mm QDot SOA and not on the gain recovery of the 2-mm QDot SOA. This fact confirms that ASE power in the long sample is much higher than in the other sample and implies also that the carrier density and the ASE power are not uniform along the SOA waveguide. Finally, thanks to effects of the strongly saturating ASE, the gain recovery dynamics can be enhanced by increasing the SOA length. Long SOAs appear therefore preferable for signal processing functions at ultrahigh data rates. On the other side, the ASE contributes also strongly to the noise added by the device. Hence, when a long SOA is used, a strong probe power should be also used to limit the overshoot and the ASE contribution to device noise.

2.3.6   Impact of probe wavelength

The influence of probe wavelength on XGM efficiency in SOA based signal processing functions such as wavelength converters has been largely studied [86], [87]. It is found that XGM efficiency, in terms of extinction ratio, is higher for shorter probe wavelengths. In presence of a pump signal, the SOA gain has a sharper drop at shorter wavelengths and the gain peak shifts to longer wavelengths [88], [86]. Combination of both mechanisms leads to a smaller extinction ratio at longer wavelengths and a higher extinction ratio at shorter wavelengths. From this point of view, shorter wavelengths appear preferable for the probe signal in wavelength converters exploiting XGM. This is completely true if the SOA dynamics is fast enough at the operating bit rate. Otherwise, at ultrahigh bit rates, when the SOA recovery is slow compared to the bit duration and patterning effects begin to degrade the converted signal quality, the wavelength dependence of the SOA recovery time should be considered because different probe wavelengths can also lead to different dynamics.

In literature, studies on SOA gain recovery wavelength dependence are investigated [89], [58], [90], [91], [92], [93] but conclusions seem still very divergent. In [79], it is reported that no wavelength dependence of the recovery rate on the probe wavelength is observed. In [91], experimental results show that the fast recovery time is almost the same for all probe wavelengths while the recovery time of the slow relaxation becomes longer at shorter wavelength. At last, in [93], it is demonstrated by experiments and simulations that the slow component of SOA gain recovery is faster at shorter wavelengths.

In our experiment, to assess the wavelength dependence of the gain recovery reflected on the XGM probe signal, we fixed the pump wavelength at 1536 nm. The gain dynamics behaviour of the SOA is probed with two different wavelengths of 1530 nm and 1544 nm. Figure (2.33) depicts the ASE spectrum of the short QDot SOA (SOA n°3) at 200 mA of bias current and respective spectral positions of pump and of probe signals in both cases.

Figure (2.34) displays the output probe waveforms for the two probe wavelengths at 3 dB of gain compression. Both curves reflect the typical time evolution of SOA gain: fast depletion, followed by fast and slower recoveries. On the other sides, temporal characteristics of the two fast and slow recoveries are clearly different. Wavelength dependence of the SOA gain recovery is observed. The gain recovers faster for a probe wavelength equal to 1530 nm compared to 1544 nm. Both recovery curves can be fitted well with simple bi-exponential functions. Extrapolated 1/e lifetimes corresponding to fast and slow processes are 2 ps and 28 ps (resp. 4.5 ps and 40 ps) at 1530 nm (resp. 1544 nm). As a consequence, 10%-90% recovery time of the SOA gain is reduced significantly from 50 ps to 39 ps when the probe is shifted to the shorter wavelength.

In our knowledge, similar results have never been reported yet. Both characteristic
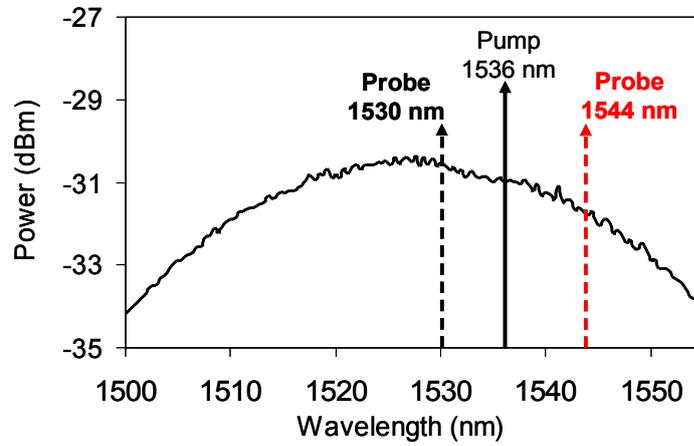
Figure 2.33: ASE spectrum of the 2-mm QDot SOA at 200 mA of bias current and respective positions of pump and probe signals in both experiments
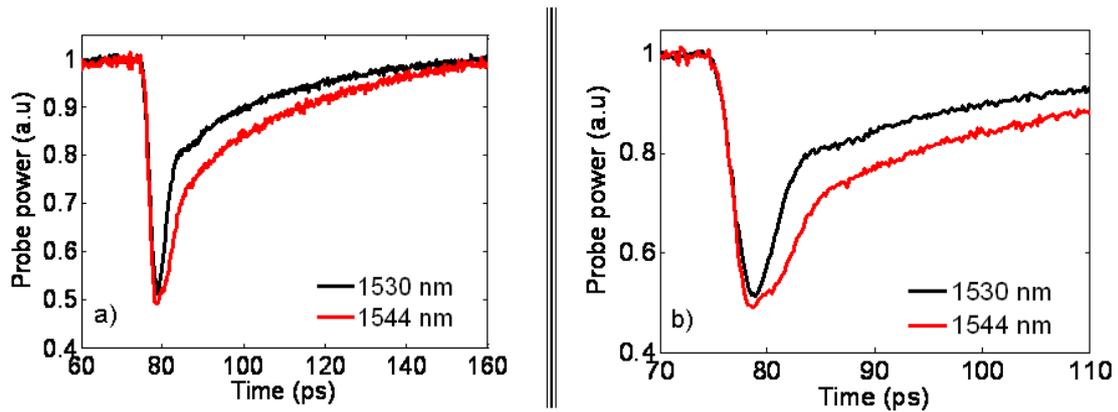
Figure 2.34: Gain recovery forms of the 2-mm QDot SOA(SOA n°3) for two different probe wavelengths (a) and time axis is expanded in (b)

times of the fast and slow recoveries are affected by the probe wavelength shift. Variations of the fast and the slow recovery versus wavelength have never been observed simultaneously [89], [91], [93]. In [89], experimental results of a bulk InGaAsP based SOA showed a greater recovery rate is obtained when the wavelength is moved from 1543 nm to 1533 nm. Despite different time scales, we observe also a sharper fast recovery at 1530 nm compared to 1544 nm. This wavelength dependence of the fast process can be explained as follows. Contributions of different processes which are characterised by different time constants such as SHB (hundreds of femtoseconds), CH (1 picosecond) and carrier density relaxation (hundreds of picoseconds) to the global SOA gain dynamics vary also with the wavelength [58]. Theoretical predictions given by numerical simulations based on simplified density matrix equations show good agreement between theory and experiment [89]. The measurements were performed by using a degenerated pump-probe set-up with typical pulsewidth of 150 fs. In another experiment [91] with similar pulse duration in order of 100 fs, but with a two colour pump-probe technique (i.e pump and probe signals are at different wavelengths) experimental results disagree with the previous results. The authors observe no change in fast recovery time for all probe wavelengths and the recovery time of the slower relaxation becomes longer for shorter wavelengths. This last observation is opposite to our results. The authors explain longer recovery time by smaller saturation powers for shorter wavelengths as shown in [88].

However, in the last experiments, the observation time is limited to only a few picoseconds and therefore does not allow the complete gain recovery dynamics to be observed. Otherwise, in our experiment as well as in [93], the observation time scale is enlarged to hundreds of picoseconds that allow the complete gain recovery to be assessed. In both experiments, wavelength dependence tendencies of the slow recovery rate are consistent. Recovery times of the slow recovery due to the interband relaxations appear shorter for shorter wavelengths. This behaviour is indeed resulted from the fact that the SOA gain spectrum is not symmetric with respect to the wavelength. During the band-to-band relaxation processes, the gain change at shorter wavelengths is larger than at longer wavelengths. Consequently, the recovery speed is greater at shorter wavelengths.

At last, a relation between the gain recovery rate dependence on wavelength and the wavelength dependence of the assessed SOA saturation power and of small-signal gain is not evident. Static gain measurements of the SOA for signals at different wavelengths are shown in Figure (2.35(a)). The small-signal gain changes are smaller than 1 dB and the saturation powers are nearly the same for all signal wavelengths in the range from 1528 nm to 1545 nm.

Gain recovery time is assessed via pump-probe measurements in XGM configuration for two different wavelengths. The dynamic gain measurement was not performed exactly at the probe wavelengths of 1528 nm and 1545 nm but it was performed at the very close wavelengths of 1530 nm and 1544 nm respectively. Therefore, the static gain curves at
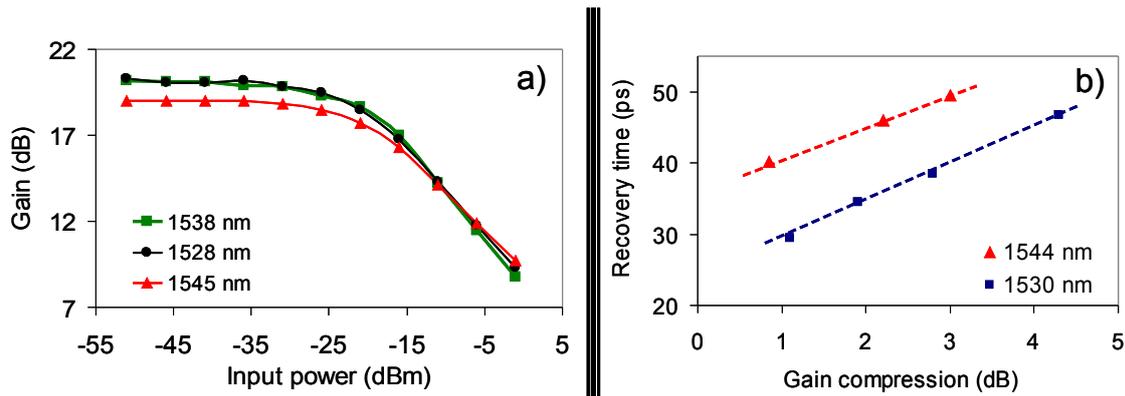
Figure 2.35: Static gain measurements (a) and recovery time evolutions as functions of gain compression (b) at different wavelengths

1528 nm (and 1545 nm) could be representative for 1530 nm (and 1544 nm). The gain dynamics results show greater recovery rates for shorter wavelengths for both fast and slow gain recoveries. The 10%-90% recovery time exhibits an average reduction of 10 ps when the probe wavelength is moved from 1544 nm to 1530 nm (Figure (2.35(b))).

The observations differ in the literature [91], [79], [93], which remain divergent and explanations are not evident yet. However, the divergences could result from the fact that recovery time is not a monotonous function of probe wavelength and change from an SOA to another. A numerical study taking into account ASE propagation and including the length dependence of the carrier density shows that recovery time dependences on probe wavelength are totally different for two SOA of different lengths [92]. Anyway, it is clearly demonstrated that SOA dynamics is wavelength dependent. Therefore, in signal processing functions exploiting XGM, the probe wavelength should be considered as a key parameter as it influences not only the XGM efficiency but also the device dynamics significantly.

2.3.7   Impact of pulse duration

In all previous SOA dynamics characterisations, pump pulses of 2.5 ps are always used in order to assess potential of various SOA for applications at 160 Gbit/s as they correspond to typical pulses in digital communications at 160 Gbit/s. To evaluate the potential of a SOA for other data rates properly and precisely, appropriate pump pulses should be considered. As mentioned in the first chapter, at 40 Gbit/s, a signal RZ 33% is largely used, in which the pulse duration is in order of 8 ps. In this section, we investigate SOA dynamics in response to exciting pulses of about 8 ps duration to evaluate the SOA performances for 40 Gbit/s applications. We compare also with the SOA dynamics when it is excited by 2.5 ps pulses.

The experimental set-up is always based on our classical pump-probe experiment described in Paragraph 2.3.1. The assessed SOA is a bulk based sample which exhibits the
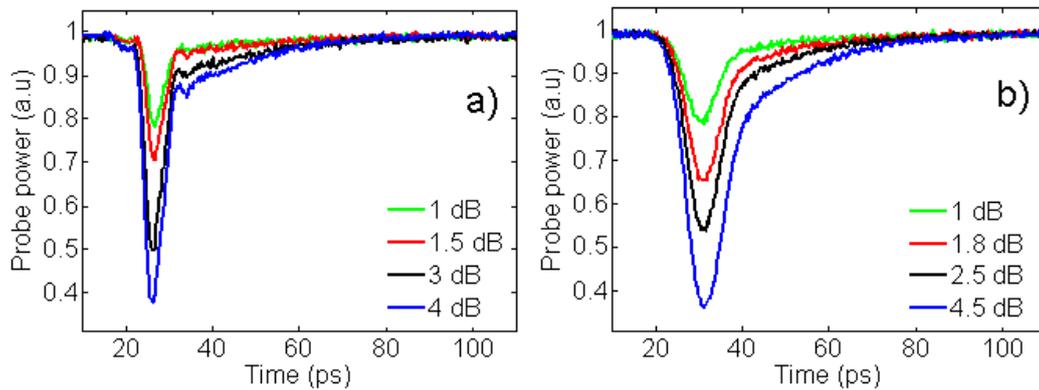
Figure 2.36: Gain recovery waveforms for various gain compressions and for pump pulse durations of 2.5 ps (a) and of 7.5 ps (b) (SOA n°6)

same length and the same optical confinement as the highly confined bulk SOA (SOA n°2) presented in Table 2.1, hereafter the investigated SOA is called SOA n°6. In this experiment, the SOA is controlled at 25°C and biased at 300 mA. Pump and probe wavelengths are 1552 nm (close to gain peak at this bias current) and 1546 nm respectively. Pump signal is a pulse stream with a pulse duration of 7.5 ps and the repetition rate is fixed at 10 GHz in order to be able to observe complete SOA gain recovery between two consecutive pulses. Gain recovery forms of the SOA n°6 for various gain compressions and for different pump pulse durations are shown in Figure (2.36).

It is shown that the general gain recovery shapes in the two cases are similar with a fast recovery due to intraband effects followed by a slower recovery due to interband relaxations. Besides, durations of the fast recovery component are clearly longer when the pump pulses of 7.5 ps are used (Figure (2.36(b))) than when the pump pulses of 2.5 ps are used. This evolution results from the fact that the fast recovery forms are determined mainly by the pump pulse shape because in the two cases, the pulse durations are longer than time constants of intraband effects, 100 fs for SHB and 1.5 ps for CH [63]. It is observed also in both cases that the proportion of the fast recovery is significantly greater compared to the slow recovery. Differences of slow recovery rates are difficult to observe. However, significant changes in fast recovery lead to clearly different 10%-90% recovery times. Gain recovery times are longer for pump pulses of 7.5 ps than for pump pulses of 2.5 ps. Recovery times as a function of gain compression for different pump pulse durations are depicted in Figure (2.37).

Under shorter pump pulse excitation, the SOA gain recovers within 20 ps for all measured gain compressions. The recovery times increase an average of 6 ps when the pump pulsewidth increase from 2.5 ps to 7.5 ps. However, for gain compression up to 4 dB, the SOA recovery time remains close to 25 ps. Therefore, with gain compressions smaller than 4 dB, this SOA can be used for signal processing applications at 40 Gbit/s for a standard RZ 33% signal RZ without impairments induced by patterning effects. This pulsewidth depen-
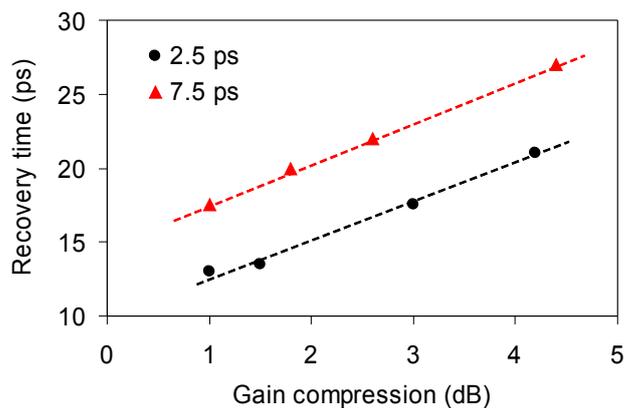
Figure 2.37: Recovery time as functions of gain compression for different pump pulse durations

dence of recovery time is one consequence of the pulsewidth dependence of gain saturation mechanisms in picosecond pulse regime. Gain saturation characteristics dependence on the pulsewidth is demonstrated experimentally and investigated theoretically in [94], [95], [96]. SOA gain compression is contributed by a suppression due to carrier density deviation and another suppression due to CH and SHB. It is found that under excitation by short pulses in order of few picoseconds and below, gain compression is dominated by intraband processes. Measurements [94], [95], [96] and calculations [94] show that 3-dB saturation energy is smaller for smaller pulsewidth. This implies also that the contribution of gain suppression due to CH and SHB to the overall gain compression is greater for shorter pulse.

In summary, gain recovery characteristics have been demonstrated experimentally dependent on pulsewidth of pump signal in order of few picoseconds. The gain recovery time is longer for longer pump pulse duration because contribution of ultrafast phenomena to overall gain compression is smaller. This result suggests that to evaluate properly an SOA based optical gate dynamic performance at a given data rate, dynamics characterisation should be investigated with adequate pulse duration. In our case, the SOA recovery time increases with an average of 6 ps when the pump pulse durations increases from 2.5 ps to 7.5 ps. For gain compressions lower than 4 dB, the recovery time is still smaller than the bit slot at 40 Gbit/s. The SOA is then adequate to be used for standard RZ 33% signal processing at 40 Gbit/s.

2.3.8   Limit of gain recovery acceleration by assist light

It is well known in the literature that by using an assist light, the recovery rates of a saturated SOA could be enhanced significantly [97], [98], [99], [100]. The recovery acceleration efficiency varies from one configuration to the other. In [99], the 10%-90% recovery time could be reduced from 140 ps to 40 ps by employing a 100 mW assist light at gain transparency wavelength. The operating principle in that case can be described as follows. When
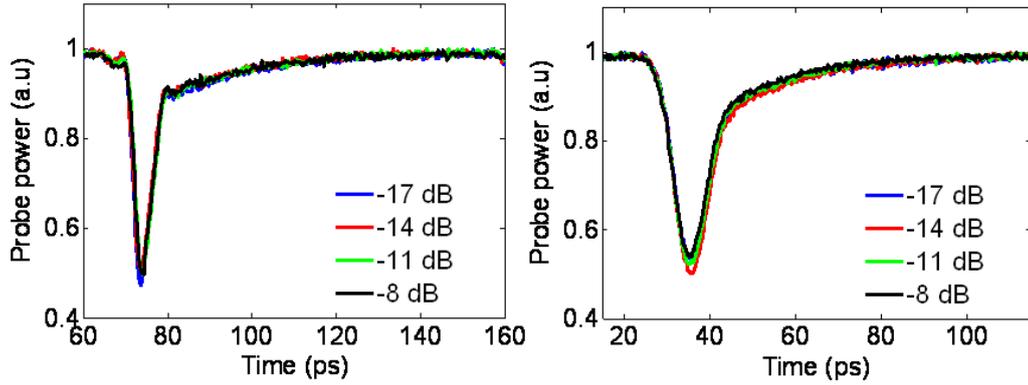
Figure 2.38: Gain recovery waveforms for various ratios P_{probe}/P_{sat} and for pump pulse durations of 2.5 ps (a) and of 7.5 ps (b) (SOA n°6). Gain compression was fixed at 3 dB.

no signal is amplified, the gain transparency occurs at the assist light wavelength. When a signal is amplified and saturates the SOA gain, the gain spectrum drops and shifts towards longer wavelengths. Consequently, the assist light is now in the absorption region. The assist light absorption creates new carriers and hence enhances rapidly the gain recovery. In [97], [100], a three-wavelength scheme is employed and the assist light (holding beam) is in the gain region. In that case, the assist light also saturates the carrier concentration. In other words, because of large assist light power, the equilibrium carrier concentration is modified which results in reduction of recovery time. The recovery time was reduced from 95 ps to about 70 ps when the assist light power increased from 10 dBm to 0 dBm. However, in these experiments, the pump signal power was fixed when the assist light power was adjusted. This indicates that the gain compression changed with the assist light power changes.

In our experiment, the influence of assist light power on gain recovery is assessed for a fixed gain compression. To do this, the pump and probe powers are adjusted simultaneously. The probe signal is adjusted to be strong enough (the average power of the probe signal is always larger than the pump average power). The results measured on the SOA n°6 for two different pulse durations are shown in Figure (2.38).

In each case, no change is observed on the gain recovery shapes when the probe power increases. The gain recovery times corresponding to the pulse duration of 2.5 ps and 7.5 ps are maintained respectively at about 17.5 ps and 22 ps over the probe power range. The conclusion could be: for probe power exceeding a certain threshold, the recovery acceleration effect provided by large probe power is saturated. In our experiment, it seems that the probe power have exceeded already this threshold. An explicit explanation is not evident. A numerical investigation will be presented later in Paragraph 3.2.2.

2.3.9   SOA dynamics assessment by degenerate pump-probe experiment

In the frame work of the European FP6 research project ePIXnet, i have spent three weeks at DTU Fotonik and could study gain dynamics of the SOA n°3 (QDot SOA 2-mm of length) in two pump-probe experiments. A degenerate pump-probe set-up with femtosecond pulses [60] is available at DTU Fotonik. Gain dynamics measurements are performed under closely similar conditions (SOA bias current and pump wavelength). Slow and fast processes are observed in both cases. However, it is also shown that gain recovery exhibits different time constants in the two experiments. Despite the last observation, the extrapolated 10%-90% gain recovery times are similar.

The first difference between the pump-probe experiment in wavelength conversion scheme (that will be called henceforth picosecond experiment) and the degenerate pump-probe experiment with heterodyne detection (that will be called hereafter femtosecond experiment) is the time resolution limited in each case by the pump pulsewidths. In the picosecond experiment, pump pulses are of 2 ps at minimum that means all gain recovery components which recover with a characteristic time smaller than 2 ps is masked by the pulse. In the femtosecond experiment, pump pulses are of 150 fs of duration, gain recovery processes that are slower than 1 ps can be observed. The second difference is the SOA gain is probed at the same wavelength as pump signal in the femtosecond experiment and in the picosecond experiment the probe signal is at another wavelength. The last principal difference between the two experiments is the probe power level. In the fs experiment, the probe signal is degenerated from the same laser as the pump signal which means that there is no 'assist' light between pulses. Probe signal power is set at very small value such that probe pulses are linearly amplified and therefore SOA can be considered as saturated by only the pump signal. Probe transmission is measured for each time delay between pump and probe pulses. Gain dynamics are then deduced from probe transmission curve. Scenario in the ps experiment is not the same. The CW probe power is comparable to the pump average power. Following the pump pulse passage, SOA gain recovery can be influenced by the presence of intense CW probe light (The experimental set-up has been shown in Figure (2.24). The different characteristics of the two experiments are summarised in Table (2.5).

	Wavelength	Probe signal	Pump pulsewidth	Probe power/pump power
ps experiment	$\lambda_{probe} \neq \lambda_{pump}$	continuous	2 ps	comparable
fs experiment	$\lambda_{probe} = \lambda_{pump}$	pulsed	150 fs	negligible

Table 2.5: Characteristics of the ps and fs experiments

Figure (2.39) displays the gain recovery trace obtained with femtosecond experiment (black) and a triple-exponential fit (red). Fast and slow processes are clearly observed. From the triple exponential fit, we deduced 3 time constants of 300 fs, 1.5 ps and 80 ps. The ultrafast recovery component associated to 300 fs time constant is attributed to phonon-
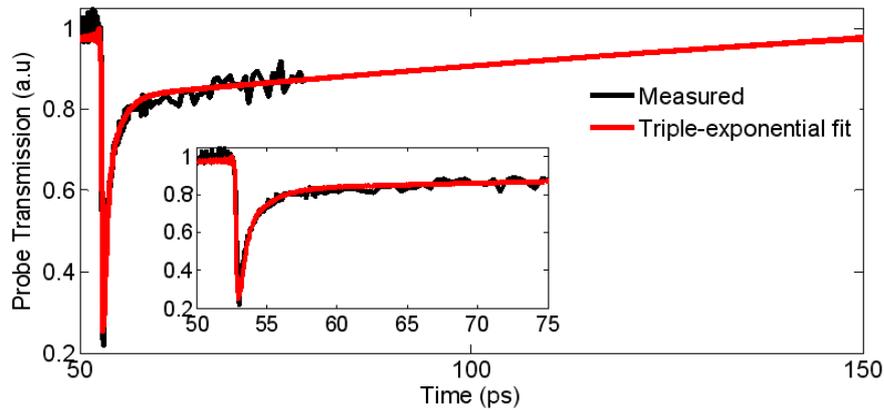
Figure 2.39: Experimental and triple-exponential fit of gain recovery trace of the SOA n°3. In inset, the curve is expanded.

mediated carrier relaxation into the dot ground state [101]. A mixture of intradot relaxation and capture processes (refilling the dot by capture from the wetting layer) is considered to be responsible for the intermediate component characterised by 1.5 ps time constant. At last, slow carrier relaxation decays with a long-lived 1/e lifetime of 80 ps. 10%-90% gain recovery time extrapolated from the fit function equal to 60 ps.

Result of gain dynamics measurement of the same SOA in picosecond experiment is presented in Figure (2.40(a)). The curve exhibits always separate fast and slow components. However, in this case the experimental curve (black) fits better with a bi-exponential response function rather than with a triple-exponential function. The 1/e time constants achieved by fit procedure are 2.5 ps and 40 ps. The first time constant is not intrinsic to the SOA, it is due directly to the pump pulse duration. Intraband effects including level-hole burning and capture processes decay with time constants smaller than 2.5 ps, they are therefore masked. Slow component characterised by the time constant 40 ps is related to interband carrier recombinations. Nevertheless, this time constant is significantly shorter than ones raised from the previous experiment (80 ps). As the probe power level is high, the probe signal plays also the role of a holding beam and leads to a significant reduction of effective carrier lifetime [97]. The measured 10%-90% gain recovery time is 65 ps that is very close to 60 ps extrapolated from femtosecond experiment. The gain recovery in femtosecond experiment benefits much more from ultrafast processes compared to the ones obtained in picosecond experiment. The last phenomenon results in similar effective gain recovery times despite the large difference between the two long time constants.

In theory, the results of the picosecond experiment can be predicted from the femtosecond experiment results. Figure (2.40(b)) shows a comparison between the experimental trace obtained from 2.5 ps experiment (black) and the theoretical trace predicted for pump pulse duration of 2.5 ps by using the triple exponential function (with the three characteris-
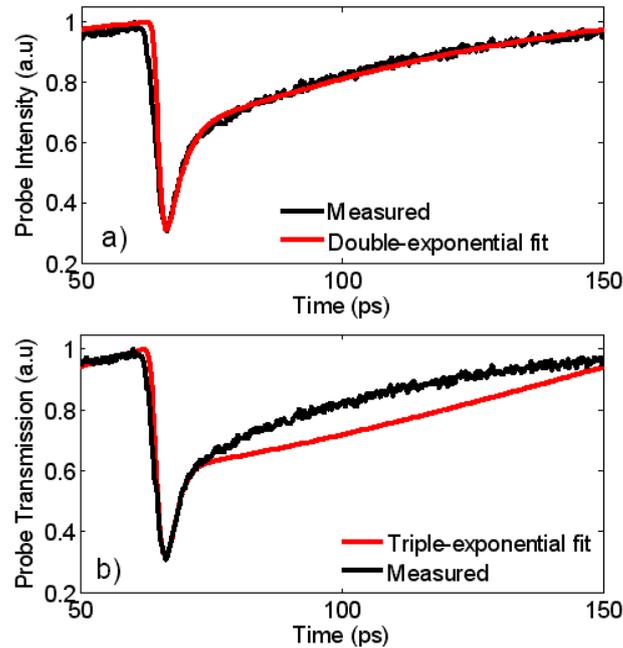
Figure 2.40: Experimental gain recovery trace of the SOA n°3 from the picosecond experiment and a bi-exponential fit (a), or a triple-exponential fit (b)

tic time constants 300 fs, 1.5 ps and 80 ps) obtained from the femtosecond experiment. The two curves are in good agreement only for the fast recovery component which is masked by the long pulse duration. The shift of the slow component between the two curves can be explained by carrier recombination acceleration resulted from the strong probe power in the picosecond experiment.

Gain dynamics measurement based on degenerate pump-probe experiment with femtosecond pulses allows characteristic time constants associated to different physical processes to be identified with high time resolution. Thanks to parameters extrapolated from this measurement, the gain behaviour of an SOA can be generally modelled and predicted for various operating conditions. On the other hand, pump-probe experiment with picosecond pulses gives a direct image of gain dynamics under operating conditions that are very close to those of an SOA-based wavelength converter or regenerator in such picosecond pulse regime, and different pump and probe wavelengths. In this circumstance, it is possible to know if the SOA gain dynamics is fast enough for a given bit rate, without any sophisticated additional calculations. On the practical side, femtosecond experiment, which requires usually complex and sensitive lenses alignment, is much more difficult to be performed than picosecond experiment, which is an all-fibre set-up. Somehow the two experiments reveal coherent facts about SOA gain dynamics.
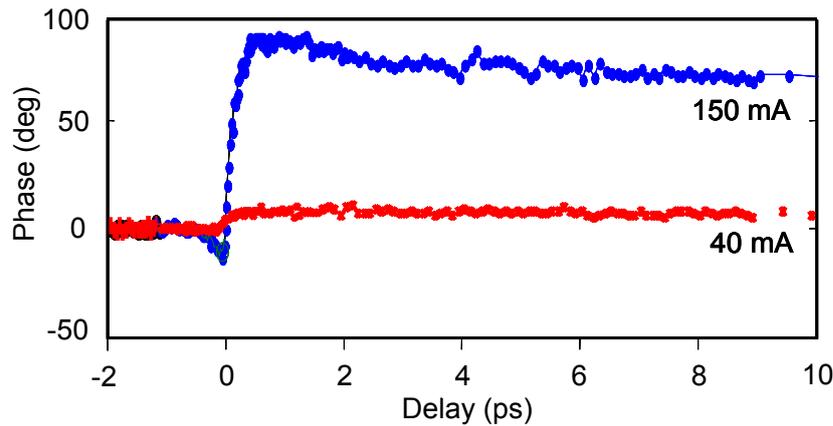
Figure 2.41: Experimental phase recovery of the 2-mm length QDot SOA for different bias currents (measurements of Per Lunnemann and Sara Ek of DTU Fotonik)

2.3.10 Phase dynamics

All-optical signal processing devices based on interferometer configurations rely not only on XGM but also on XPM in SOAs. Using such a device requires therefore information about both SOA gain and phase dynamics. A gain modulation is always accompanied by a refractive index modulation because both depend on the carrier density. And the refractive index modulation results in time dependent phase shift on the signals travelling through the SOA. Phase dynamics measurements were also performed in the same frame work of cooperation with DTU Fotonik. Thanks to degenerate pump-probe set-up with heterodyne detection, phase changes due to refractive index modulation in the SOA could be measured. The SOA under investigation is always the 2-mm length QDot SOA (SOA n°3). Experimental results are presented in Figure (2.41). Measurements are performed by Per Lunnemann and Sara Ek, PhD students at DTU Fotonik.

The optical signal wavelength is 1550 nm, pump pulse energy is estimated about 1 pJ at the SOA input. Phase dynamics is measured at two bias currents of 40 mA and of 150 mA. At 40 mA, close to the transparency current for 1550 nm, no significant phase change is observed because the pump pulse is simply transmitted and there is nearly no carrier density modulation due to optical pulse presence. At 150 mA, well above the SOA threshold current, phase shifts induced by optical pulse presence are observed. The phase recovery curve is consistent with other experimental results reported in the literature [102], [103], [72]. An instantaneous negative phase shift is observed first which is assigned to the instantaneous Two Photon Absorption (TPA) effect and the Level Hole Burning in the dots. This is followed by a large positive phase shift distributed by both CH and carrier depletion. At last, the phase shift recovers slowly. The gain, as presented previously in Paragraph 2.3.9, recovers by two distinguished steps characterised by two different time constants. On the contrary, the phase dynamics exhibits a monotonous recovery which can be characterised by

only one time constant. The phase recovery trace is measured within only few picoseconds, it is difficult to extrapolate precisely this decade time constant. However, a time constant in order of 40-100 ps seems reasonable. This long lifetime suggests that phase change is dominated by the slow processes of long lived carrier relaxations in opposition to the gain compression which is dominated rather by fast intradot processes.

These distinguished behaviours of gain and phase dynamics induced by carrier modulation originate from different linewidth enhancement factors (Henry factor) associated to slow and fast processes. Phase changes could be deduced from gain compression via the proportional factors alpha [61]. Despite the large distribution of gain suppression due to fast processes to the over all gain compression, the alpha factor associated to these fast processes CH and SHB is much smaller than the one associated to the carrier depletion and consequently the total phase shift is attributed mostly to the last one. Hence, phase changes recover with the slow carrier relaxations and is characterised by the corresponding long lived time constant.

In summary, it is experimentally demonstrated that SOA gain and phase dynamics exhibit dissimilar behaviours. Gain dynamics is dominated by intraband processes and recovers with the corresponding short time constant. On the contrary, phase dynamics is distributed mostly by the carrier depletion and hence recovers with the corresponding long time constant. Signal processing schemes exploiting XGM could take profits from this fast gain dynamics. Design of signal processing devices exploiting XPM has to take into account carefully the slow recovery of phase. And finally, devices based on differential interferometer configurations have to consider simultaneously the SOA gain and phase dynamics as in such schemes both XGM and XPM are involved in the signal processing.

2.4   Chapter summary

In this chapter, experimental characterisations of all investigated SOAs were presented. These SOAs are designed for applications in all-optical signal processing functions such as regeneration and wavelength conversion, at 40 Gbit/s and up to 160 Gbit/s. Some basic descriptions of SOA were reminded first. Qualitative description of the two main features: gain saturation and SOA dynamics was also discussed.

The second section was dedicated to present results of static characterisations. First of all, two coupling beds were presented. Using of micro-lensed fibres allows a flexible and all-fibred characterisation bed adapted for any SOA chip. With a wide range of optical mode diameter offered by micro-lensed fibres, one-side loss of fibre-chip coupling is typically only 2 dB. SOA module using lenses offers also a low-loss fibre-chip coupling could be as small as 1.5 dB with high stability and robustness. This module coupling efficiency is much greater than the commercially available butterfly package. Signal processing applications require firstly high small-signal gain, small saturation power and no ripple. Static characterisations provide this primary and fundamental information. Among the investigated SOAs, the bulk based ones exhibit small-signal chip gains as high as 30 dB with 3-dB saturation powers as low as 27 dBm, the quantum material based SOAs exhibit small-signal chip gains of at least 20 dB and 3-dB saturation powers smaller than 16 dBm. Except the ultralong QDot SOA (5-mm length QDot SOA), others SOAs expose small ripple down to 0.5 dB (technology limitation). These SOAs fulfil primary conditions for all-optical signal processing applications.

The third section is devoted entirely to experimental characterisations of SOA dynamics. Fast response is the key feature of SOA based signal processing functions for operating at ultrahigh bit rates of 40 Gbit/s and up to 160 Gbit/s. Pump-probe experiment based on XGM in SOA is elaborated. With pump pulse durations variable and in order of few picoseconds, this pump-probe set-up allows to assess SOA gain dynamics behaviour under conditions which is closed to real operating conditions in a regenerator or a wavelength converter at these data rates. Moreover, the tunability of pump and probe wavelengths on the whole C-band is also an advantage of the set-up. The first question when the bit rate increase is the device response speed. It is shown that the effective SOA gain recovery time depend on gain compression. Despite the presence of the long carrier relaxations in order of 100 ps, SOA can operate at 40 Gbit/s without significant patterning effects if the gain compression is small enough. This could be possible thanks to the fact that under saturation induced by picosecond pulses, the gain compression takes advantages from ultrafast intraband effects such as CH and SHB and hence recovers a great part with short characteristic time associated to these effects. It is also demonstrated that by increasing the bias current, SOA response time could be shortened significantly. The gain recovery time of

the long QDot SOA is decreased drastically from an average of 30 ps to 10 ps when its bias current is raised from 300 mA to its maximal value of 800 mA. Although, a gain recovery time of 10 ps is not small enough for an operation at 160 Gbit/s at which the bit slot is only about 6 ps. To attain the bit rate of 160 Gbit/s and beyond, shifted filtering appears as the simplest solution to enhance the dynamics of SOA based non-linear optical gate. Impact of position of the filter following the SOA was assessed. Results show that a red-shifted filtering does not allow to enhance the dynamics of the SOA based non-linear optical gate. On the other side, it is clearly demonstrated that a blue-shifted filtering improves efficiently the gain compression time response compromise of the gate. By placing a blue-shifted filter followed the long QDot SOA, a recovery time of 3 ps was obtained for a gain compression of 3 dB. This ultrafast response of the optical gate promises an operation at 160 Gbit/s without any patterning effects. Impact of probe wavelength on SOA based optical gate was also studied. Results show that recovery time could be smaller for shorter probe wavelength. However, the conclusion about probe wavelength influence is still divergent. This last can originate from gain spectra that could be very different from one to other SOA. It is shown also that SOA recovery time is longer for longer pump pulse duration. Because the pulse duration varies generally with the bit rate, to evaluate properly the performance of the SOA based non-linear gate performance for a precise data rate, adequate pulse duration should be considered in dynamics characterisations.

Dynamics characterisation of various SOA structures reveals also influences of waveguide design on SOA dynamics performance. A highly confined SOA will be preferable because a greater collection of injected signal into the SOA active region waveguide could result in a shorter effective recovery time. Especially, by increasing the chip length, SOA gain dynamics becomes faster thanks to the distribution of strong ASE to gain saturation and therefore to gain recovery. Finally, quantum-dot material based SOAs affirm their advantages for all-optical signal processing at ultrahigh bit rates. Despite the very small-optical confinement (1%) QDot SOAs exhibit a fast dynamics comparable to highly confined bulk based SOA. The shortest recovery time of 3 ps is obtained by associating the long QDot SOA with a blue-shifted filtering which promises a pattern free operation at 160 Gbit/s.

At last, SOA dynamics was performed with high temporal resolution in a degenerate pump-probe experiment using 150 fs pulses for the 2-mm length QDot SOA. Gain dynamics results reveals coherent physical facts with those obtained in our wavelength conversion based pump-probe experiment. Attention must be paid on phase dynamics results. Phase recovery is dominated by slow processes, on the contrary with gain recovery that is dominated rather by fast processes. This fact is imputed to the weak coupling between the gain compression due to intraband processes and the corresponding induced phase modulation. Most of SOA based all-optical signal processing devices rely on the XGM and XPM processes. Understanding of SOAs' gain and phase with reliable experimental information is a key issue to obtain optimal operating performance of SOA based non-linear optical gates.

Chapter 3

Numerical study of SOA dynamics

According to the experimental results of the SOA dynamics measurements presented in Chapter 2, the gain compression is not only contributed by a component related to interband processes but also by another component related to intraband processes. Consequently, the gain recovery exhibits an ultrafast relaxation, characterised by a time constant in order of few picoseconds, and a slow relaxation, characterised by a time constant in order of 100 ps. The fast gain recovery reveals the presence of the intraband relaxations such as Carrier Heating (CH) and Spectral Hole Burning (SHB) and the slow recovery reveals the presence of carrier interband relaxations. The effect of intraband dynamics becomes more important when the pulse width becomes smaller. Otherwise, when the pulsewidth is in order of few picoseconds (corresponding to the data rates such as 40 Gbit/s and 160 Gbit/s), the intraband dynamics has to be considered in SOA dynamics investigations. On one hand, to understand the influences of these ultrafast processes on the gain dynamics, it is necessary to develop an SOA model including the intraband phenomena. Consequently, their impact on the performance of the SOA non-linear gates could be examined. On the other hand, the model must be simple enough to be introduced easily in different regenerator schemes in order to avoid cumbersome system simulations. In this context, the model which was proposed by [14] concerning the injection laser relaxation and was adapted for the injection SOA recovery by [15] appears quite adequate. In the first section, the main backgrounds on the SOA model are presented. The results of the numerical study on the SOA dynamics are then reported in Section 3.2 and summarised in Section 3.3.

3.1   SOA model

Some hypotheses of SOA intrinsic characteristics have to be considered. The studied SOA has to be a travelling-wave amplifier and the waveguide dimensions are such that the amplifier supports only one guided mode. It is usually the case in practice. The studied SOA structures have the thickness and the width in order of 1 μm and the length in order from 1 mm to few millimetres. The width and the thickness of these active regions are smaller

than the scattering length whereas the length is much larger. The last hypothesis allows the carrier density to be considered as nearly uniform along the transverse dimensions and the carrier scattering can be neglected. Another assumption which is currently taken into account to simplify the propagation equation is that the amplifier intrinsic losses: they are considered negligible compared to the accumulated gain during pulse propagation. An assumption of operating conditions should be also respected. The model is valid for injection pulse durations exceeding 1 ps. This condition implies that the spectral width of pulses is sufficiently small compared to the SOA gain bandwidth and therefore the spectral effects could be neglected. This assumption enables the considerable simplification of density matrix formulation as proposed in [14]. In the gain dynamics experiment presented in Section 2.3, the pump pulse duration is typically 2.5 ps. Then, this SOA model could be used to simulate the gain dynamics measured in the experiment. For further studies involving SOA insertion into system simulations, the pulse duration at the considered data rates (40 Gbit/s and 160 Gbit/s) exceeds always 1 ps and thus this SOA model will still be suitable.

Indeed, the carrier population is divided into two parts, with N_1 and N_2 carriers respectively. N_1 represents the number of carriers which directly contribute to the SOA gain. That means their energies are close to the photon energy of the injected optical signal. N_2 corresponds to all the other carriers. Their energies are out of the band involved in the stimulated emission process. The carriers of these two populations are redistributed by intraband relaxations. The distribution of the final state is assumed to be the distribution at the thermal equilibrium. The rate equations associated to the two population evolutions can be written as Equations (3-1) and (3-2) [15]:

$$\frac{\partial N_1}{\partial t} = \frac{IU}{q} - \frac{PN_1}{E_s} - \frac{N_1}{\tau_s} - \frac{\Delta N}{\tau_c} \tag{3-1}$$

$$\frac{\partial N_2}{\partial t} = \frac{I\left(1 - U\right)}{q} - \frac{N_2}{\tau_s} + \frac{\Delta N}{\tau_c} \tag{3-2}$$

with:

$$U = \frac{\lambda^2}{\pi c} \times \frac{1}{\tau_c \Delta \lambda} \tag{3-3}$$

$$\Delta N = N_1\left(1 - U\right) - N_2 U \tag{3-4}$$

$$N_s = N_1 + N_2 \tag{3-5}$$

$$E_s = \frac{h\upsilon\sigma_m}{a} \tag{3-6}$$

$$g = \frac{\Gamma a}{V}N_1 \tag{3-7}$$

where:

$c = 3 \times 10^8 m/s$ is the velocity of light in vacuum,

$q = 1.6 \times 10^{-19} C$ is the electron charge,

$h = 6.625 \times 10^{-34} J.s$ is the Planck constant,

I is the injection current,

λ is the signal wavelength,

ν is the signal frequency,

$\Delta\lambda$ is the half width of the SOA spontaneous emission spectrum,

V is the active volume,

σ_m is the mode cross section,

γ is the confinement factor,

a is the gain coefficient,

E_s is the saturation energy if the amplifier,

τ_s is the interband life-time,

τ_c is the intraband life-time,

N_s is the total carrier population,

ΔN is the deviation from thermal equilibrium due to optical pulses,

P is the optical power.

The propagation of the electromagnetic field inside the SOA is governed by the following Equation (3-8):

$$\frac{\partial A}{\partial z} + \frac{1}{v_g} \times \frac{\partial A}{\partial t} = \frac{1}{2}\left(1 + i\alpha\right)gA \tag{3-8}$$

$A\left(z,t\right)$ is the slowly varying envelope associated with the optical pulse. v_g is the group velocity. α is the linewidth enhancement factor.

Equations (3-1), (3-2) and (3-8) can be simplified by applying the transformation:

$$\tau = t - \frac{z}{v_g} \tag{3-9}$$

It is also useful to separate the amplitude and the phase of the pulse by writing:

$$A = \sqrt{P}\exp\left(i\phi\right) \tag{3-10}$$

with $P\left(z,\tau\right)$ is the power and $\phi\left(z,\tau\right)$ is the phase. Consequently, Equation (3-8) is equivalent to the following set of two Equations (3-11) and (3-16):

$$\frac{\partial P}{\partial z} = gP \tag{3-11}$$

$$\frac{\partial \phi}{\partial z} = -\frac{1}{2}\alpha g \tag{3-12}$$

By using Equations (3-1), (3-2) and (3-4), ΔN and N_2 can be eliminated to obtain one rate equation of the only unknown N_1. By taking into account that $\tau_c << \tau_s$, the rate equation that governs the N_1 evolution can be expressed as Equation (3-13):

$$\frac{\partial^2 N_1}{\partial \tau^2} + \frac{1}{\tau_c} \times \frac{\partial N_1}{\partial t} = \frac{IU}{q\tau_c} - \frac{N_1}{\tau_s\tau_c} - \left(\frac{U}{E_s\tau_c} + \frac{1}{E_s\tau_s}\right)PN_1 - \frac{1}{E_s} \times \frac{\partial\left(PN_1\right)}{\partial \tau} \tag{3-13}$$

If we define the function $h(\tau)$ which physically represents the accumulated gain at each point of the pulse profile, by Equation (3-14):

$$h(\tau) = \int_0^L g\,dz \qquad (3\text{-}14)$$

and integrate Equation (3-13) over the amplifier length and Equations (3-7) and (3-11) together then lead to Equation (3-15):

$$\frac{d^2h}{d\tau^2} + \frac{1}{\tau_c} \times \frac{dh}{d\tau} = \frac{IU\Gamma aL}{qV\tau_c} - \frac{h}{\tau_s\tau_c} - \left(\frac{U}{E_S\tau_c} + \frac{1}{E_s\tau_s}\right)[\exp(h) - 1]P(\tau,0) - \frac{1}{E_s} \times \frac{d}{d\tau}\left\{[\exp(h) - 1]P(\tau,0)\right\}$$

$$(3\text{-}15)$$

Equation (3-15) could be solved numerically to obtain $h(\tau)$. All details of the intermediate calculations are reported in Appendix 1.

3.2 Gain and phase dynamics of SOA

3.2.1 Fitting process for relaxation time evaluation

Models of SOA steady-state and dynamics behaviour are important tools to predict how an SOA behaves in a particular non-linear gate configuration. In general, all SOA parameters are not well-known. Some information about the SOA could be provided by the supplier, such as the confinement factor and the active region dimensions. However, the life-time constants of the interband (τ_s) and intraband (τ_c) relaxations are unknown. These time constants could be evaluated thanks to the experimental gain dynamics characterisation. Then, the SOA can be modelised and introduced in various non-linear gate configurations for regeneration applications. An example of fitting process is given for the highly confined bulk SOA (SOA n°2). The information of the SOA structure is given in Table (3.1).

SOA description	bulk material, highly confined
Active region length	1 mm
Active region width	0.7 μm
Active region thick	0.5 μm
Confinement factor	75 %
Material gain coefficient (typical for InGaAsP)	2.5 x 10^{-20} m^2

Table 3.1: SOA structure (SOA n°2) characteristics given by the SOA supplier

These parameters are given by the SOA supplier. Otherwise, the SOA had to be previously characterised via the static gain measurement (described in Paragraph 2.2.3) and the gain dynamics measurement (described in Paragraph 2.3.1). These experiments are simulated and the calculated curves are fitted with the experimental curves by adjusting the τ_s and τ_c parameters. This simple fit process allows the unknown time constants to be evaluated rapidly. The experiment conditions which are injected into the simulation are given in Table (3.2).

Wavelength	1555 nm
Half width of the ASE spectrum	20 nm
Pump signal cadence	10 GHz
Pump pulsewidth	2.5 ps
Input pump power	variable
Input probe power	variable

Table 3.2: Operating parameters used for the SOA (n°2) modelling in the static gain and the dynamic gain experiments

A good agreement between the experimental and numerical results is obtained for the interband life-time $\tau_s \approx 80$ ps and the intraband life-time $\tau_c \approx 1$ ps (Figure (3.1)).

The intraband life-time of 1 ps is slightly superior to those reported usually in the literature, in order of 600-700 fs [104], [105], [63]. This fact originates from the different ex-
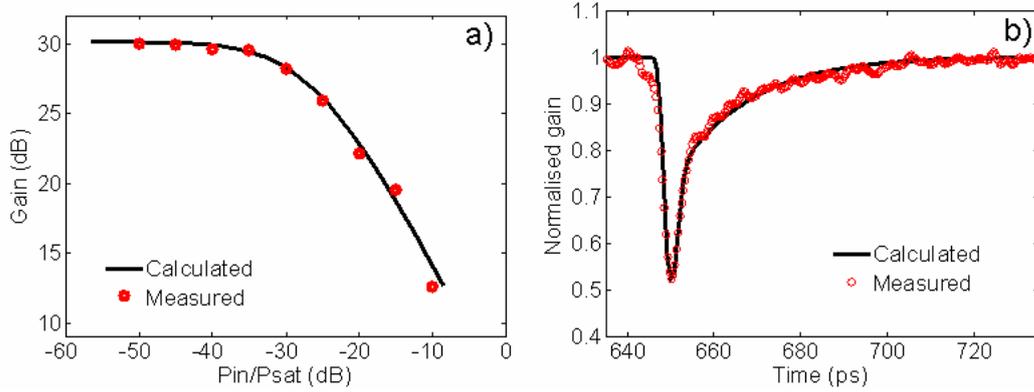
Figure 3.1: Static gain (a) and dynamic gain (b) curves of the SOA n°2. The static gain curve was obtained in auto saturation configuration without the probe signal. The dynamic gain curve was obtained with $P_{probe}/P_{sat} = 10$ dB and the gain compression was 3 dB.

perimental conditions. In these publications, the reported results were obtained with pump pulse durations of 150-200 fs. In our gain dynamics experiment, the pump pulse duration is much longer, 2.5 ps. For a saturation induced by picosecond pulses, the characteristic time of the CH phenomenon ranges from 700 fs to 1.3 ps [63]. Otherwise, the pulse width is much greater than the characteristic time of the SHB (50-100 fs). Therefore, the intraband life-time of 1 ps seems to be an adequate evaluation. The extrapolated interband life-time of 80 ps is smaller than the typical values reported in the literature (100 ps up to several ns). This characteristic time of the interband relaxations should be considered rather as an effective value but not as the intrinsic interband life-time of the SOA. Because of the strong probe signal ($P_{probe}/P_{sat} = 10$ dB), the carrier interband recombination is accelerated and its characteristic time is reduced to the effective value 80 ps.

As the characteristic times τ_s and τ_c are defined, the SOA behavior can be assessed as a function of other operating parameters of the experiments. By setting the probe signal power and adjusting the pump signal power, the SOA dynamics curves corresponding to different gain compressions can be obtained. Examples for the gain compressions of 1.7 dB and 5 dB are shown in Figure (3.2). The gain recovery shapes measured with the pump probe experiment and calculated with the model are in good agreement. The time constants $\tau_s \approx 80$ ps and $\tau_c \approx 1$ ps can therefore be considered as good estimations for the SOA. For the next investigations hereafter, these characteristic times are used to modelise the SOA n°2.

3.2.2   Gain dynamics investigation

3.2.2.1   Gain compression-response time trade-off

The experimental results presented in Paragraph 2.3.2 shows that the gain recovery time increases when the gain compression increases. By adjusting the pump signal power at the
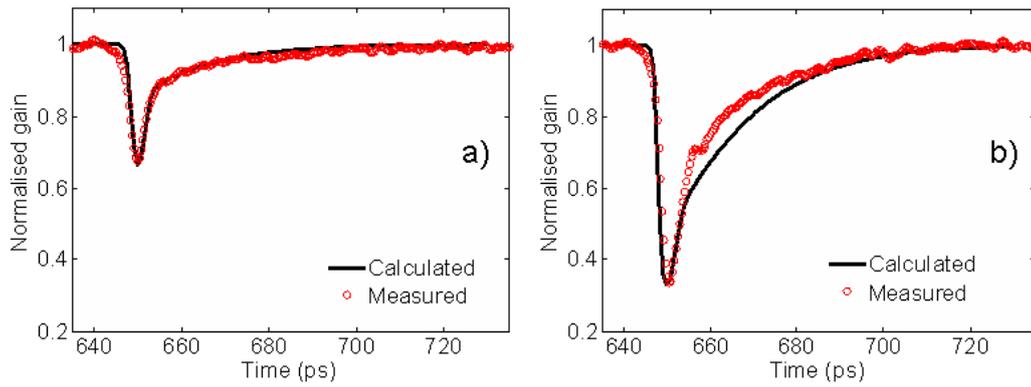
Figure 3.2: Gain recovery shapes of the SOA n°2 for gain compressions of 1.7 dB (a) and 5 dB (b) with $P_{probe}/P_{sat} = 10dB$
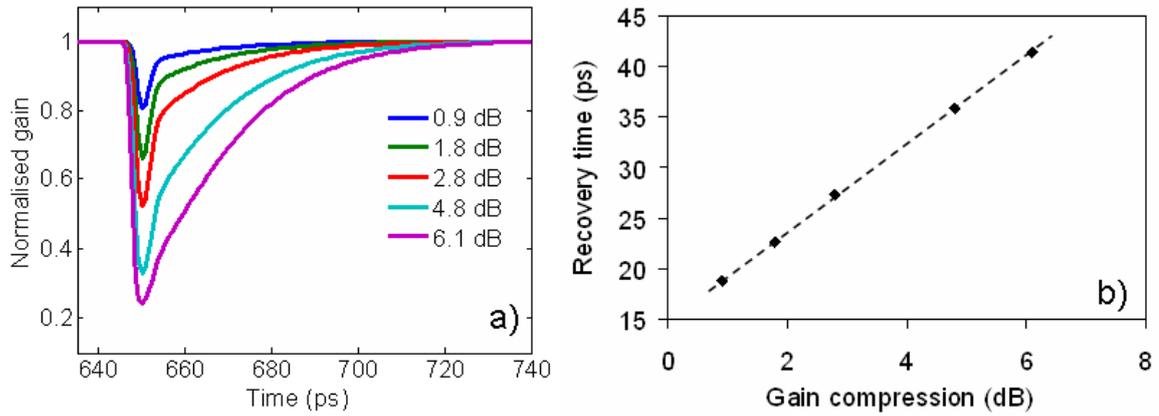
Figure 3.3: Gain recovery shapes for various gain compressions (a) and deduced recovery times (b) with $P_{probe}/P_{sat} = 10dB$

SOA input, it is possible to calculate the SOA gain responses for different gain compressions. The SOA parameters used in the modelling are those presented in Paragraph 3.2.1. The probe signal power was fixed at 10 dB above the saturation power $P_{probe}/P_{sat} = 10$ dB. The calculated gain recovery shapes and the corresponding recovery times are shown in Figure (3.3). The model predicts that the gain recovery time increases with the gain compression. This behaviour is well known in the literature [73]. The greater the gain compression is, the more the carriers are consumed. Consequently, the gain needs more time to recover its steady state value. Similar to the experimental results, the model predicts also that the gain recovery time is shorter than 25 ps only for the gain compressions as low as 2 dB. This indicates that an SOA based optical non-linear gate provides operations at 40 Gbit/s without patterning effects only if the gain compression does not exceed 2 dB.
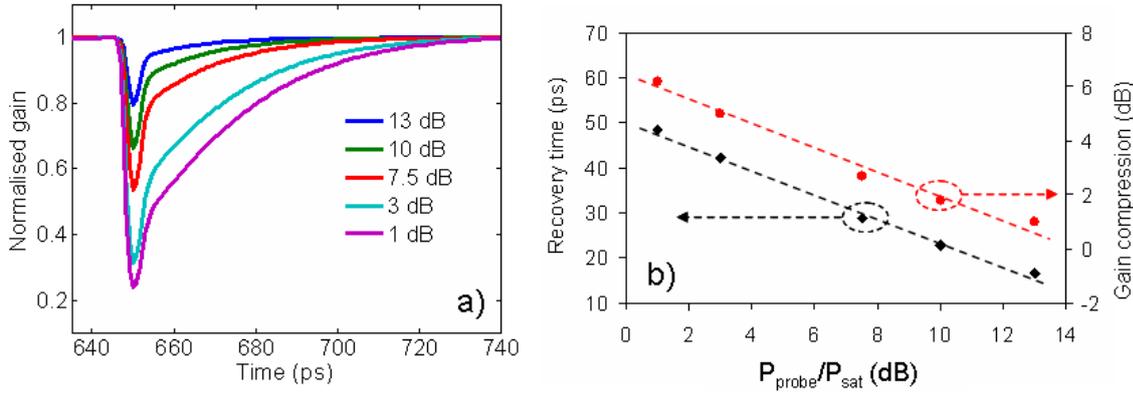
Figure 3.4: Gain recovery shapes for various ratios P_{probe}/P_{sat} (a) and evolutions of corresponding recovery time and gain compression (b) with $P_{pump}/P_{sat} = -2.5$ dB

3.2.2.2   Influence of probe signal power on gain dynamics

In the pump probe experiment, the probe signal is used to observe the temporal gain evolution and simultaneously to accelerate the carrier recombinations thanks to its high power levels. In such a situation, the SOA gain dynamics depends not only on the pump level but also on the probe level. To study the probe dependence of the gain dynamics, the pump power is fixed and the probe power is adjusted. The results are shown in Figure (3.4). The pump power was fixed at 2.5 dB under the saturation power $P_{pump}/P_{sat} = -2.5$ dB.

The curves illustrate clearly the influence of the probe signal level on the gain dynamics. On one hand, the probe signal reduces significantly the gain recovery time through the stimulated emissions. The recovery time is drastically reduced from about 50 ps to around 20 ps when the ratio P_{probe}/P_{sat} increases from 1 dB to 10 dB (Figure (3.4(b))). On the other hand, as the probe signal is amplified, the carrier population is partially consumed by this continuous signal. Hence, the available gain is reduced for the pump signal. This fact is demonstrated by the gain compression fall when the probe signal becomes stronger (Figure (3.4(b))).

3.2.2.3   Limit of gain recovery acceleration by assist light

To avoid the patterning effect at ultrahigh data rates, it is possible to work at low gain compressions to minimize the gain response time. Otherwise, it is possible to use a strong probe signal as an assist light, which accelerates the SOA gain recovery. But a power increase of the assist light is also accompanied by a gain compression reduction. The gain compression induced by the pump signal is representative of the non-linearity offered by the SOA. A reduction of the SOA compression can lead to a performance degradation of the SOA non-linear gate. It is possible to maintain the gain compression when the probe power becomes stronger by increasing simultaneously the control signal (pump signal). To study the gain recovery acceleration by the assist light when the SOA compression is maintained
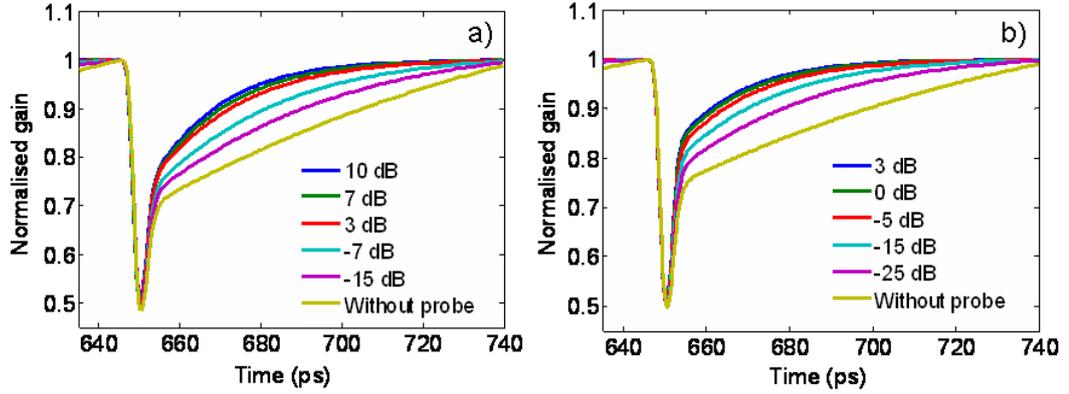
Figure 3.5: Gain recovery shapes for various ratios P_{probe}/P_{sat} at a fixed gain compression of 3 dB with (a) current density of 1 (a.u) and (b) current density of 1.5 (a.u)

at a fixed value, the pump and probe powers are adjusted simultaneously. The results are summarised in Figure (3.5) for two different current densities. All other parameters are identical to those presented in Paragraph 3.2.1. The gain compression was fixed at a typical value of 3 dB (i.e the normalised linear gain falls down from 1 to 0.5).

In both cases, the curves demonstrate the gain recovery acceleration of the probe signal through stimulated emission. When the probe level increases, the ultrafast recovery due to the intraband relaxations is unchanged while the slow recovery due to the interband relaxations is clearly shortened. This confirms that the gain recovery acceleration by using an assist light is attributed to the carrier band-to-band recombinations. Otherwise, it is observed also that the gain recovery time could not be reduced infinitely. In both cases, the gain recovery forms do not exhibit significant changes anymore when the probe power exceeds a power threshold.

In the first case (Figure (3.5(a))), the 10 %-90 % recovery time was about 70 ps without probe signal and it is reduced to a minimum of 30 ps for $P_{probe}/P_{sat} \geq 3$ dB. In the second case (Figure (3.5(b))), when the current density is increased to 1.5 unity, the shortest 10 %-90 % recovery time is 20 ps for $P_{probe}/P_{sat} \geq -5$ dB. Thus, it appears that there is always a recovery time limit even if strong assist light is used. A tentative explanation could be described as follows. On the trailing edge of the gain recovery, the carrier (electron and hole) number is recovered through the electrical pumping and the recovery speed is determined by the interband relaxation time. In the presence of an assist light, the carrier movement is sped up because of stimulated emission. However, the carrier number recovered per second can not exceed the number of electrons supplied by the electrical current. Because the bias current is finite, it imposes thus a limit to the gain recovery speed. The explanation is confirmed by comparing the results presented in Figure (3.5(a)) and Figure (3.5(b)). When the current density increases, the shortest recovery time decreases, i.e the maximal recovery rate increases with the electrical pumping. Finally, we remind that this saturation of the

gain recovery speed has been observed experimentally and presented in Paragraph 2.3.8.

3.2.3 Phase dynamics investigation

3.2.3.1 Rate equation of phase evolution

Following the developments in [15], the signal phase evolution is governed by Equation (3-16):

$$\frac{\partial \phi}{\partial z} = -\frac{1}{2}\alpha g \tag{3-16}$$

Because of the time dependence of the differential gain $g(z,\tau)$, the phase is consequently time dependent. In this case, the authors represent the coupling between the gain and the induced phase depending only on one factor α. Otherwise, it was demonstrated previously that the gain compression is attributed to both interband and intraband relaxations. The refractive index change induced by the carrier changes results in a phase modulation of the optical signal. In the literature, it is shown that the phase changes (via the index changes) related to the intraband and interband gain suppression are represented by different coupling factors [58], [62]. Therefore, it should be more accurate to consider two different coupling factors: α related to the carrier change due to the interband transitions and α_T related to the carrier change due to the intraband transitions. Moreover, if the operation point is close to the amplifier gain peak, the spectral hole burning induced by the carrier depletion is symmetric and then the SHB does not contribute to the index change. Consequently, the phase change induced by the intraband processes is dominated by the CH phenomenon. The differential gain could be expressed by Equation (3-17).

$$g = g_{lin} + g_{nonlin} = \frac{\Gamma a}{V}N_1 \tag{3-17}$$

and using $N_1 = \Delta N + N_s U$ deduced from Equation (3-4), we obtain Equation (3-18):

$$g_{lin} = \frac{\Gamma a}{V}UN_s \tag{3-18}$$

and

$$g_{nonlin} = \frac{\Gamma a}{V}\Delta N \tag{3-19}$$

Similarly to the gain, the phase change induced by the refractive index change is then expressed by Equation (3-20).

$$\frac{\partial \varphi}{\partial z} = -\frac{\Gamma a}{2V}(\alpha_T \Delta N + \alpha U N_s) \tag{3-20}$$

We remind that N_s is the total carrier population and ΔN is the deviation from thermal equilibrium due to optical pulses. The first and the second terms on the right side of Equation (3-20) correspond respectively to the contributions of intraband and interband processes to the total phase changes. Time dependence of N_1 is deduced from numerical solution of Equation (3-15). The evolution of is the solution of Equation (3-21).

$$\frac{\partial N_s}{\partial t} = \frac{I}{q} - \frac{PN_1}{E_s} - \frac{N_s}{\tau_s} \tag{3-21}$$
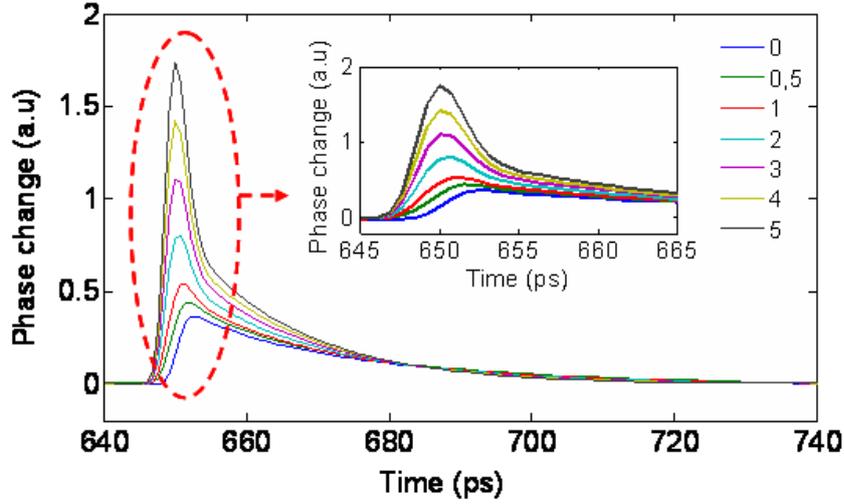
Figure 3.6: Phase recovery for various values of α_T. The gain compression was fixed at 3 dB and $\alpha = 5$. In inset, the curves are expanded.

ΔN is deduced from Equation (3-4) and the phase change induced by the gain compression is obtained by integrating Equation (3-20) over the amplifier length.

3.2.3.2 Contributions of intraband and interband processes to phase changes

On one hand, the typical value of α could be found easily in the literature. In the model, we introduce the widely used value $\alpha = 5$. On the other hand, the factor α_T related to the carrier change due to the intraband transitions is not well-known. The phase dynamics induced by the saturated SOA is investigated for different values of α_T. The gain compression is controlled at 3 dB and the probe signal power is fixed at $P_{probe}/P_{sat} = 10$ dB. The phase recovery shapes obtained for various values of α_T are displayed in Figure (3.6).

The phase response exhibits the two distinguished fast and slow recoveries only for great values of α_T ($\alpha_T > 1$). And the fast recovery contribution increases with α_T. This fact can be easily deduced from Equation (3-20). For small values of α_T ($\alpha_T \leq 1$), the phase recovery shapes are very close to the experimental results presented in Paragraph 2.3.9 and reported in [60], [62]. Therefore, it should be reasonable to consider a small value of α_T for further study. In those cases, the phase change is mainly contributed by the carrier band-to-band redistribution. Thus, the phase recovery could be characterized by only one time constant determined by the slow interband relaxations (in order of few tens of picoseconds). Hereafter $\alpha_T = 1$ is used for the SOA model. This value is close to the experimental measurements reported in [62] for a bulk based SOA.

3.2.3.3 Phase recovery time for various gain compressions

The phase recovery time is estimated for different gain compressions and compared to the gain recovery time by using the model. Similarly to the gain recovery time, the phase
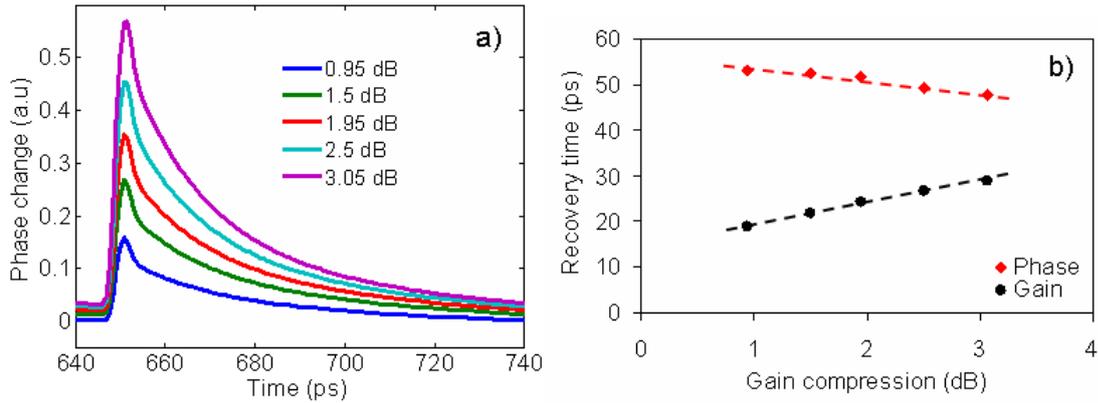
Figure 3.7: Phase recovery shapes (a) and deduced recovery times (b) for various gain compressions with $P_{probe}/P_{sat} = 10$ dB

recovery time is considered as the time that the phase needs to recover from 10 % to 90 % of its steady value. The phase recovery shapes (a) and the corresponding estimated recovery times (b) are presented in Figure (3.7). The probe power was controlled at $P_{probe}/P_{sat} = 10$ dB.

The gain compression growth induced an increase of the carrier deviation and this leads to the increase of the total phase shift. The phase recovery times appear greater than the gain recovery times (50 ps versus 25 ps for 3 dB gain compression). The intraband relaxation contribution to the phase change is smaller than to the gain compression (especially for small compressions). Consequently, the dependence of the phase recovery to the slow processes is more important. Otherwise, the phase recovery time, on the contrary to the gain recovery time, decreases with the gain compression increase. The dissimilar behaviours of the gain and phase have been already reported by [106]. This difference of the gain and phase dynamics must be considered carefully in the SOA non-linear gates exploiting both gain and phase modulations.

3.2.3.4   Gain and phase delay

At the maximum of the amplifier saturation, it is found that the phase shift is delayed with respect to the gain compression. The phenomenon is illustrated in Figure (3.8) for a gain compression of 3 dB and $P_{probe}/P_{sat} = 10$ dB.

The delay between the maximum phase shift and the maximum gain compression is estimated at $\tau_d = 1.5$ ps (numerical time resolution was 0.4 ps). This phenomenon was observed experimentally [102], [103], predicted in [107] and investigated in [62]. The time delay τ_d for 2.5 ps pump pulse duration is in well agreement with the results reported in [62]. This delay is attributed also to the fact that the ultrafast intraband effects contribute considerably to the gain compression but little to the phase deviation. This could be easily verified by taking $\alpha_T = \alpha = 5$. In that case, the contributions of the intraband effects
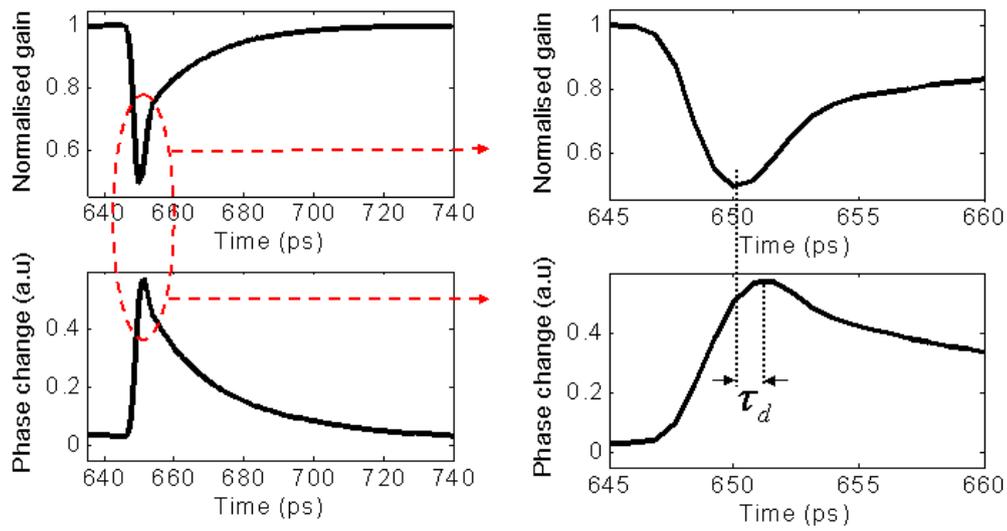
Figure 3.8: Observation of gain compression and phase deviation delay, $\alpha_T = 1$ and $\alpha = 5$

to the phase change and to the gain compression are identical and the synchronisation of phase and gain modulations is clearly demonstrated in Figure (3.9).

The delay could influence the performance of signal processing devices using both XGM and XPM. The impact will become more and more important for ultrahigh bit rates such as 160 Gbit/s, when the delay of few picoseconds is comparable to the bit duration (6 ps).
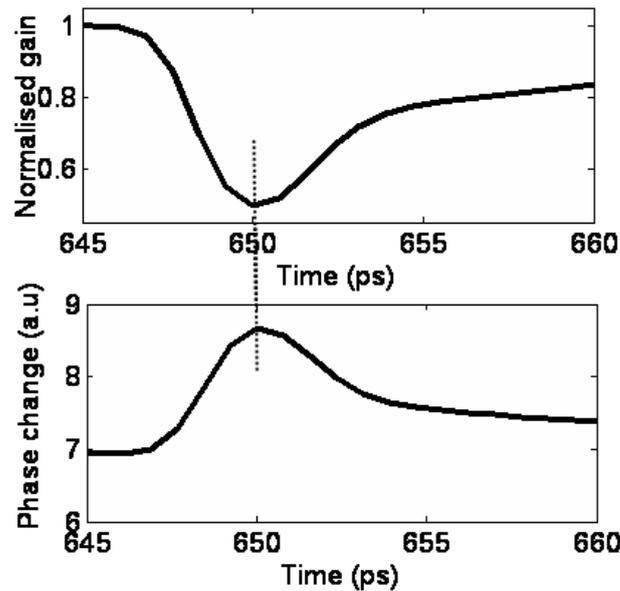
Figure 3.9: Synchronisation of phase and gain modulations in case $\alpha_T = \alpha = 5$

3.3   Chapter summary

In this chapter, an SOA model including intraband carrier dynamics was developed. When the data rate increases, the pulse duration decreases and the contribution of the intraband effects to the SOA dynamics becomes more and more important. The intraband effect introduction is then necessary to evaluate the performance of SOA based signal processing devices. Besides, the model is also easily reused because it relies on the numerical resolution of only one differential equation. By comparing the experimental results of the gain dynamics measurements and the numerical results predicted by the model, it is possible to evaluate the time constants of the carrier recovery. This allows the SOA behavior to be predicted in various non-linear optical gate configurations.

The dynamics of the phase deviation induced by the carrier modulation was also investigated. It is shown that the phase recovery is largely dominated by the slow interband carrier relaxations, on the contrary to the gain recovery which is rather dominated by the ultrafast intraband carrier relaxations. This difference between the gain and phase dynamics must be taken into account in interferometric configurations, in which the SOA optical gate performance at ultrahigh bit rates depends not only on the gain recovery time but also on the phase recovery time.

The developed model illustrates also that the phase modulation exhibits a delay in order of several picoseconds with respect to the gain modulation. The impact of this phenomenon to the SOA non-linear gate performance could not be negligible especially for the configurations using both XGM and XPM at ultrahigh data rates, at which the bit duration falls down to only few picoseconds.

Chapter 4

Investigation of SOA optical gates for 2R regeneration at 40 Gbit/s

Gain non-linearity and fast response make SOA a good candidate as a non-linear optical gate in signal processing functions. Experimental characterisations presented in Chapter 2 show clearly the high gain non-linearity characteristic of the studied SOAs. In particular, short time responses of 20 ps for the bulk based SOA and of 3 ps for the long quantum-dot SOA were demonstrated. These results indicate that SOA based non-linear optical gates for bit by bit signal processing at ultrahigh bit rates beyond 40 Gbit/s could be possible. Many devices have been reported in SOA interferometric gates [108], [109], [110] and have demonstrated regeneration efficiency. However, the interferometric configurations require in general several SOAs. A simpler solution for 2R regeneration could be achieved by cascading an SOA and a Saturable Absorber (SA) [111], [112]. A 2R regenerator based on that scheme demonstrated its regeneration efficiency in a transmission link at 10 Gbit/s [10]. In this chapter, regeneration potential of non-linear optical gates at 40 Gbit/s based on SOA in self-saturation is assessed experimentally and numerically. Noise compression effect of an SOA gate is demonstrated first. Assessment of two non-linear optical gate configurations for 2R regeneration is then presented. The regenerators are based on cascades of an SOA and an SA.

According to the gain dynamics results presented in Chapter 2, the long quantum-dot SOA (SOA n°5) exhibits the shortest recovery time and hence appears as an appropriate sample for ultrahigh speed operations. However, the available SOA exhibits an excessive gain ripple of at least 6 dB at its typical bias currents. The strong gain ripple will add large undesirable noise to the signal passing through the SOA. Therefore, the long QD SOA sample could not be used in signal regeneration experiments. Among the other SOAs, the highly confined bulk based SOA (SOA n°2) appears as the best candidate for a regeneration experiment at 40 Gbit/s. It exhibits lower ripple levels compared to the long QD SOA and gain recovery times smaller than 25 ps at maximum bias current. Indeed, this SOA is the
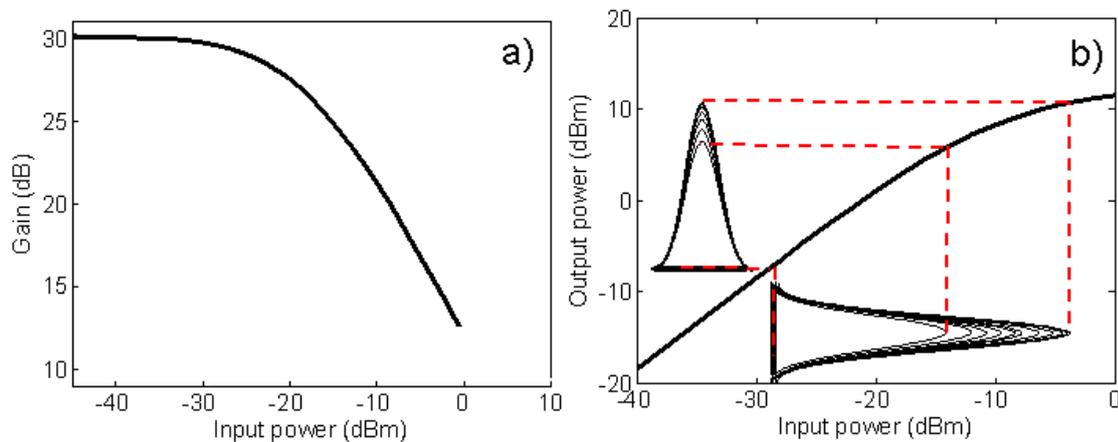
Figure 4.1: Gain as a function of input power of an SOA (a) and characteristic function of an optical gate based on the SOA in self-saturation (b)

chosen component for all the following investigations.

4.1   Semiconductor optical amplifier for noise compression

4.1.1   Principle

The gain saturation could be a representative image of the SOA non-linearity. Figure (4.1(a)) depicts the gain of an SOA as a function of input power. It shows that a strong input optical signal will undergo a smaller SOA gain in comparison to a weaker signal. For digital signals, intense pulses acquire lower gains compared to weaker pulses. This gain saturation phenomenon tends to equalise the power of all pulses, i.e of all '1' symbols. In a self-saturation regime, the SOA can thus play the role of a power equaliser reducing amplitude fluctuations of the 'mark' level. The SOA characteristic function deduced from the gain curve is depicted in Figure (4.1(b)).

The non-linear characteristic function of the optical gate constituted of the SOA in self-saturation illustrates clearly that amplitude fluctuations on the 'mark' level of a data signal could be reduced. Because the gain saturation tends to equalise the power of all pulses, the 'mark' level variance of the transmitted signal is smaller at the SOA output than at the input. In other words, the noise of the 'mark' level is compressed. The eye diagrams at the SOA output are more open compared to the input ones. However, this ideal scenario takes place only if the SOA response time is fast enough such as the gain recovers totally between two consecutive bits and therefore gain compression caused by a bit does not affect the gain compression process of the next one. On the other hand, if the gain recovery time is longer or comparable to the bit duration, the SOA gain does not have enough time to return to its steady state. In that case, undesirable gain fluctuations appear for both 'mark' and 'space' levels, and so the phenomenon is called patterning effects. The patterning effects
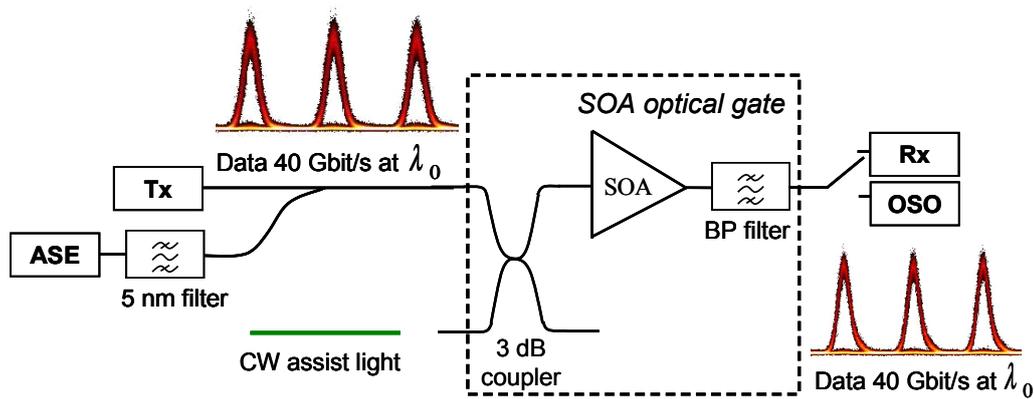
Figure 4.2: Set-up for noise compression experiment using SOA in self-saturation

lead to additional amplitude noise which degrades the signal quality. Otherwise, because the SOA optical gate performs a power equalisation, it might degrade the signal extinction ratio (ER) if the ER is not high enough at tha SOA input.

4.1.2 Noise compression assessment of SOA in self-saturation

The first conclusion when looking at Figure (4.1(b)), could be that a greater SOA gain compression will result in a stronger noise compression of the signal 'mark' level. Nevertheless, the experimental characterisations as well as the numerical study of SOA dynamics show that the gain recovery time is strongly dependent on gain compression induced by the incoming data signal. The recovery time increases with the gain compression and the patterning effects appear for large compressions. This last effect leads to an amplification of the 'space' level noise which could degrade rapidly the signal quality. At 40 Gbit/s, most of the characterised SOAs exhibit gain recovery times comparable to the bit duration, i.e 25 ps. In such situation, the gain compression response time trade-off involves directly a noise compression efficiency-patterning effects trade-off of the SOA based non-linear optical gate. To assess the SOA noise compression capability, the experimental set-up shown in Figure (4.2) is used.

The transmitter Tx generates a 40 Gbit/s RZ format signal at 1545 nm with a typical Extinction Ratio (ER) of 20 dB. The pulse duration is about 4 ps. The signal OSNR at the gate input is degraded artificially by adding ASE. As mentioned previously, the assessed SOA is the bulk based SOA with high optical confinement of 80 %. It is controlled at 25°C and biased at its maximal current of 500 mA to optimise the gain recovery time. A continuous signal at 1539.25 nm is simultaneously coupled into the SOA via a 3 dB coupler. The CW signal plays the role of an assist light. Its power is adjusted to be strong enough to accelerate the gain recovery due to the slow interband relaxations and to be small enough to preserve the SOA gain for the data signal. In all following experiments, the CW light power is in order of 8 dBm at the coupler input. A typical 5-nm flat-top band-pass filter is
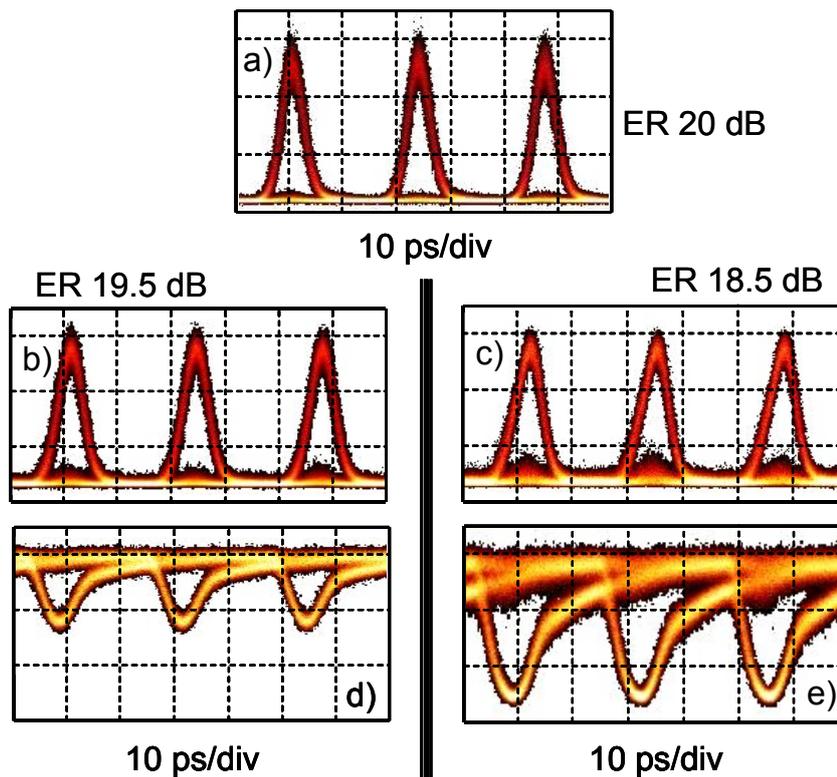
Figure 4.3: Signal eye diagrams at the SOA optical gate input (a) and at the SOA optical gate output for input signal powers of -5 dBm (b), of -2 dBm (c) and the corresponding gain compression traces (d), (e) respectively

placed at the SOA output to reject the amplified CW assist light. At the receiver, signal eye diagrams are observed thanks to the same Optical Sampling Oscilloscope (OSO) used in SOA dynamics characterisations. The received signal quality is assessed thanks to BER measurements.

The signal noise characteristics can be observed qualitatively on eye diagrams. They can be also evaluated quantitatively through the measurement of BER versus decision threshold which provides an estimation of the 'space' and 'mark' level variances. The data signal power is adjusted to assess the noise compression effect of the SOA gate under different operating conditions. The eye diagrams are displayed in Figure (4.3).

Figure (4.3(a)) shows the eye diagram of the emitted signal exhibiting an OSNR of 9.2 dB/5 nm. Figures (4.3(b)) and (4.3(c)) present the signal eye diagrams at the SOA optical gate output for two input signal powers of -5 dBm and -2 dBm respectively. The data signal powers are measured at the coupler input. The gain compression is measured on the cross-gain modulated signal at the BP filter output by shifting the filter centred on the assist light wavelength. The gain compression traces in the two cases are displayed in Figures (4.3(d-e)) and the corresponding gain compressions are 3 dB and 7 dB. With an ER measurement error of 0.5 dB, the signal ER is unchanged by passing through the
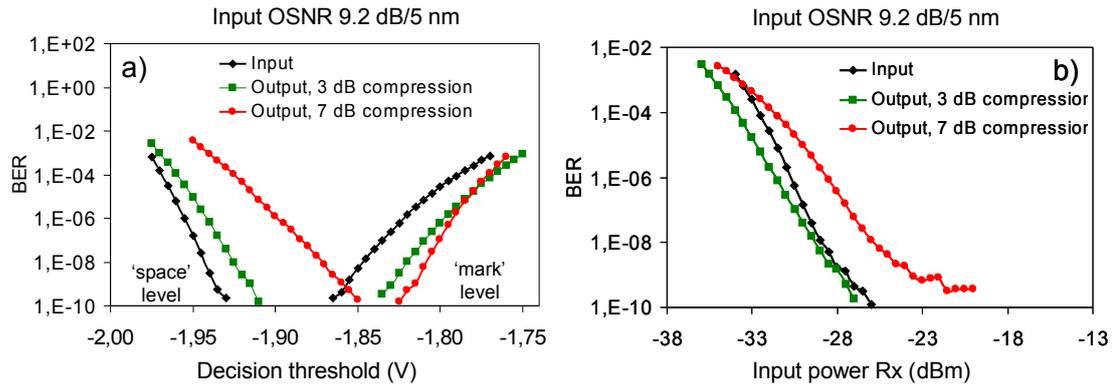
Figure 4.4: BER evolution vs decision threshold (a) and vs Rx input power (b) of the data signals at the SOA optical gate input and output for different gain compressions

SOA optical gate in the first case and is reduced about 1.5 dB in the second case. By comparing the input and output eye diagrams of the data signal, a variance reduction of the 'mark' level is clearly observed. The noise compression seems larger for the larger gain compression, i.e for the higher signal power. However, large degradations of the 'space' level are also observed. These degradations are explained by two factors. The first one is that the characteristic function of an SOA in self-saturation presents only one non-linearity at high signal powers as shown in Figure (4.1(b)). Signals with very low powers corresponding to the 'space' level are amplified quasi-linearly. Therefore, the 'space' level noise is also amplified. The second factor is the patterning effects due to the long recovery time of the SOA. Figure (4.3(e)) highlights the phenomenon when the gain compression reaches 7 dB. In that case, the patterning effects are considered as the dominating factor leading to an important amplification of the 'space' level noise.

The evolutions of the 'space' and 'mark' level variances can be observed more clearly by measuring BER evolutions. Figure (4.4(a)) displays the BER evolutions versus decision threshold. It is shown that the 'mark' level variance of the signal is reduced after travelling the SOA in both cases. Otherwise, the increases of the 'space' level noise are also illustrated. The 'space' level variance grows dramatically when the gain compression increases from 3 dB to 7 dB. These 'space' level degradations are mainly due to the patterning effects. The results are in good agreement with the eye diagrams observations.

The signal quality at the SOA gate output can be evaluated by plotting BER versus the receiver input power (Figure (4.4(b))). When the SOA gain is deeply compressed at 7 dB the signal quality is strongly damaged. This quality degradation is represented by an error floor at 10^{-9} and a penalty of 3 dB at 10^{-8} compared to the input signal. The quality loss is due partially to the signal ER reduction caused by the optical gate and principally to the large amplification of the 'space' level noise. Otherwise, the BER evolutions show that a gain compression of 3 dB is a good trade-off to obtain a significant noise compression on the 'mark' level without introducing important degradations on the 'space' level. The
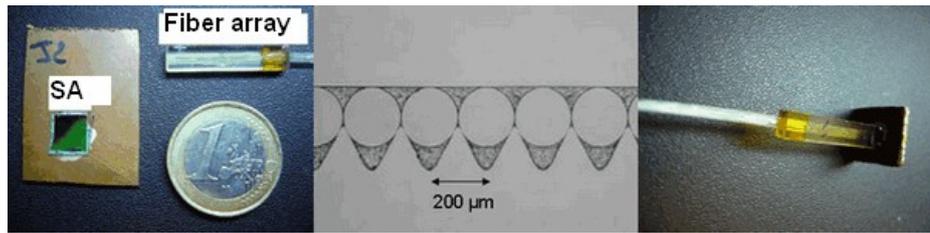
Figure 4.5: Photograph of SA chip, fibre array and SA module

sensitivity curve obtained in that case presents neither error floor nor penalty compared to the transmitted data signal.

Noise compression effect of a non-linear optical gate based on SOA in self-saturation is demonstrated. It is found that for the investigated SOA, a gain compression of 3 dB is suitable to obtain an efficient noise compression on the 'mark' level without large amplification of the 'space' level noise. This value is in good agreement with the results presented in Paragraph 2.3.3. At its maximal bias current, the SOA recovery time was found smaller than the bit duration at 40 Gbit/s for all gain compressions less than 5 dB and thus the patterning effects could be neglected. This optimal operation point must be adjusted according to SOAs exhibiting different dynamics. Otherwise, as discussed in the first chapter, a non-linear optical gate requires a characteristic function with two non-linearities to achieve a 2R regeneration function. Thus, the optical gate based on only one SOA in self-saturation regime could not provide a complete 2R regeneration operation because its characteristic function exhibits only one non-linearity at high signal power. Saturable Absorbers (SA) in self-saturation can provide a complementary function to the SOA optical gate. An experimental study of a non-linear optical gate for complete 2R regeneration based on a cascade of an SOA and an SA is presented in the next section.

4.2 Experimental assessment of 2R regenerator schemes based on cascades of SOA and SA

4.2.1 Principles

4.2.1.1 Saturable absorber for optical regeneration

A Microcavity Saturable Absorber (SA) is a quantum-well structure in a resonant cavity. The quantum-well layers are inserted between the two mirrors (front and back mirrors) constituting the resonant cavity. Further details of the studied SA sample can be found in [113]. A special fibre array has been developed by YENISTA OPTICS for efficiently interfacing the SA chip to 8 standard single mode fibres with 250 μm spacing. The fibre array is fixed to the mirror with an adhesive such that all the 8 out-coming beams typically have a Mode Field Diameter (MFD) of 4.5 μm on the surface of the mirror (Figure (4.5)).
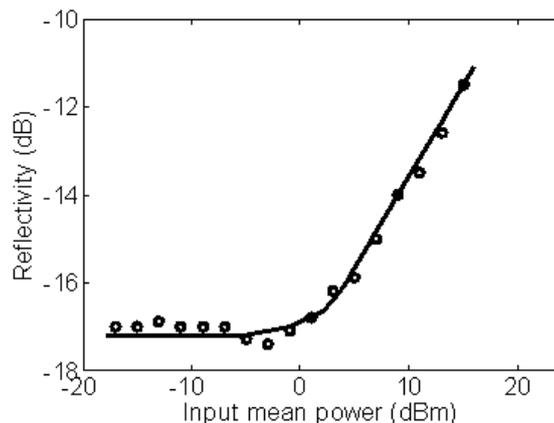
Figure 4.6: SA reflectivity as a function of input power

The SA absorption depends on the arriving signal power and this non-linearity exhibits potential for all-optical regeneration. Its efficiency was successfully demonstrated in various all-optical regenerators [40], [10], [12]. Since the studied SA operates in reflection configuration, its absorption could be mentioned hereafter as reflectivity. The measured reflectivity curve versus input power of the SA is shown in Figure (4.6). The SA exhibits 17 dB of reflectivity for weak input signals. For signal powers exceeding 4 dBm, the SA reflectivity is not constant any more and increases when the signal power increases. The reflectivity becomes signal power dependent and the phenomenon is called absorption saturation (because the negative reflectivity indicates that the signal is partially absorbed by the SA). The main function of an SA in a regenerator is the ER improvement. In self-saturation configuration, if the 'space' level power is smaller and the 'mark' level power is greater than the saturation threshold, the ratio of the SA reflectivity for a symbol '0' and for a symbol '1' corresponds to an ER enhancement.

Besides their compactness and integration possibility, SAs exhibit other attractive advantages for regeneration. They are passive components and therefore no electrical supply is required. The last distinguished feature of an SA is the potential for WDM regeneration. The SA absorption is spatially local and therefore the crosstalk between channels is negligible. Several spatially separate channels could be processed simultaneously on the same component [114]. However, an optical gate based on an SA alone could not provide a complete 2R regeneration function because the SA does not limit amplitude fluctuations on the 'mark' level. It has to be associated with a power equaliser to obtain complete 2R regeneration.

4.2.1.2   Cascade of SOA and SA for 2R regeneration

As previously discussed, optical gates based on SOA in self-saturation offer noise compression capability on the 'mark' level of a data signal. However, the gates degrade the signal ER and simultaneously amplify the 'space' level noise. On the contrary, an SA in
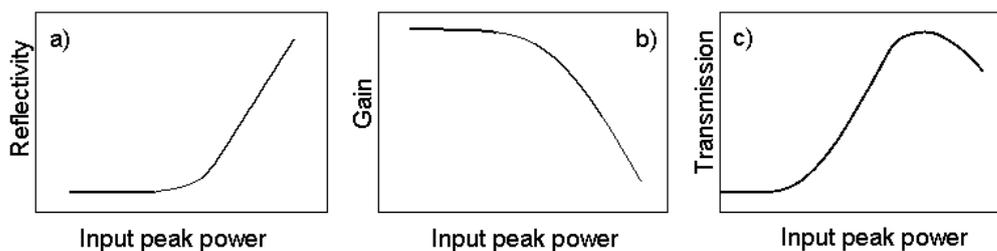
Figure 4.7: Reflectivity of an SA (a), gain of an SOA (b) and transmission function of a cascade SOA-SA (c)

self-saturation can enhance the signal ER. Moreover, if the maximal SA absorption is large enough, small-signals could be 'totally' absorbed as if amplitude fluctuations on the 'space' level are strongly attenuated. Unfortunately, an SA degrades partially the transmitted signal because it increases the 'mark' level variance. In other words, an SA 'amplifies' the amplitude fluctuations of the 'mark' level. It is clear that these two components possess complementary features and they could be combined to achieve a non-linear optical gate for 2R regeneration. The transmission functions of an SOA and an SA are depicted in Figures (4.7(a)) and (4.7(b)).

The slope of the SA reflectivity curve depends mainly on the input signal mean power and signal wavelength. For the SOA, the gain curve slope depends strongly on the assist light power. By adjusting operating conditions, it is possible to obtain a non-linear optical gate whose transmission function exhibits two non-linearities as shown in Figure (4.7(c)). Such a non-linear optical gate will be adequate for a 2R regenerator. Different SOA-SA cascade configurations were studied in this thesis. The SOA can be followed by the SA and vice-versa. The regeneration capabilities of the two configurations were assessed through a noise compression experiment. The basic scheme of the experiment was depicted in Figure (4.2). A degraded signal exhibiting amplitude noise is injected into the regenerator and the signal noise evolution is analysed at the regenerator output. The experimental results are presented in Paragraph 4.2.2 and Paragraph 4.2.3.

4.2.2   First configuration: SOA followed by SA

The first regenerator configuration consists in the SOA followed by the SA. The main advantage of such a configuration should be the small-signal power required at the gate input. This input power is related to the SOA saturation power which is typically -15 dBm. Otherwise, for the SA the saturation power is typically 10 dBm. Therefore, it seems preferable to place the SOA at the first position of the cascade. The experimental set-up for noise compression assessment is described in Figure (4.8).

The basic principle of the experiment is identical to the one presented in Section 4.1.2. The characteristics of the data signal and the assist light are not changed except for the
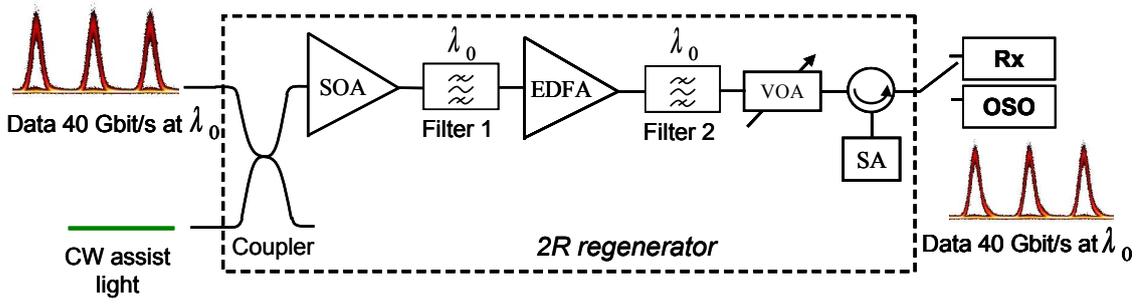
Figure 4.8: Experimental set-up for noise compression assessment of the first regenerator configuration (SOA followed by SA)

signal ER and OSNR. At the regenerator input, the data signal exhibits an OSNR of 7.4 dB/5 nm. The data signal and the CW assist light are simultaneously injected into the SOA via a 3-dB coupler. Filter 1 is used to reject the assist light. In general, the SOA is deeply saturated by the strong assist light and thus the data signal undergoes a small gain by passing through the SOA. At the filter 1 output, the signal power is probably not high enough to saturate the SA absorption. Therefore, an amplification stage constituted of an EDFA and a band-pass filter (filter 2) is inserted to provide the necessary signal power at the SA input. The signal is injected into the SA and collected via an optical circulator. The Variable Optical Attenuator (VOA) allows the signal power at the SA input to be adjusted. The setting of operating conditions to obtain a regeneration regime consists principally in adjusting of the signal powers at the SOA and SA inputs. The data signal power at the SOA input is adjusted to obtain an efficient noise compression on the signal 'mark' level without adding excessive noise on the 'space' level. The assist light power is adjusted to reduce significantly the patterning effects in the SOA without decreasing dramatically the SOA optical gain. At last, the signal power at the SA input is adjusted to obtain an efficient noise reduction on the 'space' level without large degradation of the 'mark' level noise. The setting processes of the three powers are not separable. A trade-off must be found to obtain a noise compression effect on the output optical signal. In the experiment, the best signal quality was obtained for the operating conditions presented in Table (4.1).

Data signal power at the coupler input	-1 dBm
Assist light power at the coupler input	11.5 dBm
Data signal power at the SA input	10 dBm

Table 4.1: Operating parameters of the first regenerator configuration (the SOA followed by the SA)

According to the reflectivity curve presented in Figure (4.6), the SA is well in absorption saturation when the input mean power equals to 10 dBm. For the SOA, it is in deep gain saturation regime. In presence of 11.5 dBm assist light, the SOA gain drops below 10 dB. Therefore, the EDFA amplification stage should be able to deliver a data signal
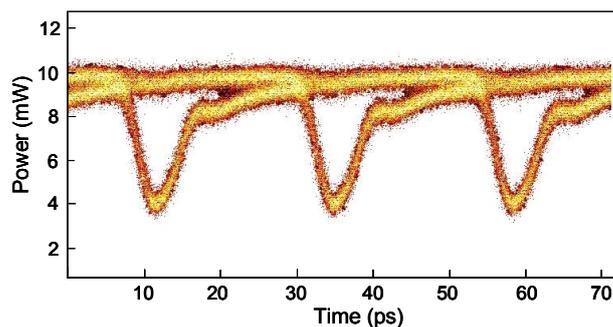
Figure 4.9: Eye diagrams of the cross-gain modulated signal at the SOA output
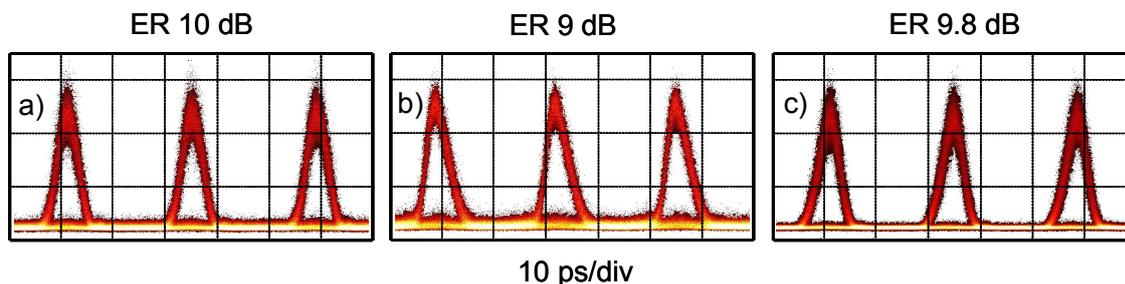
Figure 4.10: Signal eye diagrams at the regenerator input (a), after passing through the SOA (b) and at the regenerator output (SA output) (c)

power of 10 dBm at the SA input. Otherwise, the data signal power of -1 dBm at the coupler input is sufficient to provide an SOA gain compression of about 4 dB. The gain compression is measured on the cross-gain modulated signal at filter 1 output by shifting the filter centred on the assist light wavelength. The eye diagrams of the inverted signal are shown in Figure (4.9). Despite the large domination of ultrafast recovery, the gain does not recover completely within the bit duration because of the slow relaxations due to interband effects. Nevertheless, the observed patterning effect is not critical when the SOA is in a self-saturation because there is no signal inside the SOA during the slow gain recovery.

4.2.2.1   Eye diagrams observations

The eye diagrams of the data signal are observed at the regenerator input and output. They are also observed after each device inside the regenerator. The obtained eye diagrams are displayed in Figure (4.10).

The signal eye diagram after passing through the SOA is observed at Filter 1 output (Figure (4.10(b))). Comparing Figures (4.10(a)) and (4.10(b)) lets appear that the amplitude fluctuations on the 'mark' level are reduced as expected. However, the patterning effects predicted by the gain compression measurement are also confirmed. The amplitude fluctuations on the signal 'space' level increase after passing through the SOA. The signal
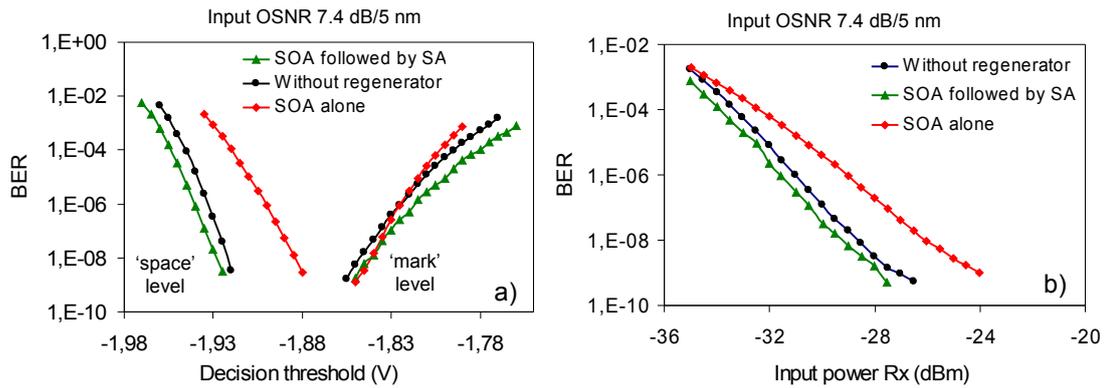
Figure 4.11: BER evolution vs decision threshold (a) and vs Rx input power (b) of data signals at the regenerator input, output and at the SOA output

ER is degraded from 10 dB at the gate input down to 9 dB at the SOA output (the ER measurement error is 0.5 dB). The signal ER measured at the SA output (Figure (4.10(c))) is about 9.8 dB. The signal ER is slightly enhanced by the SA. Especially, the noise compression effect on the 'space' level can be clearly observed. However, the noise degradation on the 'mark' level by the SA is also unavoidable. By observing the signal eye diagrams at the regenerator input and output (Figures (4.10(a)) and (4.10(b))), it is clear that a noise transformation occurred but it also appears difficult to compare the global quality of the two signals. It is clear that the eye diagram measurement can only give a rough estimation of the signal quality. Otherwise, the signal quality changes can be analysed more precisely through BER measurements.

4.2.2.2   Results of BER measurements

The results of the BER measurements are displayed in Figure (4.11). The curves which characterise the optical signal at the regenerator input are plotted first by injecting directly the transmitted data signal to the receiver block (black curves) without the regenerator. The regenerator is then inserted and the BER measurements are performed on the output signal (green curves). At last, to highlight the role of the SA, the SA is removed from the cascade and the BER is measured on the signal delivered at the SOA output (red curves). For all cases, the input OSNR is set at 7.5 dB/5 nm.

The changes of the 'space' and 'mark' level variances are observed on the BER evolutions versus decision threshold (Figure (4.11(a))). On one hand, a noise compression on the signal 'mark' level is performed by passing through the SOA because the red curve is steeper than the black one. On the other hand, on the 'space' level, the noise is strongly amplified. The shape of the red V curve is more closed compared to the reference. The global signal quality is degraded and it is clearly expressed by 2.5 dB penalty at a BER of 10^{-9}. By passing through the SA, the noise of the 'space' level is indeed compressed. The green V curve becomes even slightly more open than the reference V curve. This effect is
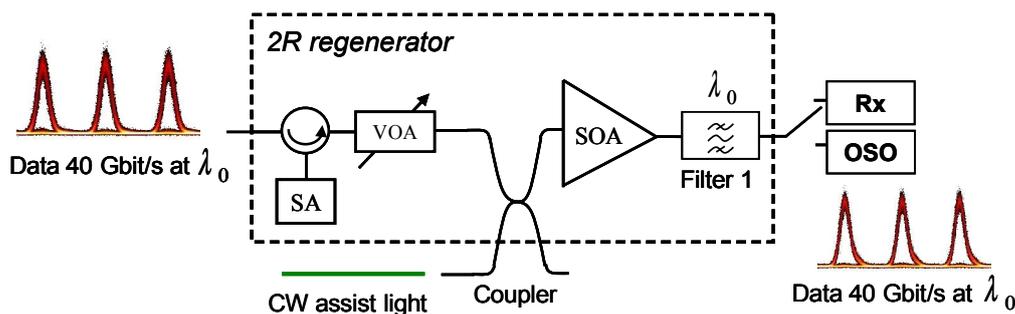
Figure 4.12: Experimental set-up for noise compression assessment of the second regenerator configuration (SA followed by SOA)

certainly due to the signal ER enhancement and the strong absorption offered by the SA. Nevertheless, this signal enhancement is probably insufficient to lead to a significant signal quality improvement. With a sensitivity measurement error of 0.5 dB, the sensitivity curves measured on the signal at the regenerator input and output can be considered as identical.

The noise transformation of the regenerator configuration including the SOA followed by the SA is demonstrated. The noise compressions are illustrated by the reduction of the 'mark' and the 'space' level variances. This could be possible only with the mutual presence of the SOA and the SA. However, the global signal quality is not improved by passing through the regenerator. The main limiting factor of the regenerator performance is the slow SOA response. The patterning effects persist despite the assist light presence and limit the regeneration efficiency. The amplification stage between the two non-linear components also degrades partially the signal OSNR. In the next paragraph, the performance of the regenerator scheme consisting in the SA followed by the SOA will be presented.

4.2.3   Second configuration: SA followed by SOA

The second regenerator scheme consists in the SA followed by the SOA. On one hand, this configuration requires certainly a higher signal power at the gate input compared to the first configuration. Because to obtain the saturation, the required input power for the SA (in order of 8 dBm) is much greater than for the SOA (in order of -15 dBm). However, this is not really a drawback as in most of 2R regenerators the non-linear optical gate is usually preceded by an amplifier. On the other hand, this configuration can be more advantageous than the first one because the SOA does not require high input powers and therefore an amplification stage between the SA and the SOA could be avoided. The signal regeneration capability of the cascade is always assessed in terms of noise compression. The experimental set-up for noise compression assessment is depicted in Figure (4.12).

The experimental set-up is identical to the one presented in Paragraph 4.2.2 except for the regenerator architecture. The transmitted data signal is injected into the SA through the optical circulator. It is then coupled into the SOA via a 3-dB coupler, simultaneously
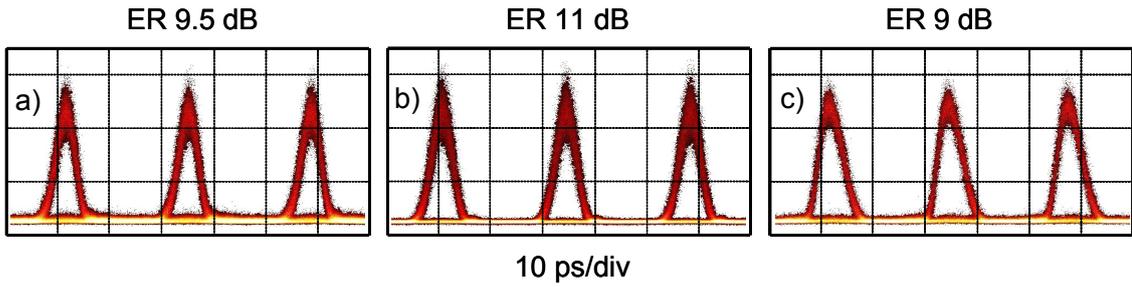
Figure 4.13: Signal eye diagrams at the regenerator input (a), after passing through the SA (b) and at the regenerator output (Filter 1 output) (c)

with the CW assist light. The typical band-pass filter (Filter 1) is used to reject the amplified assist light. A VOA placed between the SA and the coupler controls the signal power at the SOA input. In this experiment, the OSNR measured on the transmitted signal is 8 dB/5 nm. The setting process of the operating condition is also the same as presented in 4.2.2. The three powers (the data signal power at the SA input, the data signal and the assist light powers at the coupler inputs) are adjusted simultaneously to obtain the best signal at the regenerator output. In the experiment, the best signal quality was obtained for the operating conditions presented in Table (4.2).

Data signal power at the coupler input	-1 dBm
Assist light power at the coupler input	11.5 dBm
Data signal power at the SA input	11 dBm

Table 4.2: Operating parameters of the second regenerator configuration (the SA followed by the SOA)

It must be noticed that the operating point of the SOA is the same as in the first regenerator configuration. The SOA gain compression is therefore equal to 4 dB. Otherwise, the data signal power at the SA input is higher than in the first case.

4.2.3.1 Eye diagrams observations

The eye diagrams of the data signal observed at the regenerator input and output are shown in Figures (4.13(a)) and (4.13(c)). They are also observed at the SA output (Figure (4.13(b))).

By comparing Figures (4.13(a)) and (4.13(b)), it appears that the amplitude fluctuations affecting the signal 'space' level with respect to the pulse intensity are clearly reduced by passing through the SA. Moreover, the signal ER is enhanced from 9.5 dB to 11 dB. However, the intensity fluctuation increase on the 'mark' level induced by the SA is not negligible. Following the SA, this signal is injected into the SOA. At the SOA output, the fluctuation on the 'mark' level is significantly reduced without important change on the 'space' level (Figure (4.13(c))). With a measurement error of 0.5 dB, the signal ER could be
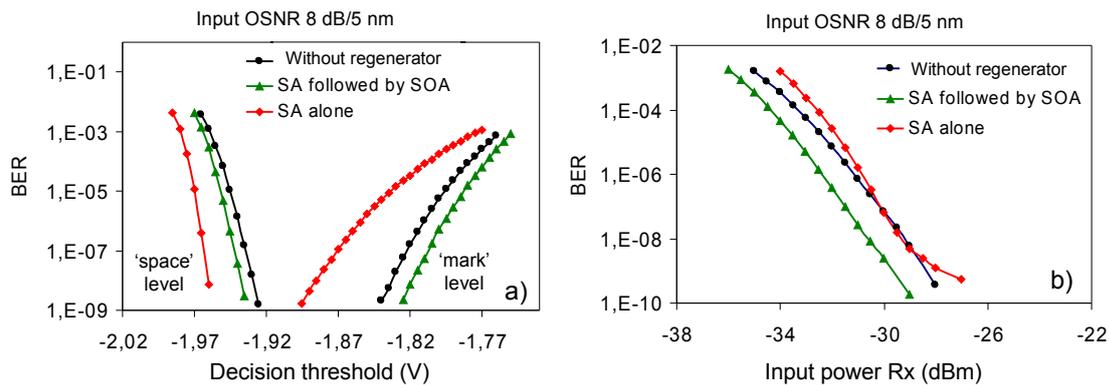
Figure 4.14: BER evolution vs decision threshold (a) and vs Rx input power (b) of data signals at the regenerator input, output and at the SA output

considered as identical at the regenerator input and output (9.5 dB and 9 dB respectively). Otherwise, at the regenerator output, the eye diagrams of the data signal appear much more open than the signal at the regenerator input. Hence, the regenerator performs a noise transformation on the optical data signal. The amplitude noise is clearly compressed. This regenerative effect can be evaluated quantitatively via the BER measurements, as for the first configuration.

4.2.3.2   Results of BER measurements

The results of the BER measurements are displayed in Figure (4.14). The BER curves without regenerator are obtained by measuring the BER on the optical signal at the regenerator input (black curves). The regenerator is then inserted and the BER measurements are performed on the output signal (green curves). At last, to highlight the role of the SOA, the SOA is removed from the cascade and the BER are measured on the signal delivered at the SA output (red curves). For all cases, the input OSNR is set at 8 dB/5 nm.

The changes of the 'space' and 'mark' level variances are clearly observed on the BER evolutions versus decision threshold (Figure (4.14(a))). The noise variances are transformed after each element of the regenerator. By passing through the SA first, the 'space' level variance of the optical signal is strongly reduced. However, the red V curve is more closed in comparison to the reference because the 'mark' level noise is badly increased. Following the SA, the optical signal is injected into the SOA. By passing through the SOA, the impairments caused by the SA on the 'mark' level noise are drastically mitigated. Despite the noise addition on the signal 'space' level caused by the SOA patterning effects, the green V curve is more open than the V curve obtained without regenerator. This indicates that the signal quality is enhanced by passing through the regenerator. The sensitivities curves (Figure (4.14(b))) are used to evaluate the global quality of the different signals. In this case of the degraded transmitted signal (OSNR 8 dB/5 nm), a gain of 1.5 dB at the BER of 10^{-9} on the receiver sensitivity is achieved by inserting the regenerator between the transmitter

and receiver. This last result confirms that the signal quality is indeed enhanced thanks to the SA-SOA cascade. The regenerative capability of the regenerator is thus demonstrated.

The noise transformation of the regenerator scheme consisting in the SA followed by the SOA is illustrated at the bit rate of 40 Gbit/s. The noise compression effect, provided by the regenerator, leads to a signal quality improvement. This quality enhancement is expressed by a gain of 1.5 dB on the receiver sensitivity. It is found that the regenerator constituted of the SOA and the SA exhibits regenerative properties thanks to the complementary non-linearities of the two components. The regenerative effect in the second configuration (the SA followed by the SOA) is better than in the first configuration (the SOA followed by the SA). The ASE power added by the amplification stage, required in the first configuration, was about 10 dBm and could not be neglected. This ASE noise addition degrades the signal OSNR could be a tentative explanation for the performance difference between the two regenerator schemes. At last, the limiting factor of the regenerator for operations at higher bit rates (> 40 Gbit/s) is the SOA response time. It should be noticed also that the SA response time is short enough for a 160 Gbit/s operation. By using an SOA exhibiting shorter gain recovery times such as the long QD SOA (SOA n°5), an operation at 160 Gbit/s of the regenerator based on an SOA-SA cascade can be expected.

4.2.4   Spectrum deformation

The regenerators transform not only the temporal characteristics but also the spectral characteristics of the optical signal. Figure (4.15) depicts the signal spectrum evolutions by passing through the two previously studied regenerator configurations.

It appears that the optical spectrum at the regenerator output exhibits a asymmetry while the signal spectrum at the regenerator input is symmetric. This spectral deformation is due to both non-linear components of the gates. As shown in the numerical study (Chapter 3), the SOAs present a strong gain phase coupling. A gain modulation is always accompanied by a phase modulation which induces chirp on the transmitted optical signal. The phenomenon is observed on the output signal spectrum by a dissymmetry and a shift towards the longer wavelengths. On the other hand, the SA reflectivity spectrum exhibits some selectivity as shown in Figure (4.16). Its bandwidth at half minimum is small (about 5 nm) compared to the SOA bandwidth (about 30 nm). The spectral selectivity of the SA reflectivity spectrum could lead to some signal spectrum deformations. However, Figure (4.15) indicates that the SOA contribution to spectral deformations is dominant. The spectral deformation effects can not be negligible especially when the regenerators are cascaded. After each regenerator, the data signal spectrum is shifted further and further towards the longer wavelengths and slips step by step out of the filters following the SOAs. This last could lead to important signal attenuations and therefore limit the transmission distance.
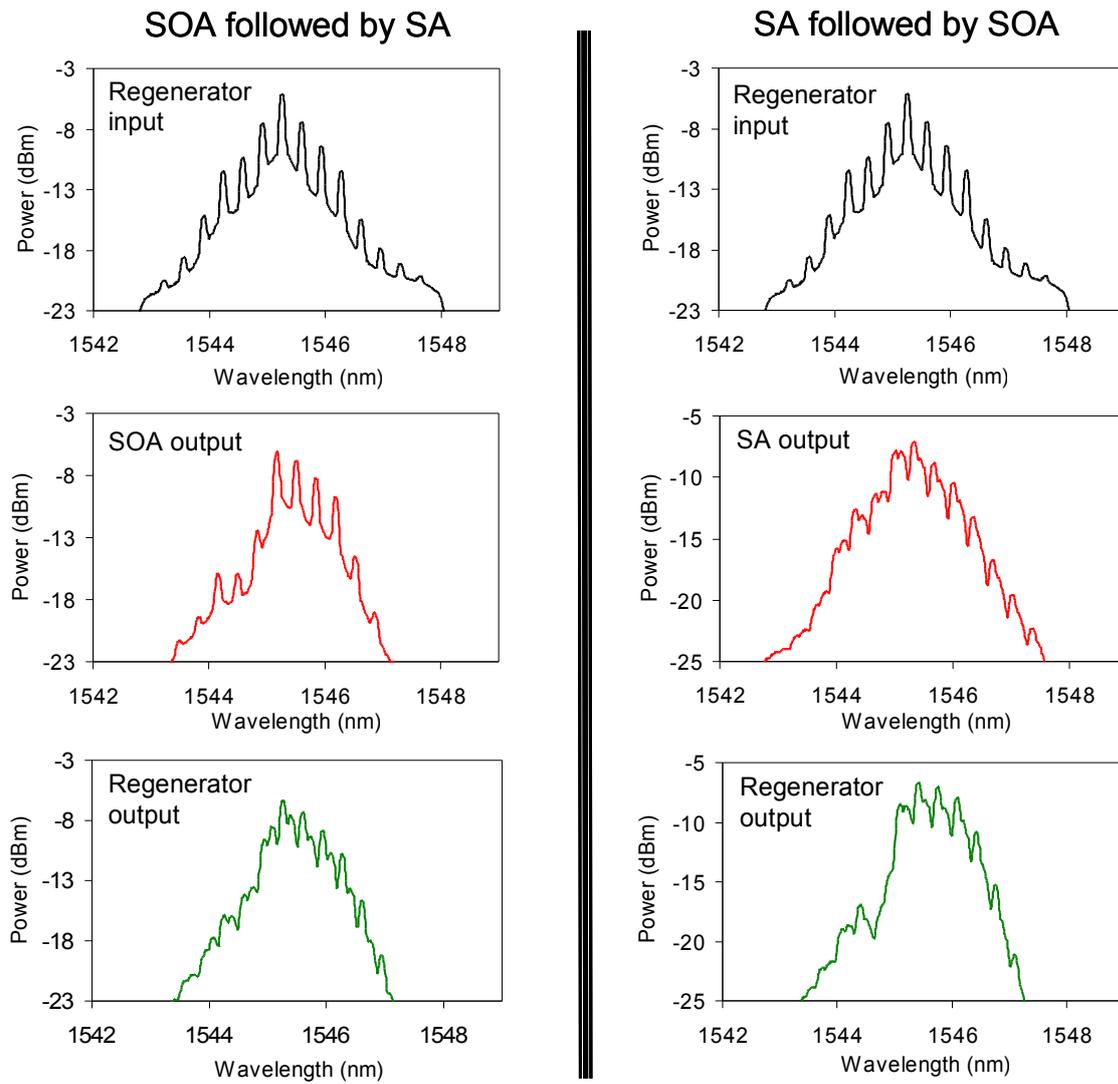
Figure 4.15: Spectrum evolutions of the optical signal passing through the regenerator in the two configurations
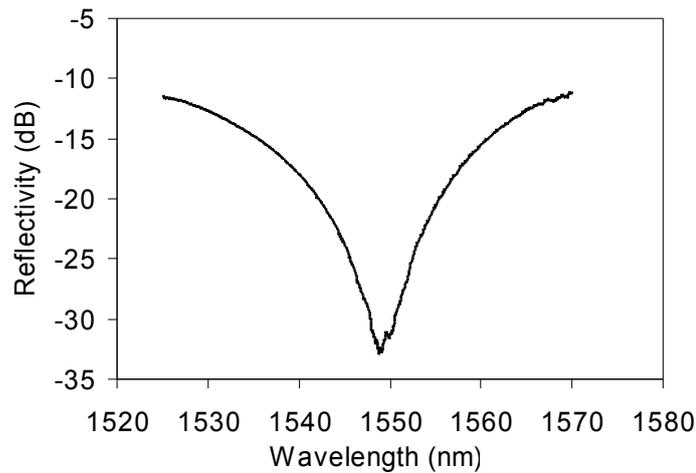
Figure 4.16: Reflectivity spectrum of the SA
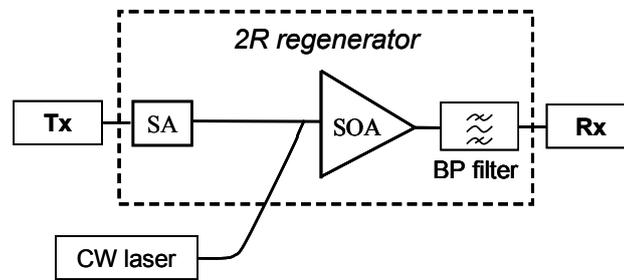
Figure 4.17: Experiment scheme of the numerical study

4.3 Numerical study of the SOA-SA regenerator

4.3.1 Modelling descriptions

In the last section, the regenerative properties of the regenerators based on an SOA-SA cascade are assessed experimentally. It is found that the signal amplitude noise could be compressed by the cascade. However, the long response time of the SOA limits the regenerator operation speed at 40 Gbit/s and the receiver sensitivity gain is limited at 1.5 dB. In this section, the numerical study of the SOA-SA regenerator is presented. The amplitude noise compression performance of the regenerator is investigated for different characteristics of the non-linear elements (SOA and SA). The information provided by the numerical study can be also useful for the device design. The scheme used for the numerical study is based on the experimental set-up and depicted in Figure (4.17).

The SOA model has been developed and presented in Chapter 3. The transmitter Tx emits a 40 Gbit/s RZ signal exhibiting amplitude noise. The pulse duration is set at 4 ps which is consistent with the experimental data signal. The CW laser provides the required assist light for the SOA operation. The BP filter, which is a typical 5-nm flat-top filter, is used to reject the amplified CW light. The receiver Rx allows the signal eye diagrams to be
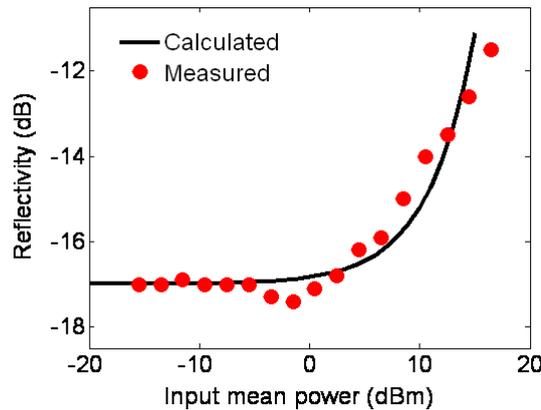
Figure 4.18: Modelled and measured SA reflectivity evolutions versus input power

observed and the BER curves versus decision threshold to be plotted. The model details of the transmitter, the receiver and the BP filter could be found in [115].

For the SA modelling, we propose to adapt the SOA model proposed in [56] by considering that the gain is negative. Such an SOA exhibiting a negative small-signal gain is equivalent to an SA with absorption. Further details of the Agrawal's SOA model are given in Appendix (6.5.3). In order to verify that the SA model could be representative for the SA behaviour, the reflectivity curves versus input power are compared in Figure (4.18). The calculated curve is in good agreement with the measured reflectivity evolution for the input power below 17 dBm. This phenomenological model of SA is adequate for the numerical study of the SOA-SA regenerator.

The parameters of the SOA and SA are summarised in Table (4.3). The SOA parameters, in particularly the interband and intraband life-times, are deduced from the fitting processes presented in Chapter 3. Such an SOA exhibits the static and dynamic behaviours similar to the highly confined bulk based SOA (SOA n°2). The small-signal reflectivity and the saturation energy of the SA model are obtained by fitting the modelled and measured SA reflectivity evolutions versus input power (Figure (4.18)). The SA carrier life-time is the typical value estimated with the experimental measurement by pump-probe experiment.

By adjusting the data signal power and the CW assist light power, the amplitude noise of the transmitted signal could be compressed as shown in Figure (4.19). The OSNR of the transmitted signal was 15 dB/nm.

The signal eye diagrams demonstrate the noise transformation effect of the regenerator (Figures (4.19(a)) and (4.19(b))). The signal eye at the regenerator output is more opened than at the input. The intensity fluctuation on the 'mark' level is reduced from 0.5 unit to 0.4 unit by passing through the regenerator. The noise transformation on the 'space' level could not be observed clearly on the eye diagrams, but it is shown on the BER evolution curves versus decision threshold (Figure (4.19(c))). It appears that the 'space' level variance

SOA	
Active region length	1 mm
Active region width	0.7 μm
Active region thick	0.5 μm
Optical confinement factor	75 %
Material gain coefficient	2.5×10^{-20} m^2
Interband life-time	80 ps
Intraband life-time	1 ps
SA	
Small-signal reflectivity	-17 dB
Saturation energy	0.22 pJ
Carrier life-time	5 ps

Table 4.3: Simulation parameters of SOA (deduced from the fitting processes of Chapter 3) and SA
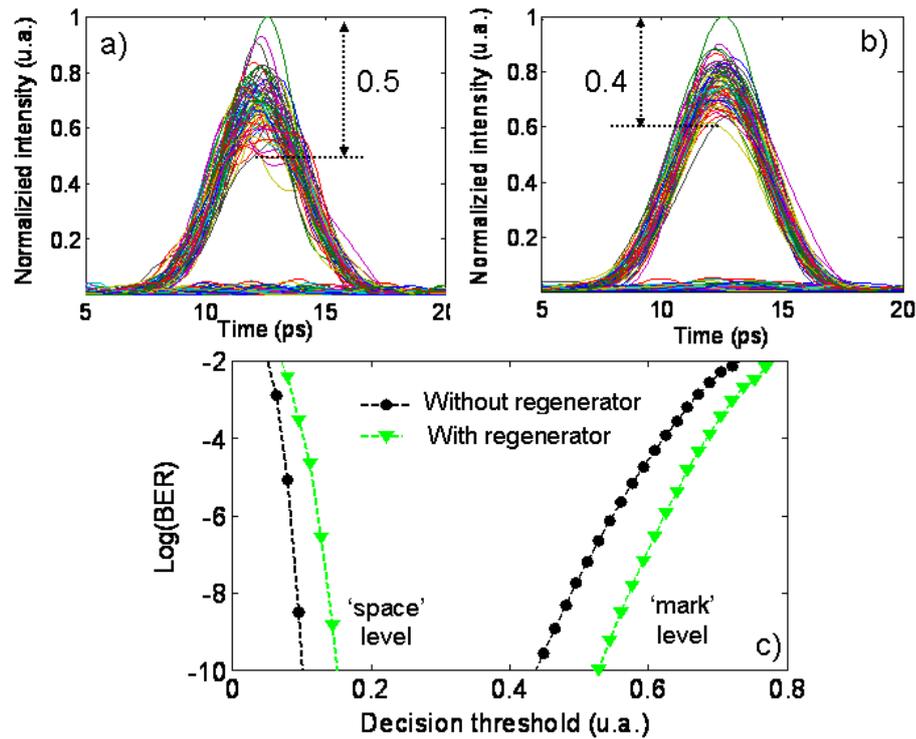
Figure 4.19: Signal eye diagrams at the regenerator input (a) and output (b) and the corresponding BER evolutions versus decision threshold (c), with an OSNR of 15 dB/nm for the transmitted signal
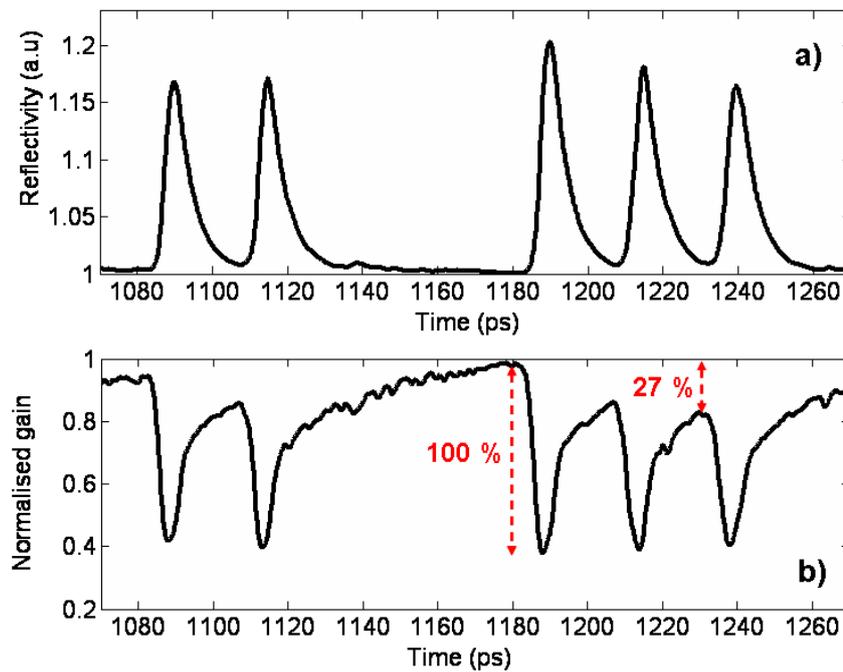
Figure 4.20: SA reflectivity (a) and SOA gain (b) recoveries

of the output signal is greater than of the input signal (transmitted signal). This 'space' level noise 'amplification' is mainly due to the ASE noise and the long response time of the SOA, which results in patterning effects. The explanation is confirmed by observing the SOA gain evolution in time (Figure (4.20).

While the SA reflectivity recovers nearly completely within the bit duration (Figure (4.20(a)), the SOA gain is far from the complete recovery (Figure (4.20(b)). The gain fluctuation amplitude corresponding to the 'space' bits is about 27 % of the maximum gain compression. This strong gain fluctuation for the 'space' bits due to the pattern effect results in the noise amplification on the signal 'space' level.

The numerical results exhibit good agreement with the experimental ones. It is shown that by cascading the SOA n°2 and the SA, the amplitude noise compression could be obtained.

4.3.2   Impact of the SOA response time

If the SOA response time is smaller, it is not only possible to reduce the noise amplification on the 'space' level but also possible to improve the noise compression effect on the 'mark' level by increasing the gain compression. The noise transformation of the cascade could lead to signal quality improvements. The regenerative property of the regenerator based on the SOA-SA cascade is assessed for various response times of the SOA at 40 Gbit/s. All the
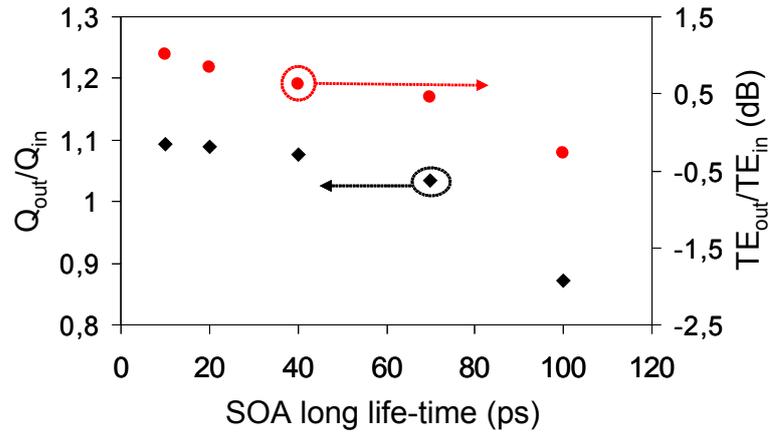
Figure 4.21: Evolutions of 40 Gbit/s signal Q factor (black squares) and of extinction ratio (red circles) for various long life-time of the SOA

parameters of the SOA and SA are identical to those presented in Table 4.3, except for the interband life-time (long life-time) of the SOA. For each case, the data signal and the assist light powers are optimised to obtain the best signal Q factor at the regenerator output. The signal Q factor is calculated by Equation (4-1) and the signal quality improvement is evaluated by comparing the signal Q factor at the regenerator input and output. The results are displayed in Figure (4.21).

$$Q = \frac{V_1 - V_0}{\sigma_1 + \sigma_0} \tag{4-1}$$

It is shown that the noise compression effect is obtained if the long life-time of the SOA is below 80 ps ($Q_{out}/Q_{in} > 1$). Exceeding this 80 ps long life-time constant, the reshaping effect of the regenerator is not efficient anymore as demonstrated by the rapidly Q factor drop of the output signal. When the SOA long life-time decreases, not only the output signal Q factor increases but also the extinction ratio does. The output ER enhancement is due to the fact that SA could be saturated deeper, thus the signal ER improvement is stronger. The 'mark' level noise amplification induced by the SA could be compensated by the deeply saturated SOA without introducing excessive patterning effect. The Q factor increase is due mainly to the reduction of the patterning effect caused by the SOA response time. The patterning effect reduction resulted from the SOA long life-time decrease is illustrated clearly on the output signal eye diagrams shown in Figure (4.22).

It should be noticed that a long life-time of 20 ps could appear not realistic for a bulk-based SOA. However, it is possible to obtain such rapid dynamics with a quantum-dot based ultralong SOA. The long QD SOA (SOA n°5) is shown to be able to recover within 10 ps at its maximal bias current. Nevertheless, for an SOA long life-time of 40 ps, the Q_{out}/Q_{in} ratio is always greater than 1 and the ER is enhanced 0.6 dB.
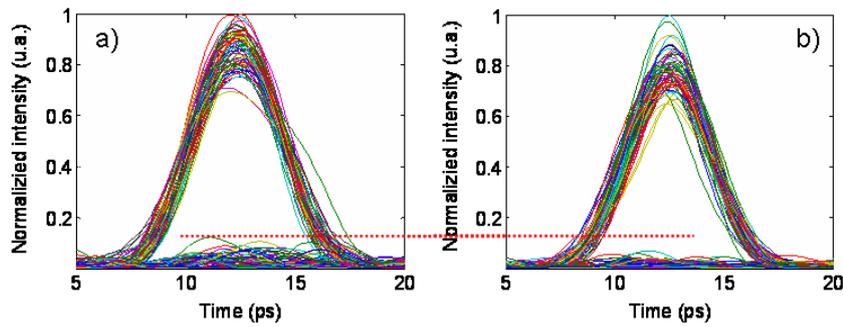
Figure 4.22: Noise reduction on the 'space' level of the output signal when the SOA long life-time decreases from 80 ps (a) to 20 ps (b)
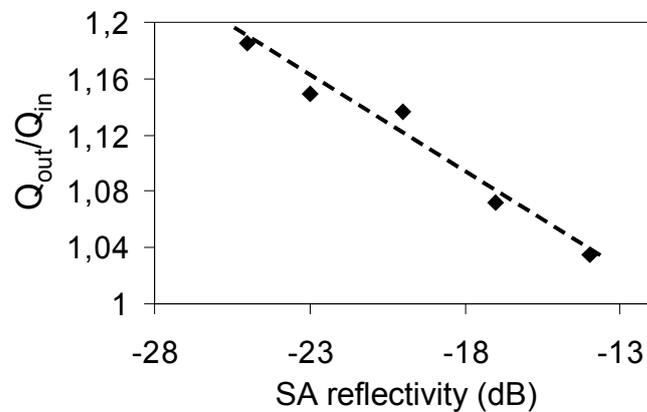
Figure 4.23: Evolution of 40 Gbit/s signal Q factor versus SA small-signal reflectivity

4.3.3   Impact of the SA reflectivity

On the contrary to the SOA, the SA response time is not a limiting factor for the cascade reshaping performance. The estimated SA time response (5 ps) is short enough such that the reflectivity recovers within the bit duration at 40 Gbit/s (Figure (4.20(a)). On the other hand, the SA reflectivity could be changed by modifying the front mirror reflectivity [113]. The influence of the SA reflectivity to the regenerator reshaping performance is investigated. All the parameters of the SOA and SA are identical to those presented in Table 4.3, except for the small-signal reflectivity of the SA. The signal quality improvement by passing through the regenerator is estimated for different SA reflectivity. The results are summarised in Figure (4.23).

It is shown that the output signal quality could be enhanced by decreasing the SA reflectivity. The Q_{out}/Q_{in} ratio increases from 1.04 to nearly 1.2 when the SA small-signal reflectivity decreases from -14 dB to -25 dB. For the same input signal, the BER evolutions versus the decision threshold of the output signal are plotted in Figure (4.24) for the two cases corresponding to the different SA reflectivities. The more opened BER curves (red curves) corresponding to the lower SA reflectivity indicates that the noise compression effect
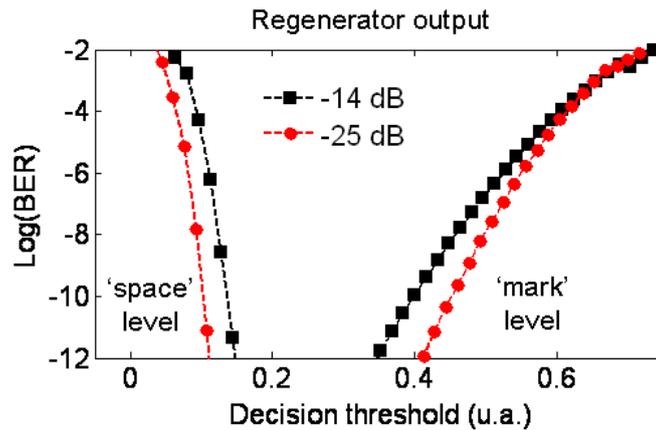
Figure 4.24: BER evolutions of the regenerator output signal for different SA reflectivities: -14 dB (black squares) and -25 dB (red circles)

provided by the regenerator are stronger in that case.

4.4 Chapter summary

In this chapter, the experimental and numerical investigations of reshaping processes of the SOA based regenerators were presented.

The first section was dedicated to illustrate the power equalisation capability of the SOA. The amplitude noise reduction obtained on the signal 'mark' level thanks to the SOA gain saturation was demonstrated. It was found that a noise compression efficiency-patterning effects trade-off has to be considered because of the slow dynamics of the SOA. At 40 Gbit/s, a gain compression of 3 dB of the SOA appears as the best choice. It was also shown that the non-linear optical gate based on the SOA in self-saturation regime degrades the signal extinction ratio and the amplitude noise on the 'space' level. Then, the SOA must be associated with another device to constitute a non-linear optical gate exhibiting a complete reshaping capability and then usable for 2R regeneration functions.

The regenerative properties of the two regenerator schemes based on the SOA-SA cascades were assessed at 40 Gbit/s and the results have been discussed in the second section. The first configuration includes the SOA followed by the SA. The noise transformation effects of each non-linear component were observed. However, the regenerator does not reduce efficiently the amplitude noise. A limiting factor is the OSNR degradation caused by the intermediate amplification stage which is required to provide necessary signal powers to the SA. The second regenerator configuration consists in the SA followed by the SOA. This regenerator scheme demonstrated an efficient amplitude noise reduction and allowed a gain of 1.5 dB at a BER of 10^{-9} on the receiver sensitivity. These results could be obtained thanks to the complementary characteristic functions of the SOA and the SA. In this

case, the SOA was placed at the second position of the cascade and thus no intermediate amplification stage was necessary because the SOA does not require high input signal powers. Indeed, the regenerator based on the SA followed by the SOA exhibit the reshaping capability for 2R regeneration functions. This scheme is an integrable solution with a low energy consumption. The signal wavelength preservation is also one of its main advantages.

The numerical study presented in the third section confirms the regenerative property of the regenerator scheme based on SOA-SA cascade. The numerical investigation demonstrated that if the SOA long life-time could be shortened, both quality factor and extinction ratio of the output signal could be improved. On the other words, the reshaping capability of the regenerator could be enhanced. Concerning the SA, an increase of the small-signal reflectivity could lead also to more efficient noise compression of the regenerator.

There are still some challenges for this 2R regenerator solution. The proposed regenerator scheme does not provide a significant ER improvement. And the other challenge may be the operating bit rate increase. The main factor limiting the SA-SOA cascade operations at bit rates higher than 40 Gbit/s is the long gain recovery time of the SOA. This response time is in order of 20 ps. Operations of this regenerator scheme at 160 Gbit/s will not be possible. Otherwise, the SA response time (5 ps) is even shorter than the bit duration (6.3 ps) at 160 Gbit/s. It could be associated with the long QD SOAs to provide promising solutions at this data rate. We remind that the long QD SOA exhibit faster gain dynamics than the bulk SOA used in these experiments. The effective gain recovery time was demonstrated as short as 3 ps when the filter following the SOA was slightly blue shifted. Moreover, QD SOAs promise lower gain phase couplings [116] compared to bulk based SOAs. This indicates that the additional chirp induced by the SOA, and thus the signal spectrum deformation, can be decreased by using QD structures. Some efforts still have to be made on the long QD SOA to reduce its gain ripple levels and to make the noise compression experiment possible.

At last, it should be noted that the noise compression capability of the regenerator was assessed only in back-to-back experiments. Further investigations should be considered to demonstrate that the regenerator performance is sufficient to maintain signal quality over long distances by preventing from noise and distortion accumulation. To ensure the SOA-SA cascade will constitute a good regenerator, it has to be assessed in re-circulating loop experiments to illustrate its efficiency in a transmission link and its cascadability. In particular, the signal spectrum deformation shown in Paragraph 4.2.4 may cause impairments to the signal quality when accumulating after long transmission fibre links.

Part II

All-Optical Clock Recovery

Introduction on all-optical clock recovery

As discussed in the first chapter, the transmitted optical signal suffers not only from random intensity fluctuations but also from random deviation of pulse position during the propagation. The 3R regeneration is elaborated to overcome all these signal degradations by associating a 2R device with a retiming function. 3R regenerators with retiming capability require clock extraction from the incoming data signal. The capacity demand growth of optical networks is irresistible and will reach electronic limitations. Semiconductor all-optical 3R regenerators promise ultra-high bit rate operation, full integration possibility and power consumption reduction. They are therefore an attractive choice to relieve physical limitations, to improve the transmission distance and to achieve better performance/cost trade-off. Furthermore, all-optical solutions offer a transparency for the optical networks. All-Optical Clock Recovery (OCR) is one of principal sub-functions of a full all-optical 3R regenerator.

The Clock Recovery (CR) function is well known in the electronic domain. Electrical CRs are usually based on a filter combined with a phase-locked loop. Nowadays, the electronic CR is well mastered up to the bit rate of 40 Gbit/s. In the last recent years, strong efforts were made to develop all-optical CR functions which promise a lower cost, a higher integration capacity and a better network transparency. In a 3R regenerator, the CR task is to emit an optical pulse stream. It has to be synchronised to the incoming data stream and match the demands for transmission over the next fibre link. High performance of all-optical CR was successfully demonstrated at 40 Gbit/s [117], [118] and at 160 Gbit/s for demultiplexing in OTDM system [119].

This second part of the manuscript is dedicated to the study of all-optical clock recovery solutions based on self-pulsating semiconductor lasers. These CR devices could be associated with a 2R optical non-linear gate to constitute a 3R regenerator. The presented work is also a part of the French national project ROTOR. The project's principal goal was to demonstrate the feasibility of simple and robust all-optical CRs operating at the bit rate of 43 Gbit/s. Thanks to the collaboration within the project, we could benefit from two Self-Pulsating (SP) lasers based on bulk and quantum-dot materials fabricated by our

partner: Alcatel-Lucent Thales III-V Lab.

Chapter 5 introduces firstly the different roles of CR function in transmission systems. All-optical clock recovery based on self-pulsating semiconductor lasers is then described in detail. The principle of the clock recovery technique is presented. At last, its advantages and limitations are discussed.

The first section of Chapter 6 presents the characterisation and performance evaluation of a clock recovery through different aspects. In this section, we present for the first time a novel characterisation technique called remodulation. This original experiment developed in our laboratory allowed studies on various OCR configurations [120], [121], [13], [122], [123], [124]. Most of studies on OCR functions in the thesis exploit this original characterisation scheme which is suitable for regeneration applications.

A performance comparison of OCR devices based on a bulk and a quantum-dot SP lasers has been carried out. The results are presented in Section 6.2. In Section 6.3, a solution consisting in using of a pre-filtering stage in front of the bulk-SP laser was proposed in order to improve the recovered clock quality. The performance enhancement is demonstrated via bit error rate measurements. In Section 6.4, the polarisation sensitivity assessment of different OCRs is investigated. At last, a primary study on OCR resistance to Polarisation Mode Dispersion is reported in Section 6.5.

Chapter 5

All-optical clock recovery for 3R regeneration

5.1 Clock recovery

In optical networks, clock recovery is a key function among the functional blocks such as receiver, in-line repeaters and demultiplexers in future OTDM systems. The role of the Clock Recovery (CR) function in these elements is extracting a stable clock which is synchronised (in frequency and in phase) to the incoming data signal and ideally with a minimal timing jitter.

5.1.1 Role of clock recovery function in optical networks

In a receiver, CRs provide a time reference to the flip-flop decision gate. Decision of value 0 or 1 of a bit is made at an accurate moment. The decisions have to be done in a regular rhythm, and duration between two successive decisions has to be equal to the bit duration. If the repetition rates of the data signal and of the flip-flop clock are different, the decision moment slips step by step far away from the optimal sampling time. This deviation introduces errors and the detection gives false information. Therefore the clock which is used for receiver time reference must be derived accurately from the received signal itself.

In future OTDM systems, temporal demultiplexing requires a CR to extract a base rate clock B/N from a transmitted OTDM data signal which is at a line rate B. The demultiplexing function allows isolating each base data stream from N interleaved streams in the data flow. For example, it is possible to extract a 40 GHz clock from an OTDM signal at bit rates of 160 Gbit/s and 320 Gbit/s [125], [126]. The CR must provide a low timing jitter clock which is synchronised to the incoming data signal. Afterwards, the recovered clock is distributed to demultiplexers, routers, channel selectors, and receivers. In OTDM systems, the aggregate data rate exceeds the state-of-the-art speed limit of electronic components, all-optical CR offers a novel solution to provide retiming signals and perform

high-speed switching.

In ponit-to-point transmission link of backbone and metropolitan networks, CR is a fundamental requirement of in-line repeaters such as 3R regenerators. We define two classes of 3R regenerators: 'Data driven' 3R regenerator and 'Synchronous modulation' 3R regenerator. In the first configuration, a non-linear optical gate carries out the reshaping task after the re-amplifying stage. The optical clock delivered by the CR block is then modulated through the non-linear optical gate to provide a 3R regenerated signal. The final regenerated signal is at the recovered clock wavelength. A wavelength conversion is performed in the retiming process. Therefore, the function of OCR in a 'Data driven' 3R regenerator is not restricted only to the retiming task but partially contributes also to the reshaping task. The pulse characteristics of the regenerated signal are defined by the recovered clock pulses. In this case, the wavelength, chirp characteristics and pulse duration of the extracted clock have to comply with the transmission requirements. In a 'Synchronous modulation' 3R regenerator, the data are synchronously modulated through an intensity or a phase modulator which is driven by the recovered clock [127]. No wavelength conversion takes place through the retiming process. In both 3R regenerator configurations, the regenerated data signal exhibits a low timing jitter. Signal distortions are corrected and the data signal could be transmitted further.

5.1.2   Different techniques for clock extraction

We can classify CR techniques in three categories according to their operating principles: spectral filtering technique, phase-locked loop technique and injection locking in oscillating systems without retroaction. In 3R applications, the PLL technique is rarely used because of its complexity. On the other hand, the filtering technique and injection locking in oscillating systems could be exploited in both 'Data driven' and 'Synchronous modulation' 3R regenerators [128], [41], [120], [12]. For each technique, there are also a lot of sophisticated approaches which exploit optoelectronic components only, optical components only, or mixing of both.

5.1.2.1   Filtering technique

Spectral filtering seems to be the simplest technique for CR function in terms of physical principles. It requires also few components. If the data signal spectrum presents a spectral line at the clock frequency, it is then possible to extract a clock signal by using a simple filter.

In optical networks, electronic approaches require an O/E interface, which is usually a high-speed photodiode followed by a high-Q filter. The electrical filter must be narrow and centred on the estimated clock frequency of the transmitter. Thanks to remarkable developments in electronic domain, optoelectronic CRs can operate up to the bit rate of 40 Gbit/s. A 10 GHz clock was extracted from both 40 Gbit/s NRZ and DPSK signals [129].
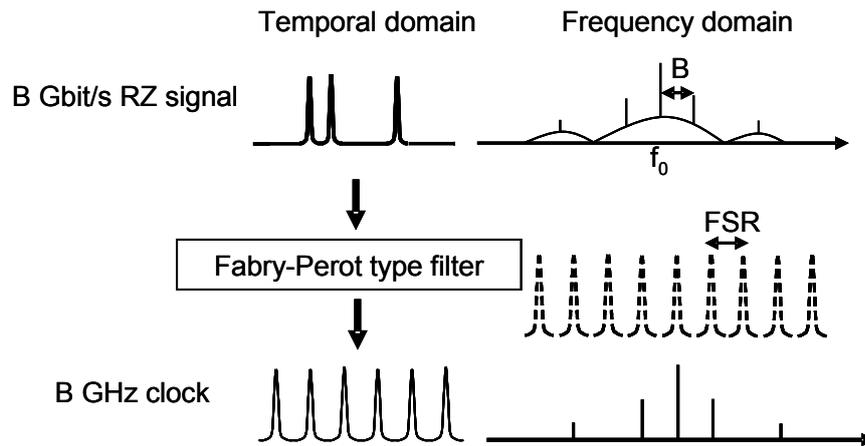
Figure 5.1: Operating principle of an optical CR based on spectral line filtering technique

Main advantages of the electrical filtering technique are their simplicity, wavelength and polarization independences. However, some drawbacks are also inevitable. As the filter centre is fixed on the transmitter clock frequency, the technique is not bit rate flexible. In addition, it is unable to recover directly the clock from a binary NRZ signal which does not exhibit any spectral line at the clock frequency. Moreover, even if this technique requires few components, CR operating at higher bit rate is not simple to implement because high-speed photodiode and high-Q electrical filter are complex and expensive.

An alternative solution to overcome the speed limitation of electronic components is optical filtering. This technique relies on the same principles as the electrical filtering except that the spectral line extraction is realized in optical domain. The optical filter could be an optical resonator exhibiting a Free Spectral Range (FSR) which is equal to the incoming signal rate. Such optical CR scheme was published by [130] under the name of 'optical tank circuit'. In this work, CRs at 2 Gbit/s using a confocal Fabry-Perot type tank circuit and at 324 Mbit/s using a fibre ring tank circuit were demonstrated. Later, operations at 10 Gbit/s and 40 Gbit/s were achieved thanks to a simple narrow filter [131] with wavelength tunability. Some other configurations with a Fabry-Perot filter assisted by an SOA [132], [133], [134] were also reported. CR schemes based on a Fabry-Perot etalon associated to a non-linear high-speed power equaliser gate show excellent capture times for packet traffic operation [135], [136].

All-optical components such as Fabry-Perot type filters or fibre ring resonators could be generally called 'periodic optical filters' according to their periodic transfer functions. Figure (5.1) describes the operating principle of a clock extraction process using optical spectral line filtering technique.

An optical data signal generated from a RZ intensity modulation consists of a continuous spectrum and discrete lines. The optical spectrum is centred on the optical carrier frequency f_0 and exhibits spectral lines at $f_0 \pm B$, where B denotes the transmitter clock frequency. All-optical CR is achieved by extracting the discrete lines at $f_0 \pm B$ and f_0. Result of the
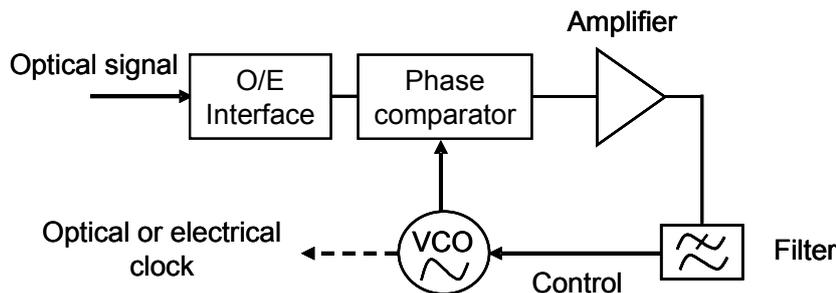
Figure 5.2: Basic structure of a conventinal phase-locked loop for CR

filtering process is an optical clock at the same wavelength as the incoming optical signal and at the same frequency as the transmitter clock. The three following conditions have to be satisfied: one of the filter resonance peaks superimposes on the optical carrier frequency, the optical filter FSR is equal to the transmitter clock rate and the optical carrier linewidth is narrower than the resonator bandwidth.

The first advantage of the optical solution is the transparency for optical networks. The second advantage is that optical CRs allow operation at ultrahigh bit rates which could not be achieved by using only optoelectronic components. This high-speed operation possibility results from the nature of the key component: optical filters.

In a CR based on optical filtering, the frequency drift of a resonance peak away from the optical carrier and filter finesse are crucial parameters which determine the CR performance. Thus, main limiting factor of the optical filtering technique is the requirement of high finesse filters. Besides, the technique suffers also from strong wavelength, polarisation and sequence length dependences [137]. Wavelength dispersion which causes irregular resonance peak intervals and temperature regulation should be also taken into account.

At last, the first CR scheme based on optical spectral filtering operating with multi-channels and at multi-rates should be referred [138]. The CR scheme consists of a birefringent resonator and a polarizer. Proof-of-principle experiment was demonstrated for 21 simultaneous channels including 20 data streams at 10 Gbit/s and one at 40 Gbit/s. This solution opens a promising alternative for dense WDM parallel-optical signal processing.

5.1.2.2 Phase-locked loop technique

Phase-locked loop (PLL) is also largely used for CR function thanks to its reliability. A PLL allows modulation frequency extraction from a data signal. In general, a PLL consists of a phase comparator, an amplifier, a filter and a local voltage-controlled oscillator (VCO). The basic structure of a conventional PLL is shown in Figure (5.2). When the input data stream is an optical signal, an O/E interface is necessary and it is usually a fast photodiode. The electrical signal delivered by the photodiode is then injected to the phase comparator.

The basic idea is that the electrical signal delivered by the photodiode beats with the

low-rate clock signal delivered by the local oscillator through the high-speed phase comparator. The produced signal is a slowly varying signal which is proportional to the phase difference between the local clock and data stream. This signal is then fed back (after having been amplified and filtered) to the VCO. The retroaction allows locking the VCO in phase with the incoming signal clock. In general, parameters of amplification and filtering stages determine the loop operating range, the locking characteristics and the residual phase mismatch between input and output signals. The PLL speed is determined mainly by the photodiode and the phase comparator. A CR based on a PLL using entirely electronic components was successfully demonstrated for 10 GHz clock extraction at an ultrahigh bit rate of 100 Gbit/s [139].

To achieve higher bit rates, speed limitation of O/E interface and especially of the electrical phase comparator can be overcome by using optical phase comparators. Response times of non-linear optical processes usually used in phase comparators are much shorter than those of electrical processes. There is a huge number of optical and optoelectronic PLL configurations. The most considered optical components in PLL based CRs are ElectroAbsorption Modulators (EAM), Semiconductor Optical Amplifiers (SOA) and also Lithium Niobate waveguides [140]. These components could be used as O/E interfaces or/and as ultrahigh-speed phase comparators. PLLs using EAM as phase comparator allowed realisation of a CR operating at 160 Gbit/s [141] and up to 320 Gbit/s [125]. Both experiments reported excellent timing jitters below 300 fs. SOA based PLLs offer a lot of sophisticated CR schemes [142], [143], [144], [126]. Most of them exploit four-wave-mixing process, cross gain and cross phase modulations and interferometric configurations. A SOA based PLL allowed to recover clock for a 640 Gbit/s lab transmission and a 320 Gbit/s field trial transmission with high timing jitter performance [126].

CR processes based on PLLs are well known for their high stability and high recovered clock quality characterised by sub picoseconds timing jitters. Jitter values below 300 fs (in the frequency range from 100 Hz to 10 MHz) are currently obtained with CRs using the PLL technique [143], [145], [140], [126]. Beside these advantages, complexity is considered as the greatest drawback of the technique. Moreover, PLL based CR functions require in general a long time for synchronization to the data stream. This last inconvenient make them not suitable for short optical packet traffic.

5.1.2.3 Injection locking in oscillating systems without retroaction

Another solution for CR function is using oscillating systems which could be synchronized to an injected optical signal without retroaction. Energy injection from an external source into an oscillator can lock the last one onto the referent source. This synchronization capability of oscillators has been largely studied in electronics and recently extensively investigated in the optical domain. The goals are not only the deployment of broadband wireless technology but also the bit rate rising in long and ultralong haul transmissions. Oscillating systems

consist of electronic or optical components or both.

Among electronic components, heterojunction bipolar phototransistor should be considered a good candidate. A CR consisting in direct optical signal injection into a self-oscillating phototransistor was proposed [146]. In this work, a 10 GHz electrical clock was extracted from 10 Gbit/s and 40 Gbit/s signals. Error-free performance at 10 Gbit/s could be achieved. EAM based ring resonator is another solution which offers compact and stable CR devices with integration possibility. Operation at bit rate of 40 Gbit/s was also demonstrated [147]. However, the reported timing jitter of about 500 fs is a poor performance in comparison to the state-of-the-art of CR devices.

Among optical oscillating systems for CR, leading roles should be distributed to SP multi-sections lasers [148], [149], [117] and mode locked lasers [150], [151], [118]. The pulsating frequency of these lasers could be locked by injecting an optical data stream. The injected signal rate must be nearby the free pulsating frequency of the laser or a multiple of this frequency. Some CR schemes using mode-locked fibre ring lasers were investigated [152], [153], [154] and ultrahigh-speed operation at 160 Gbit/s was achieved [155]. Simultaneous CR of several WDM channels at 10 Gbit/s was successfully demonstrated [156] by using a CR module in actively-mode-locked fibre ring laser configuration.

OCR schemes using fibre ring lasers can give high intensity pulse streams and large wavelength tuning ranges for the incoming data signal [154] Polarisation insensitive circuit could be also obtained with the fibre ring laser approach. On the other hand, the timing jitter of the recovered clock could be easily degraded by environmental perturbations along the fibre cavity length. Cavity stabilisation was investigated to resolve this problem [153] but the complex stabilisation circuit is an obstacle for applications in real communication systems. Another CR based on the fibre ring laser demonstrated good performances: operation at ultrahigh bit rate of 160 Gbit/s, locking range of 5 MHz and recovered clock timing jitter below 200 fs [155]. However, this timing jitter could be achieved only with assistance of a post electrical signal processing. Therefore, the transparency is not assured and this solution is not an appropriate option for all-optical 3R regeneration applications.

In the context of CR development for all-optical 3R regenerators, SP multi-sections lasers and mode locked lasers based on semiconductor technology appears as the most promising candidates. Integration potential, simple deployment and high bit rate operation are indisputable virtues of CR functions using semiconductor lasers. Operating principle, advantages and also challenges of all-optical CR devices using this technology are presented in Section 5.2.

5.2 Solution based on self-pulsating semiconductor lasers

All-optical clock recoveries based on SP semiconductor lasers attract firstly for their integration potential, low power consumption and deployment simplicity for full optical 3R regeneration applications.

5.2.1 Operation principle

Self-pulsations have been observed in various laser types such as Fabry-Perot, DFB, and DBR lasers. These lasers provide optical power which varies spontaneously and periodically without bias current modulation. They are so called self-pulsating lasers. The self-pulsation results from the laser dynamics. In a simple view, if two oscillating modes of the cavity exhibit close threshold gains, a mode competition is then established. In the active region, beating of the two modes is produced at the frequency which corresponds to the frequency difference. Gain and index of the active region are then modulated at this beating rate and the modulation result in self-pulsation. An optical clock signal is produced. At high beating frequencies (upper 100 GHz), the self-pulsation phenomenon could not be explained only by the dynamics of intraband effects any more. But the four-wave-mixing (FWM) should be also considered.

It is demonstrated that injection of a modulated optical signal into a SP laser can lead to a synchronisation of the generated clock to the injected signal. Locking mechanism relies on gain and index modulations created by the external optical signal within the active region. If the gain spectrum is homogeneously broadened, then the gain of each mode is modulated exactly at the same frequency. Modulation spectral lines of each mode appear. If the clock frequency of the injected signal is equal to the laser Free Spectral Range (FSR) then the modulation lines and the laser longitudinal modes overlay and synchronisation takes place. Operation of an OCR scheme based on SP laser is described in Figure (5.3).

Simple OCR device could be constituted of a SP laser, an optical circulator (OC) and an optical filter. The incoming data signal is injected into the laser via the OC. The optical filter is placed at the circulator output to select clock signal generated by the SP laser. When the SP laser is not synchronised to the incoming data, the OCR is in unlocked regime. In that case, temporal waveform and electrical spectrum of the detected output signal take arbitrary forms as shown in Figure (5.3 (a)). No clear pulse stream is observed on the oscilloscope. The spectral lines at the clock frequency of the data signal and at the free pulsating frequency of the laser are separated in the electrical spectrum. By adjusting the operation parameters, the SP laser synchronisation to the incoming data signal could be achieved and the OCR function is now in locked regime. In that case, the laser emits an optical clock which is in phase with the injected signal and at the transmitter clock frequency. In other words, the signal clock is recovered. In general, we observe a clear clock signal on oscilloscope and only one spectral line in the electrical RF spectrum as shown in Figure (5.3 (b)) (case of a quantum-dot based SP laser).

5.2.2 Advantages and limitations

Besides integration potential, low power consumption, deployment simplicity and high bit rate operation, OCR devices based on SP semiconductor lasers attract also a lot of investigations for other interesting features: pulsation frequency tuning possibility, ultrafast
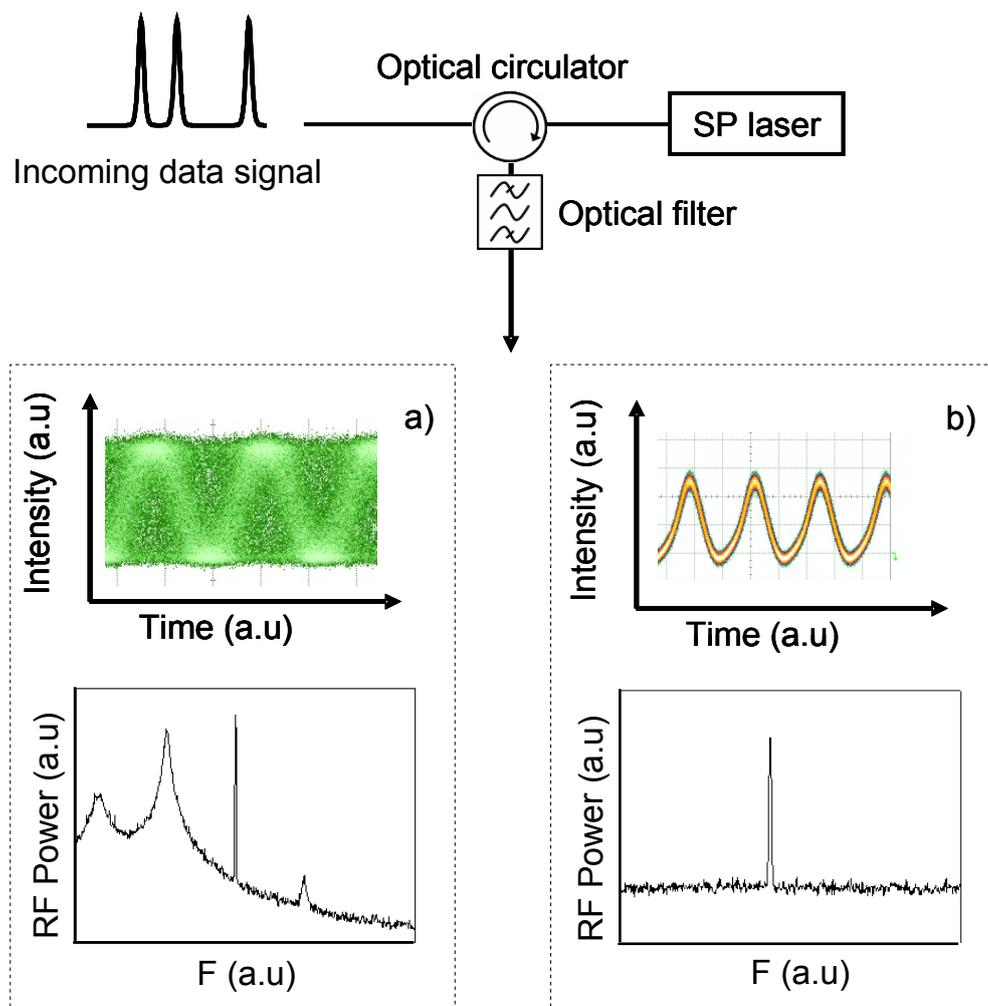
Figure 5.3: Operation of an OCR using SP laser in unlocked regime (a) and locked regime (b)

locking and polarisation insensitivity [148], [128], [41].

The first CR function operating at 35 Gbit/s and totally integrated on chip was demonstrated [157]. An SP laser based CR was performed at 80 Gbit/s with predicted operations at 160 Gbit/s and even higher [158]. Bit rate flexibility is not available with CRs based on phase-locked loop or spectral filtering. On the contrary, SP lasers offer continuous frequency tuning possibility via driving DC currents. An SP laser based OCR was reported by [148] with a frequency range from 3 to 5.2 GHz. This range was enlarged later from 10 to 40 GHz to cover different SDH bit rates [128] and from 25 to 82 GHz [158]. Bit rate flexible 3R regenerators become possible thanks to optical CR based on SP lasers.

A new challenge for CR functions is arising from the future asynchronous networks. In such system, clock extraction device has to be able to recover the signal clock packet by packet. This characteristic leads to requirement of ultrafast synchronisation. Some CR configurations based on SP lasers were proven compatible with asynchronous packet traffic thanks to short locking times of few nanoseconds [128], [159]. We remind one more time that ultrafast synchronisation to asynchronous data packets is a real problem for electronics.

Wavelength and polarization insensitivity will make a CR device ideal for all-optical 3R regeneration. In optical transmission system, the CR function should be operational independently from the wavelength of the incoming signal. SP laser based CRs can offer operating wavelength range covering entirely the C band for the incoming optical signal [149], [160].

At last, a key quality criterion of an OCR device is the timing jitter of the recovered clock. A lot of technological efforts have been and are carried out to achieve SP lasers delivering high quality clock and being compatible with telecommunications standards. RMS (root-mean square) timing jitters of an extracted clock less than 300 fs were obtained with SP semiconductor lasers [161], [162]. These results satisfy jitter performance required for 160 Gbit/s operations. New generation of SP lasers based on quantum-dot technology allows new CR perspectives. The first CR function based on a quantum-dot Fabry-Perot SP laser was reported by [118] at bit rate of 40 Gbit/s. Thanks to high spectral purity of the quantum-dot laser, CR function exhibits an excellent timing jitter suppression effect. A jitter reduction from 1.37 ps on the input signal to 310 fs on the recovered clock was reported. Moreover, another OCR scheme based on the same component type was demonstrated compatible with multi-data rates operations [13]. Low sensitivity to input chromatic dispersion and optical noise were also reported [121], [163]. To overcome the intrinsic polarisation sensitivity of quantum-dot structures, a solution consisting in placing a bulk based DBR laser in front of the QD laser has been proposed [164]. The tandem inherits polarisation insensitive characteristic of the bulk laser and the excellent jitter filtering efficiency of the QD laser [164], [123]. This CR scheme was used for a 3R regenerator in synchronous modulation configuration. Cascadability assessment in re-circulating loop showed a strong transmission distance enhancement thanks to the retiming function [12].

CR solutions based on oscillating systems are mainly limited by oscillators themselves

because the clock frequency has to be close to their free pulsating frequency (or to multiple of the SP frequency if the device is able to extract a subharmonic clock). CR devices based on SP lasers also need a spectral line at the interested frequency in the signal electrical spectrum. This is a difficulty in clock extraction from a NRZ signal with a simple SP laser. A pre-processing circuit was developed to be combined with an SP laser based CR. It consisted of an SOA followed by an optical filter. This scheme allowed clock extraction from an NRZ signal. Good timing jitter reduction and stable locking at 40 Gbit/s were obtained with this novel scheme [165].

Chapter 6

Experimental study of all-optical clock recovery devices based on self-pulsating semiconductor lasers

All-optical clock recovery (OCR) for 3R regeneration is a part of our laboratory expertise. In this work, we investigated experimental studies on different OCR functions which are principally based on SP semiconductor lasers. This chapter presents results concerning these studies.

6.1 Characterisation techniques

There are many quality criteria for an optical clock and numerous methods to assess an OCR device performance. Typical characterisations which are used to study an OCR function are: component analysis, temporal analysis, spectral analysis, analysis in wavelength conversion configuration and system analysis.

6.1.1 Components characteristics

Component analysis is usually considered first because it provides primary information about the OCR device such as: self-pulsation frequency, emitted wavelength, electrical linewidth, etc... Two main components which are used for all studied OCR functions are a Distributed Bragg Reflector (DBR) SP laser and a Fabry-Perot SP laser. The DBR-SP laser is a bulk material based laser consisting of three sections: Bragg section, phase section and gain section [166]. The Bragg and gain sections are supplied by two independent bias currents. The second SP laser is a Fabry-Perot laser based on quantum-dot material [51]. Both lasers are designed and fabricated by Alcatel-Lucent Thales III-V labs in the framework of the national project ROTOR. Component characteristics are given in Table (6.1).

Cavity type	Active layer structure	Self-pulsation frequency (GHz)	Typical electrical linewidth (kHz)	Wavelength (nm)
DBR	Bulk	∼42.66	∼1000	∼1550
Fabry-Perot	Quantum-dot	∼42.66	∼100	∼1600

Table 6.1: Basic characteristics of the two studied SP lasers

According to information given by the component supplier, the cavity type (monomode DBR or multimode Fabry-Perot) does not have any effect neither on the locking capability nor on the phase noise spectra of each laser. Then spectral performance represented by electrical modulation linewidth could be considered as intrinsically related to the laser internal structures. For all following studies, we call the first laser simply bulk-SP laser and the second one QD-SP laser.

6.1.2   Timing jitter

Timing jitter is the most important parameter which characterises the temporal quality of a signal. It represents the pulse deviations from the nominal position in the stream. It is expressed in unit interval (one clock period) or in time units. In the case of an optical clock, timing jitter represents indirectly clock phase noise characteristics. In a transmission system, the clock delivered by a CR device has to exhibit a low timing jitter even if the input signal is strongly degraded. In most cases, CR functions are implemented in the receiver or regenerators after long transmission distances and therefore the arriving signal is degraded.

If the random process ergodicity is assumed then pulse position fluctuations or signal timing jitter could be calculated from the phase noise spectrum of the signal. The Root Mean Square (RMS) jitter is expressed by:

$$J\left(rms\right) = \frac{1}{2\pi f_0} \sqrt{\int_{-\infty}^{+\infty} S_\phi\left(f\right) df}$$ (6-1)

Where f_0 is the signal modulation frequency, f is the frequency shift from f_0 and $S_\phi\left(f\right)$ is the power spectral density of signal phase noise. In general, the timing jitter of the extracted clock is determined both by the intrinsic jitter of the CR device itself and by the injected signal jitter. The intrinsic jitter is obtained by injecting a high spectral purity clock into the CR device, then measuring the phase noise spectrum of the output clock, and finally the jitter is calculated from Equation (6-1).

As we will discuss in Paragraphs 6.1.3 and 6.1.4, both temporal and spectral analysis can provide an evaluation of rms timing jitter. In general, the clock jitter value deduced from the temporal analysis is greater than the one deduced from the phase noise analysis. This difference originates from the fact that phase noise measurements do not take into account the jitter correlated with pattern effects and amplitude fluctuations [167]. On the other
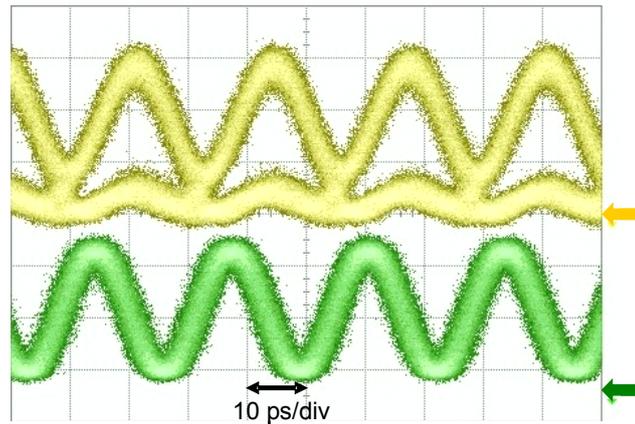
Figure 6.1: Eye diagrams of an injected data signal (yellow) and the extracted clock (green) delivered by an SP laser

hand, the accuracy of jitter measurements in the temporal analysis depends directly on the sampling number and there are no well defined criteria to evaluate CR device performances via this value. On the contrary, tolerances for the timing jitter derived from phase noise measurements within a given frequency band are standardised. Therefore, in the following studies, the timing jitter calculated from phase noise measurement is used to evaluate the recovered clock quality.

6.1.3 Temporal analysis

Temporal analysis of an optical clock is realised by using a sampling oscilloscope. The first observation offers an evaluation of intensity fluctuations induced by sequence effects. Depending on the injected signal characteristics (sequence length, modulation format, etc...) the extracted clock can suffer intensity fluctuations. An example of injected data signal eye diagrams and corresponding recovered clock is displayed in Figure (6.1). The second feature offered is a measurement of the CR capture and unlocking times by using the oscilloscope in pattern mode and the injected data in packet mode. These characteristics are particularly important in asynchronous networks. They allow to evaluate the CR capability for clock extraction packet by packet at an expected operating bit rate.

Sampling oscilloscopes allow also statistical analyses on the received signal. From histogram measurements in temporal domain, the rms and peak to peak timing jitters can be deduced. New oscilloscopes with excellent temporal resolution enable to measure timing jitters as low as 200 fs (Agilent 86100B).

6.1.4 Spectral analysis

Spectral analysis concerns principally power spectral density (PSD) measurements of clock signal phase noise. Then phase noise curves allow the jitter transfer function of the device
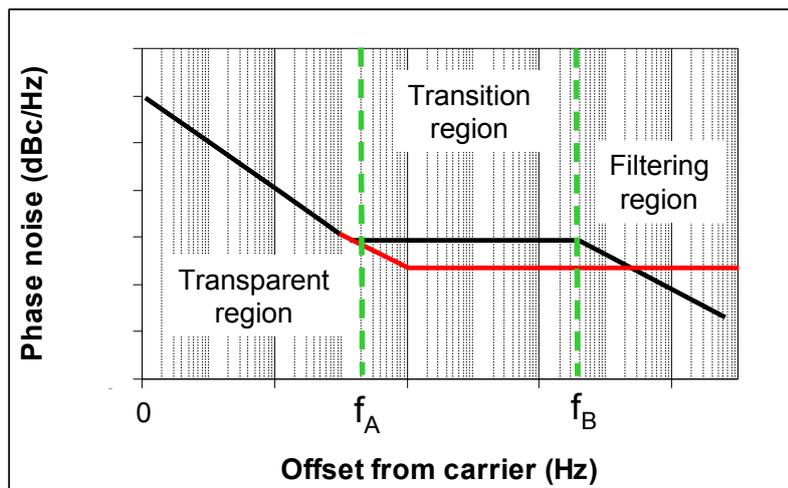
Figure 6.2: Example phase noise curve shapes of an injected data signal (red) and clock delivered by a CR(black)

to be calculated by subtracting the phase noise spectrum of the input signal from the output signal.

Clock phase noise spectra are obtained by using a phase noise analyser. The phase noise analyser demodulates intensity and phase noise by mixing the interested signal with a local reference at the same RF frequency but in quadrature. Figure (6.2) depicts a typical clock phase noise spectrum which could be obtained from an SP laser based CR. Data are injected into the SP laser and the phase noise spectrum is measured on the delivered clock. Phase noise curves can be split into 3 regions. In the frequency region below f_A, the phase noise curves of the incoming signal and delivered clock are identical. In this region, the noise is dominated by the injected signal. The CR could be considered as transparent because there is no jitter filtering effect. Conversely, for frequencies superior to f_B, a jitter filtering effect is observed and it is presented by a negative slope on the phase noise curve of the clock. In this frequency region, the noise is defined mainly by the OCR device. The range extending from f_A to f_B corresponds to a transition region in which both incoming signal and laser noise contribute.

By subtracting the input phase noise spectrum from the output, the jitter transfer function of the device could be obtained. In general, CRs exhibit transfer functions similar to low pass filters. The cut-off frequency f_C is usually used to qualify the filtering efficiency of the device. The smaller f_C is, the better jitter filtering is. In a complete study, it is demonstrated that the laser electrical linewidth is closely related to the f_C [168]. An SP laser possessing a smaller electrical linewidth will exhibit a transfer function with smaller cut off frequency f_C.

Afterwards, the clock spectral purity can be examined by analysing its phase noise spectrum. The clock quality could be quantified by using Formula 6-1 to deduce the rms timing jitter within an interested frequency band. This phase noise measurement is so
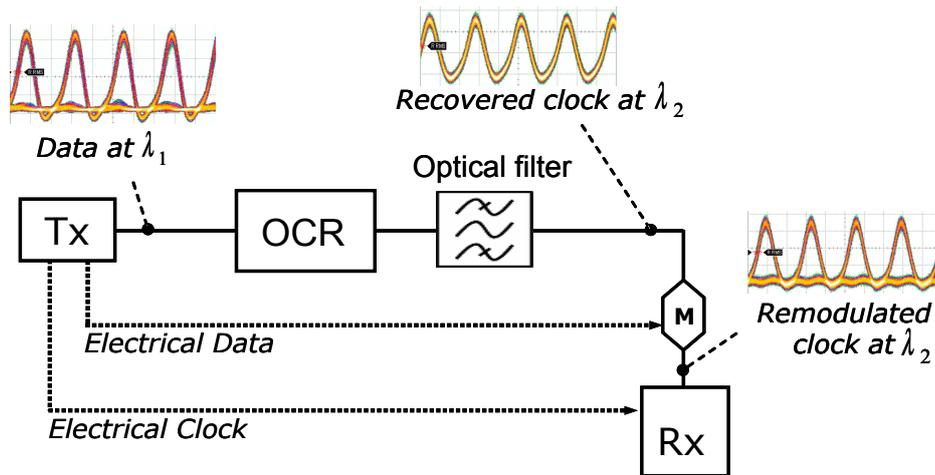
Figure 6.3: Principle of the remodulation experiment

called the 'Single Side Band Phase Noise' (SSB noise).

6.1.5 Remodulation technique

The two previous characterisations provide macroscopic information about clock quality. However, they can not allow the impact of pattern effects, which could lead to occasional CR locking loss, to be evaluated. A more adequate analysis is the bit error rate measurement realised on the resynchronised signal. The technique principle is based on a wavelength conversion experiment. It consists in information transfering from an incident signal at a wavelength λ_1 to a clock signal at a wavelength λ_2. The clock signal is extracted from the incident data stream. BER measurements are then performed on the remodulated clock signal at the receiver. Principle of the proposed remodulation experiment is depicted in Figure (6.3).

Data generated by the transmitter Tx are injected into the OCR device. The clock delivered by the OCR function is then modulated by an electro optical modulator M. The modulator can be considered as an ideal optical gate and is driven directly by the electrical data signal from the transmitter. By this way, the quality of the optical signal received at Rx corresponds to the quality of the recovered optical clock. On the other hand, the receiver is also synchronised directly to the transmitter electrical clock in order to avoid all influences of the receiver optoelectronic CR performance on BER. It is therefore possible to assess the OCR performance through BER measurements. This original characterisation is based on the OCR situation in a data driven 3R regenerator. In such regenerator, the extracted clock is modulated by an optical non linear gate. The output regenerated signal is at the wavelength of the recovered clock and inherits the low timing jitter. In our experiment, the modulation applied on the extracted clock is realised by a simple modulator which is driven by a high quality data signal. The lack of 2R regeneration function allows considering that the quality of the remodulated signal is intrinsically related to the optical clock quality.

Therefore, BER measurement can be used to quantify the CR performance under different incident signal conditions. This technique enables a lot of CR behaviour analyses by varying different input signal parameters such as: pattern sequence length, optical signal noise ratio, polarisation state, etc... Most of our experimental studies presented hereafter exploit this original characterisation technique.

6.1.6   System analysis

System characterisation focuses on CR behaviour in system environments. In a system context, the studied CR device can be introduced in a 3R regenerator. System experiments can not only demonstrate a good operation of the CR but also quantify its jitter suppression capability. The most adequate means for such study is recirculation loop experiment. This characterisation takes into account propagation effects and can be used to evaluate the CR robustness versus signal degradations accumulated after long transmission distances. Cascadability assessment of an all-optical 3R regenerator using SP laser based CR was reported [12]. The assessment was realised via a recirculation loop experiment. The 3R regenerator in synchronous modulation configuration demonstrated high performance. The CR function was constituted of a SP laser cascade and demonstrated its retiming efficiency.

6.2   Clock recovery performances of bulk based and quantum-dot based SP lasers

In this section, performance assessment of two OCR functions via remodulation experiment is reported. The first one is constituted of the bulk-SP laser and the second one is constituted of the QD-SP laser. Both lasers are presented in Paragraph 6.1.1.

6.2.1   Experimental set-up

Scheme of the experiment is described in Figure (6.4). Optical data signal at 42.66 Gbit/s is generated by the transmitter Tx at a wavelength of 1553 nm. The signal consists of a 2^{31}-1 length Pseudo Random Binary Sequence (PRBS) with 33 % RZ pulses. OSNR at the OCR device input is 18 dB/1nm. An optical circulator (OC) is used to inject the data signal into the SP laser and delivers the recovered clock. The optical filter is centred on the emitted clock wavelength. A polarisation controller (PC) is used to optimise the input signal polarisation if necessary.

For the first CR, the bulk-SP laser locked regime is achieved with bias currents of 33 mA and 141 mA for the Bragg and the gain sections respectively. The recovered clock obtained at the optical filter output exhibits an electrical linewidth of 700 kHz measured at half of maximum. For the second CR, the QD-SP laser synchronisation to the incoming data signal is acquired only with the PC help. This fact is caused by the polarisation sensitivity of quantum-dot structures. A deeper study on polarisation sensitivity characteristics of CRs
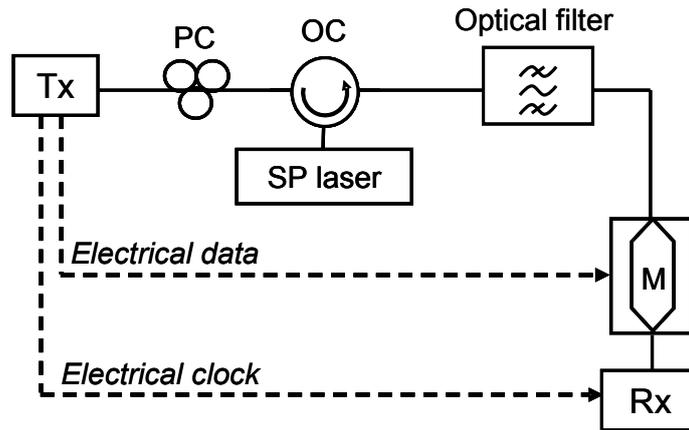
Figure 6.4: Experimental set-up for BER measurements of two CR configurations based on bulk-SP and QD-SP lasers

based on different SP lasers will be presented in Section 6.4. In locked regime, the QD-SP laser bias current is 412 mA and the electrical linewidth of the recovered clock is lower than 100 kHz.

6.2.2 Results of BER measurements

Results of BER measurements on the remodulated clocks are presented in Figure (6.5). The reference sensitivity curve (circles) is obtained in back-to-back configuration when the data signal generated by the transmitter Tx are sent directly to the receiver Rx. The receiver sensitivity curve measured on the remodulated clock signal which is recovered by the bulk-SP laser (squares) is then plotted and compared to the reference. A penalty of 7.5 dB at a BER of 10^{-8} and an error floor at a BER of 3.10^{-9} are observed. For the second configuration when the QD-SP laser is used for clock extraction, the receiver sensitivity curve (triangles) shows an error free operation for receiver input powers larger than -32 dBm and a penalty reduced to 3 dB at a BER of 10^{-8}. Penalty values in both cases seem important. Nevertheless, receiver sensitivity degradations originate not only from the OCR device insertion but also partially from the pulses format change. The reference curve is measured with pulse duration of 8 ps which is typical for a 33 % RZ signal at 40 Gbit/s. But pulse duration emitted by the two OCR configurations is about 3 ps. It was demonstrated that the receiver sensitivity depends also on duration of incoming pulses among other factors [169], [170]. Therefore, the penalty values induced by the two OCR functions include signal quality changes caused by OCR introduction and a receiver sensitivity change caused by signal pulsewidths difference.

The bulk-SP laser emits pulses of 1.8 ps duration. In the experiment, a 2 nm filter was used to enlarge the pulses to 3.5 ps. So that the pulse duration at the receiver is similar to the one emitted by the QD-SP laser and the sensitivity curves measured on the remodulated
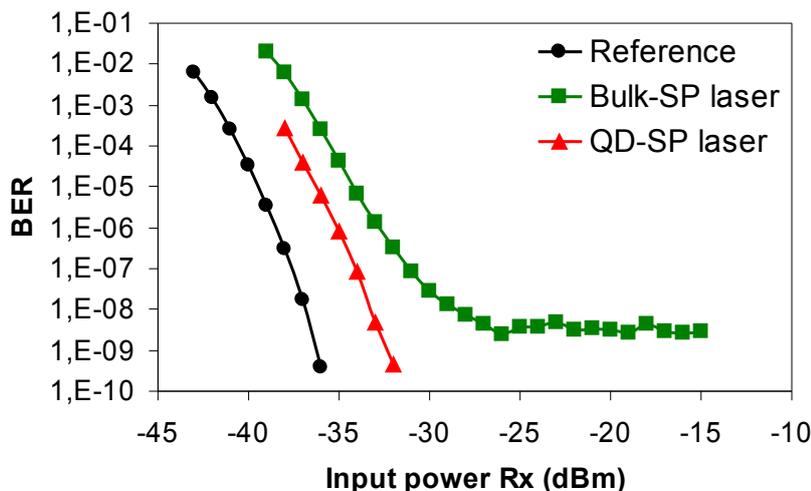
Figure 6.5: BER of a function of Rx input power for 2 OCRs based on bulk-SP laser and QD-SP laser

signals can be compared.

The BER results show clearly that the quality of the remodulated signal is better when the QD-SP laser is used for the CR. A 4.5 dB penalty reduction at BER of 10^{-8} is achieved and the error floor disappears. The signal degradations shown by the BER curves are attributed to the poor clock quality recovered by the bulk-SP laser. This is probably due to an excessive internal amplitude and phase noise in bulk structures and an insufficient jitter filtering capability of the laser. On the other hand, the error free operation demonstrates high clock quality and confirms good performance of the OCR based on QD-SP laser.

The performance difference between the OCRs based on bulk-SP laser and on QD-SP laser brought out by the remodulation experiment is consistent with results reported by other characterisations. It is shown that a QD-SP laser exhibits a better jitter suppression capability in comparison to a bulk-SP laser [168]. In the same study, it is also demonstrated that a narrower free running spectral linewidth corresponds to a transfer function with smaller cut off frequency. In our case, the clock spectral linewidth of the bulk-SP laser is 1000 kHz compared to only 100 kHz of the QD-SP laser. This implies that the QD-SP laser presents a higher jitter filtering efficiency. This advantage is achieved thanks to the high spectral purity of quantum-dot based material and considered as the main explanation for the BER measurement results.

To conclude, the bulk-SP laser shows insufficient timing jitter filtering effect. It is difficult to use the laser to fulfil retiming task without any additional device to improve the recovered clock quality. A simple and promising solution to enhance the bulk-SP laser based CR performance is discussed in Section 6.3. Otherwise, the QD-SP laser emits a good quality clock. This is demonstrated by an error free operation and a reduced penalty on the receiver sensitivity curve of the remodulated clock signal. However, it is essential to note
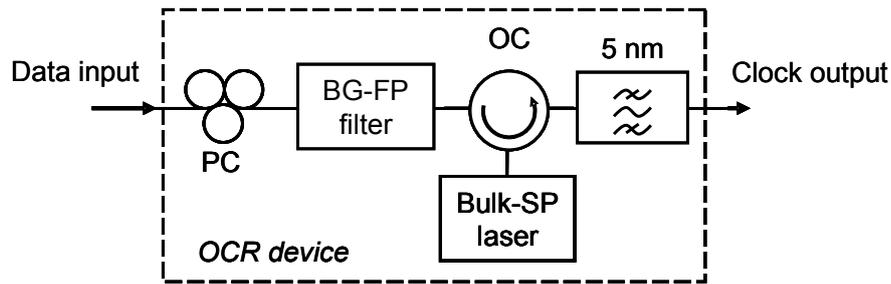
Figure 6.6: Scheme of OCR configuration consisting of a Bragg Gratings Fabry-Perot filter followed by the bulk-SP laser

that the QD-SP laser suffers from strong polarisation sensitivity because of its quantum-dot material. The control of the input signal polarisation is inevitable to obtain QD-SP laser synchronisation. A continuous polarisation state adjustment ahead of the QD-SP laser in a real transmission system context will be impossible. An OCR solution consisting in placing the bulk-SP laser in front of the QD-SP laser was proposed to overcome the polarisation sensitivity problem [164]. A polarisation sensitivity assessment of this new OCR configuration is presented in Section 6.4.

6.3 Passive pre-filtering for performance enhancement

The previous section showed that the quality of the recovered clock delivered by the bulk-SP laser is not sufficient because of excessive internal laser noise. Therefore the bulk-SP laser could not be used alone as a CR device. In this section, we propose a new configuration to enhance the extracted clock. The principle of the proposed solution is first presented. Temporal and spectral analyses to verify the OCR operating principle are then discussed. And finally, BER are measured via the remodulation technique to show the new configuration efficiency.

6.3.1 Proposed configuration using passive pre-filtering

Because the jitter filtering effect of the bulk-SP laser is limited, a signal pre processing stage could be introduced to assist the laser and consequently enhance the output clock quality. We propose an OCR configuration using a passive pre-filtering stage ahead of the bulk-SP laser. The pre-filtering stage consists in a Bragg Grating Fabry-Perot type filter (BG-FP filter). The proposed OCR scheme is depicted in Figure (6.6).

The BG-FP filter is an all-fibre-based device which has been fabricated by IXFiber. It is constituted of two identical and uniform 1.3 mm fibre Bragg gratings separated by approximately 2 mm. Because of the photoinduced birefringence, two Fabry-Perot resonances corresponding to two perpendicular polarisations exist. In order to limit influences of this problem, the gratings are photo-written in a polarisation maintaining fibre, which enables

us to select separately one of the two resonances by adjusting the input polarisation. A Polarisation Controller (PC) is therefore introduced to align the input signal polarisation on one of the two intrinsic axes of the BG-FP filter fibre. The component is packaged in a passive thermal insensitive module without temperature control. Data signal is injected to the BG-FP filter via the PC. The intermediate clock obtained at the BG-FP filter output is delivered to the bulk-SP laser via an optical circulator. A 5 nm optical band pass filter is placed at the OC output which is centred on the wavelength of the final emitted clock.

Passive technique for OCR based on spectral line filtering has been largely investigated [130], [171], [132]. Clock extraction could be obtained simply by injecting the data signal into a periodic optical filter. However, high performance clock signals can be achieved only with a very high finesse filter. In our case, the Fabry-Perot filter exhibits moderate finesse but allows extracting an intermediate clock from the incoming data signal. The basic idea is to use the filter in order to deliver a clock signal to the bulk-SP laser instead of the data signal. Hence the laser can be synchronised regardless of pattern effects. The overall CR task is shared between the pre-filtering stage and the SP laser. Thus efficiency requirements on each component can be relaxed compared to the cases when each component is used separately. At the OCR output we can expect a clock signal exhibiting a higher quality than when the bulk-SP laser is used without pre-filtering.

6.3.2   Filter characterisation

The spectral transfer function of the BG-FP filter is measured by injecting an optical white source and measuring the output optical spectrum. The measure is performed by using a high precision optical spectrum analyser called BOSA (from Aragon Photonics) which presents a spectral resolution of 0.08 pm. The transmission spectrum of the BG-FP filter is shown in Figure (6.7).

The transmission peaks of the BG-FP filter correspond to two cavity Free Spectral Range (FSR) sets because of the photoinduced birefringence mentioned previously. Separations between main peaks of the two peak classes are 347 pm and 342 pm which corresponds to FSR values of 43.2 GHz and 42.5 GHz respectively. The measured bandwidth at half maximum is 0.7 pm for the central peak and 1.5 pm for the adjacent peaks. Thus, the finesse of the central peak is very close to 500. It is important to note that with this bandwidth range, the filter is not sensitive to the frequency jitter of the transmitter laser which is typically less than 10 MHz (0.08 pm) for conventional DFB laser (used at the transmitter Tx). The filter insertion loss is 7 dB.

The data signal at 42.7 Gbit/s is injected into the BG-FP filter via the PC. The optical signal generated by the transmitter Tx is at 1553 nm. Signal polarisation at the filter input is adjusted by using the PC and is aligned on one PM fibre intrinsic axis. The signal is transmitted by the peak class exhibiting 42.5 GHz of FSR. Figure (6.8) displays the temporal trace and the spectral trace of the intermediate clock signal at the BG-FP filter
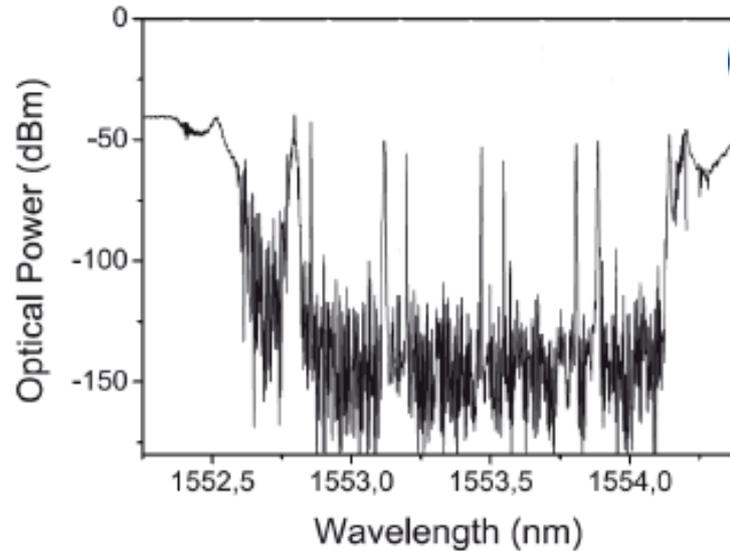
Figure 6.7: Transmission spectrum of the BG-FP filter

output.

The temporal trace is obtained by using a 50 GHz photodiode for detection and displayed with an electrical oscilloscope Agilent Infinium DCA-J 86100C. The clock signal spectrum is given by an Optical Spectrum Analyser Anritsu MS 9710 B operating at a resolution of 0.07 nm. The obtained clock presents a poor extinction ratio of only 8 dB and strong intensity fluctuations. We remind that the incoming data signal generated by the transmitter Tx exhibits an excellent Extinction Ratio (ER) of at least 16 dB and nearly no intensity noise. This ER decreases and the induced intensity noise results from the clock extraction processed by the BG-FP filter. The low quality of the emitted clock originates from three facts: filtering process which is not selective enough to eliminate the data spectral components, carrier wavelength drift and resonance detuning [172].

So, despite low intensity noise of the incoming signal, the intensity fluctuations at the filter output are inevitable. After passing through the FP filter, optical pulses are inserted in the '0' slots of the data signal with few bits [135], [173]. Then the data signal is transformed by the filter into a pulse stream with unequal amplitude. These intensity fluctuations can be limited only by increasing the filter finesse. Secondly, the drift of the filter transmission peak from the data carrier wavelength induces also clock intensity fluctuations. In our case, the optical carrier wavelength is adjusted accurately at the transmitter Tx to be superimposed on one of the filter transmission peaks. Then the carrier frequency drift impact can be neglected. However, both extinction ratio degradation and intensity noise introduction are also consequence of the filter FSR detuning from the transmitter clock frequency [172]. The clock frequency of the transmitted signal is 42.7 GHz while the filter FSR is 42.5 GHz. The FSR detuning leads to the fact that in the signal spectrum, the lateral modulation lines
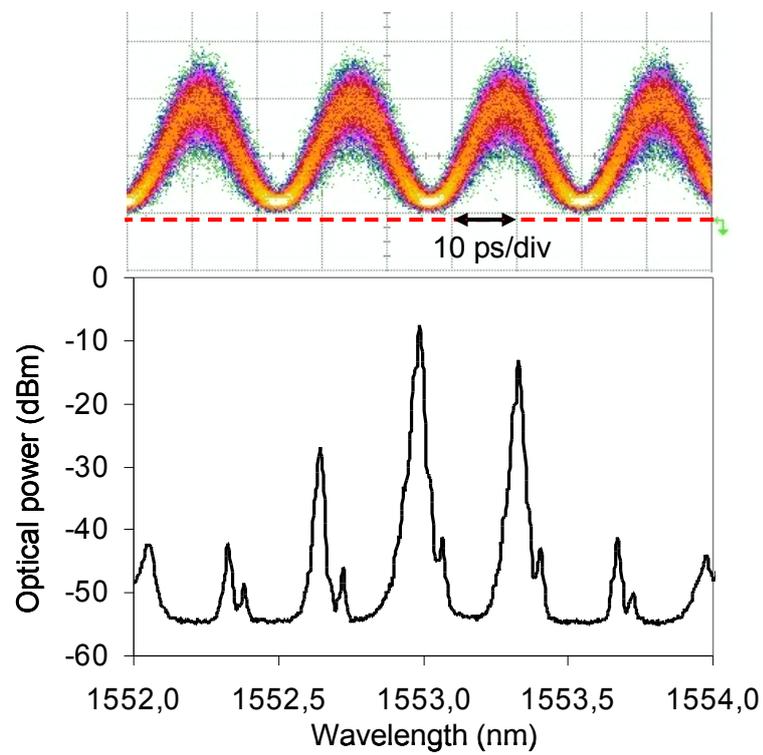
Figure 6.8: Temporal trace (upper) and spectral trace (lower) of the intermediate optical clock delivered by the BG-FP filter
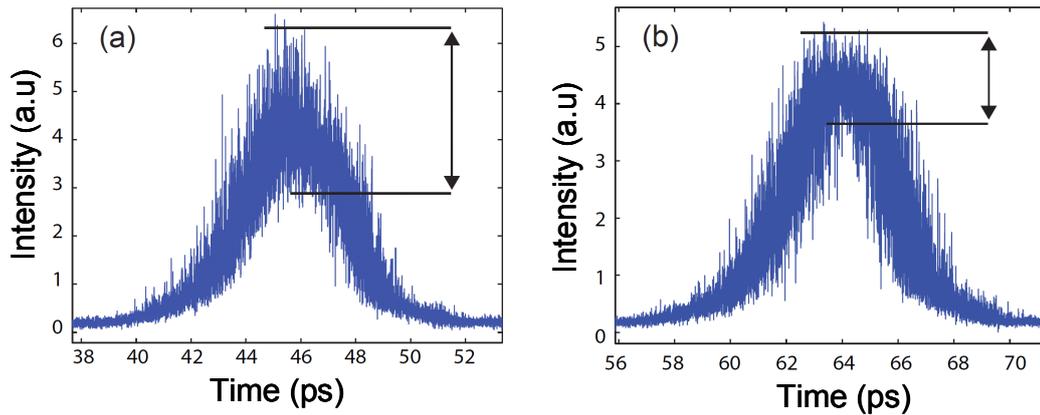
Figure 6.9: Output recovered clock pulses recovered by the bulk-SP laser when an optical data signal is injected (a) and an optical clock is injected (b)

slip out of the filter transmission peaks and then will not be correctly transmitted. That means the spectral line levels decreases while the noise inside the filter pass band increases. In addition, the asymmetric transfer function of the BG-FP filter leads to unequal spectral line transmissions. This can be observed on the output clock spectrum. Combination of all these problems makes the clock provided by the BG-FP filter not suitable for transmission. In spite of the low quality of the extracted clock, this filter is used to perform a pre-filtering for bulk-SP laser synchronisation.

6.3.3 Temporal and spectral analyses

To verify the proposed OCR principle, the bulk-SP laser behaviour is studied in two cases: the first one in which an optical data signal is injected into the laser for synchronisation and the second one in which an optical clock delivered by a modulator is injected. Input pulse durations and intensity noise characteristics are identical in both cases. Qualities of the recovered clocks in the two experiments are compared via temporal and spectral analyses.

Pulse shapes of the extracted clocks are presented in Figure (6.9). They are obtained by using an Optical Sampling Oscilloscope (OSO) in the persistent 'Eye Diagram' mode and with a time resolution of 1 ps (Picosolve, PSO 100 Series).

It appears clearly that the intensity noise is not identical in the two cases. The output clock in the first case exhibits a fluctuation of 50 % of pulse amplitude. This fluctuation is only 30 % in the second case. Hence, the intensity noise of the recovered clock is smaller if the laser is synchronised to a clock signal. This result is attributed to the absence of pattern effects in the incoming signal.

Spectral analysis is then investigated. The phase noise curves of the clock achieved by injecting optical data or an optical clock into the bulk-SP laser are displayed in Figure (6.10). The phase noise densities in both cases are identical in the low frequency region under 300 kHz. For frequencies above 300 kHz, the phase noise of the extracted clock is
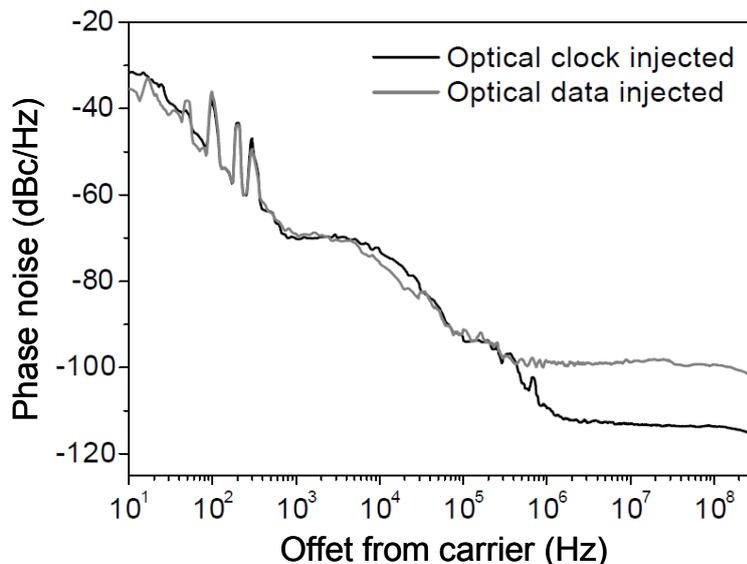
Figure 6.10: Clock phase noise curves obtained when the bulk-SP laser is injected optical data (bright curve) and an optical clock (dark curve)

lower if the laser receives a clock signal instead of a data stream. In order to have a quantitative evaluation, the phase noise results have been compared with the ITU T G825.1 recommendations. The rms timing jitter in the frequency range (16-320 MHz) has been computed. For the recovered clock in the data injection case, an rms jitter of 629 fs is deduced. This value is much larger than the maximum rms jitter tolerated at 40 Gbit/s which is of 232 fs. On the other hand, the deduced rms jitter value in the clock injection case is 125 fs. This is largely smaller than the 232 fs threshold and hence demonstrates a suitable clock quality. The results of the phase noise measurement confirm that injection of optical clock instead of optical data into the bulk-SP laser can provide a better clock quality.

6.3.4   Results of BER measurements

The recovered clocks performances delivered by the bulk-SP laser with and without pre-filtering stage are evaluated by BER measurements in remodulation experiments. The first receiver sensitivity curve measured on the remodulated clock is obtained when data from the transmitter Tx is injected directly into the laser. The second one is obtained by inserting the pre-filtering stage constituted of the BG-FP filter in front of the laser. The reference curve is plotted by connecting the transmitter Tx output to the receiver input Rx. The BER measurement results are shown in Figure (6.11).

The OCR configuration corresponding to the bulk-SP laser alone exhibits a penalty of 5 dB at 10^{-8} and an error floor at a BER of 10^{-9}. The signal degradations caused by the laser introduction can be predicted from Section 6.2. The insufficient recovered clock
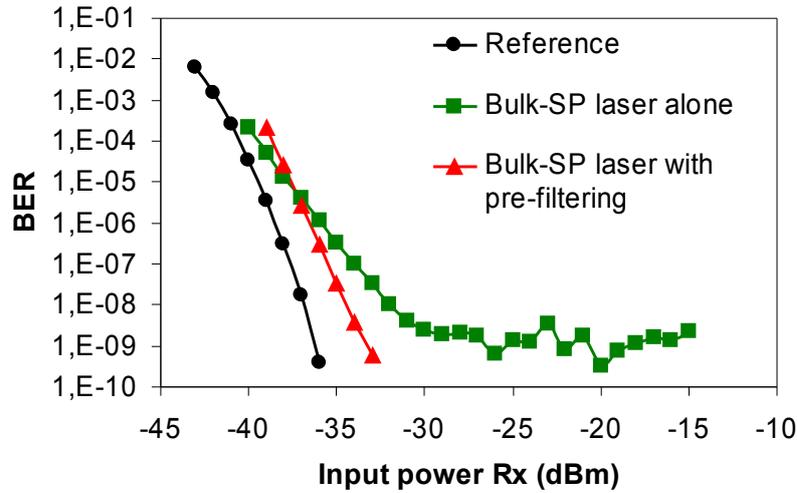
Figure 6.11: BER as a function of Rx input power for two OCR schemes: the bulk-SP laser alone (green) and with the BG-FP filter for pre-filtering (red)

quality is assigned to poor jitter filtering effect offered by the bulk-SP laser. When the BG-FP filter is introduced as pre-filtering stage in front of the laser, the corresponding BER curve shows a penalty of only 2.5 dB at 10^{-8} compared to the reference and no error floor is observed. The clock quality improvement brought by the pre-filtering is then clearly demonstrated. This OCR performance enhancement is characterised by a penalty reduction of 2.5 dB and the error floor absence. The result is in agreement with temporal and spectral analyses. The pre-filtering stage suppresses pattern effects and consequently the recovered clock quality is improved.

To conclude, the performance enhancement of an OCR based on bulk-SP laser by using a simple passive optical filter is demonstrated. The recovered clock quality is clearly improved in spite of strong amplitude fluctuations of the intermediate clock delivered by the pre-filtering stage. The results are quantified thanks to BER measurements. The temporal and spectral analyses show that the pre-filtering process leads to an intensity fluctuations reduction. The phase noise spectra measured on the recovered clock show a stronger noise level caused by pattern effects. Therefore a periodic filter will be useful if the spectral purity of the SP laser is not sufficient to assure a high clock quality.

The OCR performance can be more enhanced by optimising the pre-filtering stage. A FP filter with a higher finesse and a FSR precisely equal to 42.7 GHz will give a better intermediate clock and therefore certainly improve the recovered clock quality at the OCR output.
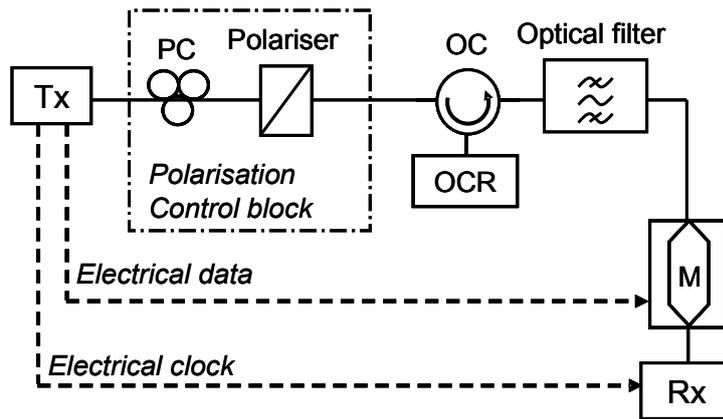
Figure 6.12: Experimental set-up for polarisation sensitivity assessment

6.4   Polarisation sensitivity assessment

As mentioned in Section 6.2, despite that OCR based on QD-SP laser shows high timing jitter filtering performance, its sensitivity to the polarisation of the incoming signal is the principal obstacle to its deployment in real transmission systems. A solution has been proposed to overcome the polarisation problem [164]. It consists in a tandem of 2 SP lasers: a polarisation insensitive bulk-SP laser followed by a QD-SP laser. The laser cascade can offer a polarisation insensitive OCR with high timing jitter performance, thanks to the polarisation insensitivity of the bulk-SP laser and to the jitter suppression of the QD-SP laser. In this section, we investigate the polarisation sensitivity of two OCR configurations via remodulation experiment. The polarisation sensitivity of the QD-SP laser based OCR is first assessed. Then the polarisation insensitivity of the laser cascade based OCR is analysed.

6.4.1   Experimental set-up

The experimental set-up used for the polarisation sensitivity assessment relies on the typical scheme of a remodulation experiment as shown in Figure (6.12). The optical data signal generated by the transmitter Tx is linearly polarised because it is delivered by a DFB laser. For this study, a polarisation control block is elaborated to control the orientation of the signal polarisation at the OCR input. The block comprises a polarisation controller (PC) and a variable polariser. By changing the polariser angle and optimising the transmitted data signal with the PC, the polarisation orientation at the OCR input can be changed without changing the input power. The fibre connecting the polariser to the OC is short and well fixed. This ensures that no important polarisation change caused by environment is induced during propagation. By this way, a polariser angle corresponds to a signal polarisation orientation at the OCR input. The BER measurements performed on the remodulated signal for various input polarisations allow to evaluate the polarisation
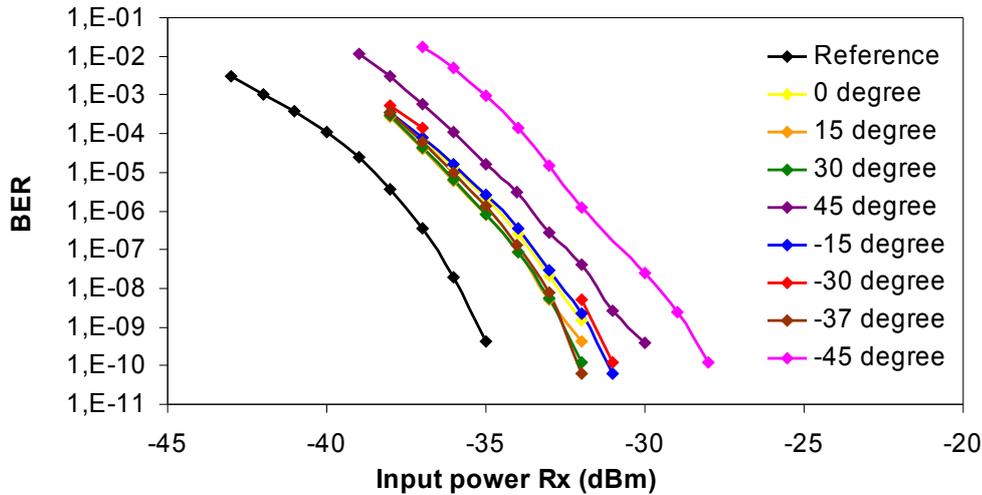
Figure 6.13: BER as a function of Rx input power measured on the remodulated clock recovered by the QD-SP laser based OCR for various input signal polarisation orientations

dependence of the recovered clock quality. Consequently BER results could be used to quantify the polarisation sensitivity of the studied OCR function.

6.4.2 Polarisation sensitivity of QD-SP laser based OCR

The polarisation sensitivity of the QD-SP laser based OCR is analysed via remodulation experiment. BER evolutions shown in Figure (6.13) illustrate the dependence of the re-modulated clock quality on the incoming polarisation angle.

At the OCR input, the data signal presents a linear polarisation. It is collinear to the polarisation privileged axis of the QD-SP laser when the variable polariser angle is zero. Firstly, the BER curves show that within the synchronisation range, no error floor is observed for all signal polarisation orientations. Secondly, the curves present a minimal penalty of 3 dB compared to the reference curve. This penalty has been already identified in Section 6.2. It is attributed to a receiver sensitivity change due to detected signal pulsewidth changes. The pulse duration at the QD-SP laser output is 3 ps while the pulse duration of the reference signal is 8 ps. At last, the BER curves show that by changing the signal polarisation state ahead of the QD-SP laser additional penalties are induced. The OCR sensitivity to the injected signal polarisation is clearly demonstrated. Figure (6.14) exhibits the induced penalty at a BER of 10^{-9} as a function of the polarisation angle.

The curve shows that an average penalty of 3 dB is maintained in the range [-40°, 40°]. When the input polarisation angle reaches the value of $\pm 45°$ the induced penalty increases steeply. From this curve, we can conclude that the tolerance of the input polarisation angle is about $\pm 45°$ with respect to the QD structure privileged axis. Out of this range, the QD-SP laser could not be synchronised anymore and BER measurements become impossible.
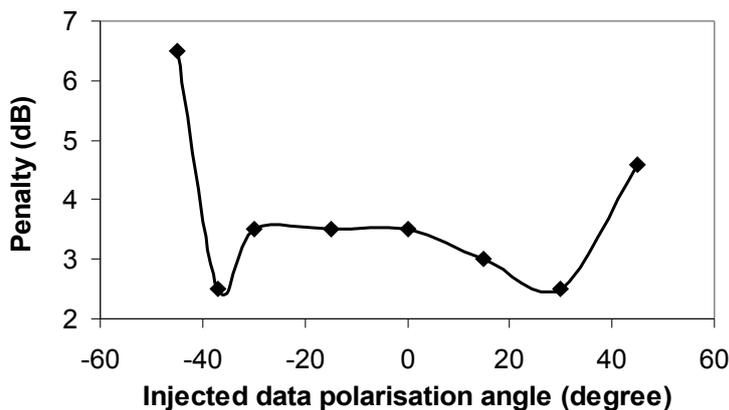
Figure 6.14: Induced penalty at a BER of 10^{-9} as a function of input signal polarisation angle
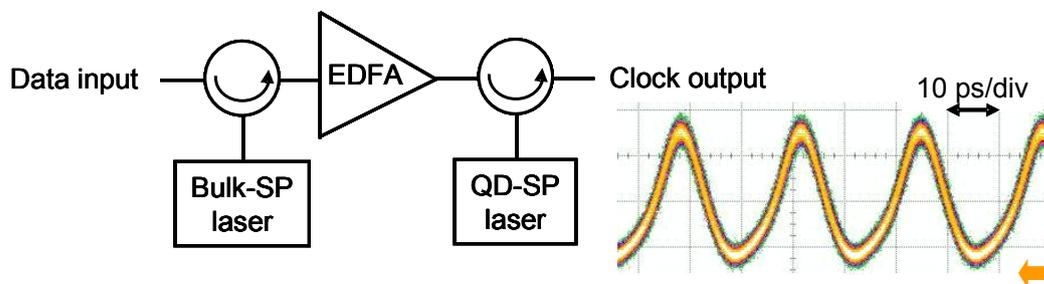
Figure 6.15: OCR configuration based on cascade of the two SP lasers

6.4.3   Polarisation sensitivity of SP laser cascade based OCR

The OCR based on the QD-SP laser presents an efficient jitter filtering function but its sensitivity to input polarisation remains a major obstacle for field applications. The OCR solution proposed to overcome this problem consists in a cascade of two SP lasers: a bulk-SP laser followed by a QD-SP laser [164]. This OCR configuration was demonstrated to maintain a stable recovered clock while the input polarisation was varied by a low speed polarisation scrambler. Moreover, the reported spectral analysis showed that the tandem recovered clock exhibits the same phase noise characteristics as the clock recovered by the QD-SP laser alone. Therefore the OCR based on laser cascade presents also a high tolerance to the OSNR degradation while ensuring a low timing jitter. The OCR scheme is depicted in Figure (6.15) with an example of recovered clock signal.

The bulk-SP laser is placed on first position to limit the impact of input polarisation variations. The QD-SP laser is placed next, to enhance the clock quality thanks to its high spectral purity. An EDFA is used to deliver the signal power required for QD-SP laser synchronisation. In the OCR set-up, the signal polarisation at the bulk-SP laser output is aligned to the QD-SP laser privileged axis. Because the bulk-SP laser emits a fixed
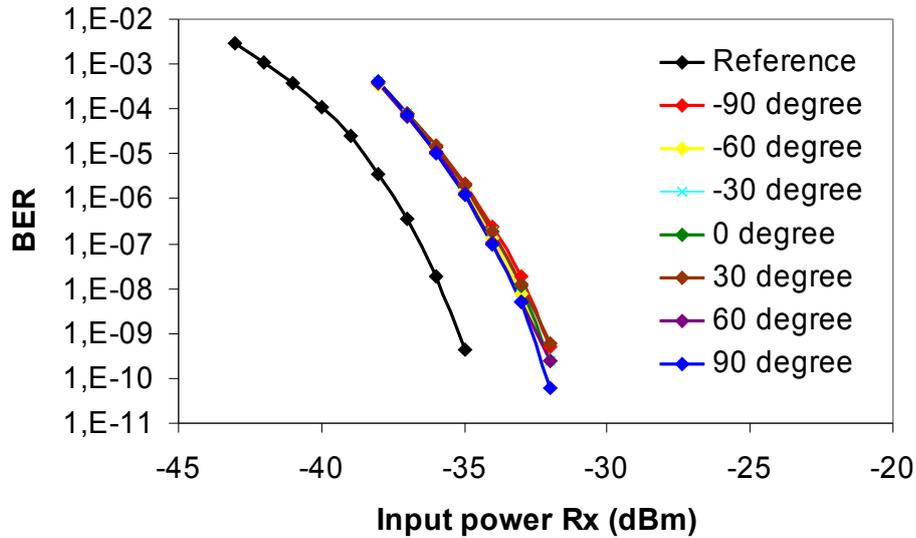
Figure 6.16: BER as a function of Rx input power of remodulated clock provided by the OCR constituted of cascade of the two SP lasers for various input signal polarisation orientations

linearly polarised optical signal, the signal polarisation state at the QD-SP laser input is well defined. The QD-SP laser is therefore in a stable locked regime and emits a steady recovered clock. Stable recovered clock signals provided by the laser cascade are obtained for any input polarisation angle as shown in Figure (6.15).

To demonstrate quantitatively the OCR insensitivity to the input signal polarisation, BER measurements are performed on the remodulated clock for different polarisation angles. The results are reported in Figure (6.16). Power levels at the bulk-SP laser and the QD-SP laser inputs are 6 dBm and 3 dBm respectively.

For all polarisation angles between -90° and 90°, neither additional penalty nor error floor due to polarisation change is observed by considering a receiver sensitivity measurement error of 0.5 dB. Because of the pulsewidth change, all curves exhibit a penalty of 3 dB at 10^{-9} in comparison to the reference. The curves superimposition demonstrates clearly an ultra stable recovered clock quality at the OCR output despite the input polarisation changes. The polarisation insensitivity of the laser cascade is experimentally confirmed by BER measurements in remodulation experiments.

6.5   Resistance to polarisation mode dispersion

Polarisation Mode Dispersion (PMD) effect causes impairments on system transmission performance. At the receiver, the PMD presence in the optical signal leads to great difficulties for optoelectronic CR operation. In this section, we investigate the PMD resistance
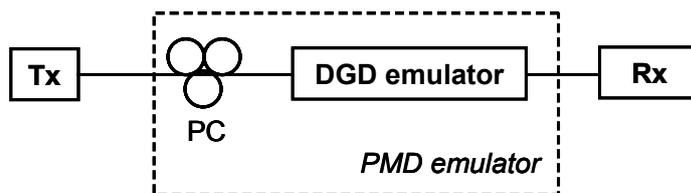
Figure 6.17: Experimental set-up for assessment of PMD impact on receiver sensitivity

of the all-optical CR based on the bulk-SP laser. Although the laser was shown insensitive to the input polarisation orientation, the PMD impact on its synchronisation performance and on the extracted clock quality is far from negligible. At first, the principle of the PMD emulator using in our study is described briefly. Then, the PMD impact on receiver sensitivity when the optoelectronic CR is used is examined. At last, PMD resistance of the bulk-SP laser based OCR is analysed via a remodulation experiment.

6.5.1 PMD emulator

A PMD emulator is a device which can simulate the PMD effect induced by a virtual fibre link (as long as several hundreds of kilometres) on an optical data signal. By passing through the PMD emulator, the two principal states of the optical signal polarisation accumulate a differential group delay (DGD). At the emulator output, the optical pulses are broadened as if they had suffered from the PMD effect after a long fibre propagation. PMD emulators use typically randomly coupled PM fibres or highly birefringent crystals mounted on rotation stages. For simplicity, we consider only the first order DGD. The used PMD emulator is a PMD platform provided by General Photonics (Model PMD-601-S). The device is dedicated for 40 Gbit/s applications and can provide first order DGD values in the range of [0 ps; 22.5 ps], with a resolution of 0.36 ps.

6.5.2 Impact of PMD on receiver sensitivity

The PMD effect can disrupt the operation of an optoelectronic CR and therefore lead to receiver sensitivity degradations. PMD influences on the receiver sensitivity can be assessed by inserting simply the PMD emulator into a back to back configuration as shown in Figure (6.17).

The transmitter Tx generates 42.7 Gbit/s RZ 33 % PRBS streams. The transmitted optical signal presents a high OSNR of 30 dB/1 nm. A manual PC allows to align the signal polarisation to principal axes of the DGD emulator. In this experiment, the signal polarisation state at the emulator input is in the worst case. The optical power is equally distributed into the two principal axes of the emulator in order to obtain a maximal pulse broadening by the first order DGD. At the receiver Rx, the optical signal is detected by a 50 GHz photodiode. The receiver CR function is performed by an optoelectronic module. The optoelectronic CR scheme can be simplified as depicted in Figure (6.18).
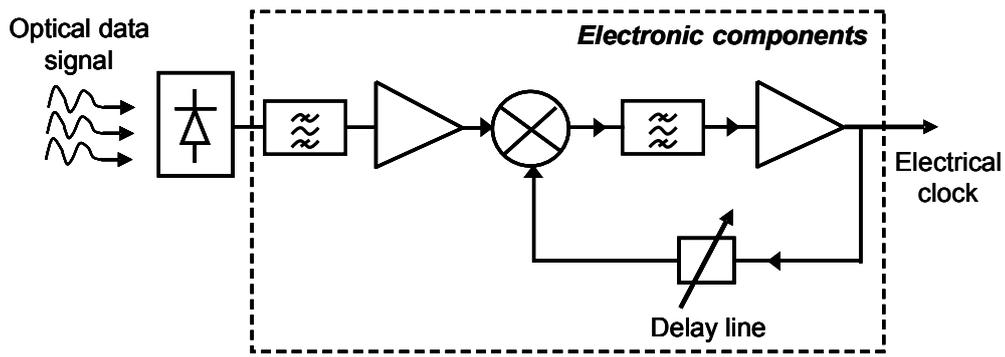
Figure 6.18: Scheme of receiver opto-electronic CR
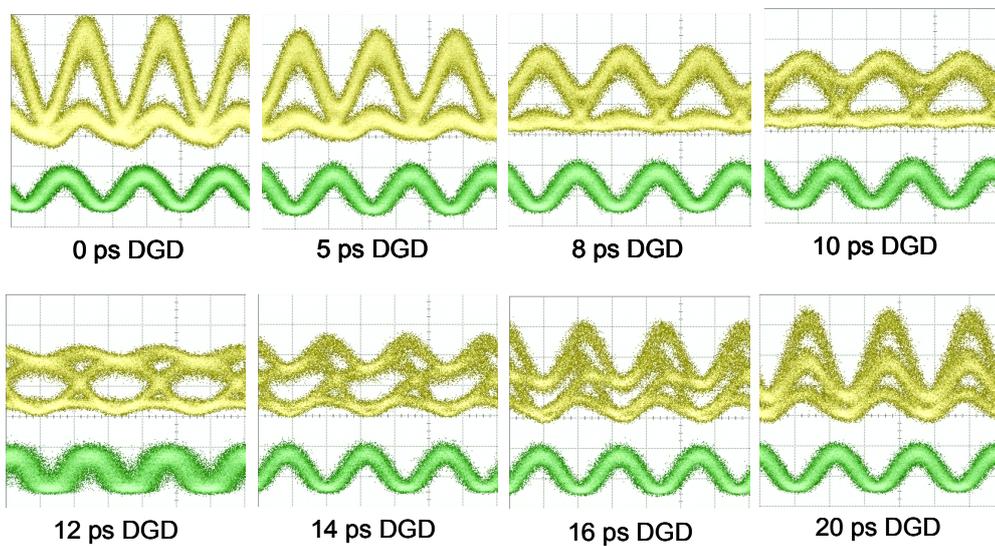
Figure 6.19: Signal eye diagrams (yellow) and clock temporal traces recovered by receiver optoelectronic CR circuit(green) for various DGD values of injected data signal

The electrical signal delivered by photodiode detection is injected into the electronic CR circuit. Its operating principle consists in modulation spectral line filtering at 40 GHz. The electrical filter stage is assisted by a retroaction circuit. The eye diagrams of the received signal and clock temporal traces recovered by the optoelectronic CR circuit for different DGD values are presented in Figure (6.19).

As long as the DGD increases, the received pulses are broadened and distorted. The eye diagrams become more and more closed on both time and amplitude axes. Good quality clocks can be obtained for DGD values up to 10 ps. However, timing jitters observed on the clock traces seem more important for the larger DGD values. At a DGD of 12 ps, the CR is not stable and reliable anymore. The electrical clock signal presents large fluctuations and moreover occasional random phase hopping is observed in real time on the electrical oscilloscope. For DGD values superior to 12 ps, the clock signals seem clearer but the random phase hopping is always present and appears more frequent. These observations
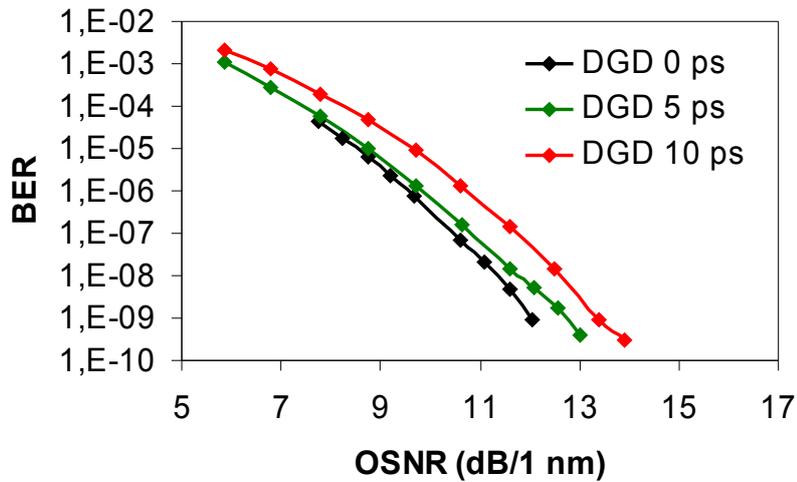
Figure 6.20: BER as a function of Rx input power in back-to-back configuration for various DGD values of optical data signal

allow a qualitative evaluation of PMD impact on the optoelectronic CR operation and on its recovered clock quality.

The penalty induced by PMD effect on the CR performance is related to the fact that PMD exhibiting in an optical signal corresponds to a selective attenuation on the signal electrical spectrum [174]. Because the receiver CR is based on the modulation lines filtering on the signal electrical spectrum, its performance and consequently the recovered clock quality are sensitive to electrical spectrum changes. If the DGD is close to a half of the bit duration, an attenuation maximum appears precisely at the modulation frequency. The attenuation is much important in our case because the signal power is equally distributed to the two principal polarisation states. The DGD value of 12 ps is very close to a half of the bit duration at 42.7 Gbit/s and the worst scenario takes place. A recovered clock with strong temporal fluctuations and random phase hopping is observed. However, the physical mechanisms of random phase hopping are not well-known yet.

In order to have a quantitative evaluation of PMD effect on receiver performance, BER measurements are performed. Signal OSNR ahead of the receiver is artificially degraded by adding ASE noise to the received optical signal. The receiver sensitivity curves are plotted for different signal DGD values as long as the synchronisation of the receiver optoelectronic CR is maintained. By this way, the induced penalties on BER curves include not only the degradations of the receiver CR performance but also of the distorted optical signal arriving on the photodiode. The BER evolutions are shown in Figure (6.20).

The receiver sensitivity curves could be plotted only for small DGD values, up to 10 ps. Because of random phase hopping appearing for DGDs superior to 10 ps, BER measurement is impossible. As long as the receiver is correctly synchronised and BER measurement is possible, the receiver sensitivity curves do not present any error floor. The sensitivity curve
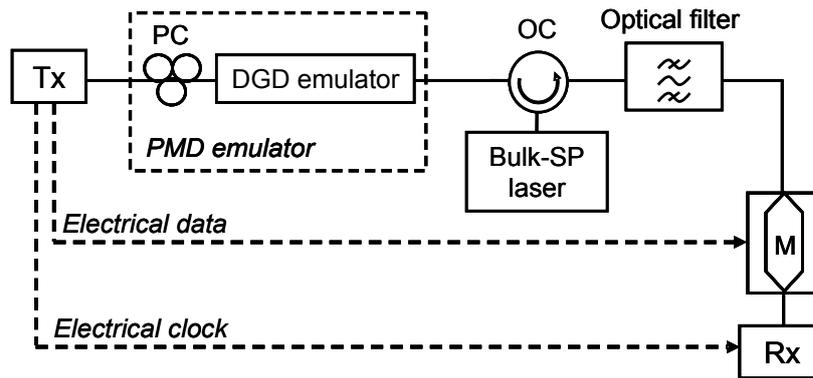
Figure 6.21: Experimental set-up for PMD resistance assessment of an OCR based on bulk-SP laser

for 0 ps DGD is considered as the reference. An induced penalty smaller than 1 dB at 10^{-9} is observed for 5 ps DGD. When DGD value becomes greater, the induced penalty increases. It reaches 1.4 dB at 10^{-9} for 10 ps DGD.

The OSNR penalty originates from two phenomena: the eye diagrams of the incoming signal become more closed and the sampling time is shifted away from its optimum position. As we can see in Figure (6.19), for 10 ps DGD, the signal eye opening is strongly degraded in comparison to the eye of a signal without PMD effect (0 ps DGD). Furthermore, when the DGD increases, the sampling time shift with respect to the eye centre increases too [175]. The combination of these two effects results in a penalty on the receiver sensitivity. The measured penalty of 1.4 dB for 10 ps DGD is very close to the 1 dB OSNR degradation predicted by [23] for a DGD close to a half of bit duration.

This section brought out the impairments caused by PMD effect on the operation of the receiver optoelectronic CR and the consequence on the receiver sensitivity. The PMD effect, especially for DGD values comparable to the bit duration, leads to an increase of the timing jitter of the recovered clock and to random phase hopping. Because of this phase hopping, the CR synchronisation is totally lost for DGD values larger than 10 ps. In addition, the eye diagrams of the incoming signal are more and more closed when the DGD increases. This results in receiver sensitivity degradations which are presented by induced OSNR penalties.

6.5.3 Resistance of bulk-SP laser based OCR to PMD effect

According to Section 6.3, the total polarisation insensitivity of the OCR based on the cascade of the two lasers is achieved thanks to the polarisation insensitivity of the bulk laser. In this section, resistance to PMD effect of the OCR based on this laser alone is investigated. The experimental set-up of this study is a typical remodulation experiment as shown in Figure (6.21).

The transmitter Tx emits a typical 42.7 Gbit/s RZ 33 % PRBS signal. The optical
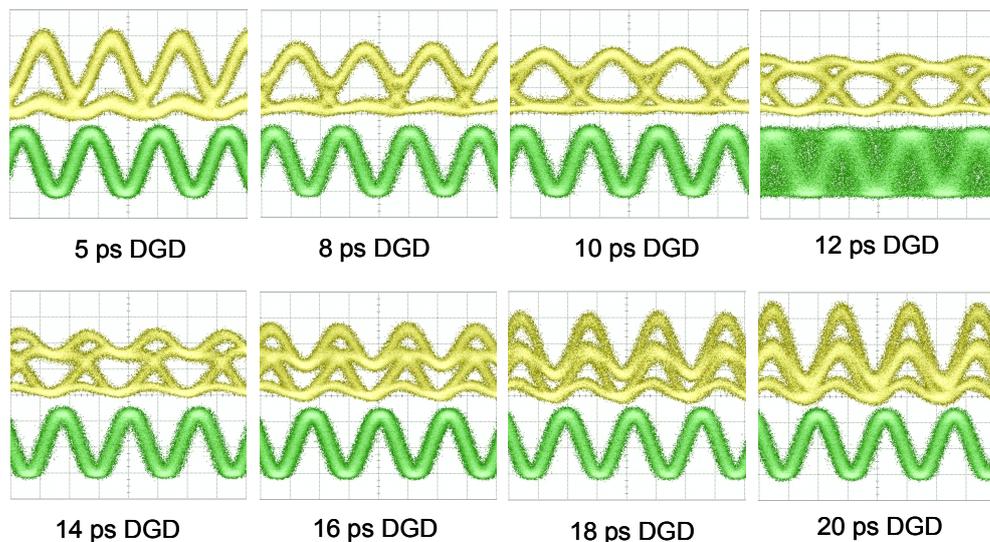
Figure 6.22: Signal eye diagrams in front of the bulk-SP laser OCR (yellow) and extracted clock signals (green) for various DGD values

data signal presents an excellent OSNR of 30 dB/1 nm. This last allows to consider that the signal arriving on the studied OCR device suffers principally PMD signal degradations. The PMD emulator is placed ahead of the OCR. BER measurements on the remodulated clock are performed for each DGD value of the incoming optical signal. In remodulation experiment, the transmitter electrical clock is used directly for the receiver synchronisation. By this way, all receiver synchronisation impairments due to the optical signal PMD can be avoided. The signal eye diagrams in front of the OCR and extracted optical clock signals for different DGD values are presented in Figure (6.22).

By observing the temporal traces of the recovered clock, the OCR behaviour seems very similar to the one of the optoelectronic CR circuit reported in Paragraph 6.5.2. The OCR device provides a stable output clock for DGD up to 10 ps. Synchronisation of the OCR device is totally lost at 12 ps DGD. For all DGD larger than 12 ps, despite the clock temporal traces can be observed, phase hopping appears frequently. Thus the recovered clock is not reliable anymore. Although the synchronisation mechanism of the OCR device is different from the one of the optoelectronic CR circuit, both CRs rely on the modulation line filtering in the signal electrical spectrum. PMD quantified by DGD decreases the modulation line level and therefore degrades CR devices synchronisation performance.

As long as the OCR function is synchronised, the recovered clock quality is assessed by measuring BER on the remodulated clock. The receiver sensitivity curves obtained for various DGD values of the incoming data signal are displayed in Figure (6.23).

For 10 ps DGD, the BER curve presents an error floor at 5.10^{-8} while the curves for DGD of 5 ps and 8 ps do not present neither error floor nor penalty compared to the reference (0 ps DGD). The error floor points out that even if the OCR is synchronised, the
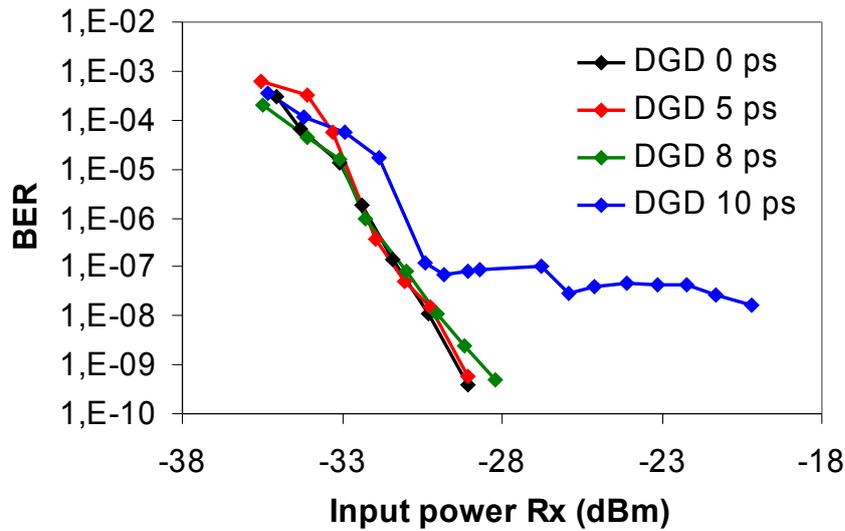
Figure 6.23: BER as a function of Rx input power of remodulated clock given by bulk-SP laser OCR for various DGD of the transmitted data signal

strong PMD degrade the extracted clock quality. This degradation could not be observed clearly on the clock temporal trace. The zero penalty shows that the performance of the OCR device is well maintained if the PMD effect of the incoming signal does not excess 8 ps DGD.

To conclude, the resistance to PMD of the bulk-SP laser based OCR is investigated. It is shown that PMD effect damages the extracted clock quality and causes synchronisation loss when the DGD is superior or equal to a half of bit duration. Nevertheless, the OCR function presents a certain tolerance to PMD effect. It is quantified by a first order DGD of 8 ps. This tolerance is insufficient in an actual transmission system context. PMD exhibit random characteristics. Sub functions of a regenerator will be interesting if they could maintain good performances despite PMD effects in order of a half of bit duration. At 40 Gbit/s, such PMD effect corresponds to a DGD of 12.5 ps.

Summary of optical clock recovery investigations

This second part of the manuscript is devoted to present the experimental assessments of different all-optical clock recovery configurations. The studied OCR functions are principally based on self-pulsating semiconductor lasers.

In the fifth chapter, roles of CR function in optical networks are firstly discussed. It is pointed out that regardless of the CR function position, at receivers, in node of OTDM systems or in in-line repeaters, the recovered clocks must have a low timing jitter. The clock quality defines the timing stability and synchronisation performance of the overall communication system. Then, different techniques which are usually exploited for CR devices are briefly reviewed. They are classified in three categories according to their operation principles: spectral filtering technique, phase-locked loop technique and injection locking in oscillating systems. The principle, virtues as well as drawbacks of each technique are discussed. It is shown that to go beyond 40 Gbit/s, the CR devices which are constituted of only electronic components will be not the solution of choice. On the other hand, CR functions operating at 40 Gbit/s and even higher can be performed thanks to the all-optical approach. This brief review brings out our motivations to use self-pulsating semiconductor lasers as the principal component of OCR functions for 3R regeneration applications. In the second section of the chapter, the operating principle, advantages and limitations of the OCR solutions based on these novel lasers are discussed.

The last chapter is dedicated to present the experimental study of various OCR configurations based on SP lasers. The used characterisation techniques and evaluation methods are developed in Section 6.1. An original characterisation technique called remodulation experiment is proposed to assess the performance of OCR functions.

Section 6.2 reports a comparison of two OCR functions: one is based on a bulk-SP laser and the other is based on a quantum-dot SP laser. Bit error rate measurements obtained via the remodulation technique show a better quality of the clock recovered by the QD-SP laser. Error free operation is possible by using the QD-SP laser based CR. On the contrary, an error floor at BER of 3.10^{-9} is observed when the bulk-SP laser is used. This

performance difference of the two OCRs is in agreement with other studies. It is attributed to the higher spectral purity of quantum-dot structures in comparison to bulk structures.

In Section 6.3, a solution is proposed to enhance the clock quality delivered by the CR using the bulk-SP laser. It consists in placing a passive pre filtering stage which is a Bragg Gratings Fabry-Perot filter ahead of the bulk-SP laser. In the presence of the pre filtering stage, an intermediate clock is extracted from the incoming data signal and provided to the bulk-SP laser. The laser is therefore synchronised regardless of pattern effects. This fact leads to an attenuation of the intensity fluctuations and a timing jitter reduction on the recovered clock. The timing jitter improvement is confirmed by phase noise measurements. The quality enhancement of the recovered clock is clearly demonstrated on the BER curves obtained thanks to the remodulation experiment. It is illustrated by an error floor removal and a penalty reduction of 2.5 dB.

Next, a polarisation sensitivity assessment of various OCRs is presented in Section 6.4. The QD-SP laser shows a good performance for OCR functions thanks to its high spectral purity but the strong sensitivity of QD structures to incoming signal polarisations causes impairments for OCRs operation. By adjusting the input polarisation orientation, it is shown that the QD-SP laser based OCR tolerates an input polarisation angle in the range of [-40°, 40°] with respect to the privileged axis of the QD structure. Out of this range the synchronisation to the incoming signal is totally lost. On the contrary, the OCR constituted of the bulk-SP laser followed by the QD-SP laser presents a total insensitivity to the polarisation of the input signal. The cascade does not introduce any penalty on BER curves for any input polarisation angle. This performance is achieved thanks to the polarisation insensitivity of the bulk based laser.

At last, a primary study is dedicated to the resistance to polarisation mode dispersion of CR functions. PMD effect is an inevitable degradation of transmitted optical signals in long and long haul fibre links. At 40 Gbit/s, it is demonstrated that the synchronisation of the receiver optoelectronic CR is not reliable anymore when the incoming signal presents a DGD superior to 10 ps. Moreover, the PMD presence leads to receiver sensitivity penalties and the induced penalties increase when the DGD becomes more and more important. For the OCR function based on the bulk-SP laser, the synchronisation is lost when the DGD value of the input optical signal exceeds 10 ps. At 10 ps DGD, the receiver sensitivity curve measured on the remodulated clock exhibits an error floor at BER of 5.10^{-8}. On the other hand, up to 8 ps of DGD, neither error floor nor additional penalty compared to the reference curve is observed. Thus, the bulk-SP laser based OCR shows a certain resistance to PMD effect. The tolerance is limited at 8 ps DGD at the bit rate of 40 Gbit/s. Such tolerance is insufficient in a real system context in which a functional device is interesting only if it is able to resist to a PMD effect of at least a half of bit duration. Nevertheless, this modest resistance of the OCR leaves a hope on the way to reach PMD tolerant OCR solutions.

Different OCR configurations principally based on SP semiconductor lasers are examined and their performances are analysed via remodulation experiments. The OCR configuration of choice should be the cascade of the two SP lasers: the bulk-SP laser followed by the QD-SP laser. This CR function presents a high performance in terms of jitter suppression thanks to the QD-SP laser spectral purity. Moreover, it is totally polarisation insensitivity thanks to the bulk-SP laser. This OCR device demonstrated its efficiency in a 3R regenerator [12]. The lasers cascade was associated with a 2R regenerator to build a 3R regenerator in synchronous modulation configuration. Thanks to the implementation of the OCR for synchronous modulation, the accumulation of timing jitter was considerably reduced. Consequently the maximal transmission distance was enhanced more than twice compared to the case when the 2R regenerator is employed alone without the OCR function.

Conclusions

The works carried out in this thesis could be viewed from two aspects associating with studies of two key elements of optical signal regeneration: 2R regenerator and Optical Clock Recovery.

Investigations on 2R regenerators were focussed on configurations exhibiting simplicity, wavelength preservation and compability with WDM, which is a key issue for the possible use of optical regenerators in future optical networks. Such a regenerator scheme could be either integrated in 3R regenerators or directly used as a 2R regenerator. It consists in a cascade of an SOA and a Saturable Absorber (SA), both in self-saturation, and exhibit promising features in agreement with the aforementioned requirements. Earlier, this type of regenerator demonstrated its efficiency for 2R regeneration at 10 Gbit/s and it was shown that the main limiting factor for higher speed operations is the SOA response time [170]. In my thesis, the ultrafast dynamics of different SOA structures is specially investigated in order to explore their limits and their potential for signal reshaping at 40 Gbit/s. Both experimental and numerical results demonstrated that intraband effects play an important role in gain dynamics of SOAs saturated by short pulses (a few picoseconds). Consequently, SOA recovery times could be found as short as 25 ps despite the presence of slow interband relaxations (lifetime in order of several hundred picoseconds).

Among the different studied structures, the highly confined bulk based SOA and the long quantum-dot based SOA (QDot SOA) appear as the best candidates for operations at bit rates exceeding 40 Gbit/s. At maximal bias current, their gain recovery times are respectively 20 ps and 10 ps for 3 dB gain compression. Moreover, by associating the long QDot SOA with a blue shifted filter, the response time could be reduced to 3 ps. This ultrafast recovery promises 160 Gbit/s operation without any patterning effect. Unfortunately, the long QDot SOA sample exhibits excessive gain ripple which makes its assessments in system environment impossible. Only the highly confined bulk based SOA could be studied in noise compression experiment. The reshaping capability at 40 Gbit/s of the regenerator scheme consisting in the bulk based SOA cascaded an SA was proven by both experimental and numerical results. The cascade insertion in back-to-back configuration allowed amplitude noise of the transmitted optical signal to be reduced. The signal quality enhancement was clearly put in evidence by a penalty reduction of 1.3 dB on the receiver sensitivity.

In outlook, some further assessments of the regenerator should be taken into consideration. First of all, the pulse duration used in the noise compression experiment was 4 ps. It is necessary to perform the same investigations with 8 ps pulses, which are the typical when using the RZ 33 % signal format currently used in 40 Gbit/s systems. Secondly, the regenerator has to be assessed in re-circulating loop experiment to prove its cascadability and transmission distance enhancement..

Exploration of different OCRs using self-pulsating lasers have been focussed on quality improvement of extracted optical clocks and on polarisation sensitivity of the OCR devices.

For the first time, remodulation technique is proposed to assess the performance of OCR functions. This original technique allows the recovered optical clock to be modulated in the same way as in a data-driven 3R regenerator and thus, impact of pattern effects on the OCR performance could be taken into account. The studied OCR devices are based on two self-pulsating (SP) semiconductor lasers and their operations were demonstrated previously (within the framework of ROTOR project) at 40 Gbit/s. One SP laser is constituted of bulk material and the other is constituted of quantum-dot based material.

Characterisations showed that the quality of the recovered clock obtained with the bulk-SP laser is insufficient because of the excessive internal phase noise of the laser. In this thesis, we propose using a passive pre-filtering in front of the bulk-SP laser to improve the extracted clock quality. By inserting the pre-filtering stage, the timing jitter of the extracted clock could be reduced and the quality of the remodulated signal was enhanced. This signal quality improvement is illustrated by the absence of error floor on the BER curve and a penalty reduction of 2.5 dB on the receiver sensitivity.

Concerning the OCR based on the QD-SP laser, the greatest drawback for applications in actual systems is the strong polarisation dependence. Its polarisation sensitivity was estimated via BER measurements. It is shown that the input polarisation angle tolerance is about ±45° (compared to the privileged axis of the quantum-dot structure). Out of this range the QD-SP laser could not be synchronised anymore. The OCR solution consisting in introducing the bulk-SP laser in front of the QD-SP laser was demonstrated totally polarisation insensitive via BER measurements.

At last, a primary study about the OCR tolerance to Polarisation Mode Dispersion (PMD) was investigated. It was shown that the tolerance to PMD effect of the OCR constituted of the bulk-SP laser is about 8 ps DGD at 40 Gbit/s. Such a tolerance is not sufficient for an actual 40 Gbit/s optical transmission system yet, but it is an encouraging progress offered by all-optical technique in comparison to classical opto-electrical CR circuit.

Bibliography

[1] T. Miya, Y. Terunuma, T. Hosaka, and T. Miyashita, "Ultimate low-loss single-mode fibre at 1.55 μm," *Electron. Lett.*, vol. 15, p. 106, 1979.

[2] G. P. Agrawal, *Fiber-optic Communication Systems*, 3rd ed., ser. Microwave and Optical Engineering, K. Chang, Ed.   J. Wiley & Sons, 2002.

[3] P. V. Mamyshev, "All-optical data regeneration based on self-phase modulation effect," in *European Conference on Optical Communications*, Madrid, Spain, 1998, pp. 475–476.

[4] M. Asada, Y. Miyamoto, and Y. Suematsu, "Gain and the threshold of three-dimensional quantum-box lasers," *IEEE J. Quantum Electron.*, vol. 22, no. 9, pp. 1915–1921, 1986.

[5] *http://fibre-optique.sfr.fr/avantages-fibre-optique/*, 27th April 2010.

[6] *http://www.smw3.com/smw3/SignIn/Background.aspx*, 27th Apri 2010.

[7] N. S. Bergano, "The Capabilities of the Undersea Telecommunications Industry," in *Optical Fiber Communication Conference*, San Diego, California, 2010, p. OTuD3.

[8] R. Ludwig, U. Feiste, C. Schmidt, C. Schubert, J. Berger, E. Hilliger, M. Kroh, T. Yamamoto, C. Weinert, and H. Weber, "Enabling transmission at 160 Gbit/s," in *Optical Fiber Communication Conference*, Anaheim, California, 2002, pp. 1–2.

[9] L. Bramerie, M. Gay, G. Girault, V. Roncin, S. Feve, and J.-C. Simon, "Performance of a polarization insensitive 3R optical regenerator based on a new SOA-NOLM architecture," in *European Conference on Optical Communications*, Stockholm, Sweden, 2004, p. We2.5.2.

[10] M. Gay, L. Bramerie, J.-C. Simon, A. O'Hare, D. Massoubre, J.-L. Oudar, and A. Shen, "Cascadability and wavelength tunability assessment of a 2R regeneration device based on saturable absorber and semiconductor optical amplifier," in *Optical Fiber Communication Conference*, California, USA, 2006, p. OThB1.

[11] L. Bramerie, Q. T. Le, S. Lobo, M. Gay, M. Joindot, J.-C. Simon, A. Poudoulec, M. Van der Keur, C. Devemy, D. Massoubre, J.-L. Oudar, G. Aubin, A. Shen, and J. Decobert, "Cascadability and wavelength tunability assessment of a 2R regeneration device based on a 8 channel saturable absorber module," in *Optical Fiber Communication Conference*, Anaheim, California, 2007, p. PDP1.

[12] Q. T. Le, L. Bramerie, V. Roncin, S. Lobo, M. Gay, M. Joindot, J.-C. Simon, D. Massoubre, J.-L. Oudar, A. Shen, F. Van Dijk, and G.-H. Duan, "Cascadability assessment of an all optical 3R regenerator based on synchronous modulation in a saturable absorber and optical clock recovery," in *European Conference on Optical Communications*, Berlin, Germany, 2007, p. Tu.4.3.5.

[13] V. Roncin, A. O'Hare, S. Lobo, E. Jacquette, L. Bramerie, P. Rochard, Q. T. Le, M. Gay, J.-C. Simon, A. Shen, J. Renaudier, F. Lelarge, and G.-H. Duan, "Multi-data-rate system performance of a 40-GHz all-optical clock recovery based on a quantum-dot Fabry–Pérot laser," *IEEE Photonics Technol. Lett.*, vol. 19, no. 19, pp. 1409–1411, 2007.

[14] K. Furuya, Y. Suematsu, Y. Sakakibara, and M. Yamada, "Influence of intraband electronic relaxation on relaxation oscillation of injection lasers," *The Transactions of the IECE of Japan*, vol. E 62, no. 4, pp. 241–245, 1979.

[15] E. Jahn, N. Agrawal, and W. Pieper, "Ultrafast gain and phase dynamics in monolithically integrated sla based mach-zehnder interferometers for otdm applications," in *Optical Amplifiers and Their Applications*, 1996, pp. 262–265.

[16] H. Sunnerud, M. Karlsson, and P. A. Andrekson, "A comparison between NRZ and RZ data formats with respect to PMD-induced system degradation," in *Optical Fiber Communication Conference*, Anaheim, California, 2001, pp. WT3–1.

[17] I. P. Kaminow and T. L. Koch, *Optical Fiber Telecommunications III-A*. Academic Press, 1997.

[18] M. M. Dummer, J. Klamkin, E. J. Norberg, J. W. Raring, A. Tauke-Pedretti, and L. A. Coldren, "Periodic loading and selective undercut etching for high-impedance traveling-wave electroabsorption modulators," in *Optical Fiber Communication Conference*, San Diego, California, 2008, p. OThC6.

[19] D. M. Gill, D. Jacobson, C. A. White, C. D. W. Jones, Y. Shi, W. J. Minford, and A. Harris, "Ridged LiNbO3 modulators fabricated by a novel oxygen-ion implant/wet-etch technique," *J. Lightw. Technol.*, vol. 22, no. 3, pp. 887–894, 2004.

[20] R. H. Derksen, G. Lehmann, C.-J. Weiske, C. Schubert, R. Ludwig, S. Ferber, C. Schmidt-Langhorst, M. Moller, and J. Lutz, "Integrated 100 Gbit/s ETDM Re-

ceiver in a Transmission Experiment over 480 km DMF," in *Optical Fiber Communication Conference*, San Diego, California, 2009, p. PDP37.

[21] *http://www.u2t.de/en/products/by-product/photodetectors/#c196*, 17th May 2010.

[22] A. Beling, H.-G. Bach, G. G. Mekonnen, R. Kunkel, and D. Schmidt, "Miniaturized waveguide-integrated pin photodetector with 120-GHz bandwidth and high responsivity," *IEEE Photonics Technol. Lett.*, vol. 17, no. 10, pp. 2152–2154, 2005.

[23] Irène et Michel Joindot et douze co-auteurs, *Les tétécommunications par fibres optiques.* DUNOD et CNET-ENST, 1996.

[24] O. AitSab and V. Lemaire, "Block turbo code performances for long-haul DWDM optical transmission systems," in *Optical Fiber Communication Conference*, Baltimore, Maryland, 2000, pp. ThS5–1.

[25] J.-C. Simon, "GaInAsP semiconductor laser amplifiers for single-mode fiber communications," *J. Lightw. Technol.*, vol. 5, no. 5, pp. 1286–1295, 1987.

[26] M. N. Islam, "Raman amplifiers for telecommunications," *IEEE J. Sel. Topics Quantum Electron.*, vol. 8, no. 3, pp. 548–55, 2002.

[27] N. J. Doran and D. Wood, "Nonlinear-optical loop mirror," *Optics Letters*, vol. 13, no. 1, pp. 56–58, 1988.

[28] Z. Huang, A. Gray, I. Khrushchev, and I. Bennion, "10-Gb/s transmission over 100 Mm of standard fiber using 2R regeneration in an optical loop mirror," *IEEE Photonics Technol. Lett.*, vol. 16, no. 11, pp. 2526–2528, 2004.

[29] F. Seguineau, B. Lavigne, J. Remy, and O. Leclerc, "Experimental loop demonstration of cascaded 42.7Gbit/s NOLM-based 2R regeneration performance versus timing jitter and optical ASE noise," in *European Conference on Optical Communications*, Stockholm, Sweden, 2004, p. We 2.5.5.

[30] M. Matsumoto, "Efficient all-optical 2R regeneration using self-phase modulation in bidirectional fiber configuration," *Optics Express*, vol. 14, no. 23, pp. 11 018–11 023, 2006.

[31] L. Provost, F. Parmigiani, P. Petropoulos, and D. J. Richardson, "Investigation of Simultaneous 2R Regeneration of Two 40-Gb/s Channels in a Single Optical Fiber," *IEEE Photonics Technol. Lett.*, vol. 20, no. 4, pp. 270–272, 2008.

[32] F. Parmigiani, P. Vorreau, L. Provost, K. Mukasa, M. Takahashi, M. Tadakuma, P. Petropoulos, D. J. Richardson, W. Freude, and J. Leuthold, "2R regeneration of two 130 Gbit/s channels within a single fiber," in *Optical Fiber Communication Conference*, San Diego, California, 2009, p. JThA56.

[33] D. Apostolopoulos, K. Vyrsokinos, P. Zakynthinos, N. Pleros, and H. Avramopoulos, "An SOA-MZI NRZ Wavelength Conversion Scheme With Enhanced 2R Regeneration Characteristics," *IEEE Photonics Technol. Lett.*, vol. 21, no. 19, pp. 1363–1365, 2009.

[34] D. Wolfson, P. B. Hansen, A. Kloch, T. Fjelde, C. Janz, A. Coquelin, I. Guillemot, F. Garorit, F. Poingt, and M. Renaud, "All-optical 2R regeneration at 40 Gbit/s in an SOA-basedMach-Zehnder interferometer," in *Optical Fiber Communication Conference*, 1999, p. PD36.

[35] K. Chan, C.-K. Chan, W. Hung, F. Tong, and L. Chen, "Waveform restoration in semiconductor optical amplifier using fiberloop mirror," *IEEE Photonics Technol. Lett.*, vol. 14, no. 7, pp. 995–997, 2002.

[36] J. Leuthold and M. Kauer, "power equalisation and signal regeneration with delay interferometer all-optical wavelength converters," *Electron. Lett.*, vol. 38, no. 24, pp. 1567–1568, 2002.

[37] H. Chayet, S. Ben-Ezra, N. Shachar, S. Tzadok, S. Tsadka, and J. Leuthold, "Regenerative all-optical wavelength converter based on semiconductor optical amplifier and sharp frequency response filter," in *Optical Fiber Communication Conference*, Los Angeles, California, 2004, p. ThS2.

[38] G. Contestabile, R. Proietti, N. Calabretta, and E. Ciaramella, "All Optical Regeneration by Cross Gain Compression in Semiconductor Amplifiers," in *European Conference on Optical Communications*, Glasgow, UK, 2005, p. We 2.4.7.

[39] G. Contestabile, R. Proietti, M. Presi, and E. Ciaramella, "40 Gb/s Wavelength Preserving 2R Regeneration for both RZ and NRZ Signals," in *Optical Fiber Communication Conference*, San Diego, California, 2008, p. OWK1.

[40] D. Rouvillain, P. Brindel, O. Leclerc, J. P. Hamaide, H. Choumane, G. Aubin, and J.-L. Oudar, "Novel polarization-insensitive synchronous modulator for 20 Gbit/s all-optical regeneration," in *Optical Fiber Communication Conference*, Anaheim, California, 2002, p. TuN3.

[41] O. Leclerc, B. Lavigne, E. Balmefrezol, P. Brindel, L. Pierre, D. Rouvillain, and F. Seguineau, "Optical regeneration at 40 Gb/s and beyond," *J. Lightw. Technol.*, vol. 21, no. 11, pp. 2779–2790, 2003.

[42] H. T. Nguyen, J.-L. Oudar, S. Bouchoule, G. Aubin, and S. Sauvage, "A passive all-optical semiconductor device for level amplitude stabilization based on fast saturable absorber," *Appl. Phys. Lett.*, vol. 92, p. 111107, 2008.

[43] M. Gay, L. Bramerie, H. T. Nguyen, S. Lobo, G. Aubin, Q. T. Le, M. Joindot, J.-L. Oudar, and J.-C. Simon, "Regeneration and Cascadability Assessment of a New

Passive 2R Regenerator Based on a Dual-Stage Saturable Absorber gate," in *European Conference on Optical Communications*, Brussels, Belgium, 2008, p. Tu.4.D.2.

[44] C. Zah, C. Caneau, F. Shokoohi, S. Menocal, F. Favire, L. Reith, T. Lee, B. Inc, and R. Bank, "1.3 μm GaInAsP near-travelling-wave laser amplifiers made bycombination of angled facets and antireflection coatings," *Electron. Lett.*, vol. 24, no. 20, pp. 1275–1276, 1988.

[45] P. P. Iannone, K. C. Reichmann, X. Zhou, and S. Gray, "A discrete SOA-raman hybrid amplifier with 80-nm bandwidth," in *European Conference on Optical Communications*, Cannes, France, 2006, p. Th 2.3.7.

[46] M. J. Connelly, *Semiconductor optical amplifiers*. Kluwer academic publishers, 2002.

[47] N. K. Dutta and Q. Wang, *Semiconductor Optical Amplifiers*. World scientific, 2006.

[48] C. Ware, "Récupération d'horloge par boucle à verrouillage de phase utilisant le mélange à quatre ondes dans un amplificateur optique à semi-conducteurs," Ph.D. dissertation, Télécom Paris, 2003.

[49] P. Doussière, "Recent advances in conventional and gain clamped semiconductor optical amplifiers," in *Optical Amplifiers and Their Applications*, vol. 5, 1996, pp. 170–188.

[50] M. Sugawara, *Self-Assembled InGaAs/GaAs Quantum Dots*. Academic Press, 1999.

[51] F. Lelarge, B. Dagens, J. Renaudier, R. Brenot, A. Accard, F. Van-Dijk, D. Make, O. Le-Gouezigou, J.-G. Provost, F. Poingt, J. Landreau, O. Drisse, E. Derouin, B. Rousseau, F. Pommereau, and G.-H. Duan, "Recent advances on InAs/InP quantum dash based semiconductor lasers and optical amplifiers operating at 1.55 μm," *IEEE J. Sel. Topics Quantum Electron.*, vol. 13, no. 1, pp. 111–124, 2007.

[52] T. Akiyama, M. Ekawa, M. Sugawara, H. Sudo, K. Kawaguchi, A. Kuramata, H. Ebe, K. Morito, H. Imai, and Y. Arakawa, "An Ultrawide-Band (120 nm) Semiconductor Optical Amplifier Having an Extremely-High Penalty-Free Output Power of 23 dBm Realized with Quantum-Dot Active Layers," in *Optical Fiber Communication Conference*, Los Angeles, California, 2004, p. PDP12.

[53] J. Mørk, M. L. Nielsen, and T. W. Berg, "The dynamics of semiconductor optical amplifiers: Modeling and applications," *Optics and Photonics News*, vol. 14, no. 7, pp. 42–48, 2003.

[54] T. Akiyama, M. Ekawa, M. Sugawara, K. Kawaguchi, H. Sudo, H. Kuwatsuka, H. Ebe, A. Kuramata, and Y. Arakawa, "Quantum Dots for Semiconductor Optical Amplifiers," in *Optical Fiber Communication Conference*, Anaheim, California, 2005, p. OWM2.

[55] G. Contestabile, A. Maruta, S. Sekiguchi, K. Morito, M. Sugawara, and K. Kitayama, "160 Gb/s Cross Gain Modulation in Quantum Dot SOA at 1550 nm," in *European Conference on Optical Communications*, Vienna, Austria, 2009, p. PD 1.4.

[56] G. P. Agrawal and N. A. Olsson, "Self-phase modulation and spectral broadening of optical pulses insemiconductor laser amplifiers," *IEEE J. Quantum Electron.*, vol. 25, no. 11, pp. 2297–2306, 1989.

[57] P. Brosson, "Analytical model of a semiconductor optical amplifier," *J. Lightw. Technol.*, vol. 12, no. 1, pp. 49–54, 1994.

[58] J. Mørk and A. Mecozzi, "Theory of the ultrafast optical response of active semiconductor waveguides," *J. Opt. Soc. Am. B*, vol. 13, no. 8, pp. 1803–1816, 1996.

[59] M. Sugawara, T. Akiyama, N. Hatori, Y. Nakata, H. Ebe, and H. Ishikawa, "Quantum-dot semiconductor optical amplifiers for high-bit-rate signal processing up to 160 Gb/s and a new scheme of 3 R regenerators," *Measurement Science and Technology*, vol. 13, no. 11, pp. 1683–1691, 2002.

[60] P. Borri, W. Langbein, J. Mørk, and J. M. Hvam, "Heterodyne pump-probe and four-wave mixing in semiconductor optical amplifiers using balanced lock-in detection," *Optics Communications*, vol. 169, pp. 317–324, 1999.

[61] C. Henry, "Theory of the linewidth of semiconductor lasers," *IEEE J. Quantum Electron.*, vol. 18, no. 2, pp. 259–264, 1982.

[62] J. Wang, A. Maitra, C. G. Poulton, W. Freude, and J. Leuthold, "Temporal dynamics of the alpha factor in semiconductor optical amplifiers," *J. Lightw. Technol.*, vol. 25, no. 3, pp. 891–900, 2007.

[63] A. Mecozzi and J. Mørk, "Saturation induced by picosecond pulses in semiconductor optical amplifiers," *J. Opt. Soc. Am. B*, vol. 14, no. 4, pp. 761–770, 1997.

[64] L. Schares, C. Schubert, C. Schmidt, H. G. Weber, L. Occhi, and G. Guekos, "Phase dynamics of semiconductor optical amplifiers at 10-40 GHz," *IEEE J. Quantum Electron.*, vol. 39, no. 11, pp. 1394–1408, 2003.

[65] A. J. Zilkie, J. Meier, M. Mojahedi, P. J. Poole, P. Barrios, D. Poitras, T. J. Rotter, C. Yang, A. Stintz, K. J. Malloy, P. W. E. Smith, and J. S. Aitchison, "Carrier dynamics of quantum-dot, quantum-dash, and quantum-well semiconductor optical amplifiers operating at 1.55 μm," *IEEE J. Quantum Electron.*, vol. 43, no. 11, pp. 982–991, 2007.

[66] L. Zhang, I. Kang, A. Bhardwaj, N. Sauer, S. Cabot, J. Jaques, and D. T. Neilson, "Reduced recovery time semiconductor optical amplifier using p-type-doped multiple quantum wells," *IEEE Photonics Technol. Lett.*, vol. 18, no. 22, pp. 2323–2325, 2006.

[67] M. Thual, P. Chanclou, O. Gautreau, L. Caledec, C. Guignard, and P. Besnard, "Appropriate micro-lens to improve coupling between laser diodes and singlemode fibres," *Electron. Lett.*, vol. 39, no. 21, pp. 1504–1506, 2003.

[68] M. Thual, D. Malarde, B. Abhervé-Guégen, P. Rochard, and P. Chanclou, "Truncated Gaussian beams through microlenses based on a graded-index section," *Optical Engineering*, vol. 46, p. 015402, 2007.

[69] T. Akiyama, H. Kuwatsuka, T. Simoyama, Y. Nakata, K. Mukai, M. Sugawara, O. Wada, and H. Ishikawa, "Nonlinear gain dynamics in quantum-dot optical amplifiers and its application to optical communication devices," *IEEE J. Quantum Electron.*, vol. 37, no. 8, pp. 1059–1065, 2001.

[70] D. R. Matthews, H. D. Summers, P. M. Smowton, and M. Hopkinson, "Experimental investigation of the effect of wetting-layer states on the gain-current characteristic of quantum-dot lasers," *Appl. Phys. Lett.*, vol. 81, no. 26, p. 4904, 2002.

[71] P. Lever, M. Buda, H. H. Tan, and C. Jagadish, "Investigation of the blueshift in electroluminescence spectra from MOCVD grown InGaAs quantum dots," *IEEE J. Quantum Electron.*, vol. 40, no. 10, pp. 1410–1416, 2004.

[72] A. J. Zilkie, J. Meier, P. W. E. Smith, M. Mojahedi, J. S. Aitchison, P. J. Poole, C. N. Allen, P. Barrios, and D. Poitras, "Femtosecond gain and index dynamics in an InAs/InGaAsP quantum dot amplifier operating at 1.55 μm," *Optics Express*, vol. 14, no. 23, pp. 11453–11459, 2006.

[73] L. Occhi, Y. Ito, H. Kawaguchi, L. Schares, J. Eckner, and G. Guekos, "Intraband gain dynamics in bulk semiconductor optical amplifiers: measurements and simulations," *IEEE J. Quantum Electron.*, vol. 38, no. 1, pp. 54–60, 2002.

[74] T. Akiyama, Y. Hatori, N. Nakata, H. Ebe, and M. Sugawara, "Wavelength Conversion Based on Ultrafast (< 3 ps) Cross-Gain Modulation in Quantum-Dot Optical Amplifiers," in *European Conference on Optical Communications*, Rimini, Italy, 2003, p. PD Th.4.3.7.

[75] M. Van der Poel, J. Mørk, A. Somers, A. Forchel, J. P. Reithmaier, and G. Eisenstein, "Ultrafast gain and index dynamics of quantum dash structures emitting at 1.55 μm," *Appl. Phys. Lett.*, vol. 89, p. 081102, 2006.

[76] I. Valiente, L. Lablonde, J.-C. Simon, and L. Billes, "Effects of Amplified Spontaneous Emission on Gain Recovery Dynamics of Semiconductor Optical Amplifiers," in *Optical Amplifiers and Their Applications*, vol. 5, 1996, pp. 189–192.

[77] F. Girardin, G. Guekos, and A. Houbavlis, "Gain recovery of bulk semiconductor optical amplifiers," *IEEE Photonics Technol. Lett.*, vol. 10, no. 6, pp. 784–786, 1998.

[78] F. Ginovart and J. C. Simon, "Semiconductor optical amplifier length effects on gain dynamics," *Journal of Physics D: Applied Physics*, vol. 36, pp. 1473–1476, 2003.

[79] R. Giller, R. J. Manning, G. Talli, R. P. Webb, and M. J. Adams, "Analysis of the dimensional dependence of semiconductor optical amplifier recovery speeds," *Optics Express*, vol. 15, no. 4, pp. 1773–1782, 2007.

[80] Y. Liu, E. Tangdiongga, Z. Li, H. De Waardt, A. M. J. Koonen, G. D. Khoe, H. J. S. Dorren, X. Shu, and I. Bennion, "Error-free 320 Gb/s SOA-based wavelength conversion using optical filtering," in *Optical Fiber Communication Conference*, Anaheim, California, 2006, p. PDP28.

[81] Y. Liu, E. Tangdiongga, Z. Li, S. Zhang, H. Waardt, G. D. Khoe, and H. J. S. Dorren, "Error-free all-optical wavelength conversion at 160 Gb/s using a semiconductor optical amplifier and an optical bandpass filter," *J. Lightw. Technol.*, vol. 24, no. 1, pp. 230–236, 2006.

[82] A. D. Ellis, A. E. Kelly, D. Nesset, D. Pitcher, D. G. Moodie, and R. Kashyap, "Error free 100 Gb/s wavelength conversion using grating assisted cross-gain modulation in 2 mm long semiconductor amplifier," *Electron. Lett.*, vol. 34, no. 20, pp. 1958–1959, 1998.

[83] M. L. Nielsen, B. Lavigne, and B. Dagens, "Polarity-preserving SOA-based wavelength conversion at 40 Gbit/s using bandpass filtering," *Electron. Lett.*, vol. 39, no. 18, pp. 1334–1335, 2003.

[84] A. Clarke, G. Girault, P. Anandarajah, C. Guignard, L. Bramerie, L. Barry, J.-C. Simon, and J. Harvey, "FROG Characterisation of SOA-based Wavelength Conversion using XPM in Conjunction with Shifted Filtering up to Line Rates of 80 GHz," in *IEEE Lasers & Electro-Optics Society*, Montreal, Canada, 2006, p. MP 2.

[85] Y. Liu, J. P. Turkiewicz, S. Zhang, E. Tangdiongga, E. J. M. Verdurmen, H. De Waardt, Z. Li, D. Lenstra, G. D. Khoe, and H. J. S. Dorren, "40 Gbit/s SOA-based wavelength conversion assisted by a narrow optical bandpass filter," in *IEEE Lasers & Electro-Optics Society*, Ghent, Belgium, 2004, pp. 251–254.

[86] A. E. Willner and W. Shieh, "Optimal spectral and power parameters for all-optical wavelength shifting: single stage, fanout, and cascadability," *J. Lightw. Technol.*, vol. 13, no. 5, pp. 771–781, 1995.

[87] A. Bilenca, R. Alizon, V. Mikhelashhvili, D. Dahan, G. Eisenstein, R. Schwertberger, D. Gold, J. P. Reithmaier, and A. Forchel, "Broad-band wavelength conversion based on cross-gain modulation and four-wave mixing in InAs-InP quantum-dash semiconductor optical amplifiers operating at 1550 nm," *IEEE Photonics Technol. Lett.*, vol. 15, no. 4, pp. 563–565, 2003.

[88] K. Inoue, T. Mukai, and T. Saitoh, "Gain saturation dependence on signal wavelength in a travelling-wave semiconductor laser amplifier," *Electron. Lett.*, vol. 23, no. 7, pp. 328–329, 1987.

[89] J. Mark and J. Mørk, "Subpicosecond gain dynamics in InGaAsP optical amplifiers: Experiment and theory," *Appl. Phys. Lett.*, vol. 61, no. 19, pp. 2281–2283, 1992.

[90] F. Ginovart and J. C. Simon, "Wavelength dependence of gain recovery time in a semiconductor optical amplifier based wavelength shifter," in *European Conference on Lasers and Electro-Optics*, 2003, p. 181.

[91] T. Katayama and H. Kawaguchi, "Measurement of ultrafast cross-gain saturation dynamics of a semiconductor optical amplifier using two-color pump-probe technique," *IEEE Photonics Technol. Lett.*, vol. 16, no. 3, pp. 855–857, 2004.

[92] X. Li, D. Alexandropoulos, M. J. Adams, and I. F. Lealman, "Wavelength dependence of gain recovery time in semiconductor optical amplifiers," in *Proceedings of SPIE*, vol. 5722, 2005, pp. 343–350.

[93] W. Mathlouthi, F. Vacondio, P. Lemieux, and L. A. Rusch, "SOA gain recovery wavelength dependence: simulation and measurement using a single-color pump-probe technique," *Optics Express*, vol. 16, no. 25, pp. 20 656–20 665, 2008.

[94] A. V. Uskov, J. Mørk, and J. Mark, "Theory of short-pulse gain saturation in semiconductor laseramplifiers," *IEEE Photonics Technol. Lett.*, vol. 4, no. 5, pp. 443–446, 1992.

[95] P. Borri, S. Scaffetti, J. Mørk, W. Langbein, J. M. Hvam, A. Mecozzi, and F. Martelli, "Measurement and calculation of the critical pulsewidth for gain saturation in semiconductor optical amplifiers," *Optics Communications*, vol. 164, no. 1-3, pp. 51–55, 1999.

[96] S. Nakamura, Y. Ueno, and K. Tajima, "Femtosecond switching with semiconductor-optical-amplifier-based symmetric Mach–Zehnder-type all-optical switch," *Appl. Phys. Lett.*, vol. 78, no. 25, pp. 3929–3931, 2001.

[97] R. J. Manning and D. A. O. Davies, "Three-wavelength device for all-optical signal processing," *Optics Letters*, vol. 19, no. 12, pp. 889–991, 1994.

[98] K. Inoue and M. Yoshino, "Gain dynamics of a saturated semiconductor laser amplifier with 1.47-μm LD pumping," *IEEE Photonics Technol. Lett.*, vol. 8, no. 4, pp. 506–508, 1996.

[99] M. A. Dupertuis, J. L. Pleumeekers, T. P. Hessler, P. E. Selbmann, B. Deveaud, B. Dagens, and J. Y. Emery, "Extremely fast high-gain and low-current SOA by

optical speed-up at transparency," *IEEE Photonics Technol. Lett.*, vol. 12, no. 11, pp. 1453–1455, 2000.

[100] G. Talli and M. J. Adams, "Amplified spontaneous emission in semiconductor optical amplifiers: modelling and experiments," *Optics Communications*, vol. 218, no. 1-3, pp. 161–166, 2003.

[101] M. Van der Poel, E. Gehrig, O. Hess, D. Birkedal, and J. M. Hvam, "Ultrafast gain dynamics in quantum-dot amplifiers: Theoretical analysis and experimental investigations," *IEEE J. Quantum Electron.*, vol. 41, no. 9, pp. 1115–1123, 2005.

[102] C. T. Hultgren, D. J. Dougherty, and E. P. Ippen, "Above-and below-band femtosecond nonlinearities in active AlGaAs waveguides," *Appl. Phys. Lett.*, vol. 61, no. 23, pp. 2767–2769, 1992.

[103] P. Borri, W. Langbein, J. M. Hvam, F. Heinrichsdorff, M.-H. Mao, and D. Bimberg, "Ultrafast gain dynamics in InAs-InGaAs quantum-dot amplifiers," *IEEE Photonics Technol. Lett.*, vol. 12, no. 6, pp. 594–596, 2000.

[104] B. N. Gomatam and A. P. DeFonzo, "Theory of hot carrier effects on nonlinear gain in GaAs-GaAlAslasers and amplifiers," *IEEE J. Quantum Electron.*, vol. 26, no. 10, pp. 1689–1704, 1990.

[105] K. L. Hall, Y. Lai, E. P. Ippen, G. Eisenstein, and U. Koren, "Femtosecond gain dynamics and saturation behavior in InGaAsP multiple quantum well optical amplifiers," *Appl. Phys. Lett.*, vol. 57, no. 27, pp. 2888–2890, 1990.

[106] T. Vallaitis, C. Koos, R. Bonk, W. Freude, M. Laemmlin, C. Meuer, D. Bimberg, and J. Leuthold, "Slow and fast dynamics of gain and phase in a quantum dot semiconductor optical amplifier," *Optics Express*, vol. 16, no. 1, pp. 170–178, 2008.

[107] A. Mecozzi and J. Mørk, "Saturation effects in nondegenerate four-wave mixing between short optical pulses in semiconductor laser amplifiers," *IEEE J. Sel. Topics Quantum Electron.*, vol. 3, no. 5, pp. 1190–1207, 1997.

[108] K. E. Stubkjaer, "Semiconductor optical amplifier-based all-optical gates for high-speed optical processing," *IEEE J. Sel. Topics Quantum Electron.*, vol. 6, no. 6, pp. 1428–1435, 2000.

[109] C. Janz, "All-optical signal processing with photonic integrated circuits," in *Optical Fiber Communication Conference*, Baltimore, Maryland, 2000, p. ThF6.

[110] J. Leuthold, B. Mikkelsen, R. E. Behringer, G. Raybon, C. H. Joyner, and P. A. Besse, "Novel 3R regenerator based on semiconductor optical amplifier delayed-interference configuration," *IEEE Photonics Technol. Lett.*, vol. 13, no. 8, pp. 860–862, 2001.

[111] Z. Bakonyi, G. Onishchukov, C. Knoll, M. Golles, F. Lederer, and R. Ludwig, "In-line saturable absorber in transmission systems with cascaded semiconductor optical amplifiers," *IEEE Photonics Technol. Lett.*, vol. 12, no. 5, pp. 570–572, 2000.

[112] F. Ohman, S. Bischoff, B. Tromborg, and J. Mørk, "Noise and regeneration in semiconductor waveguides with saturable gain and absorption," *IEEE J. Quantum Electron.*, vol. 40, no. 3, pp. 245–255, 2004.

[113] D. Massoubre, J. L. Oudar, J. Dion, J. C. Harmand, A. Shen, J. Landreau, and J. Decobert, "Scaling of the saturation energy in microcavity saturable absorber devices," *Appl. Phys. Lett.*, vol. 88, p. 153513, 2006.

[114] Q. T. Le, L. Bramerie, S. Lobo, M. Gay, M. Joindot, J.-C. Simon, A. Poudoulec, M. Van Der Keur, C. Devemy, D. Massoubre, J. L. Oudar, G. Aubin, A. Shen, and J. Decobert, "WDM compatible 2R regeneration device based on eight-channel saturable absorber module," *Electron. Lett.*, vol. 43, pp. 1305–1306, 2007.

[115] Q. T. Le, "Contribution à l'étude de fonctions optiques pour la régénération du signal dans les systèmes de transmission à haut débit," Ph.D. dissertation, ENSSAT - Université de Rennes 1, 2010.

[116] R. Brenot, M. D. Manzanedo, J.-G. Provost, O. Legouezigou, F. Pommereau, F. Poingt, L. Legouezigou, E. Derouin, O. Drisse, B. Rousseau, F. Martin, F. Lelarge, and G.-H. Duan, "Chirp reduction in quantum dot-like semiconductor optical amplifiers," in *European Conference on Optical Communications*, Berlin, Germany, 2007, p. We 8.6.6.

[117] C. Bornholdt, B. Sartorius, S. Schelbase, M. Mohrle, and S. Bauer, "Self-pulsating DFB laser for all-optical clock recovery at 40Gbit/s," *Electron. Lett.*, vol. 36, no. 4, pp. 327–328, 2000.

[118] J. Renaudier, B. Lavigne, M. Jourdran, P. Gallion, F. Lelarge, B. Dagens, A. Accard, O. Legouezigou, and G.-H. Duan, "First demonstration of all-optical clock recovery at 40 GHz with standard-compliant jitter characteristics based on a quantum-dots self-pulsating semiconductor laser," in *European Conference on Optical Communications*, Glasgow, UK, 2005, pp. Postdeadline paper – Th4.3.4.

[119] O. P. Brox, S. Bauer, G. Bramann, J. Kreissl, B. Sartorius, M. Schmidt, K. Schuh, B. Junginger, and E. Lach, "160 to 40Gb/s Demultiplexing Using a Self-Pulsating Laser Based Clock Recovery," in *Optical Fiber Communication Conference*, Atlanta, Georgia, 2003, p. MF85.

[120] V. Roncin, S. Lobo, L. Bramerie, and J.-C. Simon, "Phase Noise Reduction in All Optical Clock Recovery at 43 Gb/s for 3R Regeneration Applications," in *European Conference on Optical Communications*, Cannes, France, 2006, p. We 3.P.91.

[121] V. Roncin, S. Lobo, L. Bramerie, P. Rochard, A. Shen, F. Van Dijk, G.-H. Duan, and J.-C. Simon, "Demonstration of Chromatic Dispersion and Optical Noise insensitivity of a Quantum-Dash based Fabry-Perot Laser in All-optical Clock Recovery at 40 Gbit/s," in *European Conference on Optical Communications*, Berlin, Germany, 2007, p. Tu 4.3.4.

[122] M. N. Ngo, V. Roncin, Q. T. Le, L. Bramerie, D. Chevallier, L. Lablonde, A. Shen, G.-H. Duan, and J.-C. Simon, "Bit-Error-Rate Performance Enhancement of All-Optical Clock Recovery at 42.66 Gb/s Using Passive Prefiltering," *IEEE Photonics Technol. Lett.*, vol. 20, no. 18, pp. 1557–1559, 2008.

[123] M. N. Ngo, V. Roncin, Q. T. Le, S. Lobo, M. Gay, L. Bramerie, J.-C. Simon, A. Shen, and G.-H. Duan, "High Performance and Polarisation-Insensitive BER Assessment of a 42.66 Gbit/s All-Optical Clock Recovery," in *European Conference on Optical Communications*, Brussels, Belgium, 2008, p. Mo.3.C.6.

[124] V. Roncin, S. Lobo, M. N. Ngo, L. Bramerie, A. O'Hare, M. Joindot, and J. C. Simon, "Patterning effects in All-Optical Clock recovery: Novel Analysis using a clock remodulation technique," *Journal of selected topics in quantum electronics on enabling technologies for digital optical communication systems*, p. (DOI : 10.1109/JSTQE.2010.2040246), 2010.

[125] C. Boerner, V. Marembert, S. Ferber, C. Schubert, C. Schmidt-Langhorst, R. Ludwig, and H. G. Weber, "320 Gbit/s clock recovery with electro-optical PLL using a bidirectionally operated electroabsorption modulator as phase comparator," in *Optical Fiber Communication Conference*, Anaheim, California, 2005, p. OTuO3.

[126] H. C. H. Mulvad, E. Tangdiongga, O. Raz, J. Herrera, H. De Waardt, and H. J. S. Dorren, "640 Gbit/s OTDM lab-transmission and 320 Gbit/s field-transmission with SOA-based clock recovery," in *Optical Fiber Communication Conference*, San Diego, California, 2008, p. OWS2.

[127] G. Aubin, T. Montalant, J. Moulu, F. Pirio, J.-B. Thomine, and F. Devaux, "40 Gbit/s OTDM soliton transmission over transoceanic distances," *Electron. Lett.*, vol. 32, no. 24, pp. 2188–2189, 1996.

[128] B. Sartorius, "All-Optical 3R Signal Regeneration," in *European Conference on Optical Communications*, Munich, Germany, 2000, p. We 9.4.1.

[129] S. B. Jun, P. K. J. Park, H. Kim, and Y. C. Chung, "Ultra-fast clock recovery based on pre-embedded sub-harmonic clock in optical burst/packet networks," in *Optical Fiber Communication Conference*, Anaheim, California, 2007, p. JThA55.

[130] M. Jinno and T. Matsumoto, "Optical tank circuits used for all-optical timing recovery," *IEEE J. Quantum Electron.*, vol. 28, no. 4, pp. 895–900, 1992.

[131] B. Franz, "Optical signal processing for very high speed ($>$ 40 Gbit/s) ETDM binary NRZ clock recovery," in *Optical Fiber Communication Conference*, Anaheim, California, 2001, p. MG1.

[132] V. Roncin, B. Le-Guyader, S. Lobo, B. Clouet, and J. C. Simon, "43 Gbit/s Bit Error Rate Assessment of a Simple All Optical Clock Recovery Scheme," in *European Conference on Optical Communications*, Glasgow, UK, 2005, p. Th 1.3.7.

[133] M. Funabashi, Z. Zhu, Z. Pan, and S. J. B. Yoo, "Packet-by-packet all-optical burst-mode 3R regeneration in an optical-label switching router," in *Optical Fiber Communication Conference*, Anaheim, California, 2006, p. OFJ1.

[134] G. Contestabile, R. Proietti, N. Calabretta, A. D'Errico, M. Presi, and E. Ciaramella, "40 Gb/s WDM NRZ-DPSK All-Optical Clock Recovery and Data Demodulation based on a Periodic Bragg Filter," in *Optical Fiber Communication Conference*, San Diego, California, 2008, p. OMN2.

[135] C. Bintjas, K. Yiannopoulos, N. Pleros, G. Theophilopoulos, M. Kalyvas, H. Avramopoulos, and G. Guekos, "Clock recovery circuit for optical packets," *IEEE Photonics Technol. Lett.*, vol. 14, no. 9, pp. 1363–1365, 2002.

[136] L. Stampoulidis, E. Kehayas, H. Avramopoulos, Y. Liu, E. Tangdiongga, and H. J. S. Dorren, "40 Gb/s fast-locking all-optical packet clock recovery," in *Optical Fiber Communication Conference*, Anaheim, California, 2005, p. OThE2.

[137] V. Roncin, Q. T. Le, J. Poette, S. Lobo, L. Bramerie, and J. C. Simon, "Passive All-optical Clock Recovery demonstration at 42.66 Gbit/s with Bragg-gratings based Fabry-Perot Filter," in *European Conference on Optical Communications*, Berlin, Germany, 2007, p. Tu 4.5.4.

[138] T. Von Lerber, J. Tuominen, H. Ludvigsen, S. Honkanen, and F. Kueppers, "Multi-channel and rate all-optical clock recovery," *IEEE Photonics Technol. Lett.*, vol. 18, no. 12, pp. 1395–1397, 2006.

[139] I. D. Phillips, A. D. Ellis, T. Widdowson, D. Nesset, A. E. Kelly, and D. Trommer, "100 Gbit/s optical clock recovery using electrical phaselocked loop consisting of commercially available components," *Electron. Lett.*, vol. 36, no. 7, pp. 650–652, 2000.

[140] F. G. Agis, C. Ware, D. Erasme, S. Kurimura, and H. Nakajima, "Opto-Electronic Phase-Locked Loop Using Adhered-Ridge-Waveguide Periodically Poled Lithium Niobate for High-Bit-Rate Clock Recovery," in *Optical Fiber Communication Conference*, San Diego, California, 2008, p. JWA72.

[141] D. T. K. Tong, K. L. Deng, B. Mikkelsen, G. Raybon, K. F. Dreyer, and J. E. Johnson, "160 Gbit/s clock recovery using electroabsorption modulator-based phase-locked loop," *Electron. Lett.*, vol. 36, no. 23, pp. 1951–1952, 2000.

[142] O. Kamatani and S. Kawanishi, "Ultrahigh-speed clock recovery with phase lock loop based onfour-wave mixing in a traveling-wave laser diode amplifier," *J. Lightw. Technol.*, vol. 14, no. 8, pp. 1757–1767, 1996.

[143] T. Yamamoto, C. Schmidt, E. Dietrich, C. Schubert, J. Berger, R. Ludwig, and H. G. Weber, "40 GHz optical clock extraction from 160 Gbit/s data signals using PLL-based clock recovery," in *Optical Fiber Communication Conference*, Anaheim, California, 2002, p. TuN5.

[144] L. K. Oxenløwe, D. Zibar, M. Galili, A. T. Clausen, L. J. Christiansen, and P. Jepepesen, "Filtering-Assisted Cross-Phase Modulation in a Semiconductor Optical Amplifier Enabling 320 Gb/s Clock Recovery," in *European Conference on Optical Communications*, Glasgow, UK, 2005, p. We 3.5.5.

[145] C. Boerner, C. Schubert, C. Schmidt, V. Hilliger, E. Marembert, J. Berger, S. Ferber, E. Dietrich, and H. G. Ludwig, R. Weber, "160 Gbit/s Clock Recovery With Electro-Optical PLL Using a Bidirectionally Operated Electroabsorption Modulator as Phase Comparator," in *Optical Fiber Communication Conference*, Los Angeles, California, 2003, p. FF3.

[146] J. Lasri, D. Dahan, A. Bilenca, G. Eisenstein, and D. Ritter, "Clock recovery at multiple bit rates using direct optical injection locking of a self-oscillating InGaAs-InP heterojunction bipolar phototransistor," *IEEE Photonics Technol. Lett.*, vol. 13, no. 12, pp. 1355–1357, 2001.

[147] Z. Hu, H. F. Chou, J. E. Bowers, and D. J. Blumenthal, "40-Gb/s optical clock recovery using a compact traveling-wave electroabsorption modulator-based ring oscillator," *IEEE Photonics Technol. Lett.*, vol. 16, no. 5, pp. 1376–1378, 2004.

[148] P. Barnsley, H. Wickes, G. Wickens, and D. Spirit, "All-optical clock recovery from 5 Gb/s RZ data using a self-pulsating 1.56 μm laser diode," *IEEE Photonics Technol. Lett.*, vol. 3, no. 10, pp. 942–945, 1991.

[149] B. Sartorius, C. Bornholdt, O. Brox, H. J. Ehrke, D. Hoffmann, R. Ludwig, and M. Mohrle, "All-optical clock recovery module based on self-pulsating DFB laser," *Electron. Lett.*, vol. 34, no. 17, pp. 1664–1665, 1998.

[150] K. Smith and J. K. Lucek, "All-optical clock recovery using a mode-locked laser," *Electron. Lett.*, vol. 28, no. 19, pp. 1814–1816, 1992.

[151] S. Bigo and E. Desurvire, "20 GHz all-optical clock recovery based on fibre laser mode-locking with fibre nonlinear loop mirror as variable intensity/phase modulator," *Electron. Lett.*, vol. 31, no. 21, pp. 1855–1857, 1995.

[152] A. D. Ellis, K. Smith, and D. M. Patrick, "All optical clock recovery at bit rates up to 40 Gbit/s," *Electron. Lett.*, vol. 29, no. 15, pp. 1323–1324, 1993.

[153] H. K. Lee, J. T. Ahn, M.-Y. Jeon, K. H. Kim, D. S. Lim, and C.-H. Lee, "All-optical clock recovery from NRZ data of 10 Gb/s," *IEEE Photonics Technol. Lett.*, vol. 11, no. 6, pp. 730–732, 1999.

[154] K. Vlachos, G. Theophilopoulos, A. Hatziefremidis, and H. Avramopoulos, "30 Gb/s all-optical clock recovery circuit," *IEEE Photonics Technol. Lett.*, vol. 12, no. 6, pp. 705–707, 2000.

[155] E. Tangdiongga, J. P. Turkiewicz, G. D. Khoe, and H. De Waardt, "Clock recovery by a fiber ring laser employing a linear optical amplifier," *IEEE Photonics Technol. Lett.*, vol. 16, no. 2, pp. 611–613, 2004.

[156] V. Mikhailov and P. Bayvel, "Multiwavelength all-optical clock recovery using an integrated semiconductor optical amplifier array," in *European Conference on Optical Communications*, Munich, Germany, 2000, p. We 7.4.2.

[157] B. R. Koch, J. S. Barton, M. Masanovic, Z. Hu, J. E. Bowers, and D. J. Blumenthal, "35 Gb/s monolithic all-optical clock recovery pulse source," in *Optical Fiber Communication Conference*, Anaheim, California, 2007, p. OWP2.

[158] C. Bornholdt, S. Bauer, M. Mohrle, H.-P. Nolting, and B. Sartorius, "All optical clock recovery at 80 GHz and beyond," in *European Conference on Optical Communications*, vol. 4, 2001, pp. 502–503.

[159] D. Chiaroni, B. Lavigne, A. Dupas, P. Guerber, A. Jourdan, F. Devaux, C. Bornholdt, S. Bauer, B. Sartorius, and M. Mohrle, "All-optical clock recovery from 10 Gbit/s asynchronous data packets," in *European Conference on Optical Communications*, Munich, Germany, 2000, p. Th 10.4.5.

[160] H. Yokoyama, Y. Hashimoto, H. Kurita, and I. Ogura, "Two-stage all-optical subharmonic clock recovery using modelocked semiconductor lasers," *Electron. Lett.*, vol. 36, no. 18, pp. 1577–1578, 2000.

[161] C. Bornholdt, J. Slovak, M. Mohrle, and B. Sartorius, "Application of a 80 GHz all-optical clock in a 160 km transmission experiment," in *Optical Fiber Communication Conference*, Anaheim, California, 2002, p. TuN6.

[162] T. Ohno, K. Sato, T. Shimizu, T. Furuta, and H. Ito, "Recovery of 40 GHz optical clock from 160 Gbit/s data using regeneratively modelocked semiconductor laser," *Electron. Lett.*, vol. 39, no. 5, pp. 453–455, 2003.

[163] P. J. Maguire, D. A. Reid, L. P. Barry, A. O'Hare, S. Lobo, V. Roncin, M. Gay, L. Bramerie, and J. C. Simon, "Dispersion insensitive, high-speed optical clock recovery based on a mode-locked laser diode," in *Optical Fiber Communication Conference*, San Diego, California, 2008, p. OWS4.

[164] B. Lavigne, J. Renaudier, F. Lelarge, O. Legouezigou, H. Gariah, and G. Duan, "First demonstration of a polarization insensitive low time jitter and optical noise tolerant all-optical clock recovery at 40 GHz using a self-pulsating laser tandem," in *Optical Fiber Communication Conference*, Anaheim, California, 2006, p. PDP24.

[165] J. Slovak, C. Bornholdt, S. Bauer, J. Kreissl, M. Schlak, and B. Sartorius, "Novel concept for all-optical clock recovery from NRZ format PRBS data streams," in *Optical Fiber Communication Conference*, Anaheim, California, 2006, p. OThS6.

[166] J. Renaudier, G. H. Duan, J. G. Provost, H. Debregeas-Sillard, and P. Gallion, "Phase correlation between longitudinal modes in semiconductor self-pulsating DBR lasers," *IEEE Photonics Technol. Lett.*, vol. 17, no. 4, pp. 741–743, 2005.

[167] C. Bornholdt, J. Slovak, M. Mohrle, and B. Sartorius, "Jitter analysis of all-optical clock recovery at 40 GHz," in *Optical Fiber Communication Conference*, Atlanta, Georgia, 2003, p. MF97.

[168] J. Renaudier, "Etude de l'autopulsation par verrouillage de modes passif dans les lasers à semi-conducteurs à réflecteur de Bragg distribué. Application à la récupération d'horloge tout-optique à 40 Gbit/s," Ph.D. dissertation, ENST Paris, Paris, France, 2006.

[169] W. Idler, A. Klekamp, R. Dischler, J. Lazaro, and A. Konczykowska, "System performance and tolerances of 43 Gbit/s ASK and DPSK modulation formats," in *European Conference on Optical Communications*, Rimini, Italy, 2003, p. Th.2.6.3.

[170] M. Gay, "Étude théorique et expérimentale de l'impact de la régénération 2R dans un système de transmission optique haut débit," Ph.D. dissertation, Institut National des Sciences Appliquées de Rennes, Lannion, France, 2006.

[171] G. Contestabile, A. D'Errico, M. Presi, and E. Ciaramella, "40-GHz all-optical clock extraction using a semiconductor-assisted Fabry-Pérot filter," *IEEE Photonics Technol. Lett.*, vol. 16, no. 11, pp. 2523–2525, 2004.

[172] X. Zhou, C. Lu, P. Shum, H. H. M. Shalaby, T. H. Cheng, and P. Ye, "A performance analysis of an all-optical clock extraction circuitbased on Fabry-Perot filter," *J. Lightw. Technol.*, vol. 19, no. 5, pp. 603–613, 2001.

[173] T. Wang, Z. Li, C. Lou, Y. Wu, and Y. Gao, "Comb-like filter preprocessing to reduce the pattern effect in theclock recovery based on SOA," *IEEE Photonics Technol. Lett.*, vol. 14, no. 6, pp. 855–857, 2002.

[174] B. Clouet, "Etude de la dispersion modale de polarisation dans les systèmes régénérés optiquement," Ph.D. dissertation, ENSSAT - Université de Rennes 1, Lannion, France, 2007.

[175] Y. Benlachtar, R. I. Killey, and P. Bayvel, "The effects of polarization-mode dispersion on the phase of the recovered clock," *J. Lightw. Technol.*, vol. 24, no. 11, pp. 3944–3952, 2006.

Appendix 1: Jahn's SOA model

The amplitude and phase of the pulses travelling the SOA are separated by using:

$$A = \sqrt{P} \exp(i\Phi) \tag{6-2}$$

and Equation (6-2) is injected in the propagation equation of the optical field:

$$\frac{\partial A}{\partial z} + \frac{1}{v_g} \times \frac{\partial A}{\partial t} = \frac{1}{2} g A \tag{6-3}$$

with $P(t, z)$ is the power, $\Phi(t, z)$ is the phase of pulses, and we change $A(t, z)$ to $A(\tau, Z)$ to be in the reference frame moving with the pulse:

$$A(\tau, Z) = \sqrt{P(\tau, Z)} \exp(i\Phi(\tau, Z)) \tag{6-4}$$

$$z = Z \tag{6-5a}$$

$$\tau = t - \frac{z}{v_g} \tag{6-5b}$$

The first term on the left side of Equation (6-3) is now written by:

$$\frac{\partial A}{\partial z} = \frac{\partial A}{\partial Z} - \frac{1}{v_g} \times \frac{\partial A}{\partial \tau} \tag{6-6}$$

and the second term becomes:

$$\frac{\partial A}{\partial t} = \frac{\partial A}{\partial \tau} \tag{6-7}$$

Introducing Equations (6-6) and (6-7) in (6-3), we obtain:

$$\frac{\partial A}{\partial z} = \frac{1}{2} g A \tag{6-8}$$

Equations (6-4) and (6-8) together lead to the following system:

$$\frac{\partial P}{\partial z} = g P \tag{6-9a}$$

$$\frac{\partial \Phi}{\partial z} = -\frac{1}{2} \alpha g \tag{6-9b}$$

System (6-9) can be integrated over the SOA length to provide:

$$P(\tau, L) = P(\tau, 0) \exp[h(\tau)] \tag{6-10}$$

$$\Phi(\tau, L) = \Phi(\tau, 0) - \frac{\alpha}{2} h(\tau) \tag{6-11}$$

The function $h(\tau)$, which represents the accumulated gain at each point of the pulse profile is defined by:

$$h(\tau) = \int_0^L g(z, \tau) \, dz \tag{6-12}$$

If the solution of the differential gain is known, then the evolution of the pulse at the amplifier output is too. While the differential gain $g(z, \tau)$ is a function of the population N_1 only, the evolutions of the two populations N_1 and N_2 are given by the following rate equations:

$$\frac{\partial N_1}{\partial t} = \frac{IU}{q} - \frac{PN_1}{E_s} - \frac{N_1}{\tau_s} - \frac{\Delta N}{\tau_c} \tag{6-13}$$

$$\frac{\partial N_2}{\partial t} = \frac{I(1-U)}{q} - \frac{N_2}{\tau_s} + \frac{\Delta N}{\tau_c} \tag{6-14}$$

with N_1 and ΔN are defined by:

$$N = N_1 + N_2 \tag{6-15}$$

$$\Delta N = N_1(1-U) - N_2 U = N_1 - UN \tag{6-16}$$

Sum of Equations (6-13) and (6-14) leads to:

$$\frac{\partial N}{\partial t} = \frac{I}{q} - \frac{PN_1}{E_s} - \frac{N}{\tau_s} \tag{6-17}$$

Otherwise, by replacing (6-16) into (6-13), we obtain:

$$\frac{\partial N_1}{\partial t} = \frac{IU}{q} - \frac{PN_1}{E_s} - \frac{N_1}{\tau_s} - \frac{N_1}{\tau_c} + \frac{UN}{\tau_c} \tag{6-18}$$

For all next calculations, we take into account the approximation: $\tau_c \ll \tau_s$. By isolating N from Equation (6-18) the following system can be obtained:

$$N = \frac{\tau_s}{U} \times \frac{\partial N_1}{\partial t} - \frac{I\tau_c}{q} + \frac{\tau_c}{UE_s}PN_1 + \frac{N_1}{U} \tag{6-19a}$$

$$\frac{\partial N}{\partial t} = \frac{\tau_c}{U} \times \frac{\partial^2 N_1}{\partial t^2} + \frac{\tau_c}{UE_s} \times \frac{\partial (PN_1)}{\partial t} + \frac{1}{U} \times \frac{\partial N_1}{\partial t} \tag{6-19b}$$

Introduction of system (6-19) into Equation (6-17) leads to one partial differential equation of only one unknown N_1:

$$\frac{\partial^2 N_1}{\partial t^2} + \frac{1}{\tau_c} \times \frac{\partial N_1}{\partial t} = \frac{IU}{q\tau_c} - \frac{1}{\tau_s\tau_c}N_1 - \left(\frac{U}{E_s\tau_c} + \frac{1}{E_s\tau_s}\right)PN_1 - \frac{1}{E_s} \times \frac{\partial (PN_1)}{\partial t} \tag{6-20}$$

This equation corresponds to Equation (3-13) of Chapter 3. To clarify Equation (6-20), we introduce some notations for all the constants:

$$A_1 = \frac{1}{\tau_c}$$

$$A_2 = \frac{IU}{q\tau_c}$$

$$A_3 = \frac{1}{\tau_s\tau_c}$$

$$A_4 = \frac{U}{E_s\tau_c} + \frac{1}{E_s\tau_s}$$

$$A_5 = \frac{1}{E_s}$$

Then, Equation (6-20) becomes:

$$\frac{\partial^2 N_1}{\partial t^2} + A_1 \frac{\partial N_1}{\partial t} = A_2 - A_3 N_1 - A_4 P N_1 - A_5 \frac{\partial (P N_1)}{\partial t} \tag{6-21}$$

To obtain the equation representing the evolution of the differential gain g, the two following relations are used:

$$g = \frac{\Gamma a}{V} N_1 \tag{6-22}$$

$$A_6 = \frac{\Gamma a}{V} A_2 \tag{6-23}$$

Consequently, the differential gain is the solution of:

$$\frac{\partial^2 g}{\partial t^2} + A_1 \frac{\partial g}{\partial t} = A_6 - A_3 g - A_4 P g - A_5 \frac{\partial (Pg)}{\partial t} \tag{6-24}$$

If (6-24) is integrated over the SOA length and we make use of (6-9) and (6-10) to eliminate the product Pg, then $h(\tau)$ is the solution of the following differential equation:

$$\frac{d^2 h}{d\tau} + A_1 \frac{dh}{d\tau} = \int_0^L A_6 dz - A_3 h - A_4 \int_0^L \frac{dP(\tau, z)}{dz} dz - A_5 \frac{d}{d\tau} \left(\int_0^L \frac{dP(\tau, z)}{dz} dz \right) \tag{6-25}$$

We remind that:

$$\int_0^L \frac{dP(\tau, z)}{dz} dz = P(\tau, L) - P(\tau, 0) = P(\tau, 0) \left[\exp(h) - 1 \right] \tag{6-26}$$

Introduction of Equation (6-26) into (6-25) gives:

$$\begin{aligned}
\frac{d^2 h(\tau)}{d\tau^2} + A_1 \frac{dh(\tau)}{d\tau} &= A_6 L - A_3 h(\tau) - A_4 P(\tau, 0) \left[\exp(h(\tau)) - 1 \right] \\
&\quad - A_5 \exp(h(\tau)) \frac{dP(\tau, 0)}{d\tau} - A_5 P(\tau, 0) \exp(h(\tau)) \frac{dh(\tau)}{d\tau} \\
&\quad + A_5 \frac{dP(\tau, 0)}{d\tau}
\end{aligned} \tag{6-27}$$

Equation (6-27) is in fact Equation (3-15) of Chapter 3, with $P(\tau, 0)$ is the power of the input pulse.

Appendix 2: Agrawal's SOA model

The same transformations are applied to optical field expression as described in Appendix 1 and the function $h(\tau)$, which represents the accumulated gain at each point of the pulse profile, is always defined by Equation (6-12). In this model [56], it is considered that all available carriers, which relax with the interband time constant τ_s, contribute directly to the amplifier gain and the rate equation of the carrier density M is given by:

$$\frac{\partial M}{\partial t} = \frac{I}{qV} - \frac{M}{\tau_s} - \frac{g(M)}{\hbar\omega_0}|A|^2 \tag{6-28}$$

The differential gain $g(z,\tau)$ is related to the total carrier density M by:

$$g(M) = \Gamma a(M - M_0) \tag{6-29}$$

We remind that:

I is the current

a is the gain coefficient

ω_0 is the signal pulsation

M is the carrier density

M_0 is the carrier density required for transparency

By injecting (6-29) into Equation (6-28), we obtain:

$$\frac{\partial g}{\partial t} = \frac{g_0 - g}{\tau_s} - \frac{gP}{E_s} \tag{6-30}$$

with $g_0 = \Gamma a M_0 \left(\frac{I}{I_0} - 1\right)$ is the small-signal gain

$I_0 = \frac{qVM_0}{\tau_s}$ is the current required for transparency

If we integrate Equation (6-30) over the SOA length and make use of (6-9) to eliminate the product gP, then $h(\tau)$ is the solution of the following ordinary differential equation:

$$\frac{dh}{d\tau} = \frac{g_0 L - h}{\tau_s} - \frac{P(\tau,0)}{E_s}[\exp(h) - 1] \tag{6-31}$$

For a given input pulse profile $P(\tau,0)$, Equation (6-31) can be solved to obtain $h(\tau)$ and the output pulse profile is deduced from Equation (6-10).

Appendix 3: Publications

1. V. Roncin, S. Lobo, **M. N. Ngo**, L. Bramerie, A. O'Hare, M. Joindot, and J.-C. Simon, "Patterning effects in All-Optical Clock recovery: Novel Analysis using a clock remodulation technique," *Journal of selected topics in quantum electronics*, vol. 16, no. 5, pp. 1495–1502, 2010.

2. **M. N. Ngo**, Q. T. Le, V. Roncin, M. Gay, L. Bramerie, and J.-C. Simon, "Etude numérique de l'impact du filtrage optique sur les propriétés régénératives d'un convertisseur de longueur d'onde interférométrique en configuration différentielle," in *Journées Nationales d'Optique Guidée*, Lille, France, 2009, p. A10.2.

3. **M. N. Ngo**, M. Gay, L. Bramerie, G. Girault, Q. T. Le, J.-C. Simon, R. Brenot, G.-H. Duan, D. Reid, and L. Barry, "Characterisation of semiconductor optical amplifiers for all-optical regeneration," in *5th Optoelectronic and Photonic Winter School, CMOS Photonics*, Trento, Italia, 2009.

4. **M. N. Ngo**, V. Roncin, Q. T. Le, L. Bramerie, D. Chevallier, L. Lablonde, A. Shen, G.-H. Duan, and J.-C. Simon, "Bit-Error-Rate Performance Enhancement of All-Optical Clock Recovery at 42.66 Gb/s Using Passive Prefiltering," *IEEE Photonics Technol. Lett.*, vol. 20, no. 18, pp. 1557–1559, 2008.

5. **M. N. Ngo**, M. Gay, L. Bramerie, G. Girault, Q. T. Le, J.-C. Simon, R. Brenot, G.-H. Duan, D. Reid, and L. Barry, "Characterisation of semiconductor optical amplifiers for all-optical regeneration," in *International workshop on photonics and applications*, Nha Trang, Vietnam, 2008, p. B35.

6. **M. N. Ngo**, V. Roncin, Q. T. Le, S. Lobo, M. Gay, L. Bramerie, J.-C. Simon, A. Shen, and G.-H. Duan, "High Performance and Polarisation-Insensitive BER Assessment of a 42.66 Gbit/s All-Optical Clock Recovery," in *European Conference on Optical Communications*, Brussels, Belgium, 2008, p. Mo.3.C.6.

7. **M. N. Ngo**, V. Roncin, Q. T. Le, L. Bramerie, D. Chevallier, L. Lablonde, A. Shen, G.-H. Duan, and J.-C. Simon, "Amélioration de la qualité d'une récupération d'horloge tout-optique en utilisant un filtrage passif," in *Journées Nationales d'Optique Guidée*, Lannion, France, 2008, p. Ma.3.6.

8. **M. N. Ngo**, V. Roncin, Q. T. Le, S. Lobo, M. Gay, L. Bramerie, A. Shen, G.-H. Duan, and J.-C. Simon, "Caractérisation de dispositifs de récupération d'horloge tout-optique par la mesure de taux d'erreur binaire," in *Journées Nationales d'Optique Guidée*, Lannion, France, 2008, p. A.5.2.

9. J. C. Simon, M. Gay, L. Bramerie, V. Roncin, M. Joindot, T. Chartier, Lobo, G. Girault, Q. T. Le, T. N. Nguyen, and **M. N. Ngo**, "Long Distance Transmission Using Optical Regeneration," in *Optical Fiber Communication Conference*, San Diego, California, 2008, p. OWS1.

10. **M. N. Ngo**, G. Girault, J.-C. Simon, and V. Roncin, "Utilisation du mélange à quatre ondes dans une fibre optique pour la création d'une source impulsionnelle accordable synchronisée sur un train d'impulsions maître," in *Journées Nationales d'Optique Guidée*, Grenoble, France, 2007, p. P8.

11. G. Girault, **M. N. Ngo**, D. Delubac, J.-C. Simon, and V. Roncin, "Analyse de la sensibilité à la polarisation de SOA utilisés en conversion de longueur d'onde," in *Journées Nationales d'Optique Guidée*, Grenoble, France, 2007, p. ME5.
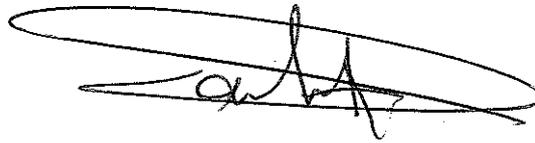
VU :

Le Directeur de thèse

VU :

Le Responsable de l'École Doctorale

DT ue| 2olo/EussAT |7 no 95

VU pour autorisation de soutenance

Rennes, le 15 juillet 2olo

Le Président de l'Université de Rennes 1

Guy Cathelineau

VU après soutenance pour autorisation de publication :

Le Président de Jury,

FoCCLoT Hervé

Résumé

Face à l'augmentation constante du trafic lié notamment à Internet, la demande de capacité dans les réseaux coeur ne cesse de croître : le débit par canal des systèmes WDM a atteint 40 Gbit/s et va bientôt atteindre 100 Gbit/s et 160 Gbit/s. A partir de 40 Gbit/s, le traitement tout-optique du signal peut offrir une solution intéressante pour réduire la consommation ainsi que le coût des systèmes optiques du futur. L'objectif de cette thèse est de développer des portes optiques non-linéaires et d'explorer des méthodes de récupération d'horloge optique, toutes à base des semiconducteurs, pour la régénération tout-optique de signaux à un débit égal ou supérieur à 40 Gbit/s. La dynamique ultrarapide du gain des amplificateurs optiques à semiconducteurs (SOA) est étudiée afin de l'exploiter pour développer des fonctions simples et compactes permettant la remise en forme du signal. Concernant la fonction de resynchronisation, différentes récupérations d'horloge tout-optiques ont été étudiées dans cette thèse.

La première partie des travaux a été consacrée entièrement aux portes optiques non-linéaires à base des SOA pour des applications à la régénération 2R. L'expérience pompe-sonde permettant mesurer le temps de récupération du gain a été réalisée pour étudier la dynamique des SOA. Dans cette thèse, il a été démontré que le SOA massif à fort confinement et le SOA ultra-long à boîtes quantiques sont les plus adaptés pour un fonctionnement à 40 Gbit/s avec des temps de récupération du gain respectivement de 20 ps et 10 ps. Les études expérimentales ainsi que numériques ont mis en évidence la contribution importante des effets intrabandes à la dynamique du gain lorsque des SOA sont saturés par des impulsions courtes (quelques picosecondes). Le SOA massif de fort confinement a été associé avec un absorbant saturable (SA) pour constituer une fonction de régénération 2R complète. L'efficacité du régénérateur SOA-SA pour la remis en forme du signal à 40 Gbit/s a été démontrée expérimentalement and numériquement.

La deuxième partie des travaux a été dédiée à la récupération d'horloge à base de lasers auto-pulsants en vue d'une application à la régénération 3R à 40 Gbit/s. Nous avons proposé une technique originale pour évaluer la performance des fonctions de récupération d'horloge, qui consiste à remoduler l'horloge récupérée. Une nouvelle configuration a été élaborée pour améliorer la qualité de l'horloge récupérée par le laser auto-pulsant à base de matériau massif. Elle consiste à introduire un pré-filtrage passif devant le laser. La sensibilité à la polarisation des récupérations d'horloge a été également étudiée. La récupération d'horloge utilisant le laser massif suivi par le laser à boîtes quantiques a montré son insensibilité à la polarisation du signal injecté par la mesure du taux d'erreur binaire. Enfin, une étude préliminaire sur la tolérance des récupérations d'horloge à la dispersion modale de polarisation a été menée.

Mots-clés : amplificateurs optiques à semiconducteurs, lasers auto-pulsants à semiconducteurs, récupération d'horloge optique, régénération tout-optique

Abstract

The optical backbone networks are facing a continuous and tremendous growth of the Internet traffic, requiring to increase the capacity of the transmission systems: WDM systems with a bit rate of 40 Gbit/s do exist and 100 Gbit/s and 160 Gbit/s will be reached soon. At the bit rates of 40 Gbit/s and higher, all-optical signal processing techniques are a very interesting approach in order to reduce the power consumption and the cost of future optical networks. The objective of this work is to develop non-linear optical gates and explore Optical Clock Recovery (OCR) functions based on semiconductor technology for all-optical regeneration at 40 Gbit/s and above. The non-linear dynamic gain of Semiconductor Optical Amplifiers (SOA) was investigated in order to perform simple and compact signal reshaping devices. For retiming function, several OCR configurations based on Self-Pulsating (SP) lasers were investigated during this thesis.

The first part of this work is devoted to the SOA-based non-linear optical gates for all-optical 2R regeneration. Gain dynamics assessments using the pump-probe experiment were performed to measure the SOA recovery time. In this work, it is demonstrated that the highly confined bulk based SOA and the long quantum-dot based SOA exhibiting respectively gain recovery times of 20 ps and of 10 ps are suitable for 40 Gbit/s operation. The numerical and experimental studies clarified the important role of intraband effects in SOA dynamics under short pulse (a few of picoseconds) saturations, which makes these SOAs compatible for ultrahigh bit rate operations. The highly confined bulk based SOA was cascaded with a Saturable Absorber (SA) to constitute a complete 2R regeneration function. The reshaping capability of the SOA-SA regenerator has been successfully demonstrated at 40 Gbit/s by experiments and simulations.

The second part of this work explores some clock recovery functions based on SP lasers for 3R regeneration at 40 Gbit/s. An original characterisation technique consisting in remodulating the extracted clock was proposed to evaluate the OCR performance. A simple solution using passive pre-filtering was developed to enhance the clock quality extracted by a bulk based SP laser. The polarisation sensitivity of various OCR devices was evaluated. The OCR based on the bulk based SP laser followed by the quantum-dot based SP laser exhibits a total insensitivity to the arriving signal polarisation thanks to Bit-Error-Rate measurements. At last, a preliminary study was devoted to investigate OCR tolerance to Polarisation Mode Dispersion (PMD).

Key words: semiconductor optical amplifiers, self-pulsating semiconductor lasers, optical clock recovery, all-optical regeneration